Periodic variability in Active Galactic Nuclei

INAUGURAL-DISSERTATION

zur Erlangung des Doktorgrades
der Matematisch-Naturwissenschaftlichen Fakultät
der Universität zu Köln

vorgelegt von

Nadezhda Kudryavtseva
aus Riga, Lettland

Köln 2008

Berichterstatter: Prof. Dr. J. Anton Zensus

Prof. Dr. Andreas Eckart

Tag der mündlichen Prüfung: 15.10.2008

0.1 Abstract

In this doctoral thesis, multi-frequency very long baseline interferometry observations together with multi-frequency total flux-density variability data of compact relativistic jets in active galactic nuclei are presented and analyzed. The main goal of the thesis is to investigate the physical mechanisms in relativistic jets responsible for such phenomena as the co-existence of moving and stationary jet components, jet wiggling and precession. We also aim to study the connection between the structural changes in the relativistic jets and flares in the total flux-density light curves and to find observational evidences for the appearance of a primary perturbation in the base of the jet and its further propagation. In this thesis we also investigate which physical mechanisms are responsible for periodical total flux-density variability and to search for periodicities as a sign of jet precession.

In order to study the jet physics we used the multi-frequency very long baseline interferometry technique which gives the highest possible in astronomy resolution. We also compared jet structural changes with single-dish multi-frequency observations spanning more than 30 years together with optical and γ-ray data. In particular, analysis of the long-term kinematics of two active galactic nuclei S5 1803+784 and 0605-085 shows evidence for jet precession. The jet is precessing with a timescale similar to a period in the total flux-density light curves. Moreover, I show that jet structural changes are correlated with the total flux-density variability. Analyzing the long-term kinematics of S5 1803+784 I found for the first time that its jet consists of seven "oscillating" jet features which were observed for more than 20 years.

We found five blazars and quasars (3C 454.3, 3C 446, CTA 102, 0133+476, and 0605-085) which show clear periodical total flux-density radio variability. Moreover, in the case of 3C 454.3 and 3C 446 the predicted flares were meanwhile observed. In this thesis I propose a new physical approach for searching periodicities and calculating flaring activity cycles in radio total flux-density variability. I use the separation of the flares into "core" and "jet" outbursts. I found that for the sources 3C 454.3 and 3C 446 optically thick "core" outbursts appear periodically.

0.2 Zusammenfassung

In dieser Doktorarbeit werden Multi-Frequenz-Beobachtungen mit Hilfe der Interferometrie mit langen Basislinien (Very Long baseline Interferometry - VLBI) zusammen mit Multi-Frequenz-Flussdichte-Variabilitätsdaten kompakter relativistischer Jets präsentiert und analysiert. Das Hauptziel der Arbeit ist die Erforschung physikalischer Mechnismen in relativistischen Jets, die verantwortlich sind für Phänomene wie die Koexistenz von beweglichen und stationaeren Jet-Komponenten, Jet-"Schlängeln" und -Präzession. Wir sind ebenfalls bestrebt, den Zusammenhangs zwischen strukturellen Veränderungen der relativistischen Jets und sogenannten "Flares" in den Lichtkurven der totalen Flussdichte zu untersuchen sowie Beobachtungsnachweise für das Auftreten einer primaeren Störung in der Basis des Jets und ihrer weiteren Ausbreitung zu finden. In dieser Arbeit prüfen wir weiterhin, welche physikalischen Mechanismen für eine periodische Variabilität der totalen Flussdichte verantwortlich zeichnen und wir suchen nach Periodizitäten als Anzeichen einer Jet-Präzession.

Um die Jet-Physik zu untersuchen, verwendeten wir die Technik der Multi-Frequenz-Interferometrie mit langen Basislinien, die die höchstmögliche astronomische Auflösung bietet. Ferner haben wir strukturelle Veränderungen des Jets mit Multi-Frequenz-Einzelteleskop-Beobachtungen aus mehr als 30 Jahren zusammen mit optischen und Gamma-Daten verglichen. Insbesondere die Analyse der Langzeit-Kinematik der beiden Aktiven Galaxienkerne S5 1803+784 und 0605-085 zeigt Anhaltspunkte für eine Präzession des Jets. Der Jet präzediert auf einer Zeitskala vergleichbar mit einer Periode in den Lichtkurven der totalen Flussdichte. Überdies zeige ich, dass strukturelle Änderungen im Jet mit der Variabilität der totalen Flussdichte korrelieren. Bei der Analyse der Langzeit-Kinematik von 1802+784 gelang mir zum ersten Mal der Nachweis, dass der Jet aus sieben "oszillierenden" Jet-Merkmalen besteht, die über mehr als 20 Jahre beobachtet wurden.

Wir konnten fünf Blazare ausmachen (3C454.3, 3C446, CTA102, 0133+476 und 0605-085), die deutlich eine periodische Variabilität der totalen Radioflussdichte aufweisen. Zudem wurden die im Fall von 3C454.3 und 3C446 vorhergesagten Flares zwischenzeitlich beobachtet. Im Zuge der Doktorarbeit stelle ich einen neuen physikalischen Ansatz zur Suche nach Periodizitäten und zur Berechnung von Aktivitätszyklen in der Variabilität der totalen Radioflussdichte vor. Dazu verwende ich die Einteilung der Flares

in "Kern-" und "Jet-"Ausbrüche. Ich habe festgestellt, dass für die Quellen 3C454.3 und 3C446 optisch dichte "Kern-"Ausbrüche periodisch auftreten.

0.3 The structure of the thesis

In the first chapter different types of active galaxies and the main topics I want to study will be presented. In the second chapter, the analysis of the variability of four sources 3C 454.3, 3C 446, CTA 102, and 0133+476 is discussed. The periodicities, the spectral energy distribution, and the opacity will be analysed. In the third chapter, I will discuss the analysis of the jet structure of S5 1803+784. The source shows unusual jet structure and evidence for jet precession. In the fourth chapter, jet kinematics and total flux-density variability of the highly periodic quasar 0605-085 will be presented. There is evidence for jet precession in 0605-085. In the last chapter I will summarize the results of this thesis and will list the main conclusions.

Contents

0.1 Abstract . . . 3
0.2 Zusammenfassung . . . 4
0.3 The structure of the thesis . . . 6

1 Introduction **11**
1.1 Questions we want to discuss in the thesis . . . 22

2 Periodicities in blazars **23**
2.1 Introduction . . . 23
2.2 Observations and Methods . . . 24
2.2.1 Time series analysis . . . 25
2.2.2 Autocorrelation method . . . 26
2.2.3 Jurkevich method . . . 26
2.2.4 Frequency-dependent time delays . . . 28
2.3 Results – 3C 454.3 (2251+158) . . . 31
2.3.1 Introduction . . . 31
2.3.2 Search for periodicity . . . 32
2.3.3 Jet components ejections . . . 34
2.3.4 Frequency-dependent time delays . . . 35
2.3.5 Binary black hole in 3C 454.3 . . . 40
2.3.6 Summary . . . 42
2.4 Results – 3C 446 (2223-052) . . . 47
2.4.1 Introduction . . . 47
2.4.2 Search for periodicity . . . 47
2.4.3 Jet components ejections . . . 50
2.4.4 Predicted flare . . . 51
2.4.5 Frequency-dependent time delays . . . 52
2.4.6 Summary . . . 56
2.5 Results – CTA 102 (2230+114) . . . 59

2.5.1 Introduction . . . 59
2.5.2 Search for periodicity . . . 59
2.5.3 Jet components ejections . . . 62
2.5.4 Frequency-dependent time delays . . . 63
2.5.5 Summary . . . 67
2.6 Results – 0133+476 . . . 71
2.6.1 Introduction . . . 71
2.6.2 Search for periodicity . . . 71
2.6.3 Frequency-dependent time delays . . . 73
2.6.4 Jet components ejections . . . 75
2.6.5 Summary . . . 76
2.7 Shapes of the flares . . . 80
2.8 Frequency-dependent core shifts . . . 82

3 Kinematics of S5 1803+784 87
3.1 Introduction . . . 87
3.2 Observations and data reduction . . . 88
3.2.1 Component Identification . . . 90
3.3 Oscillating jet components . . . 101
3.3.1 Comparison with literature data . . . 102
3.3.2 Comparison with geodetic VLBI data . . . 105
3.3.3 Flux-density evolution along the jet . . . 106
3.3.4 Displacement of **Ca** . . . 107
3.4 The "fast" component **B3** . . . 107
3.5 Significant position angle changes . . . 108
3.6 Evolution of the mean jet ridge line . . . 108
3.7 Evolution of the jet width . . . 109
3.8 Summary: kinematic results . . . 116
3.9 Opacity of 1803+784 . . . 117
3.10 Correlations & Anti correlations . . . 121
3.10.1 Correlation between core separation, position angle and the flux for each particular jet component: . . . 122
3.10.2 Correlations between the core flux and the core separation, position angle and the flux for each particular jet component: . . . 123
3.10.3 Correlation between the core separation, position angle and the flux for different jet components: . . . 125

3.10.4 Correlation between the core separation, position angle and the total flux-density variability: 128
3.11 Periodicity analysis 133
3.12 Binary black holes 141
3.13 Discussion 141

4 Kinematics of 0605-085 **145**
4.1 Introduction 145
4.2 Total flux-density light curves 146
4.3 Periodicity analysis 149
4.4 Frequency-dependent time delays 151
4.5 Spectral evolution 152
4.6 Kinematics of 0605-085 155
4.6.1 Component ejections 156
4.6.2 Stationary component $C1$ 157
4.6.3 Comparison of the trajectories 159
4.7 Precession model 165
4.8 Summary of the results 167
4.9 Discussion 168

5 Summary **171**

6 Abbreviations **177**

7 Acknowledgements **197**

8 Erklärung **199**
8.1 Curriculum Vitae 201

Chapter 1

Introduction

The main idea of this thesis is to study the physics of Active Galactic Nuclei (AGN), in particular phenomena related to the flux-density and structural variability of the parsec-scale jet. In general the term "active galactic nucleus", or AGN, refers to the existence of energetic phenomena in the nuclei, or central regions of galaxies, which cannot be attributed clearly and directly to stars.

The common picture of an AGN is that the material, pulled by the supermassive ($\sim 10^6 - 10^{10}$ solar masses) black hole's gravity in the center of a galaxy, streams toward the black hole in the center. Due to angular momentum conservation, this material forms the disc around the black hole, which is called accretion disc. Part of the disc material streams toward the black hole horizon and accretes, whereas another part of the disc material is accelerated by strong magnetic fields and forms the jet, ejected perpendicular to the accretion disc (Fig. 1.1). The jet is collimated and forms a very narrow outflow, which is observed up to kiloparsec scales. Around the jet, the low-velocity clouds and high-velocity clouds are observed, which are referred to as the broad-line region and the narrow-line region. The accretion disc is surrounded by an obscuring torus (or other geometrical form) of gas and dust, which hides the broad-line region in some directions. Therefore, when we look from the line of sight close to the jet direction, it is believed that we will see an object with the properties of blazars and quasars, whereas when we see from the line of sight which is more perpendicular to the jet direction, we see an object with the properties of a Seyfert I, Seyfert II or narrow-line radio galaxy (e.g. Antonucci et al. 2003, Urry & Padovani 1995).

This work is mainly intended to study two classes of active galactic nuclei

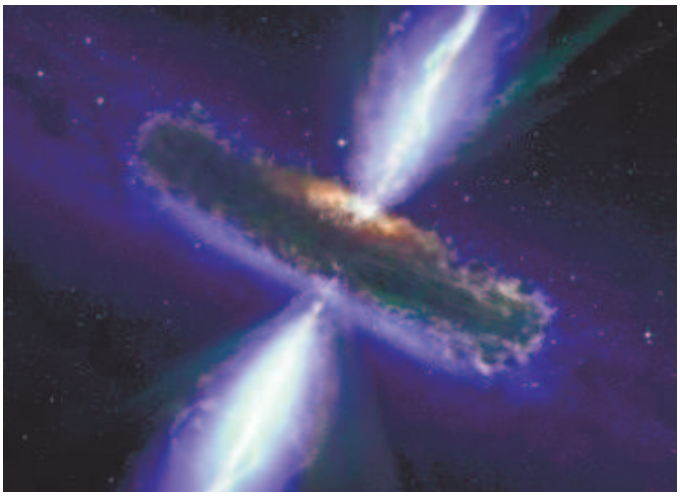

Figure 1.1: Cartoon of an active galactic nucleus with the jet streaming out perpendicular to the accretion disc.

- quasars and blazars, which are radio-loud (bright at radio wavelengths). Both of these classes of AGN have powerful radio jets and therefore are the best candidates to study the jet kinematics. Quasars are distant star-like objects in the optical wavelengths, identified with radio sources at high redshift. They show a time-variable continuum flux, large ultra-violet flux and evidence for broad emission lines. Blazars represent a small number of AGN that are extremely variable and have unusual spectral characteristics. They show high optical and radio polarization and lack emission features in the optical spectra. Their radio structure is mostly dominated by a compact radio core component and it is believed that the line of sight towards the blazars is smaller than that of quasars and is probably near 0 degrees (e.g. Urry et al. 2004). The variability of blazars is a very complex process, which is observed at all frequencies, from Gamma to radio wavelenghts and at all timescales, from hours to tenths of years (Wagner 1999 and references therein). A mixture of effects are most likely responsible for the flux-density variability, spectra and kinematics of blazars. Interstellar scincillation, jet instabilities and the presence of a secondary black hole in the middle of a galaxy nuclei can cause flux-density variability on different time scales.

One of the best techniques, which allows to study the closest vicinities of the black holes with the highest resolution is Very Long Baseline radio Interferometry (VLBI). It is based on the principle, that the spatial resolu-

tion of a telescope depends on the wavelength λ and the telescope diameter D, $\delta = \lambda/D$. By connecting different single-dish radio telescopes into a network and observing simultaneously the sources, we can create a telescope with a resolution proportional to the longest distance between different antennas. This technique gives the highest possible resolution in astronomy and allows us to study the parsec scale jets of distant blazars and quasars (see for more details http://www.aoc.nrao.edu/aips/cook.html). Figure 1.2 shows produced with the help of the VLBI technique images of the inner parsecs of AGN.

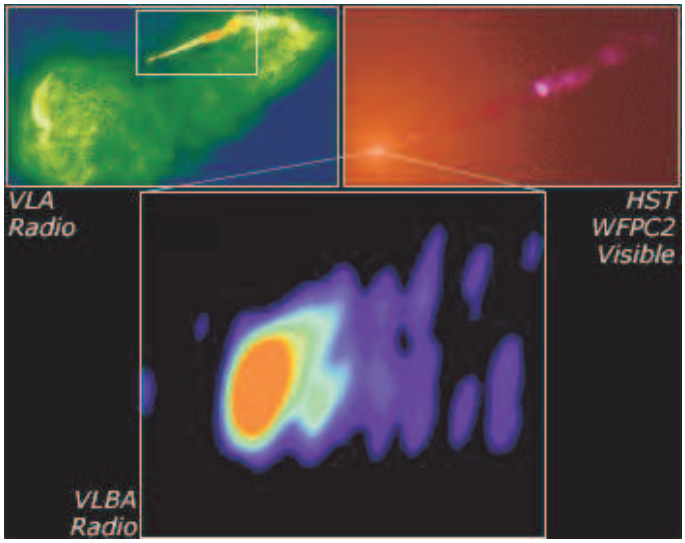

Figure 1.2: M 87 jet at different resolutions (from kpc-scales with VLA to parsec scales with VLBI).

Blazars and quasars attracted attention of the astronomical community for the last few decades. However, there are still many open questions about the physics of blazars and quasars, as well as about AGN in general. It is still unclear how the jet is formed and what physical mechanism can preserve the jet collimation on such long spatial scales as kiloparsecs. We still do not know what physical mechanisms cause the jet wiggling or precession, periodicities in the total flux-density light curves or how the emission of quasars and blazars at different wavelengths is connected. In the next subsections I will describe in more detail these phenomena in AGN and discuss which questions I would like to address in this thesis.

Relativistic jets

The central compact radio cores of quasars and blazars have a bright inner core with an elongated feature or a series of blobs stretching for up to ∼50 parsec away from it. The brightest inner feature observed with the VLBI technique is called VLBI core. *The VLBI core* is the compact, optically thick, flat-spectrum, stationary component at one end of the jet in the VLBI image of a typical blazar or quasar. Nearly all compact cores are variable, changing their luminosity on timescales from days to years. Motion of plasma components was observed for many blazars and quasars. In some sources, apparent motion is *superluminal* (e.g. Britzen et al. 2008) – the jet components appear to move away from the core with apparent transverse speeds of a few speeds of light (up to ∼50c) (see Zensus 1997 and references therein). Superluminal motion is an apparent effect that appears when relativistic motion is observed under small viewing angles.

Stationary jet components

However, as it was shown for many sources, the moving blobs usually co-exist with the jet components which are staying at almost the same positions (e.g. Jorstad et al. 2001, Britzen et al. 2008, Alberdi et al. 2000). *Stationary jet components* are features in a jet, which are staying at fixed position.

Stationary features have been explained by standing shocks, caused by the interaction of a jet with an ambient medium (Gomez et al. 1994) or jet recollimation shocks (e.g. Wehrle et al. 2001). Another explanation can be bending of the jet and a corresponding increase of the flux in the bend area due to Doppler beaming (e.g. Alberdi 2000). Moving jet features can drag a stationary jet component. When the moving component is going through a stationary jet component they are blended and observed as one jet feature at approximately an average position of moving and stationary jet component. When the moving component continues motion along the jet, the stationary jet feature is visible again. Therefore, a backwards motion of a stationary jet components is observed. The quasar 4C 39.25 was the first source for which dragging of a stationary jet component by moving through it features was observed (e.g. Alberdi 2000). However, Gomez 2005 and Aloy et al. 2003 have shown that the internal jet structure variability is much more complex and that the ejection of a new jet component from the VLBI core will cause appearance of other jet components, including stationary features appearing

further along the jet. One of the main goals of this thesis is to study the physics of the jets and to ask the question how moving and stationary jet components are interacting and what can cause the appearance of stationary features in the jet.

Jet precession

In general, precession refers to a change in the direction of the axis of a rotating object. *Precession* is a phenomenon associated with the action of a gyroscope or a spinning top and consists of a comparatively slow rotation of the axis of rotation of a spinning body about a line intersecting the spin axis. The smooth, slow circling of a spinning top is precession, the uneven wobbling is nutation. Precession was studied in detail in different branches of physics. In astronomical contexts, precession is a change in the movement of a rotating or orbiting body. The best example of the precession in astronomy is the revolution of the direction of the Earth's axis, which carries each celestial pole in a circle around the sky in a period of 25,800 years.

In this thesis we will discuss *jet precession* as a change in the direction of the main axis of the jet. In other words, jet precession is a change in the viewing angle of the jet with time. A few jets were found which were precessing on timescales of about tenths of years, such as e.g. in BL Lac (Stirling et al. 2003), 3C 345 (Lobanov et al. 2005), and NRAO 150 (Agudo et al. 2007). In general, there is no restriction how exactly the jet orientation should change, but a few models were invented which modelled a precessing jet as movement of a jet around a particular axis with a constant angular velocity and period, forming a conical surface (e.g. Caproni & Abraham 2004). Figure 1.3 illustrates jet precession for the special case when its caused by the presence of a secondary black hole M_2, which is rotating around the primary black hole M_1.

Jet precession on parsec scales (seen with VLBI technique) can be found using different observational methods. Each of these methods can be explained by the change of the jet orientation with time. However, all these methods are indirect evidences and therefore it will be a stronger prove for the jet precession if one can detect more than one evidence or correlated changes of them. We list below observational evidences for the jet precession:

- Changes of the position angles of the jet component ejections (or changes of the jet structural position angles). For a few sources, such

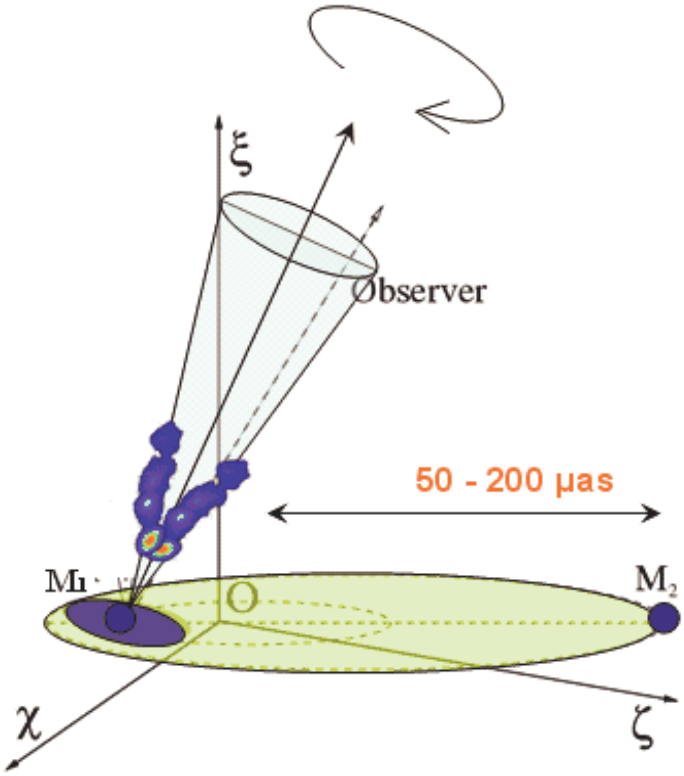

Figure 1.3: Cartoon visualizing jet precession. The jet is forming a conical surface. Here the jet precession is shown for the special case when its caused by the presence of a secondary black hole M_2, which is rotating around the primary black hole M_1.

as e.g. 3C 345 and BL Lac, it was found that the features in the jet appear at different position angles which are changing gradually with time, which was explained by changes of the jet orientation (e.g. Klare et al. 2005, Stirling et al. 2003, Savolainen et al. 2006).

- Sinusoidal changes of the absolute electric vector position angles of the core. (Stirling et al. 2003)

- Periodicities in the radio and optical total flux-densities. The viewing angle of the jet will change with time due to jet precession, which will cause the changes in the Doppler beaming (e.g. Nesci et al. 2005, Rieger 2005 and references therein).

- Sinusoidal changes of the jet opacity. Change of the jet orientation will affect the opacity of the central region. This can be measured using frequency-dependent core shifts with the phase-referencing technique. It can also be measured by determining frequency-dependent time delays of the flares in the total flux-density light curves (Caproni & Abraham 2004).

- Sinusoidal changes of the jet component speeds during the ejection. (Abraham 2000).

- It is also believed that helical structures of parsec-scale jets and jet bends are caused by jet precession (e.g. Dhawan et al. 1998).

A few physical mechanisms were proposed to explain jet precession, including jet instabilities, secondary black holes, and accretion disc instabilities (e.g. Camenzind & Krockenberger 1992, Hardee & Norman 1988, Lobanov & Roland 2005). The physical origin for the observed jet precession is still poorly understood. It is still unclear how common the phenomenon of jet precession in blazars and quasars is and what the exact physical mechanism is. However, as this phenomenon is triggered in the innermost regions of the jets, it must be tied to fundamental properties of the inner regions of the accretion system. Thus jet precession may be an interesting potential tool for supermassive black hole, accretion, and jet launching studies. Therefore one of the main aims of this thesis was to find more sources which show jet wiggling and jet precession and to investigate possible reasons for jet precession.

"Core" and "jet" outbursts

One of the most widely accepted model explaining apparent superluminal motion and stationary features in the jet is the shock-in-jet model (Blandford & Königl 1979, Marscher & Gear 1985). According to this model, an appearance of a new jet component from the VLBI core is caused by a shock wave, starting in the base of the jet, which propagates further along the jet. These relativistic shocks may result from changes of the physical conditions in the region where the jet is formed. Region where the jet is formed is *Base of the jet*. It is shown close to a black hole at Fig. 1.4, where a sketch from Marscher 2005 of the physical structure and emission regions of AGN is presented.

We will further call the changes of the physical condition in the base of the jet and subsequent shock wave formation a *primary perturbation*. Appearance and propagation of shock waves can explain in general radio total flux-density variability from radio to x-ray flares. It is believed, that relativistic shock waves are responsible for the particle accelerations which are needed for non-thermal emission generation, and that they appear as superluminal components in the VLBI maps.

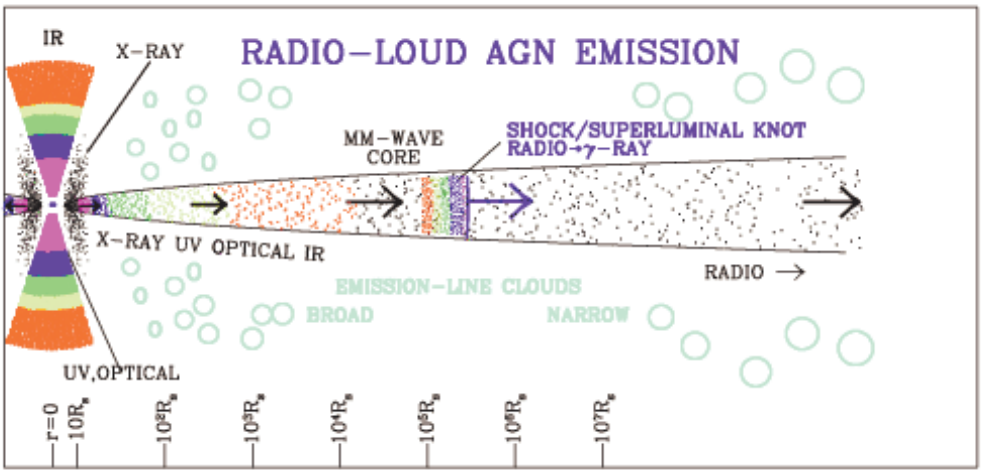

Figure 1.4: Cartoon of the physical structure and emission regions of a radio-loud AGN (Marscher 2005)

However, the connection between jet component ejections and total flux-density outbursts is still poorly understood. There is clear evidence that jet component ejections can be connected with flares in the light curve, but not all flares are connected with the appearance of new VLBI components and not all new components produce a flare (e.g. Savolainen et al. 2002). Moreover, Agudo et al. 2001 has shown that the emergence of a new jet component from the core can cause the appearance of many trailing components. These trailing components are much fainter and appear at the wake of the primary jet component. Therefore, taking into account the complex physics of AGN jets, a comparison between the appearance of new VLBI components and total flux-density flares becomes much more complicated. We propose in this thesis a new physical approach for comparison between the jet structure changes and total flux-density radio light curves. Here we propose to compare separately optically thick "core" radio outbursts and optically thin "jet"

outbursts with the jet structure evolution. *"Core" outbursts* are connected with the primary perturbation in the base of the jet and *"Jet" outbursts* are connected with the propagation of a primary perturbation along the jet.

According to theoretical arguments (e.g. Marscher 1996; Gomez et al. 1997), a shock induced by a primary excitation at the base of the jet is initially manifest in radio light curves as an outburst that is delayed at lower frequences due to the combined effects of the frequency stratification of the emitting electrons, non-zero opacity and light-travel delays. On the other hand flares, connected with the optically thin jet will appear almost simultaneously at different frequencies. The spectral evolution of a primary perturbation in the base of the jet will evolve through three phases: Compton, Synchrotron, and Adiabatic and will be accompanied by the emergence of a new jet component on parsec-scales (Marscher 1992). Investigating the frequency-dependent time lags of the total flux-density flares and comparing the spectral properties of the flares with the structure evolution on the VLBI scales, we can separate the "core" (connected with the primary perturbation in the base of the jet) and "jet" outbursts (connected with the propagation of a primary perturbation along the jet).

Another goal of this thesis is to study the long-term processes in the variability of active nuclei, starting from the primary perturbation in the vicinity of a supermassive black hole to the propagation of this perturbation along the jet and to compare "core" and "jet" outbursts with the changes of the jet structure.

Flaring activity cycles

Total flux-density radio light curves show timescales from days up to years. Different authors calculated timescales of variability using the structure functions method (e.g. Hughes et al. 1992), the Fourier transform analysis (e.g. Kelly et al. 2003) and other mathematical methods, which are not directly connected with physical processes in active galactic nuclei. Here I propose a new physical approach to calculate the flaring activity cycle of blazars and quasars. We can investigate the *flaring activity cycle* of blazars and quasars, calculating the duration of a flaring activity cycle as a time between two optically thick "core" outbursts. The "core" outbursts are optically thick flares connected with a primary perturbation in the base of the jet. Thus, studying the flaring activity cycles will provide us information on how often a primary perturbation of the jet appears. This will allow us to study how long is the

duration of flaring activity cycles and how stable the flaring activity cycles are, which will improve our understanding of the physical processes near the close vicinity of a supermassive black hole. The separation between "core" outbursts and "jet" outbursts allows us to calculate flaring activity cycles of blazars and quasars. We can determine how often do primary perturbations occur in the base of the jet and to find duration of flaring activity of active galactic nuclei.

Total flux-density periodicity

The investigation of the total flux-density variability can tell us about the nature of blazar and quasar activity, as well as the mechanisms responsible for it. The analysis of variability provides us with the opportunity to investigate the structure of AGN on the smallest scales, which can not be traced with any other observational technique. One of the most interesting topics concerning AGN variability is the search for periodicity of quasars and blazars. In optical wavelengths many AGN were found which show periodical variability (e.g. Hagen-Thorn et al. 2002, Fan et al. 2002, Lainela et al. 1999). However, at radio wavelengths, only several sources with periodical light curves were found (e.g. Kelly et al. 2003, Ciaramella et al. 2004, Raiteri et al. 2001).

The periodical variations of the flux density can be caused by different physical mechanisms, such as an orbiting secondary black hole, helical trajectories of the jet components (Camenzind & Krockenberger 1992), accretion disc instabilities, the propagation of shocks along the jet (Gomez et al. 1997) or recollimation (Gomez et al. 2005) or precession of the jet (e.g. Stirling et al. 2003). Therefore, one of the goals of this thesis is to answer the question what physical mechanism is responsible for the periodicities.

Jet precession is caused by changes of the jet orientation. This will also change the jet viewing angle and change the Doppler boosting and will cause periodical total flux-density variability. Thus one of the possible methods to find quasars and blazars which can show jet precession is to study the total flux-density variability and to search for the sources with periodical radio light curves. If the jet is precessing, the total flux-density should show periodical variability due to variations of the Doppler factor. Therefore, one main goal of this thesis was to find blazars and quasars with periodicities in flux-density light curves in the radio.

In order to find more sources with periodicities, we used a new physical approach for searching periods (together with the standard time series

analysis). We propose to separate the outbursts into "core" and "jet" and search for periodicity in the "core" outbursts which are optically thick, display low-frequency delays and are associated with primary perturbations in the core. This new method allows us to search for periodical processes which are directly connected to the central engine, whereas the traditionally used time series methods find all possible timescales independently whether they have a physical meaning or not.

Optical - radio connection

Statistically significant correlations between radio and optical light curves have been detected in several cases (e.g. BL Lac, Belov et al. 1989; 3C 279, Bregman et al. 1986; 3C 345, Tornikoski et al. 1994 etc.). Typically, the time delay between radio and optical variability maxima ranges from several months to ~ 2 yr. This is believed to be associated with a source burst evolving from an optically thick to an optically thin regime. For a few blazars and quasars, such as e.g. 1302-102 (Hutchings et al. 1994) the position of a radio jet coincides with an optical jet. This can be an evidence that optical and radio emission has the same synchrotron nature and is generated in the same region or regions which are not far away from each other. However, the connection between optical and radio flux-density variability is not completely clear yet. Not all active galactic nuclei show correlated behavior of optical and radio variability. Quite often for the same sources during different times of observations, different times are found between optical and radio flux-density changes. Some sources even do not show a correlation at all. Therefore, it is of high importance to study optical and radio connections for more sources in order to understand how common is the correlation and from where the optical and radio emission is generated.

For a few sources periods found in the optical coincide with periods found in the radio. The best example is AO 0235+164 (Raiteri et al. 2001) were the same period of $\sim$5.7 years was found in optical and radio. However, such sources are quite rare. The total number of blazars and quasars for which periodicity in the radio coincides with the optical is only seven (Rieger 2007). Therefore one of the main aims of this thesis is to find more sources which show similar timescales of variability in the optical and the radio. It is worth to notice, that according to theoretical arguments, coincidences of optical and radio periodicities can be most likely caused by supermassive binary black hole in the center of a galaxy (Rieger 2007). Therefore, searching for more

quasars and blazars for which optical radiation has the same periodicity as radio variability will increase the number of known binary black hole candidates.

1.1 Questions we want to discuss in the thesis

In the thesis I would like to discuss the questions:

1. We would like to study physics of the jets and to ask the question how moving and stationary jet components are co-existing and what can cause appearance of the stationary features in the jet?

2. Which sources show jet wiggling and jet precession and what are possible reasons for jet precession?

3. Can we describe the long-term processes in the variability of active nuclei, starting from the primary perturbation in the vicinity of a supermassive black hole to the propagation of this perturbation along the jet? What is duration of the flaring activity cycles of blazars and quasars?

4. Can we apply a new physical approach for comparison between the jet structure changes and total flux-density radio light curves (compare separately optically thick "core" radio outbursts and optically thin "jet" outbursts with the jet structure evolution)?

5. How many blazars and quasars show periodicities in flux-density light curves in the radio? Can we apply a new physical method of searching for periodicity in the "core" outbursts which are optically thick, display low-frequency delays and are associated with primary perturbations in the core?

6. Are periodicities in jet kinematics and periodicities in the total flux-density changes connected?

7. Are timescales of radio and optical variability are connected? How many sources show similar periods of variability in optical and radio (which can be binary black hole candidates)?

Chapter 2

Periodicities in blazars

2.1 Introduction

Studies of the variability of active galactic nuclei (AGN) represent an effective tool for investigating the nature of the activity and the mechanisms leading to its observable manifestations. The long-term variability of AGN, including possible periodicities of variations, has been studied and discussed in detail in a number of works (e.g., Aller et al. 2003, Kelly et al. 2003, Ciaramella et al. 2004, Fan et al. 2002). The source OJ 287 is the best studied example of an active galactic nuclei with a periodical total flux-density variability. The detection of an optical flare in 1995 had been predicted based on the period of 11.9 yr detected in the historical light curve (Pursimo et al. 2000). The detection of a predicted flare is the best prove for periodical variability of the source. Possible periodicity in the radio light-curves has recently been detected also for several other objects (Kelly et al. 2003, Ciaramella et al. 2004, Raiteri et al. 2001), but the predicted outbursts have never been observed. The main goal of our work was to find active galactic nuclei with pronounced periodicity in the total flux-density light curves and to understand the relation between light-curve periodicities and the jet kinematics. For this purpose we used a new physical approach for searching the periods in addition to the standard time series analysis. We tried to separate the outbursts into "core" and "jet" and search for periodicity in the "core" outbursts which are optically thick, display low-frequency delays and are associated with primary perturbations in the core.

The quasi-periodical variations of the flux density can be caused by dif-

ferent reasons, such as an orbiting secondary black hole, the propagation of shocks along the jet (Gomez et al. 1997), recollimation (Gomez et al. 2005) or precession of the jet (e.g. Stirling et al. 2003). Different physical processes forming in various regions of the jet can co-exist and cause quasi-periodic processes with various timescales. Superposition of these processes will make the light curve more complicated. However, this new method allows us to search for periodical processes which are directly connected to the central engine, such as accretion disc instabilities and binary black holes, whereas the traditionally used time series methods find all possible timescales independently on their physical origin.

One widely accepted hypothesis explaining both periodicity in the activity of AGNs and the activity itself is the presence of a multiple black hole at the galactic nucleus (Lobanov et al. 2002). As was shown in Sundelius et al. 1997, in models with multiple black holes, the process leading to the appearance of the primary perturbation in the vicinity of the multiple black holes may not have a strictly periodic character. Therefore, we will think in terms of the presence of quasi-periods in the light curves of AGN, rather than some strict periodic process. A good example is provided by OJ 287, which is the best observed and studied object in this context, and shows the presence of precisely quasi-periodic flux-density variations (Kidger et al. 2000). Nevertheless, the presence of such quasi-periodic behavior can be used in order to predict the epochs of future flares within known limits. This will make possible to verify multiple black-hole models, study the propagation of the associated perturbations along the jet in more detail, and plan future observations based on the expected activity phase of the source.

Different physical processes which can cause the periodical variability have different characteristic time scales. Therefore, another question we want to address is, what is the characteristic duration of the periodical processes in AGN variability. This will allow us to understand which physical mechanism gave rise to the particular periodical process. Part of this analysis is published in Kudryavtseva et al. 2006, Pyatunina et al. 2006, 2007, Qian et al. 2007, Kudryavtseva et al. (in prep.).

2.2 Observations and Methods

The University of Michigan radio astronomy observatory (Aller at al. 1985) monitoring program and Metsähovi radio astronomy observatory monitor-

ing database (Teräsranta et al. 1998) together with archival historical radio data were used to carry out the search for periodicities. Data at five frequencies 4.8, 8, 14.5, 22 and 37 GHz, spanning a period of more than 30 years were analyzed. The sources for the analysis were selected by means of visual inspection of the multi-frequency light curves. We found five sources, such as 3C 454.3, 3C 446, CTA 102, 0605-085 and 0133+476, for which visual inspection has shown that the bright outbursts appeared with similar time separation. The standard time series analysis, as well as the estimation of the flaring activity cycle from the "core" outbursts were further applied to the light curves of these sources.

2.2.1 Time series analysis

In order to find possible periodicities in the light curves of selected blazars, the Discrete Autocorrelation method and Jurkevich method were applied. For this purpose, I wrote the software, which implements the algorithms for searching the periods with the means of the discrete autocorrelation function and the Jurkevich method. The Discrete Autocorrelation method is based on the self-correlation of the data and shows high correlation coefficients at the time scale of the periodicity in the data. Whereas the Jurkevich method is based on the construction of the phase curves for different trial periods and shows the smallest dispersion of these phase curves for the correct period. I have compared the derived periods with the duration of the flaring activity cycles for the sources. The duration of the flaring activity cycles was calculated as the time interval between two successive core (optically thick) outbursts, which occur increasingly later at lower and lower frequencies. For this purpose, we attempted to distinguish core outbursts in the total flux-density light curves, which show frequency-dependent time-delays and are associated with a brightening of the core, from jet outbursts, which appear nearly simultaneous at all frequencies and are accompanied by the emergence of new jet components and their subsequent evolution. The comparison between the time scales, obtained with the time series methods and the duration of the flaring activity cycles, will give us an opportunity to understand what is the physical reason for this periodicity. Repeated core outbursts with similar time separations will provide some evidence, that something is happening near the central engine in a quasi-periodical way.

2.2.2 Autocorrelation method

The Discrete Auto-Correlation Function (DACF) method (Edelson & Krolik 1988) allows us to study the level of auto-correlation in unevenly sampled data sets. The values of the data sets are combined in pairs (a_i, b_j), for each $0 \leq i, j \leq N$, where N is the number of data points. First, the unbinned discrete correlation function is calculated for each pair

$$UDCF_{ij} = \frac{(a_i - \bar{a})(b_j - \bar{b})}{\sqrt{\sigma_a^2 \sigma_b^2}}, \tag{2.1}$$

where $\bar{a}$, $\bar{b}$ are the mean values of the data series and σ_a, σ_b are the corresponding standard deviations. The discrete correlation function for each time interval $\Delta t_{ij} = t_j - t_i$ is calculated as an average of all UDCF values, whose time intervals fall into the range $\tau - \Delta\tau/2 \leq \Delta t_{ij} \leq \tau + \Delta\tau/2$

$$DCF(\tau) = \frac{1}{M} \sum UDCF_{ij}(\tau), \tag{2.2}$$

where M is the number of pairs in the group. The higher the value of $\Delta\tau$ the better the accuracy and the worse is the time resolution of the correlation curve. The error of DACF is calculated as a standard deviation of the DCF value from the group of unbinned UDCF values

$$\sigma(\tau) = \frac{1}{M-1} \{\sum [UDCF_{ij} - DCF(\tau)]^2\}^{1/2}. \tag{2.3}$$

The DACF method gives different number of UDCF per bin, which can affect the final correlation curve. We used different $\Delta\tau$ values in order to check how this affects the results. We have selected the $\Delta\tau$ value in such a way that it gives reasonable accuracy and resolution. We found that the best $\Delta\tau$ values are $\sim$0.1 years, which gives at least 10 UDCF per bin. In order to check the results from DACF we also applied the Fisher z-transformed DACF method, which allows to create the data bins with equal number of pairs (Alexander 1997).

2.2.3 Jurkevich method

The Jurkevich method (Jurkevich 1971) is based on the analysis of the dispersions of the phase curves constructed for a series of trial periods and has

no preference for a particular periodic shape as a Fourier analysis. For each trial period P, the phase curves are constructed $\varphi = [(T_i - T_0)/P] \ (mod\ 1)$, where T_0 is the time corresponding to the zero phase, which is usually selected to be the middle of the data set. Phase curve was constructed folding the whole light curve as a phase of a particular period. The rms deviation is then obtained binning all the data points x_i into m groups according to their phases

$$V_l^2 = \sum_{i=1}^{m_l} x_i^2 - m_l \bar{x_l}^2, 1 \leq l \leq m, \tag{2.4}$$

where m_l is the number of points in the group and $\bar{x_l}$ is the mean value of x_i for the group. For each trial period, the sum of the mean square deviations for all groups is calculated

$$V_m^2 = \sum_{i=1}^{m} V_l^2. \tag{2.5}$$

The closer is the trial period to the real period, the smaller is the scatter of the points in the phase curve and the smaller is the value of V_m^2. The trustworthiness of the periods is estimated from the value $f = (1-V_m^2)/V_m^2$ for normalized value of V_m^2. Values of $f \geq 0.5$ indicate a very strong periodicity, while values $0.25 \leq f \leq 0.5$ show only marginal periodicity (Kidger 1992). This method can generate false periods due to unevenly sampled data. In order to separate spurious periods from the real variability, we carried out Monte-carlo simulations on artificial data sets generated from the real data (Fan 2002).

The irregularity of the observational series can lead to the appearance of spurious periods. We carried out Monte-Carlo simulations in order to separate out periods associated with real variability of the objects from those associated with the irregularity of observations. The synthetic light curves generated in this way were repeatedly analyzed using the method of Jurkevich. The artificial light curves were constructed from the real observations using the method presented in Fan et. al. 2002: the observation times were retained, and the fluxes were chosen at random from the real light curve. Thus, any period found for these light curves can only be a consequence of the time distribution of the observations. If periods detected in the synthetic data coinciding with periods found for the real light curves, they were classified as false and were not considered further.

2.2.4 Frequency-dependent time delays

Core and Jet outbursts: Physically, the activity of a source on the timescales of years can be described using two independent time scales: T_{act}, the characteristic time scale for the activity of the central engine, and T_{ev}, the time scale for evolution of the jet after it has been disturbed by a perturbation at it's base. The time scale T_{ev} includes a whole sequence of events, from the initial appearance of the perturbation to the time when the propagating perturbation fades and merges into the quiescent jet emission. At present, it may be difficult to define this important time scale observationally. The time scale T_{act} can be thought of as the duration of one complete "flaring activity cycle," which we propose to define as the characteristic time interval between two successive events marking onsets of phases of activity. With this definition, for example, a blazar that shows a pattern of being active for five years, then quiescent for ten years, then active five years, and so forth, would have $T_{act} \simeq 15$ yrs. If the time scale for activity exceeds the time scale for the jet's evolution ($T_{act} \geq T_{ev}$), two subsequent flaring activity cycles should be easily distinguishable; otherwise, manifestations of core activity and jet evolution associated with different cycles can be superimposed and complicate the observed picture. It is worth to notice that the observed T_{act} may be affected by the source's redshift, while the observed T_{ev} may be affected by both the redshift and the Doppler factor of the jet (for more detail, see the discussion in Lister 2001).

According to theoretical arguments (e.g. Marscher 1996; Gomez et al. 1997), a shock induced by a primary excitation at the base of the jet is initially manifest in radio light-curves as an outburst that is delayed at lower frequences due to the combined effects of the frequency stratification of the emitting electrons, non-zero opacity, and light-travel delays. Such time-delayed outbursts are associated observationally on milliarcsecond (mas) scales with the brightening of the VLBI core, and can be considered "core" outbursts. The propagation of the shock downstream in the jet is revealed via the emergence of a new optically thin jet component (or components) in the VLBI image, sometimes accompanied by "jet" outbursts, which evolve nearly simultaneously at all frequencies in the radio light curve. The integrated monitoring data support the division of observed outbursts into such core and jet outbursts, at least in some sources (0202+149, Pyatunina et al. 2000; 0420–014 Britzen et al. 1999, Zhou et al. 2000; 0059+581, Pyatunina et al. 2003). Thus, in practice, it is reasonable to approximate the duration of an

flaring activity cycle as the time interval between two successive "core" outbursts. On the other hand, if the accretion disc is precessing or a secondary black hole is rotating around the primary black hole we can expect, that the primary perturbation at the base of the jet will repeat periodically and we will see periodical "core" outbursts in the total flux-density light curves.

Gaussian decomposition: I wrote a software package was written in order to separate the most prominent outbursts in the radio light curves into individual components using Gaussian model fitting. We chose to fit Gaussian components for the simple reason that most of the observed centimetre-wavelength outbursts are symmetrical and have shapes that are approximately Gaussian. In particular, the shapes of the centimetre-wavelength outbursts do not correspond well to the exponential profiles used, e.g., by Valtaoja et al. (1999) to fit millimeter flares. The highest of the five frequencies for which we obtained light-curve decompositions is 37 GHz, while the exponential behaviour pointed out by Valtaoja et al. (1999) is manifest at frequencies of 90 and 230 GHz. An example of the shape of the centimeter flare is shown in Fig. 2.1 (left).

Long-term trends in the total flux-density variations described using polynomial approximations for the deepest minima in the light curves were subtracted before the fitting. My software package is working in such a way, that it first removes the trend, then finds the highest peak in the light curve and fits the Gaussian function in the peak finding the best chi-square value. It is possible to change interactively the time range in which the Gaussian function is fitted in order to obtain the best fit. Then the fitted Gaussian function is removed from the light curve and the procedure repeats again until all the peaks are fitted with the Gaussian functions. An example result of the long-term trend determination and Gaussian decomposition is shown in Fig. 2.1 (right). This example illustrates the general criterion that the smallest number of Gaussians providing a complete description of the light curve was used. The number of Gaussians used depended on the time interval covered by the light curve and the characteristic time scale for the source variability.

The light curves of the sources considered here could all be decomposed into Gaussian components with a goodness of fit satisfying the χ^2 test at a significance level of 0.01. The frequency-dependent time delays for individual components, $\Delta T_{max}(\nu) = T_{max}(\nu) - T_{max}(\nu_0)$, where ν_0 is the highest frequency observed, were determined and approximated by exponential functions of frequency of the form $\Delta T_{max}(\nu) \propto \nu^{\alpha}$ (Gomez et al. 1997; Lobanov

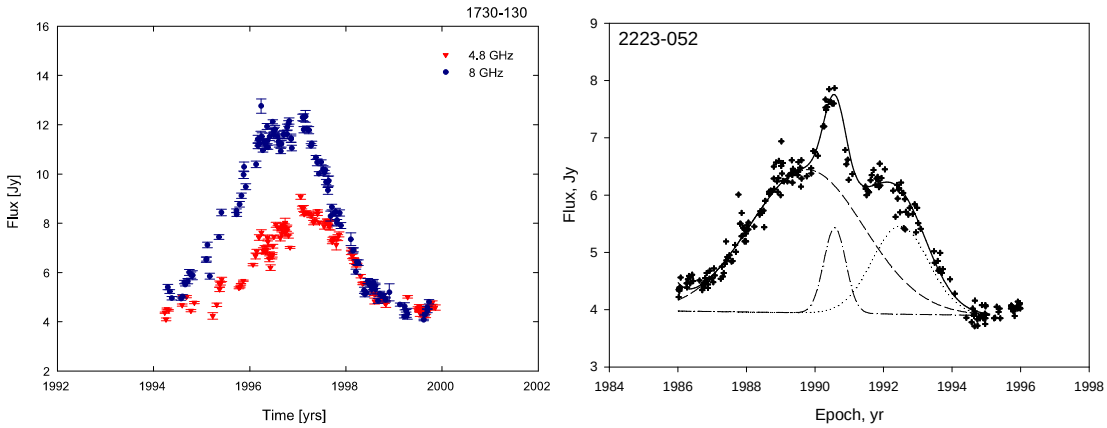

Figure 2.1: *Left:* Example of the shape of a centimeter outburst. The bright flare of 1730-130 at 4.8 (triangles) and 8 GHz (circles) is plotted. The shape of the flare is symmetric and can be fitted with a Gaussian function; *Right:* Example of the decomposition of an outburst into Gaussian components. Shown is outburst $B1$ (solid curve) in 3C 446 (2223-052) at 14.5 GHz, which has been decomposed into the components $B1a$ (dashed), $B1b$ (dash–dotted), and $B1c$ (dotted)

1998).

In the following section we present the analysis of the light curves of 3C 454.3, 3C 446, CTA 102 and 0133+476. We decomposed the light curves of these sources into Gaussian components, applied the time series methods in order to find the periodicity, and compared the total flux-density variability with the VLBI jet components ejections.

2.3 Results – 3C 454.3 (2251+158)

2.3.1 Introduction

3C 454.3 (2251+158) is a gamma-ray blazar with a redshift of z=0.859 (Blom et al. 1995). It is an optically violent variable with a relatively high total linear polarization (up to 17%, Rusk 1990). The source is one of the brightest in the sky with a total flux-density at 5 GHz of 10-15 Jy level and shows all the typical properties of a blazar: large intensity variations at all frequencies, high radio and optical polarization, superluminal motion and a Spectral Energy Distribution (SED) showing two broad peaks attributed to synchrotron and inverse Compton radiation. The map of 3C 454.3 at 15 GHz (from MOJAVE database, Lister & Homan 2005) is shown in Fig. 2.2. In April-May 2005, 3C 454.3 had an unprecedented bright flare at optical wavelengths with a magnitude in the R band of 12.0 (Villata et al. 2006). This exceptionally bright optical outburst was accompanied by hard X-ray activity (Pian et al. 2006), which was followed by a radio outburst with about a one-year delay (Villata et al. 2007).

Several authors searched for periodicity in the total flux-density light curves of 3C 454.3. Ciaramella et al. 2004 found a period of 6.07 – 6.55 years in the radio total flux-density light curves at 4.8, 8, 14.5, 22 and 37 GHz. In the optical wavelengths, three weak periods of 6.4, 3.0 and 0.8 years were found in the B band light curve by Webb et al. 1988 and a period of 12.39 years was found in the historical light curve, spanning almost 100 years (Su et al. 2001). It is worth to notice, that 3C 454.3 is one of the rare sources for which the periodicity in the optical wavelengths is consistent with the periods found in the radio variability.

Various time scales of 3C 454.3 variability were reported before, e.g. Salonen et al. 1983 found in the radio light curves at 37 GHz a time scale of variability of 0.83 years. Using structure function analysis, Lainela & Valtaoja 1993 found a time scale of 2.3 years (22 GHz and 37 GHz), whereas Hughes et al. 1992 found a timescale of 1.8 year (4.8 GHz, 8 GHz, and 14.5 GHz). However, most of the time scales are quite short and are no longer than 3 years.

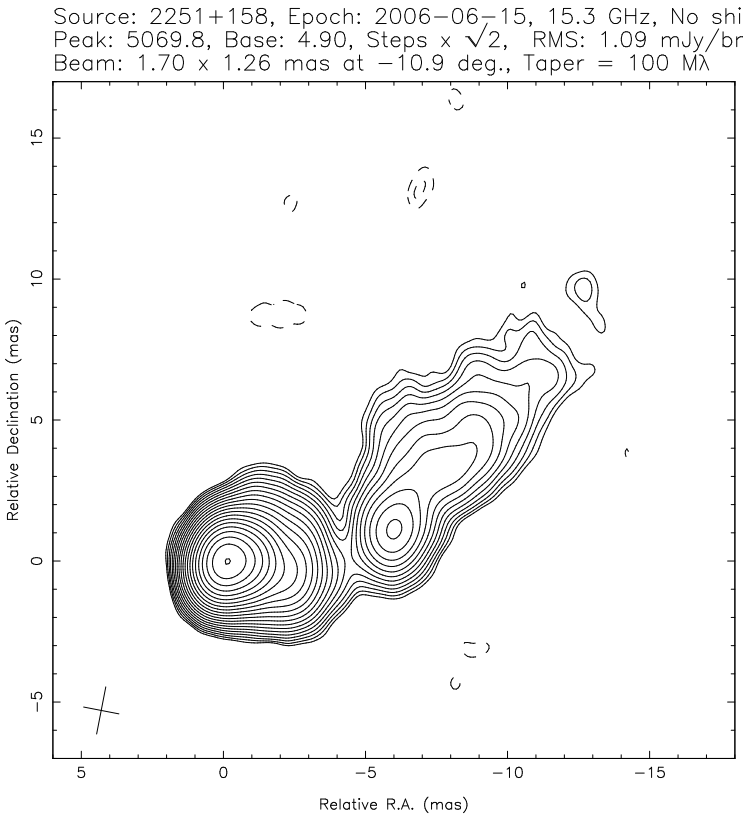

Figure 2.2: Map of 3C 454.3 at 15 GHz from MOJAVE database (Lister & Homan 2005).

2.3.2 Search for periodicity

The light curve of 3C 454.3 at 4.8, 8, 14.5, 22, and 37 GHz is presented in Fig. 2.3. Three major powerful outbursts happened in 1969, 1982 and 1994, which were followed by broader and weaker outbursts with substructure. The periodicity of about 12 years is clearly seen in the light curve, since the time duration between all major flares is ∼12 years. A shorter six-year period is also evident in the light curve, which is a characteristic time scale between the major flares and less powerful broad intermediate flares in 1975 and 1987. The discrete autocorrelation method has revealed the presence of two periods: 6.1 – 6.3 and 11.8 – 13.4 years for all five frequencies. Similar periods were found also with the Jurkevich method: 5.5 – 6.7 and 10.5 – 13.5 years. You can see the results for the discrete autocorrelation function and Jurkevich

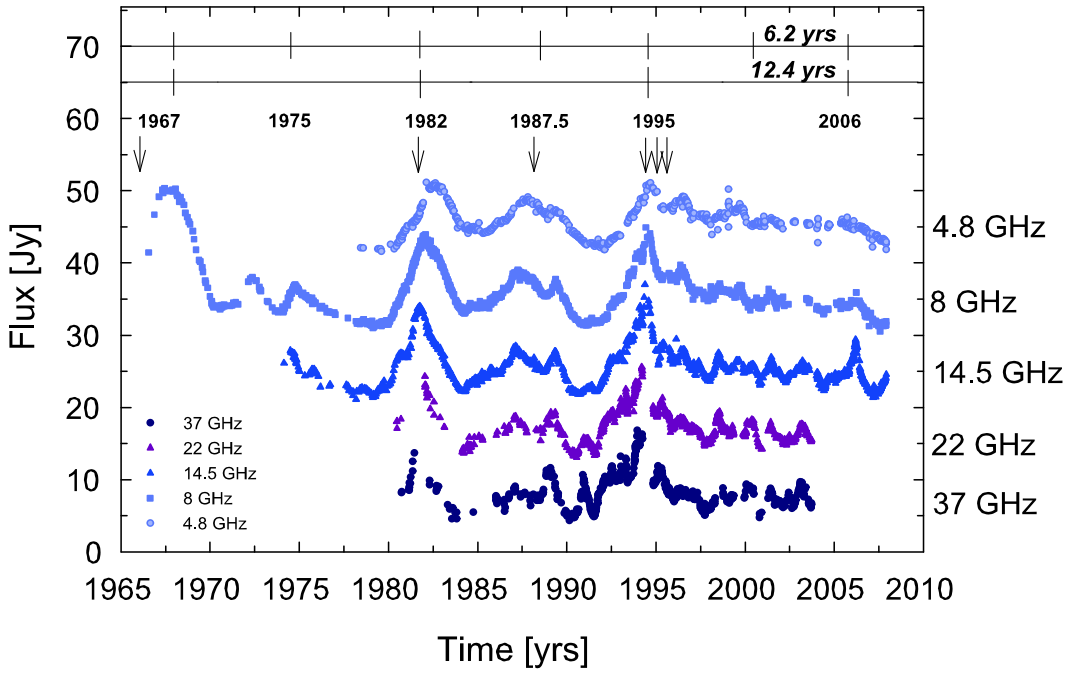

Figure 2.3: Light curve for 3C 454.3 at 37, 22, 14.5, 8, and 4.8 GHz. For ease of viewing, the curves have been shifted relative to each other by 8 Jy. The arrows mark the birth epochs of VLBI components.

method for 4.8 GHz in Fig. 2.4. However, the scatter for the periods is much larger for the Jurkevich method. Table 2.1 shows all the periods found for all five frequencies, where ν is the observing frequency in GHz, P_{Jurk} is the period found with the Jurkevich method, f the confidence measure for P_{Jurk}, P_{DACF} the period found using the discrete autocorrelation function, and k the corresponding correlation coefficient. Both methods have revealed similar periods of about 6 and ∼12 years. Averaging the periods obtained with different methods at different frequencies give periods of 6.2 ± 0.1 and 12.4 ± 0.6, which will be 3.3 and 6.7 years in the source rest frame. The light curves of 3C 454.3 cover more than 30 years of observations. Therefore, during this period six cycles of a 6-year period and three cycles of a 12-year period appeared. A six-year period is in a good agreement with the 6.07–6.55 years period found before by Ciaramella et al. 2004 and similar to the period of 6.4-year period in the optical light curve. Similarly, the 12-year period unexpectedly coincide with a period 12.39 years found in the historical

optical light curve (Su et al. 2001).

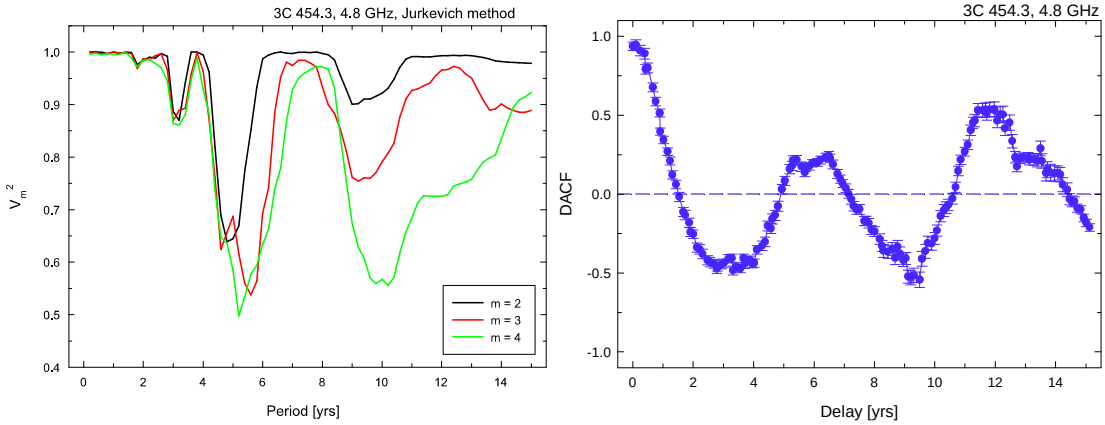

Figure 2.4: *Left:* Results of the period search for 3C 454.3 at 4.8 GHz using the method of Jurkevich. Plots for various bin numbers for the phase curve are presented.; *Right:* Discrete autocorrelation function for 3C 454.3 at 4.8 GHz.

2.3.3 Jet components ejections

The quasar 3C 454.3 is one of the brightest and the best observed radio sources. A large amount of information about its VLBI structure has been published (e.g. Pauliny-Toth et al. 1984, Jorstad et al. 2001), making it possible to compare variations in the source structure with variations in the light curves. We searched for the information about the jet component ejections in the literature and list them in Table 2.4, where the time of the jet component ejection in years T, the time difference between two component ejections ΔT, the frequency of the observations in GHz and the references are listed. The jet components observed by Pauliny-Toth et al. 1984 in 1981.4 and 1982.1 were ejected at the position angle of $-65°$ and the jet components observed by Jorstad et al. 2001 in 1994.5, 1995.1, and 1995.6 were ejected at similar position angles of $-74°$, $-81°$, and $-88°$ correspondingly. The new VLBI components have different fluxes, but since different jet components were observed at different frequencies it is difficult to compare the component fluxes.

There is evidence for a similar time period between different jet component ejections. For example, the time separation between the component

Table 2.1: Detected periods for 3C 454.3

ν [GHz]	P_{Jurk} [yr]	f	P_{DACF} [yr]	k
37 GHz	5.7 ± 1.8	0.88	6.2 ± 1.4	0.24
	11.6 ± 2.8	1.0	12.6 ± 1.4	0.26
22 GHz	6.7 ± 0.9	0.35	6.3 ± 1.9	0.14
	12.1 ± 0.9	0.47	12.6 ± 2.4	0.52
14.5 GHz	5.7 ± 1.0	0.86	6.2 ± 2.5	0.24
	10.5 ± 0.9	0.45	12.5 ± 1.6	0.63
8 GHz	6.7 ± 0.8	0.19	6.1 ± 3.5	0.15
	13.5 ± 1.2	0.44	13.4 ± 1.8	0.45
4.8 GHz	5.5 ± 1.1	0.86	6.1 ± 1.4	0.24
	11.7 ± 2.6	0.95	11.8 ± 1.2	0.55

ejection in 1969 and 1981 is 12.4 years, between 1982 and 1988 is 6.1 years and between 1988 and 1994 is also about 6.25 years. We can assume, that there is a characteristic period of about six years in the jet component ejections. Almost simultaneous jet component ejections in 1981.4 and 1982.1 and in 1994.4, 1995.0 and 1995.59 can be caused by the same primary perturbation in the base of the jet, as was suggested by Gomez et al. (1997). Moreover, the time of the birth of the jet components is in good agreement with the epochs of the powerful outbursts in the radio total flux-density light curves (See Fig. 2.3). Thus, based on the available data on the birth epochs of VLBI components, the time interval between the generation of new components is about 6.3 years, in good agreement with the six-year period we have found for the radio light curves.

2.3.4 Frequency-dependent time delays

In order to study the properties of the outbursts, we decomposed the light curves into Gaussian components. Before the decomposition, the long-term trends were calculated via a linear interpolation across the local/global minima in 1977, 1985, 1997 and 2003. Multi-frequency light curves at frequencies from 4.8 GHz to 90 GHz are given in Fig. 2.5. In addition to the 4.8 GHz, 8 GHz, and 14.5 GHz data from the UMRAO and the 22 and 37 GHz points from the Metsähovi Radioastronomical Observatory we used for analysis the

90 GHz flux densities from the IRAM data of Steppe et al. 1988, Steppe et al. 1992, Steppe et al. 1993 and Reuter et al. 1997. The light curves cover a time interval of ∼40 yr and show four prominent events with maxima in 1969, 1982, 1994 and 2006 each followed by less powerful multi-component flares. The parameters of the Gaussian components used to decompose the outbursts are presented in Tables 2.2 and 2.3. Decomposed Gaussian components are showen with the vertical marks at the Fig. 2.5.

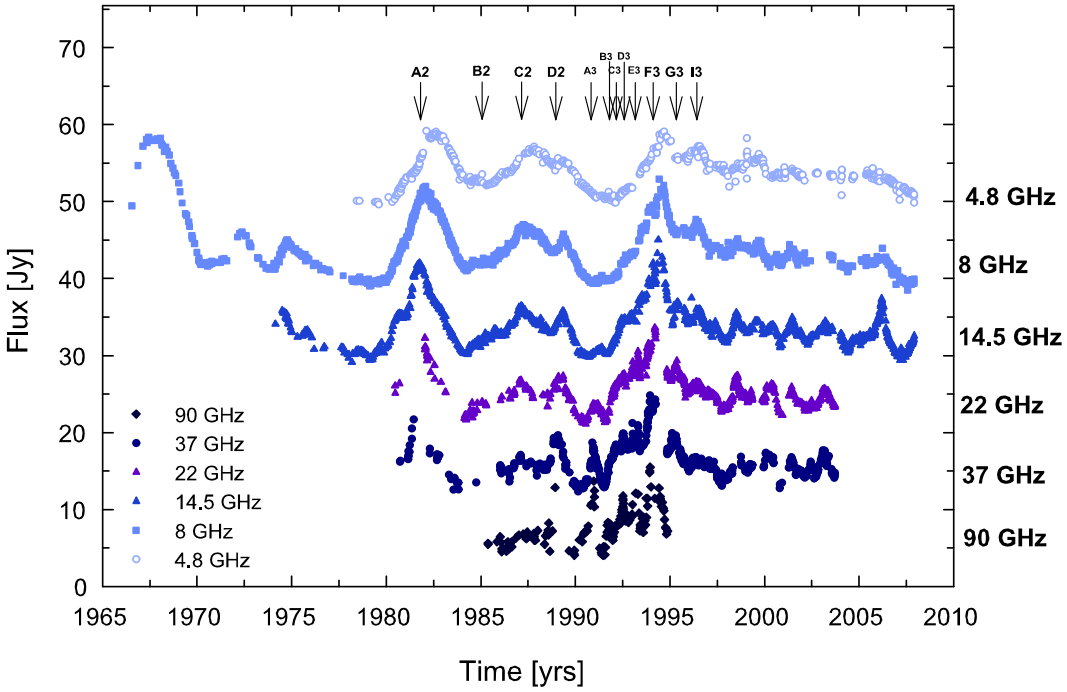

Figure 2.5: Light curve for 3C 454.3 at 90, 37, 22, 14.5, 8 and 4.8 GHz. For ease of viewing, the curves have been shifted relative to each other by 8 Jy. The arrows mark the flares, decomposed by means of Gaussian function fitting.

We divided the light curves into 12-year cycles, according to a visual inspection and periodicity analysis of Fig. 2.5 in order to analyze the flares from different cycles separately. We took the beginning of the first cycle to be in 1966, in accordance with the shape of the prominent outburst in 1968. The second cycle starts in 1978.4, the third begins in 1990.8 and the fourth cycle starts in 2003 with the major flare which happened recently in 2006. The

precise beginning of a cycle is defined by the high frequency observations, and depends slightly on frequency. The peak of the most prominent event is delayed by 2-3 years in each cycle relative to its onset. The analysis of outbursts from different cycles has shown, that there are similarities in the time delays, widths and spectra evolution of the flares in each cycle. Tables 2.2 and 2.3 lists the Gaussian parameters of the individual outbursts for cycles 2 and 3 accordingly, while Fig. 2.6 shows the time lags and amplitudes of the outbursts as functions of frequency. Each flaring activity cycle starts with outbursts with moderate time lags ($\Delta T \leq$0.6 yr), which are dominated by high-frequency components and show steep amplitude spectra (e.g., $A2$, $A3$ and $B3$). The delay reaches its maximum value ($\sim$1 yr) for outbursts $B2$ and $D3$ in cycles 2 and 3, respectively, and then gradually decreases. The spectra of the flares' amplitudes are steep in the beginning of the cycle ($A2$, $A3$, and $B3$), then start to flatten and become the flattest during the brightest peaks of the cycle ($B2$ and $F3$). After that the spectra start to gradually become steeper ($E2$, $E3$). Near the second half of a cycle, outbursts with simultaneous maxima at all frequencies are observed ($C2$, $I3$, and $M3$). Moreover, the width of the flares changing when the cycle proceeds. Figure 2.8 shows the width evolution with time during the end of the second cycle and beginning of the third cycle. The cycle starts with narrow flares, such as $B3$, $C3$, then the width is gradually growing until the maximum value during the brightest peaks in the cycles ($B2$, $F3$) is reached and decreases again ($D2$, $E2$, $G3$+$H3$, $I3+J3$). These changes with time (spectra, time delays and widths) indicate the presence of a similar scenario of evolution of the flares of each cycle.

The evolution of the time lag and amplitude at 37 GHz for consecutive outbursts in cycle 3 is presented in Fig. 2.7, which shows that the time lag and amplitude increase as a cycle proceeds, reaching their maximum values during the first half of the cycle. The peak time lags occur $\sim$1.5 yr before the peak amplitudes. This can easily be understood if the outbursts are associated with shocks in the innermost part of the jet. In this case, the maximum time lag corresponds to the maximum optical depth of the shocked region, while the maximum amplitude corresponds to the region where the optical depth becomes equal to unity, and the region becomes transparent at a given frequency.

VLBI observations of the quasar obtained at 10.6 GHz at 9 epochs between 1981.4 and 1985.9 (Pauliny-Toth et al. 1984, 1987) show dramatic changes in the jet structure and the appearance of superluminal components at position angle $PA \sim -95^\circ$ with high apparent speeds between 1982.1 and

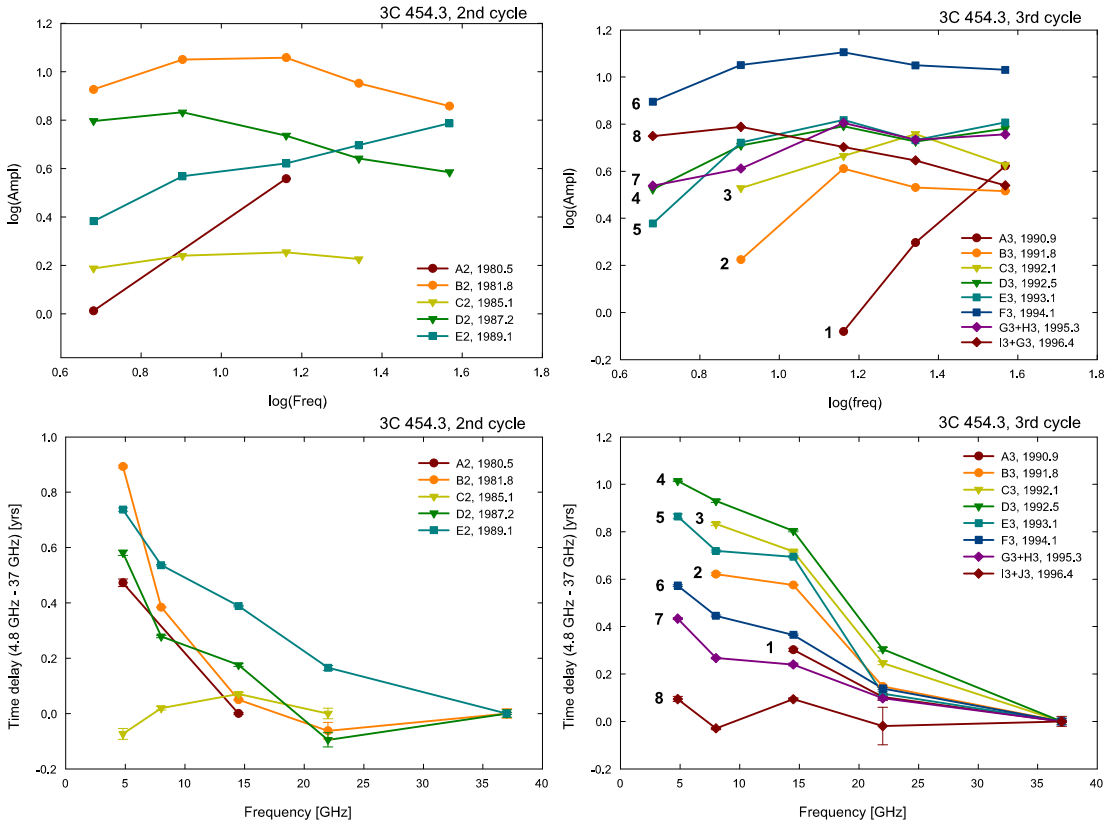

Figure 2.6: Amplitudes *(top)* and time delays *(bottom)* as functions of frequency for the second *(left)* and third *(right)* cycles in 3C 454.3.

1983.8. These can confidently be associated with outburst $B2$. Therefore, the low-frequency-delay outburst $B2$ is accompanied by the ejection of superluminal components, and so can be classified as a mixed outburst. The maxima of the next outburst, $C2$, are almost simultaneous at all frequencies. The parsec-scale jet of 3C 454.3 contains a quasi-stationary feature, C, $\sim$0.7 mas from the core in $PA \sim -90°$ (e.g. Gómez et al. 1999). The most prominent superluminal component ejected near 1982–1983 had a proper motion of ~ 0.35 mas/yr (Pauliny-Toth et al. 1987), implying that the component should have reached the stationary feature near 1984–1985. This epoch coincides with the peak of outburst $C2$, suggesting we should classify $C2$ as a jet outburst that is associated with an interaction between moving and stationary shocks in the jet. The only VLBI data available during outbursts $D2$

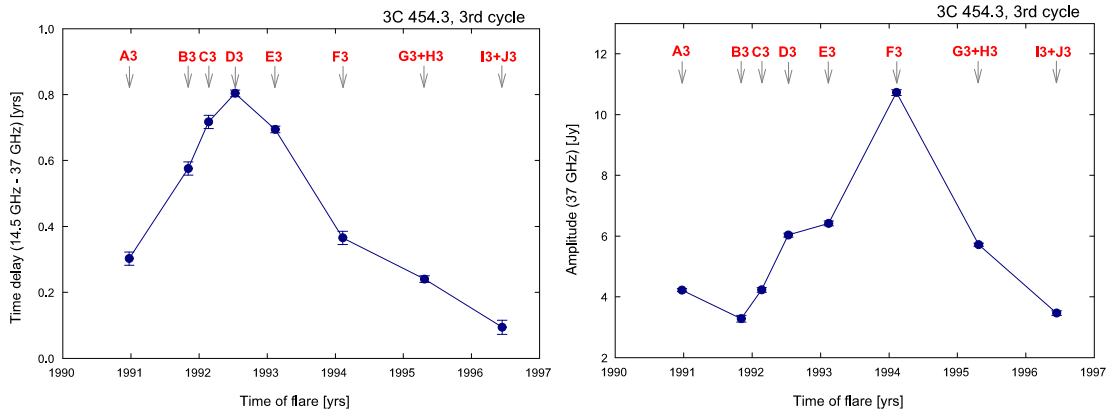

Figure 2.7: Time lags *(Left)* and amplitude *(Right)* at 37 GHz of individual outbursts as functions of time during cycle 3 in 3C 454.3.

and $E2$ are the 5-GHz data for epoch 1988.2 of Cawthorne & Gabuzda, 1996. The polarization structure of the source led these authors to conclude that 3C 454.3 may have been in the process of ejecting a new jet component at the epoch of their observation. In this case, this component could be associated with outburst $E2$. Though outburst $E2$ exhibits a significant low-frequency delay, its steep amplitude spectrum and the possible connection with a jet component lead us to classify it as a mixed out associated with the evolution of the jet. Outburst $D2$ shows moderate time-lags and a spectrum dominated by a low-frequency component, and may be associated with reverse shocks behind the primary perturbation that partially affect the core region.

Figure 2.9 presents the 37 GHz light curve together with the 43 GHz light curves of individual VLBI components ejected from 1994 to 2001 (Jorstad et al. 2001, 2005). The ejection of knots B1 and B2 occurs within ΔT of $T_{max}(37\ GHz)$ for the brightest outburst $F3$. Therefore, the outburst has the same properties as the most prominent outburst $B2$ in cycle 2. The much weaker knots B3, B4, and B6 can be associated with outbursts $G3$, $M3$, and $P3$, respectively. The synchronous outburst $M3$ is a pure jet outburst. Another synchronous outburst, $I3$, may be associated with the interaction of knots B1 and/or B2 with the stationary feature C, as was the case for outburst $C2$ in cycle 2. Although outbursts $G3$ and $P3$ show low-frequency delays, ΔT is moderate. These mixed outbursts are more likely associated with the evolution of the jet than with activity of the central engine. The outburst $K3$ is very similar to $G3$ and $P3$, although it is not accompanied by

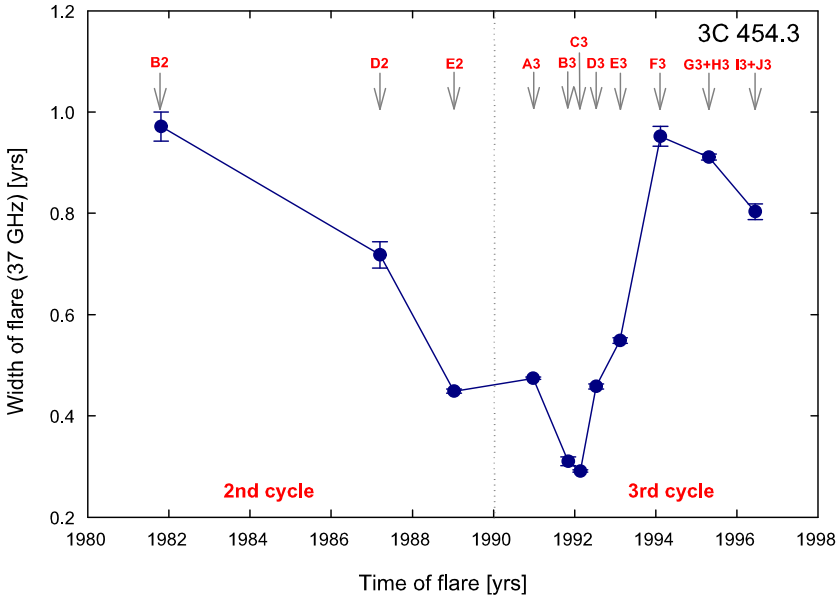

Figure 2.8: Evolution of widths of the flares at 37 GHz in 3C 454.3.

a jet component. Therefore, each cycle contains an outburst that is strongest, and has the flattest amplitude spectrum and a significant low-frequency time delay: $B2$ in cycle 2 and $F3$ in cycle 3. We associate these outbursts with activity of the central engine, and define the duration of the flaring activity cycle to be $T^{F3}_{max} - T^{A2}_{max}$ at 37 GHz: 12.30 ± 0.04 yr.

2.3.5 Binary black hole in 3C 454.3

For 3C 454.3 we found periodicities not only in the total flux-density light curves, but also in the "core" flares. The "core" flares in these sources appear with the same period. This suggests, that the primary perturbation in the base of the jet appears periodically. Therefore, the found periodicities in 3C 454.3 are likely connected with the vicinity of a black hole and are not caused by the propagation in the jet effects. The periodical "core" flares can be caused by different reasons. It can be caused by periodical instabilities in the accretion disc or can be caused by the tidal interaction with a secondary black hole.

In collaboration with Prof. S.J. Qian we applied the binary black hole model to the variability of radio data of 3C 454.3. We proposed that the

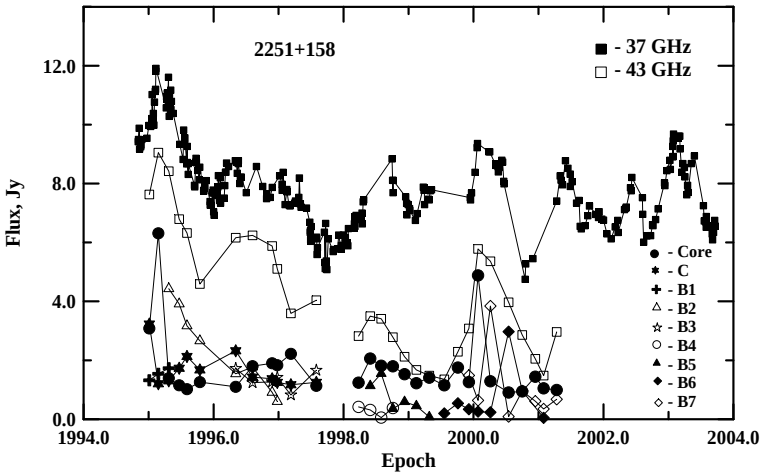

Figure 2.9: 37 GHz light curve (filled squares) and flux densities of VLBI components at 43 GHz located within 0.6 mas of the core in 3C 454.3 (the open squares represent the sum of all components)

periodicity in 3C 454.3 can be interpreted in the frame of a binary black hole model in which two jets from the two black holes rotate with a period ($\sim$13 year) of the orbital motion. In this case, one jet produces the main bump and the other jet produces the secondary bump. Both the jets rotate together with a period, which could be due to the orbital motion of the binary system, and thus the different Doppler boosting profiles determine the relative timing of the optical flaring and radio flaring. The combination of the effects of accretion (mass-energy transfer into the jets) and Doppler boosting determine the strength of the optical and radio outbursts.

We fitted the model with a Lorentz factor $\Gamma = 20$, period of the jet rotation in the observer's frame $T_{obs} = 12.8$ yrs. The observer direction makes an angle $i = 2^\circ$ with the normal of the orbital plane. The outer parts of the jet are bent backwards with respect to their orbital motion due to magneto-hydrodynamic interaction between the magnetized jet flows and the ambient medium. The bent parts which emit optical and radio emission make angles $\psi_1 = 3^\circ$ and $\psi_2 = 10^\circ$ with the normal of the orbital plane. The final fit of this model is shown in Fig. 2.10. The solid line there shows the fitted binary black hole model. It is clearly seen that the described model fit the observed radio total flux-density light curve of 3C 454.3 very well. Therefore, we can conclude that the periodicity in the 3C 454.3 radio light curves can be caused

by the presence of a secondary black hole.

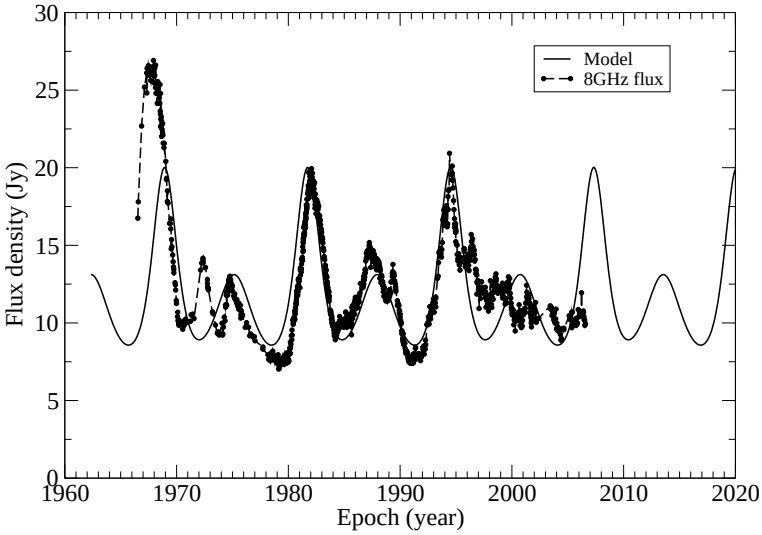

Figure 2.10: The total flux-density light curve of 3C 454.3 at 8 GHz. The solid line shows the fitted binary black hole model with two jets.

2.3.6 Summary

Using time series analysis, we have found two periods of 6.2±0.1 and 12.4±0.6 years (which will be 3.3 and 6.7 years in the source rest frame) in the radio total flux-density light curves at five frequencies. We also find the duration of the flaring activity cycle, estimated as the time period between two "core" outbursts to be 12 years. We find the characteristic time scale of the jet components ejections to be about six years. The periods in the total flux-density light curves are in good agreement with the characteristic time scale for the VLBI jet component ejections as well as the duration of the flaring activity cycle. Moreover, the 12-year period in radio variability is in very good agreement with a 12-year period in the optical light curves found before by Su et al 2004. It is especially noteworthy that this period predicted that the next powerful radio flare will happen in ∼2006, which actually was recently observed by UMRAO and Effelsberg monitorings (Villata et al. 2007).

Since the flaring activity cycle of the source is repeated periodically, we can tell that a primary perturbation in the base of the jet is repeated periodically, which is in a good agreement with the periodically appearing jet

components on the VLBI scale and similarity of radio and optical periods. Therefore, the periods are more likely connected with the closest vicinity of a black hole. A few processes can cause a periodical appearance of the "core" flares and the jet component ejections. It is possible, that the accretion rate of the black hole is changing periodically, which can be due to accretion disc precession, some instabilities in the accretion disc or, possibly, due to the periodical approach of a secondary black hole, which changes the accretion rate periodically due to tidal interactions.

According to our estimates, if the 12-year and 6-year periodicities are correct and will stay unchanged, the next powerful flare in 3C 454.3 should have maximum in 2012 and have an amplitude of about 5 Jy (reaching the flux value of about 10 Jy at 37 GHz). This flare should be followed by much more powerful outburst in about 2018, which will reach the flux level of about 15 Jy at 37 GHz. Both of the outbursts will be accompanied by the appearance of new VLBI components.

We found that the light curves of 3C 454.3 can be decomposed in "core" and "jet" outbursts. Moreover, we found that during the cycle, the time lags, amplitudes and spectra of different flares are changing gradually and the activity of 3C 454.3 is much less strong than it was thought before. The evolution of outbursts during the cycle shows that the peak in the amplitude appears after the peak in the time lags with a delay of about 1.5 years. This can be explained with the shock in jet model.

Table 2.2: 3C 454.3: Parameters of outbursts I - Cycle 2

Comp.	Freq. GHz	Amplitude Jy	T_{max} yr	Θ yr	Time delay yr	σ^2
A2	14.5	3.62±0.03	1980.51±0.01	0.29±0.01	0.00±0.01	0.43
A2	4.8	1.03±0.07	1980.99±0.01	0.24±0.01	0.47±0.01	0.35
B2	36.8	7.22±0.21	1981.81±0.02	0.97±0.03	0.00±0.02	1.13
B2	22.2	8.97±0.17	1981.74±0.03	1.06±0.02	-0.07±0.04	0.49
B2	14.5	11.44±0.03	1981.86±0.02	0.82±0.01	0.05±0.03	0.34
B2	8.0	11.23±0.02	1982.19±0.01	1.16±0.01	0.38±0.03	0.11
B2	4.8	8.45±0.03	1982.70±0.01	1.15±0.01	0.89±0.03	0.12
C2	22.2	1.68±0.09	1985.04±0.02	0.33±0.02	0.00±0.02	0.27
C2	14.5	1.80±0.02	1985.11±0.01	0.65±0.01	0.07±0.03	0.14
C2	8.0	1.74±0.02	1985.06±0.01	0.62±0.01	0.02±0.03	0.09
C2	4.8	1.54±0.05	1984.97±0.02	0.49±0.02	-0.07±0.03	0.10
D2	36.8	3.85±0.05	1987.20±0.02	0.72±0.03	0.00±0.02	0.56
D2	22.2	4.38±0.06	1987.11±0.03	1.03±0.04	-0.09±0.04	0.39
D2	14.5	5.46±0.02	1987.38±0.01	1.35±0.01	0.18±0.03	0.21
D2	8.0	6.80±0.02	1987.48±0.01	1.32±0.01	0.28±0.03	0.14
D2	4.8	6.27±0.02	1987.78±0.01	1.41±0.02	0.58±0.03	0.14
E2	36.8	6.13±0.05	1989.03±0.01	0.45±0.01	0.00±0.01	0.49
E2	22.2	4.97±0.08	1989.19±0.01	0.56±0.01	0.16±0.02	0.25
E2	14.5	4.18±0.03	1989.41±0.01	0.42±0.01	0.38±0.02	0.11
E2	8.0	3.70±0.03	1989.56±0.01	0.47±0.01	0.53±0.02	0.07
E2	4.8	2.42±0.03	1989.76±0.01	0.62±0.01	0.73±0.02	0.14

Table 2.3: 3C 454.3: Parameters of outbursts II - Cycle 3

Comp.	Freq. GHz	Amplitude Jy	T_{max} yr	Θ yr	Time delay yr	σ^2
A3	90.0	7.14±0.23	1990.86±0.01	0.60±0.01	–	1.39
A3	36.8	4.19±0.05	1990.97±0.02	0.47±0.02	0.00±0.02	0.19
A3	22.2	1.98±0.07	1991.08±0.03	0.64±0.02	0.11±0.04	0.11
A3	14.5	0.83±0.03	1991.28±0.01	0.48±0.01	0.31±0.03	0.03
B3	90.0	3.69±0.12	1991.79±0.01	0.29±0.01	–	0.36
B3	36.8	3.28±0.11	1991.84±0.02	0.31±0.01	0.00±0.02	0.07
B3	22.2	3.39±0.08	1991.99±0.01	0.35±0.01	0.15±0.03	0.18
B3	14.5	4.08±0.03	1992.42±0.01	0.45±0.01	0.58±0.03	0.07
B3	8.0	1.68±0.05	1992.46±0.01	0.41±0.01	0.62±0.03	0.09
C3	36.8	4.23±0.07	1992.14±0.02	0.29±0.02	0.00±0.02	0.09
C3	22.2	5.73±0.17	1992.39±0.01	0.40±0.02	0.25±0.03	0.44
C3	14.5	4.62±0.04	1992.86±0.02	0.40±0.01	0.72±0.03	0.27
C3	8.0	3.37±0.05	1992.97±0.01	0.57±0.01	0.83±0.03	0.08
B3+C3	4.8	1.28±0.02	1992.86±0.01	0.52±0.02	0.72±0.03	0.03
D3	90.0	5.74±0.11	1992.54±0.01	0.71±0.01	–	0.57
D3	36.8	6.03±0.07	1992.53±0.01	0.46±0.01	0.00±0.01	0.19
D3	22.2	5.32±0.14	1992.83±0.01	0.40±0.01	0.30±0.02	0.30
D3	14.5	6.19±0.08	1993.33±0.01	0.47±0.01	0.80±0.02	0.89
D3	8.0	5.11±0.10	1993.46±0.01	0.30±0.01	0.93±0.02	0.49
D3	4.8	3.33±0.03	1993.54±0.01	0.45±0.01	1.01±0.02	0.05
E3	90.0	7.02±0.91	1993.16±0.01	0.29±0.01	–	0.83
E3	36.8	6.41±0.08	1993.12±0.01	0.55±0.01	0.00±0.01	0.82
E3	22.2	5.40±0.14	1993.24±0.01	0.39±0.01	0.12±0.01	0.76
E3	14.5	6.57±0.07	1993.81±0.01	0.48±0.01	0.69±0.02	0.63
E3	8.0	5.26±0.07	1993.84±0.01	0.43±0.01	0.72±0.02	0.19
E3	4.8	2.39±0.05	1993.98±0.01	0.38±0.01	0.86±0.02	0.13
F3	90.0	9.32±0.23	1994.15±0.01	1.15±0.02	–	1.52
F3	36.8	10.72±0.10	1994.11±0.02	0.95±0.02	0.00±0.02	0.48
F3	22.2	11.20±0.13	1994.25±0.01	1.29±0.01	0.14±0.03	0.34
F3	14.5	12.74±0.10	1994.47±0.01	0.80±0.01	0.36±0.03	1.14
F3	8.0	11.23±0.07	1994.55±0.01	1.04±0.01	0.44±0.03	0.42
F3	4.8	7.85±0.05	1994.68±0.01	1.10±0.01	0.57±0.03	0.18
G3+H3	36.8	5.71±0.05	1995.31±0.01	0.91±0.01	0.00±0.01	0.27
G3	22.2	5.41±0.08	1995.41±0.01	0.51±0.01	0.10±0.02	0.15
G3+H3	14.5	6.39±0.10	1995.55±0.01	0.83±0.02	0.24±0.02	0.43
G3+H3	8.0	4.09±0.09	1995.58±0.01	0.58±0.01	0.27±0.02	0.08
G3+H3	4.8	3.45±0.04	1995.74±0.01	0.74±0.01	0.43±0.02	0.10
I3+J3	36.8	3.46±0.07	1996.45±0.02	0.80±0.02	0.00±0.02	0.20
I3	22.2	4.42±0.77	1996.20±0.08	0.48±0.04	-0.25±0.08	0.09
I3+J3	14.5	5.04±0.04	1996.54±0.01	0.71±0.02	0.11±0.03	0.43
I3+J3	8.0	6.14±0.04	1996.42±0.01	1.11±0.02	-0.03±0.03	0.14
I3+J3	4.8	5.61±0.05	1996.54±0.01	0.83±0.03	0.09±0.03	0.27

Table 2.4: List of component ejections in the jet of 3C 454.3 collected from the literature. The time of the jet component ejection T is given in years, the time difference between two component ejections ΔT, frequency of the observations in GHz, and the references are listed.

T [yr]	ΔT [yr]	Freq.	Reference
1969.0	–	2.3, 10.7 GHz	Gubbay et al. 1977, Wu et al. 1988
1981.4	12.4	5 GHz	Pauliny-Toth et al. 1984
1982.1	0.7	5 GHz	Pauliny-Toth et al. 1984
1988.2	6.1	5 GHz	Cawthorne & Gabuzda 1996
1994.45	6.25	22 GHz	Jorstad et al. 2001
1995.05	0.6	22 GHz	Jorstad et al. 2001
1995.59	0.54	22 GHz	Jorstad et al. 2001

2.4 Results – 3C 446 (2223-052)

2.4.1 Introduction

The source 3C 446 (z=1.404 Hewitt & Burbidge 1980; Wright et al. 1983) has intermediate properties between those of quasars and BL Lac objects, displaying prominent broad emission lines (typical for quasars) during its quiescent state and high linear polarization and a strong, featureless continuum (typical for BL Lac objects) in its active state (Barbieri et al. 1985). It also shows another BL Lac characteristics: a high degree ($\sim 10\%$) of variable optical polarization (Mead et al. 1990). 3C 446 is one of the most luminous X-ray quasars and shows a high degree of variability at optical and radio wavelengths. The map of 3C 446 at 15 GHz (from MOJAVE database, Lister & Homan 2005) is shown in Fig. 2.11. The source exhibits rapid variability in the optical, X-ray and radio wavelengths (Teräsranta et al. 1998, Sambruna 1997). Previous studies of the periodicity in the optical light curves of 3C 446 have shown a prominent periodicity of 4.2 years, which was found and confirmed by several authors (Barbieri et al. 1985; Webb et al. 1988; Barbieri et al. 1990) and a period of 5.8 years which was detected by Barbieri at al. 1985. However, no periodical changes in the radio total flux-density variability of the source have been reported before.

Various time scales of 3C 446 variability were reported before. For example, Lainela & Valtaoja 1993 using structure function analysis found a time scale of 1.5 years (22 GHz and 37 GHz), whereas Hughes et al. 1992 found a timescale of 1.25 years (4.8 GHz, 8 GHz, and 14.5 GHz). However, most of the reported time scales are quite short and are no longer than $\sim$2 years.

2.4.2 Search for periodicity

Multi-frequency radio light curves of 3C 446 at five frequencies from 4.8 GHz to 37 GHz between 1980 and 2004 are shown in Fig. 2.12. Flares of two types alternate in the light curve: narrow, single flares occurred in 1984 and 1996, and broad flares with possible substructure in 1990 and 2000. The time interval between a narrow flare and the following broad flare is about 6 yr, while the interval between two successive flares of the same type is about 12 yr. Applying the method of Jurkevich to the light curves of 3C 446 yielded with a high degree of confidence the presence of periods of 5.8 ± 0.5 yr for all five frequencies, and 9.8 ± 0.5 yr for all frequencies except 4.8 GHz. The

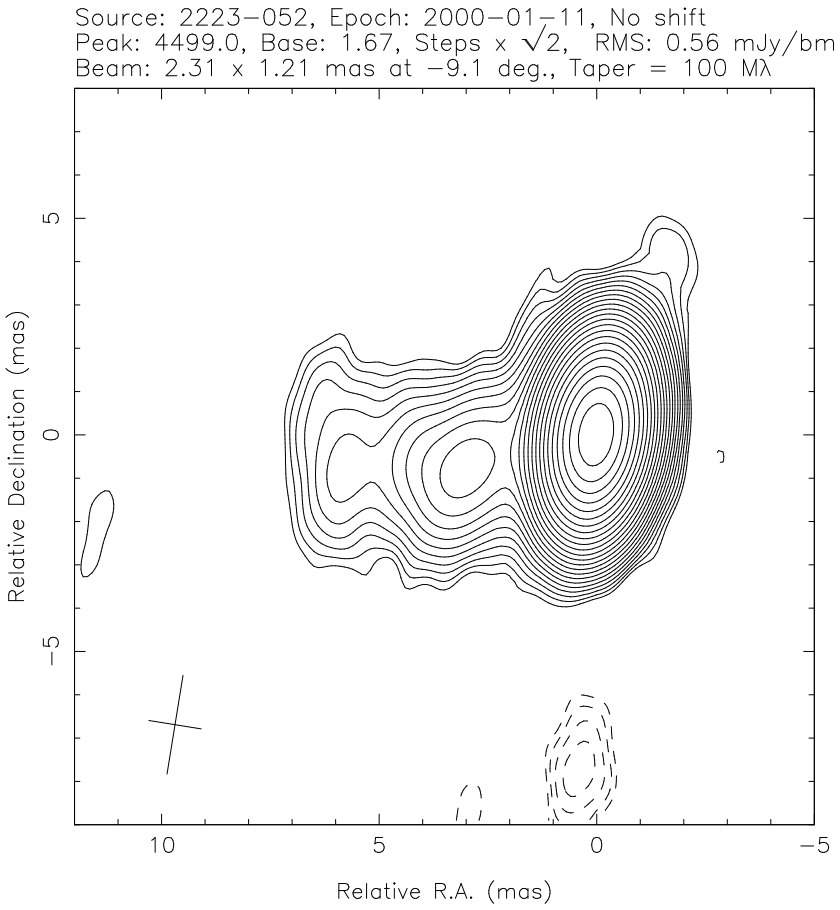

Figure 2.11: Map of 3C 446 at 15 GHz from MOJAVE database (Lister & Homan 2005).

presented periods are the average values over the various frequencies. The discrete autocorrelation function, similarly to the Jurkevich method, yielded a period of 10.9 ± 0.2 yr for 37, 22, and 14.5 GHz. However, the 6-year period has not been detected with this method. The results of the Jurkevich method for the 8 GHz data and results of the discrete autocorrelation function for 14.5 GHz can be seen in Fig. 2.13, left and right accordingly.

Table 2.5 gives a list of the derived periods for all five frequencies. Taking into account the redshift of the source, $z = 1.404$, and applying the relation $P = P_{obs}/(1+z)$, the detected periods in the rest frame of the source are 2.4 and 4.5 yr. Figure 2.12 shows light curves for $3C$ 446 for all the frequencies,

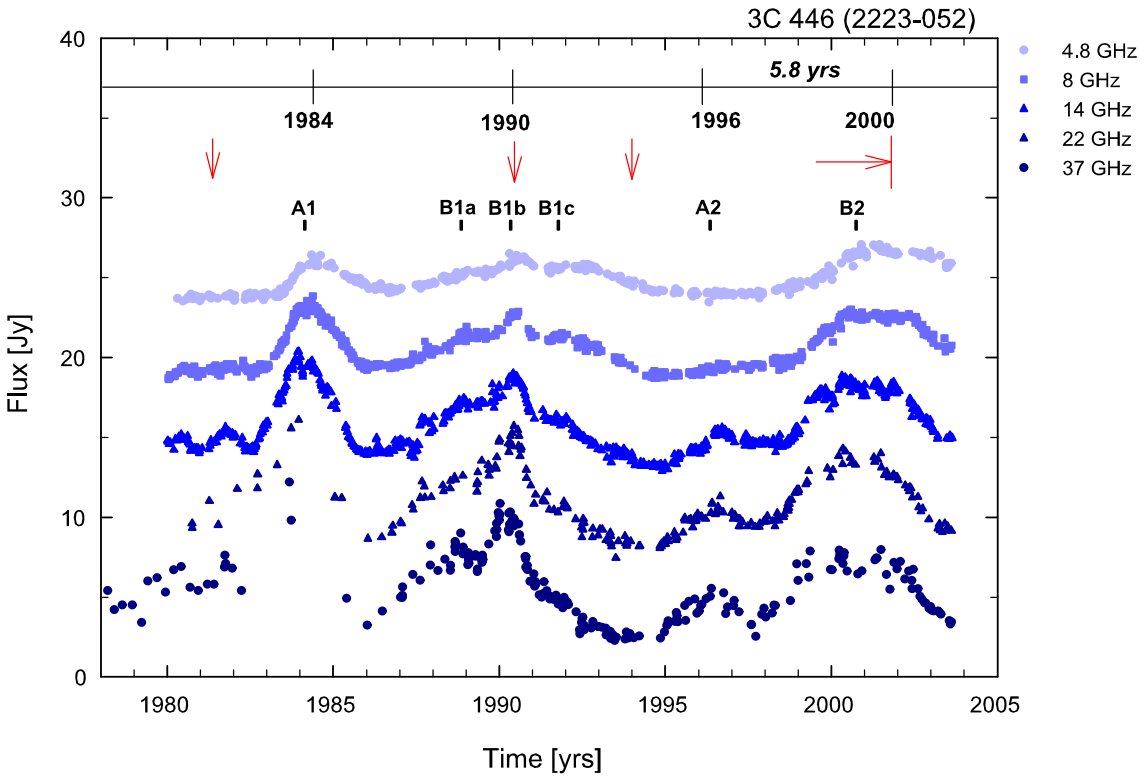

Figure 2.12: Light curve for 3C 446 at 37, 22, 14.5, 8 and 4.8 GHz. For ease of viewing, the curves have been shifted relative to each other by 5 Jy. The red arrows mark the ejection times of VLBI components. Vertical marks show the names of the outbursts, decomposed by means of the Gaussian functions fitting.

with the flares corresponding to a period of 5.8 ± 0.5 yr found with a high confidence level f using the method of Jurkevich indicated. We can see that the period describes the activity of the source well, i.e., the flares of 1984, 1990, 1996, and 2000. On the other hand, the discrete autocorrelation function detected only the 11-year period, possibly due to the coincidence in the structure of the "broad" and "narrow" flares when the light curve is shifted by 11 years.

Table 2.5: Detected periods for 3C 446 (2223-052)

ν (GHz)	P_{Jurk},yr	f	P_{DACF},yr	k
37 GHz	4.2 ± 0.4	0.26		
	8.9 ± 2.5	2.55	10.7 ± 2.5	0.85
22 GHz	6.9 ± 2.2	1.83		
	11.1 ± 2.4	2.55	10.6 ± 1.6	0.85
14.5 GHz	5.6 ± 1.3	0.52		
	9.5 ± 0.7	1.21	11.3 ± 3.3	0.25
8 GHz	5.3 ± 1.1	0.56	—	—
	9.9 ± 1.1	0.54		
4.8 GHz	7.2 ± 0.7	0.39	—	—

2.4.3 Jet components ejections

The question whether both types of flares are associated with the ejection of new superluminal components can be addressed using VLBI observations. The high-resolution image of the source was obtained by Lerner et al. 1993 at 100 GHz in April 1990 and shown in Fig. 2.14. The map shows a bright component near the core, which could plausibly have been ejected in the beginning of 1990, close to the flares in 1988–1992. The blazar 3C 446 was observed by Kellermann et al. 2004 as part of a program of 2-cm survey MOJAVE VLBI monitoring of AGN at 15 GHz. These 15 GHz observations can provide information about large-scale processes in the evolution of the source and indicate the characteristic time scale for flaring activity cycles. Kellermann et al. 2004 report the ejections of VLBI components at epochs 1981.4 ± 1.6 and 1994.0 ± 0.8, marked on the light curve (Fig. 2.12) by vertical arrows. Given the possible uncertainties in determining the birth epochs of the components, these epochs are fairly close to the powerful flares of 1984 and 1996. The plot of the core separation versus time for the VLBI jet components of 3C 446 at 15 GHz, available on the MOJAVE website (Lister et al. 2005, Lister & Homan 2005) shows that two components were ejected at about 2000 and 2001. We can see from Fig. 2.12 that this component could be associated with the decay of a powerful flare in 2000. A visual analysis of the maps of MOJAVE 15-GHz monitoring program, suggests the ejection of a new VLBI component in 2007. Taking into account the uncertainties in the

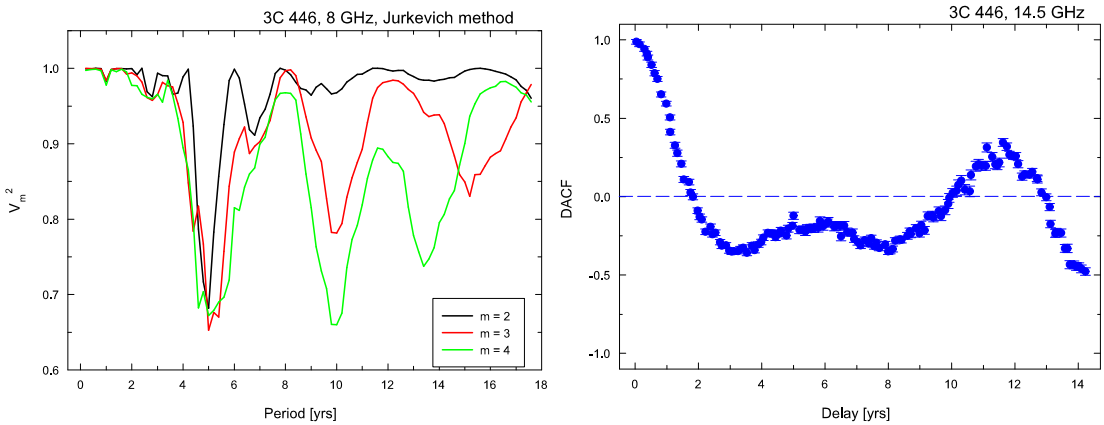

Figure 2.13: *Left:* Results of the period search for 3C 446 at 8 GHz using the method of Jurkevich. Plots for various bin numbers for the phase curve are presented.; *Right:* Discrete autocorrelation function for 3C 446 at 14.5 GHz.

birth epochs of VLBI components, the births of observed components agree fairly well with the epochs of the powerful flares described by the period of 5.8 ± 0.5 yr. However, the detailed analysis of archival long-term VLBI observations is needed in order to check this periodicity in the jet component ejections of 3C 446.

2.4.4 Predicted flare

According to our estimates, we predicted the next flare to occur in 2007. It should have a similar amplitude as the 1996 flare and be accompanied by the birth of a new component on VLBI scales. This flare was observed in January 2007 by the University of Michigan Radio astronomical observatory at the predicted time. Figure 2.15 (Left) shows a new flare at 8 GHz marked with a red box. The flare was observed at three frequencies at 4.8 GHz, 8 GHz, and 14.5 GHz (Fig. 2.15 (Right)). The new flare shows brightness similar to the 1996 flare. Moreover, as we mentioned before, the visual analysis of the maps of the MOJAVE 15-GHz monitoring program, suggests the ejection of a new VLBI component in 2007, which was also predicted. The appearance of a new flare and a new jet component at the predicted time proves that the 6-year period is correct. The same flux level of a new flare as the 1996 flare also proves the liability of a 12-year periodicity.

Since we proved that the 6-year and the 12-year periodicities are correct,

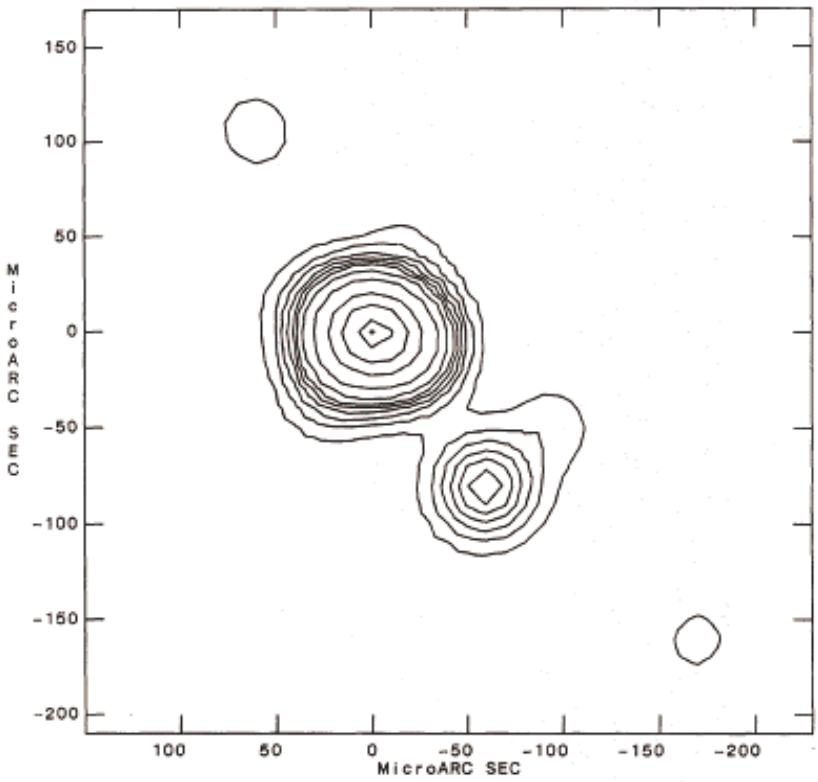

Figure 2.14: High resolution map of 3C 446 at 100 GHz with a 40 μas restoring beam from Lerner et al. 1993.

we can predict the next flare to happen in about 2013, with similar amplitude and width as the 2001 flare, and be accompanied by the birth of a new jet component on VLBI scales.

2.4.5 Frequency-dependent time delays

In order to study the properties of the outbursts, we decomposed the light curves into Gaussian components. Before the decomposition, the long-term trends, calculated via a linear interpolation across the local/global minima in 1981, 1986, 1994 and 2004 were removed from the data. In addition to the UMRAO and MRO data, the light curves contain 33.5 GHz data of Flett & Henderson (1981, 1983) and 36.8 GHz and 22 GHz data of Salonen et al. (1987). The parameters of the Gaussian components used to decompose the

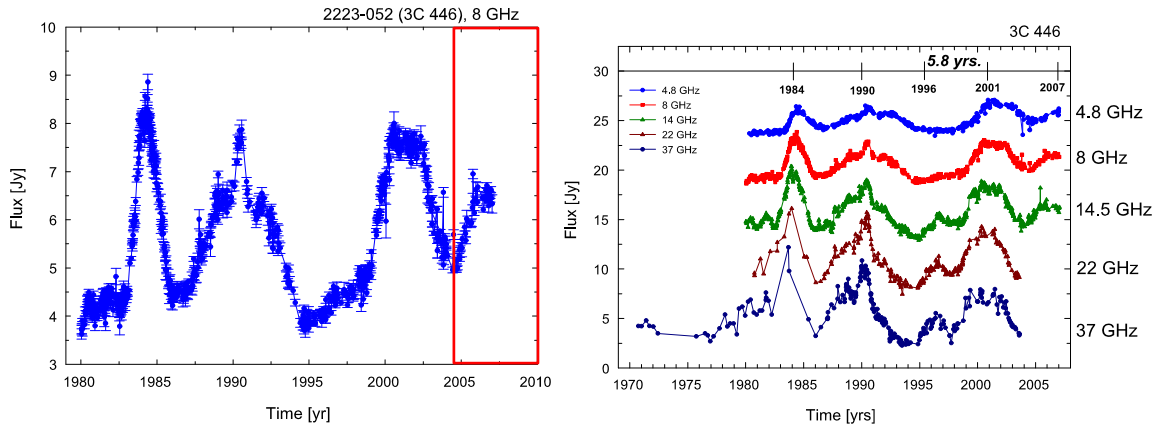

Figure 2.15: *Left:* The light curve of 3C 446 at 8 GHz. The red box marks a new flare, which appeared in 2007 at the predicted time. This proved that the 6-years period is correct; *Right:* The total flux-density light curve of 3C 446 at 4.8, 8, 14.5, 22, and 37 GHz. It is clearly seen that the 2007 flare appeared at 4.8, 8, and 14.5 GHz in predicted time.

outbursts are presented in Table 2.6 and maxima of the Gaussian components shown with vertical marks in Fig. 2.12.

As was shown before, the light curves of 3C 446 reveal two periods: $P_1 = 10.9 \pm 0.2$ yr and $P_2 = 5.8 \pm 0.5$ yr. As we can see from Fig. 2.12, the shorter period characterizes the average interval between the maxima of prominent outbursts, while the longer period reflects similarities in the shapes of the outbursts. We divided the light curves into 12-year cycles in order to analyze the flares from different cycles separately. We took the beginning of the first cycle to be in 1982 and the second cycle in 1994. Each long cycle starts with an isolated outburst ($A1$ in 1984 and $A2$ in 1996), which is followed by a prolonged, multi-component sub-outbursts ($B1a$, $B1b$, $B1c$ and $B2$). Unfortunately, the parameters of $A1$ at 37 and 22 GHz are affected by the small number of data points at high frequencies prior to 1986.

Figure 2.16 shows the amplitudes and time lags of all components as functions of frequency. The amplitude spectra of the outburst $A1$ and flares $B1a$ and $B1b$ are dominated by high-frequency components. The low-frequency delay of outburst $A1$ is ~ 0.9 yr, while the flares $B1a$ and $B1b$ display the moderate delay of $\Delta T \sim 0.6$ yr. The time lag for the flare $B1c$ increases to $\Delta T \sim 1.0$ yr, accompanied by flattening of the spectrum. This evolution sug-

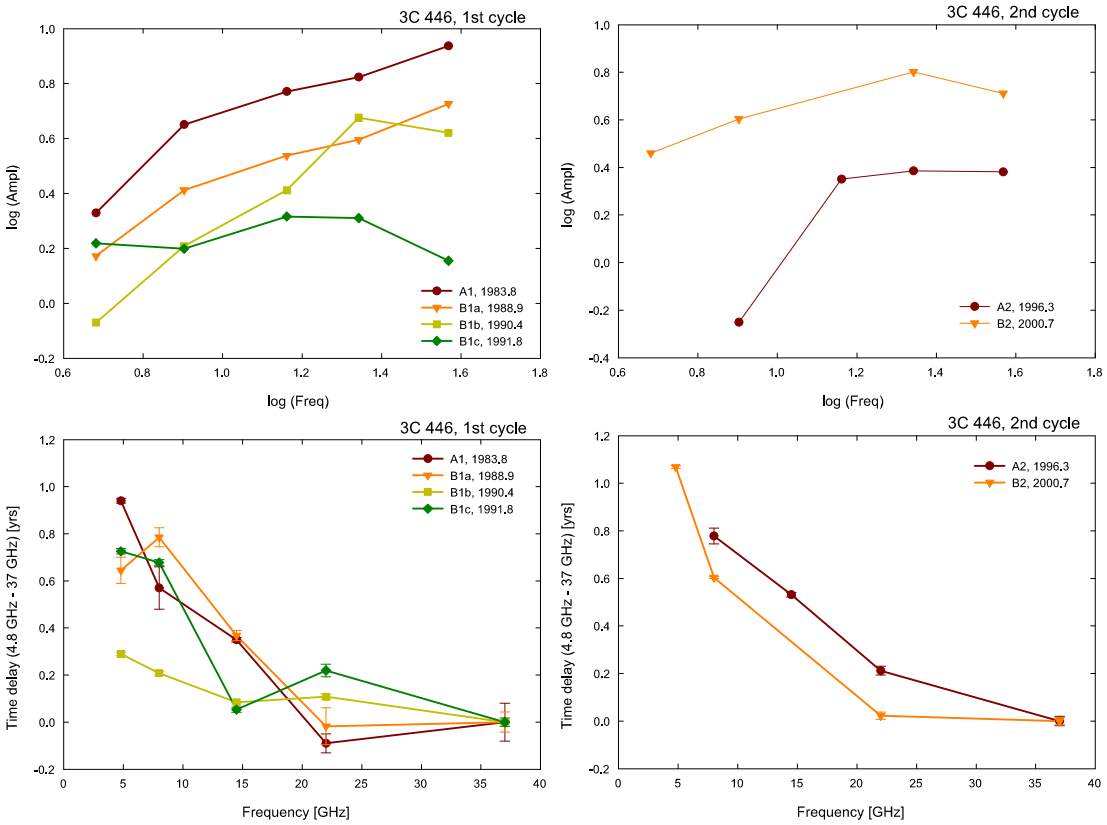

Figure 2.16: Amplitudes *(top)* and time delays *(bottom)* as functions of frequency for the first *(left)* and second *(right)* cycles in 3C 446.

gests that $B1a, B1b$, and $B1c$ represent the fine structure of a single event, $B1$. The low-frequency delay and steep amplitude spectrum of the outburst $A2$ are similar to those observed for $A1$. Sub-outburst $B2$ has a long time-lag ($\Delta T \sim 1.3$ yr) and a flat spectrum, like $B1c$. We were not able to decompose the fine structure of sub-outburst $B2$, because it has characteristics similar to those of white noise.

We constructed the spectra for the light curves at five frequencies from 1986 to 2004 using quasi-simultaneous data points at different frequencies. The data points were selected in such a way, that the time separation between each point is no more than two weeks (14 days). The evolution of spectral indices is shown in Fig. 2.17 (Right). The cycle starts with a steep spectrum ($A2$), then it gradually flattens ($B1a$, $B1b$) and reaches the flattest spectrum

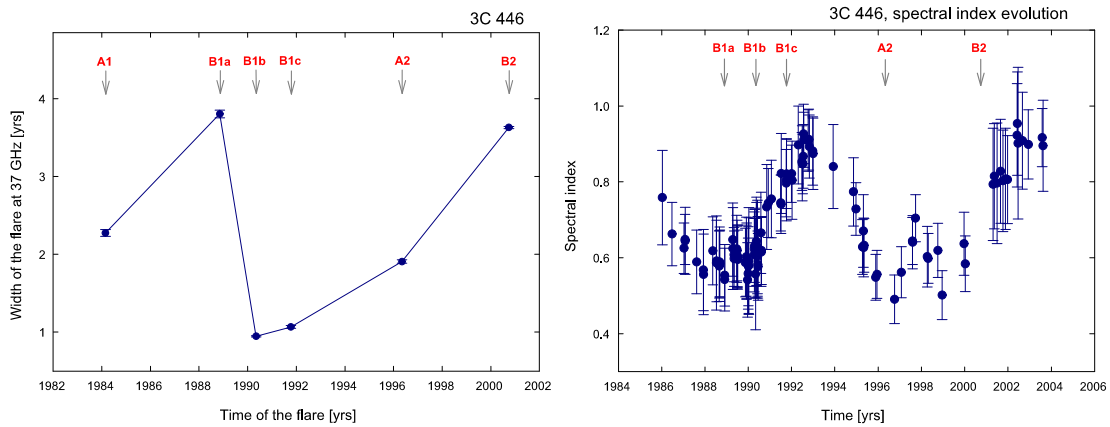

Figure 2.17: *Left:* Evolution of the widths of the bright outbursts of 3C 446 at 37 GHz. The arrows indicate the names of the outbursts.; *Right:* Spectral indexes' evolution of 3C 446.

during the bright flares $B1c$ and $B2$ and then steepens again. Moreover, the width of the flares is also changing when the cycle proceeds. Figure 2.17 shows that the cycle starts with narrow flares, such as $A1$ and $A2$, then the width is gradually growing and reaches its maximum during the bright flat-spectrum flares $B1a$ and $B2$. These changes with time (spectra, time delays and widths), similarly to 3C 454.3, indicate the presence of a similar scenario of evolution of the flares of each cycle.

The VLBI data for 3C 446 prior to 1995 are sparse: the only high-resolution image referring to this time is that of Lerner et al. 1993, obtained at 100 GHz in April 1990. This map reveals a compact, nearly unresolved core and a fairly strong component $\sim 100\ \mu as$ to the southwest. This component could plausibly have been ejected in the beginning of 1990, in which case it could be associated with the flare $B1b$. Since 1995, the source has been observed more regularly as part of the 15 GHz multi-epoch MOJAVE VLBA program of Kellermann et al. 1998, 2004. These data reveal new jet components ejected in 1981.4 ± 1.6 and 1994.0 ± 0.8. Given the large uncertainties in the ejection times, the first component may be associated with outburst $A1$ and the second with $A2$. Recent results from the MOJAVE 15-GHz survey (Lister et al. 2005) indicate that another new component was ejected prior to 2001. This knot is probably associated with the complex outburst $B2$. According to our classification, all the outbursts show mixed properties. However, the A outbursts have a steep amplitude spectrum (the

amplitude of the Gaussian component vs. frequency), similar to that expected when a flux decrease is dominated by adiabatic expansion (Hughes et al. 1985). The B outbursts have a flat amplitude spectrum and longer low-frequency time delays, consistent with synchrotron losses being responsible for the electron-energy distribution (Marscher & Gear 1985). This suggests that the A outbursts represent minor perturbations, e.g., associated with shocks formed during interactions between the jet and external medium ("jet" events), while the B outbursts correspond to primary perturbations due to activity in the central engine ("core" events). This leads us to define the flaring activity cycle of this blazar to be the time interval between two successive B outbursts, or $\sim$12 yr.

2.4.6 Summary

Using time series analysis, we have found two periods of $P_1 = 10.9 \pm 0.2$ yr and $P_2 = 5.8 \pm 0.5$ yr. (which correspond to 4.5 and 2.4 years in the source rest frame) in the radio total flux-density light curves at five frequencies. We found that the flaring activity cycle of this source is $\sim$ 12 years, which is much longer than it was thought before. The jet components on VLBI scales are ejected with a characteristic timescale of $\sim$6 years. The periods in the total flux-density light curves are in good agreement with the characteristic time scale for the VLBI jet component ejections as well as the duration of the flaring activity cycle. Moreover, the detected period 5.8 ± 0.5 yr coincides with the period of 5.8 yr found in Barbieri et al. 1985 for the optical light curve of 3C 446. It is worth to notice, that this makes the source 3C 446 one of a few sources for which a period in the radio total flux-density light curve coincides with a period in the optical light curves.

We predicted a new flare to appear in 2007 and be accompanied by the ejection of a new jet component. This was actually observed in the predicted time at radio wavelengths. An appearance of a new jet component is seen from the maps at 15 GHz of the MOJAVE monitoring campaign. This makes 3C 446 one of the best sources with periodical light curves, which is comparable with OJ 287, for which the flare was also predicted. The next flare should appear in about 2013 and will have an amplitude comparable with the 2000 flare. It will be much broader than the 2007 flare and will be accompanied by the ejection of a new VLBI component.

The results for this source are similar to 3C 454.3. We found that the time period between two "core" outbursts coincides with the timescale of jet com-

ponent ejections and with the periods found with the periodicity analysis of the total flux-density variability. Therefore, we can conclude that the periodical variability of this source is caused by the periodical primary perturbation in the base of the jet, which can be caused by e.g. the precession of an accretion disc, instabilities in the accretion disc or a passage of a secondary black hole.

Table 2.6: 3C 446: Parameters of outbursts

Comp.	Freq. GHz	Amplitude Jy	T_{max} yr	Θ yr	Time delay yr	σ^2
A1	33.5	8.65±0.27	1983.80±0.08	2.27±0.05	0.00 ±0.08	1.84
A1	22.2	6.66±0.33	1983.71±0.04	2.36±0.04	-0.09±0.09	0.57
A1	14.5	5.90±0.02	1984.15±0.01	1.65± 0.01	0.35±0.09	0.12
A1	8.0	4.48±0.02	1984.37±0.01	1.66± 0.01	0.57±0.09	0.12
A1	4.8	2.13±0.04	1984.74±0.02	1.88± 0.02	0.94±0.09	0.05
B1a	36.8	5.33±0.05	1988.87±0.05	3.80± 0.05	0.00±0.05	0.36
B1a	22.2	3.94±0.10	1988.85±0.08	2.80± 0.07	-0.02±0.09	0.21
B1a	14.5	3.45±0.02	1989.23±0.02	3.01± 0.02	0.37±0.05	0.17
B1a	8.0	2.58±0.02	1989.65±0.04	3.89± 0.03	0.78±0.06	0.04
B1a	4.8	1.49±0.01	1989.51±0.06	3.09± 0.08	0.64±0.08	0.02
B1b	36.8	4.17±0.08	1990.35±0.01	0.95± 0.01	0.00±0.01	0.26
B1b	22.2	4.74±0.12	1990.46±0.02	1.12± 0.02	0.11±0.02	0.30
B1b	14.5	2.58±0.03	1990.43±0.01	0.74± 0.01	0.08±0.02	0.11
B1b	8.0	1.62±0.04	1990.56±0.01	0.71± 0.01	0.21±0.02	0.06
B1b	4.8	0.85±0.02	1990.64±0.01	0.72± 0.01	0.29±0.02	0.02
B1c	36.8	1.43±0.05	1991.78±0.02	1.07± 0.02	0.00±0.02	0.10
B1c	22.2	2.04±0.08	1992.00±0.03	1.41± 0.02	0.22±0.04	0.18
B1c	14.5	2.07±0.01	1991.83±0.01	1.95± 0.02	0.05±0.03	0.03
B1c	8.0	1.58±0.02	1992.46±0.02	2.01± 0.02	0.68±0.03	0.04
B1c	4.8	1.65±0.01	1992.51±0.02	2.72± 0.02	0.73±0.03	0.02
A2	36.8	2.40±0.07	1996.35±0.02	1.91± 0.02	0.00±0.02	0.16
A2	22.2	2.43±0.05	1996.56±0.02	1.87± 0.02	0.21±0.03	0.11
A2	14.5	2.24±0.02	1996.88±0.01	1.87± 0.01	0.53±0.03	0.05
A2	8.0	0.56±0.02	1997.13±0.03	1.71± 0.03	0.78±0.04	0.02
B2	36.8	5.14±0.06	2000.74±0.02	3.63± 0.02	0.00±0.02	0.48
B2	22.2	6.32±0.08	2000.76±0.02	3.59± 0.02	0.02±0.03	0.14
B2	8.0	4.01±0.01	2001.34±0.01	3.75± 0.01	0.60±0.03	0.09
B2	4.8	2.88±0.01	2001.81±0.01	3.65± 0.01	1.07±0.03	0.05

2.5 Results – CTA 102 (2230+114)

2.5.1 Introduction

CTA 102 is a gamma-ray blazar at $z = 1.037$ (Blom et al. 1995). Observations of CTA 102 with the EGRET telescope at the high-energy γ-rays (> 100 MeV) have shown that the source exhibits a high γ-ray luminosity, $L_\gamma = 10^5$ erg/s (Nolan et al. 1993). The X-ray flux is correspondingly high, $F_{\rm X} = 0.75$ μJy. CTA 102 is an optical variable with a mean magnitude of 17.33 and a high polarized quasar. The arcsecond scale structure of the source is dominated by a central core and two other components (Spencer et al. 1989). The map of CTA 102 at 15 GHz (from MOJAVE database, Lister & Homan 2005) is shown in Fig. 2.18. Observations at λ6 cm (Wehrle & Cohen 1989), at λ18 cm, and at λ1.3 cm (Rantakyrö et al. 1996) show a central double knot feature (separated in NS direction by $\sim$3 mas) with an extended diffuse tail bending sharply to the SW. Rantakyrö et al. (1996) showed that the source exhibits fast structural changes (on the months timescale). In 1965, Sholomitsky published the first report of variability of this source, with a period of 102 days at 902 MHz, which was the first detection of a periodicity in the light curves of blazars. However, this result was not subsequently confirmed (Terzian 1966).

2.5.2 Search for periodicity

Figure 2.19 (Left) presents the light curves of CTA 102 at all five frequencies. Figure 2.19 (Right) shows the light curve of CTA 102 at 14.5 GHz, which allows us to see the substructure of particular flares. We can see that bright flares occurred in about 1982, 1990 and the enormously bright flare happened in 1998. The time separation between these outbursts is similar and they are observed approximately every eight years. The bright flares in 1982, 1990, and 1998 were followed by fainter flares in 1986, 1995, and 2003 (see Fig. 2.19, right). It is worth to notice, that the faint flares appeared four-five years after each bright outburst. Since the bright flares were observed every eight years and the fainter flares around four-five years after we can expect that there is a periodicity of about 4 years and about 8 years in the radio total flux-density light curves of CTA 102.

To test whether there is a quasi-periodicity in the appearance of the outbursts, we subtracted the epochs for corresponding sub-outbursts in consec-

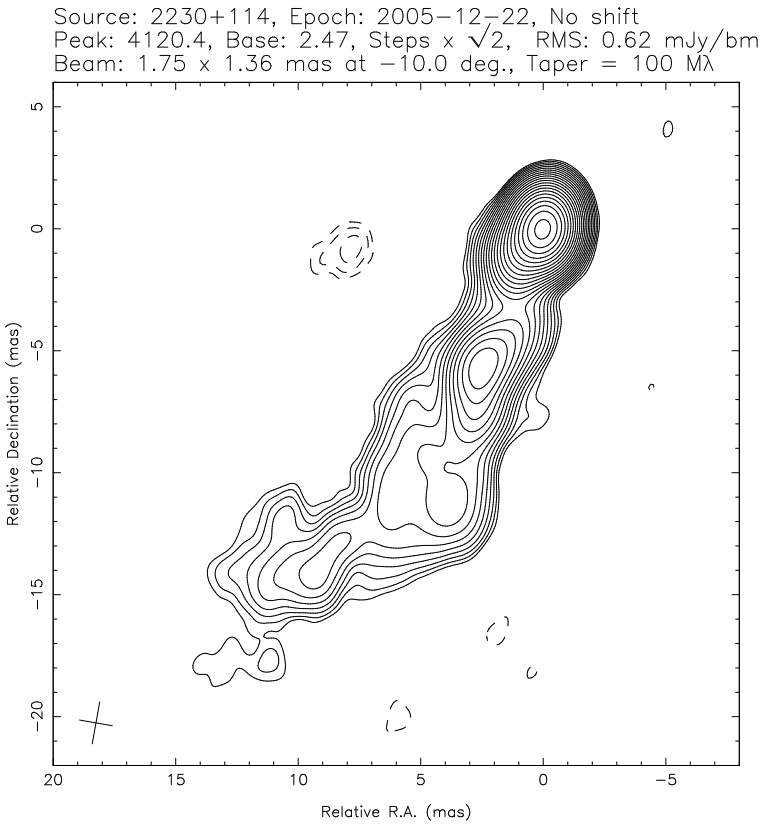

Figure 2.18: Map of CTA 102 at 15 GHz from MOJAVE database (Lister & Homan 2005).

utive cycles at all available wavelengths (Table 2.8). The mean time intervals between the peaks of consecutive corresponding sub-outbursts are 8.14 ± 0.30 for the interval from cycle 2 to cycle 1 and 7.95 ± 0.31 for the interval from cycle 3 to cycle 2. Given the time delays between the various frequencies and the possible dependence of these time delays on the amplitudes of individual sub-outbursts (see below), the agreement between these two mean values is good. Therefore, we tentatively suggest that outbursts in this source repeat every 8.04 ± 0.30 years, preserving the relative positions in time of individual sub-outbursts within the outbursts, even when the amplitudes of the sub-outbursts change substantially.

The flares of the source are not smooth, but are rather characterized by the presence of fine structure on time scales appreciably shorter than

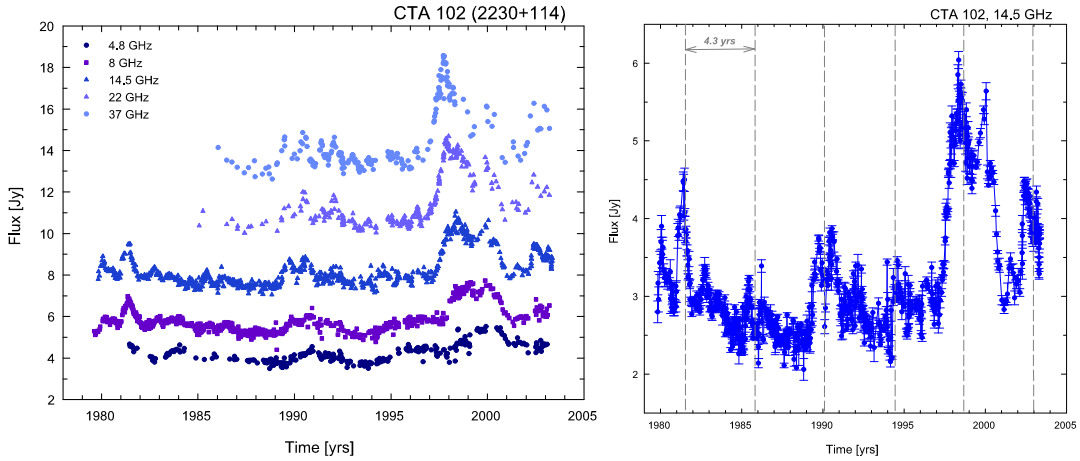

Figure 2.19: *Left:* Light curve of CTA 102 at 37, 22, 14.5, 8 and 4.8 GHz. For ease of viewing, the curves have been shifted relative to each other in flux.; *Right:* Light curve of CTA 102 at 14.5 GHz. The dotted lines mark intervals corresponding to the 4.3 ± 0.5-year period.

one year. The major 1982, 1990, and 1998 flares have different amplitudes, but interestingly have similar shape and similar sub-structure. All the major flares have a double-peak structure, where each peak lasted for about one year. However, the amplitudes of the substructure peaks are changing. In case of 1982 and 1998 outbursts, the first peak in the double-peak is the brightest, whereas during the 1990 outburst, two peaks had equal brightness.

The discrete autocorrelation function yielded periods of 4.3 ± 0.5 yr at 14.5 GHz and 8.4 ± 0.1 yr at 14.5 and 4.8 GHz (Table 2.7). Figure 2.21 (Right) presents the discrete autocorrelation function for 14.5 GHz. The method of Jurkevich yields periods of 4.6 ± 0.7 yr at 37, 22, and 4.8 GHz and 9.3 ± 0.6 yr at all frequencies except 8 GHz (Table 2.7, Fig. 2.21 (Left)). Figure 2.19 (Right) presents the 14.5 GHz light curve with the intervals corresponding to the period 4.3 ± 0.5 yr indicated. We can see that this period describes well both the powerful flares of 1981, 1990, and 1999 and the weaker flares 1986, 1995, and 2003, while the period 8.4 ± 0.1 yr describes only the large-amplitude flares (1981, 1990, and 1999). The available light curve encompasses about six four-year and three eight-year periods. Taking into account the source redshift, the derived periods in the rest frame of the source are 2.1 and 4.1 yr.

The optical monitoring of CTA 102 has shown, that the optical outbursts appear almost simultaneously with the radio outbursts. Figure 2.20 shows the light curve in the optical B, V, R, and I bands, observed with the 80-cm optical telescope AZT-8 at the Crimean Astrophysical Observatory.

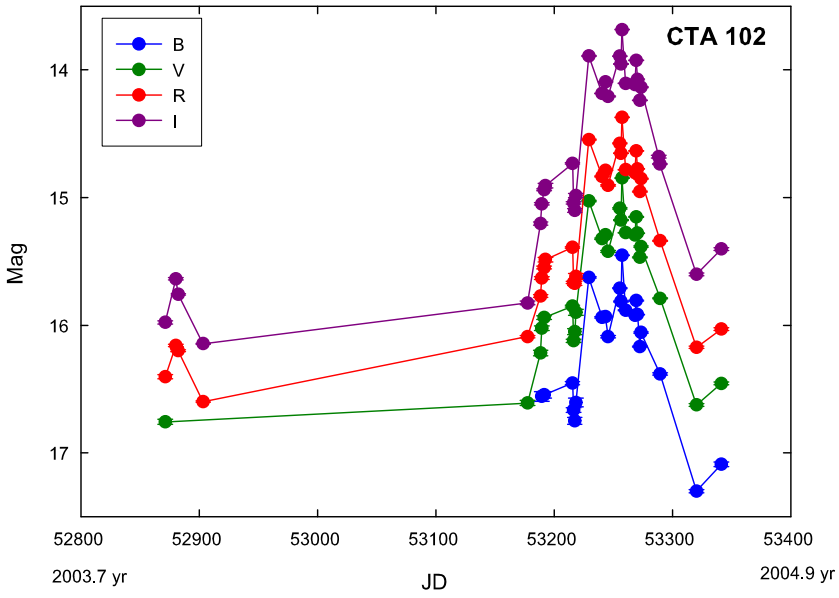

Figure 2.20: Optical light curve of CTA 102 in the optical bands B, V, R, and I.

If the four-year period is correct, than the next strong outburst in the light curves of CTA 102 would appear in about 2011. The brightness of the flare will be comparable with the brightness of the 1981, 1990, and 1999 flares and will be about 4–6 Jy. The next outburst should also be accompanied by a jet component ejection. In order to check our prediction for the next flare and to check the periodicity the multi-wavelength monitoring of CTA 102 should be organized. The source should be observed at least in radio in optical and be complemented with the very long baseline interferometric observations.

2.5.3 Jet components ejections

Jorstad et al. (2001, 2005) reported ejection of VLBI components in CTA 102 at epochs 1994.28 ± 0.02, 1995.19 ± 0.04, 1996.08 ± 0.02, 1997.9 ± 0.2, and 1999.54 ± 0.04 at 43GHz . Rantakyrö et al. 2003 estimated the emergence

Table 2.7: Detected periods for CTA 102 (2230+114)

ν (GHz)	P_{Jurk},yr	f	P_{DACF},yr	k
37 GHz	5.2 ± 0.7	0.60	—	—
	9.7 ± 1.5	0.62		
22 GHz	4.9 ± 0.4	0.60	—	—
	8.4 ± 2.3	0.47		
14.5 GHz			4.3 ± 0.5	0.41
	9.2 ± 2.0	0.22	8.3 ± 1.2	0.17
4.8 GHz	3.8 ± 0.8	0.28		
	9.8 ± 2.1	0.46	8.5 ± 1.2	0.10

epochs and speeds of jet components based on all available VLBI observations in the literature. In addition to the jet components found by Jorstad et al. (2001, 2005), Rantakyrö et al. 2003 found a few VLBI components ejected in 1930.3, 1964.4, 1984.4, 1988.9, 1989.2, and 1991.9. Piner et al. 2007 have found that all the jet components observed in 1996-2002 at 8 and 2 GHz RRFID snapshot images are stationary and they have not found any jet component ejections. Piner et al. 2007 based on the dense homogeneous RRFID data, whereas Rantakyrö et al. 2003 based their analysis on the data, calibrated and analyzed by different authors. The ejection epochs of the 43-GHz VLBI components are marked by arrows on the 37 GHz light curve (Fig. 2.22). Each ejection epoch coincides with a flare at 37 GHz, but the irregular and insufficiently dense series of VLBI observations prevents a detailed comparison of the evolution of the light curve with the evolution of the VLBI source structure.

2.5.4 Frequency-dependent time delays

Radio light curves of this quasar display strong outbursts that repeat approximately every ∼8 years (Fig. 2.19). At millimeter wavelengths, the outbursts can be decomposed into six narrow sub-outbursts A, B, C, D, E and F (Fig. 2.23, *Right*); only the two leading sub-outbursts A and B can be distinguished at cm wavelengths, while the other sub-outbursts merge into two broad features (C+D and E+F; Fig. 2.23, *Left*).

We expected in this case that the leading sub-outburst of the next out-

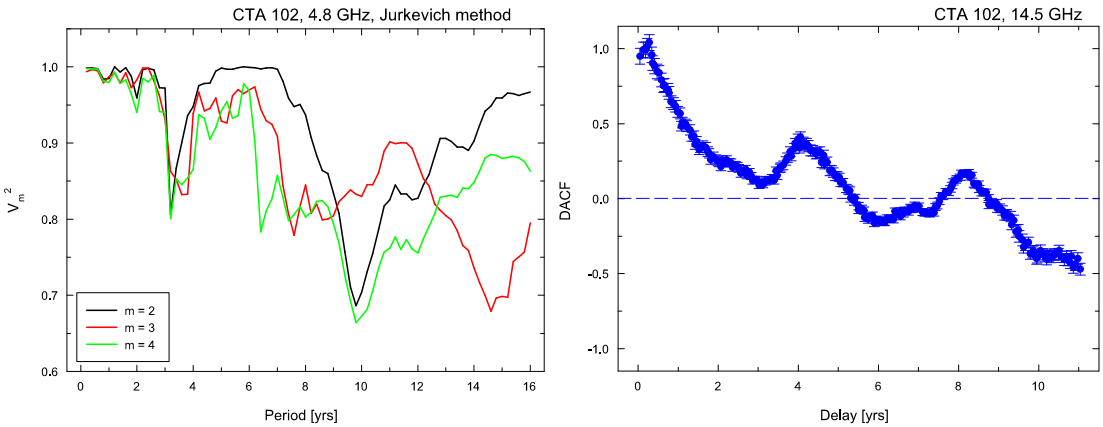

Figure 2.21: *Left:* Results of the period search for CTA 102 at 4.8 GHz using the method of Jurkevich. Plots for various bin numbers for the phase curve are presented.; *Right:* Discrete autocorrelation function for CTA 102 at 14.5 GHz.

burst reached its maximum at 37 GHz near 2005.5 ± 0.3, and its maximum at $\simeq 15$ GHz near 2006.0 ± 0.3. The MOJAVE VLBI images clearly indicate an outburst in the VLBI core starting sometime in the second half of 2004: the observed peak flux-densities for successive epochs are 1.05 (April 10, 2004), 1.87 (February 5, 2005), 2.00 (September 19, 2005), 3.94 (December 22, 2005) and 4.40 Jy/beam (February 12, 2006). This may well represented the predicted leading sub-outburst of the next outburst cycle, but further VLBI and integrated monitoring data are needed to determine the epoch of the maximum flux and the spectrum of this outburst. The leading 8 GHz maximum of the outburst prior to 1981 should have occurred near 1973.5. However, 8 GHz monitoring data (Dent & Kapitzki 1976) show only slow flux variations with an amplitude of $S \leq 1$ Jy during 1970.5–1974.5. If our hypothesis of quasi-periodicity in the activity of the source is correct, then the weak activity observed during the 1970s testifies that the activity as a whole is strongly modulated in amplitude by some geometric effect (e.g. variation of the viewing angle) or some intrinsic reason, such as orbiting secondary black hole, shock propagation along the jet or jet recollimation.

Owing to the merging of sub-outbursts C, D and E, F at cm wavelengths, time lags were determined only for the two main sub-outbursts A and B (Table 2.9, Fig. 2.24 (Left)). CTA 102 is the only source for which we were able to analyze outbursts that may belong to different flaring activity cycles. The

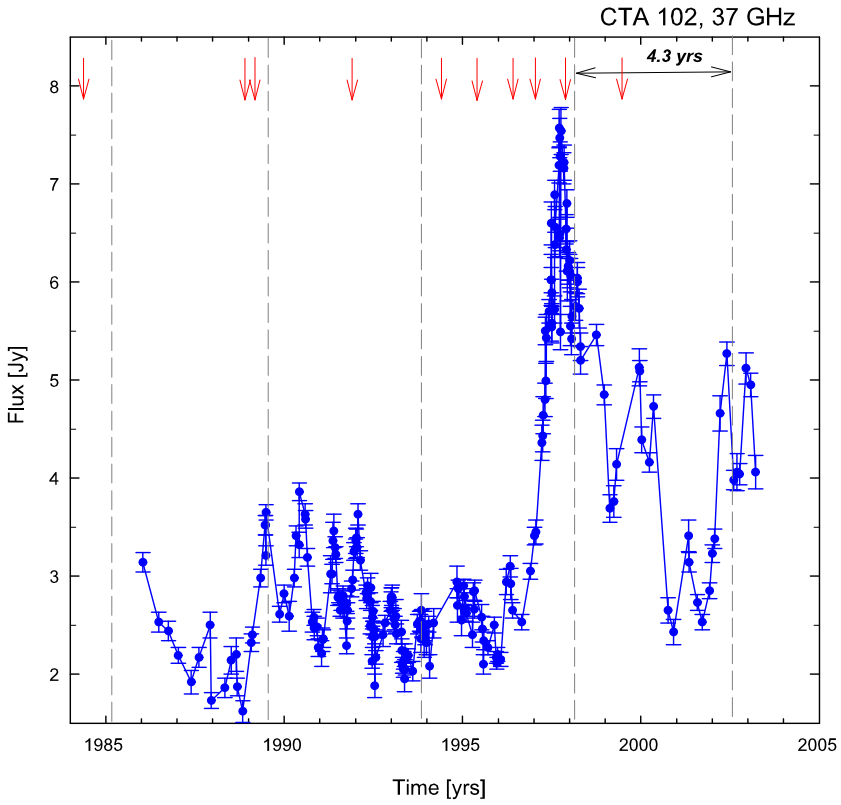

Figure 2.22: Light curve of CTA 102 at 37 GHz. The dotted mark intervals corresponding to the 4.3 ± 0.5 year period. The arrows mark the ejection epochs of VLBI components at 43 GHz (Jorstad et al. 2001, 2005, Rantakyrö et al. 2003)

time lags for the two periods of activity are correlated with the corresponding outburst amplitudes: sub-outbursts A and B of the brightest outburst, with its maximum near 1997.5, show greater time lags than sub-outbursts A and B of the more modest outburst with its maximum near 1989.6 (see below).

Four moderate γ-ray flares ($S > 7 \times 10^{-7}$phot·cm^{-2}·sec^{-1}) detected during 1992–1994 coincide with sub-outbursts D2 and E2 (Fig. 2.23, *Right*). Unfortunately we have no high resolution VLBI data for epochs prior to 1995. Multi-epoch 43-GHz VLBA observations (Jorstad 2001, 2005) covering the time interval from 1995 to 2001 reveal three faint ($S \leq 0.3$ Jy) superluminal components, which could have been ejected during the final stage of cycle 2 (B1, $T_0 = 1994.12$; B2, $T_0 = 1995.19$; B3, $T_0 = 1996.08$), as well

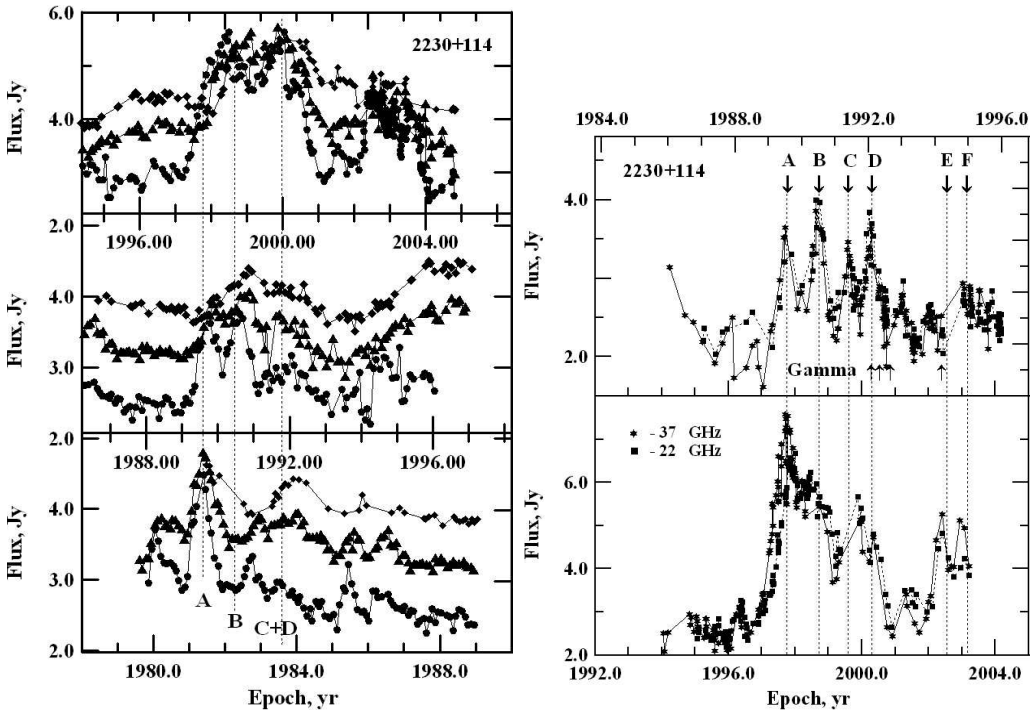

Figure 2.23: *Left:* Quasi-periodicity of outbursts in the light curves of CTA 102 at 14.5 GHz (circles), 8 GHz (triangles) and 4.8 GHz (diamonds). *Right*: Quasi-periodicity in the light curves of CTA 102 at 37 and 22 GHz. In both figures, the years covered by each individual panel are indicated beneath that panel, with some overlap between panels that cover adjacent time intervals.

as two superluminal components B2a and B3a, which seem to be associated with sub-outbursts B3 and C3. The variations of the flux densities of the core and new-born jet components are shown in Fig. 2.25. The frequency-dependent-delay sub-outburst A can be classified as a "core" outburst, and is associated with a brightening of the core. The sub-outburst B is a mixed outburst, which displays low-frequency delays but is also associated with the appearance of new superluminal components.

Table 2.8: CTA 102: Quasi-period in activity

Freq	Cycle 1		Cycle 2		Cycle 3		P(2-1)	P(3-2)
	Comp.	T_{max}	Comp.	T_{max}	Comp.	T_{max}		
37			A2	1989.57	A3	1997.48		7.91
22			A2	1989.67	A3	1997.90		8.22
14.5	A1	1981.36	A2	1989.74	A3	1998.00	8.39	8.25
8	A1	1981.40	A2	1989.95	A3	1998.34	8.55	8.39
37			B2	1990.50	B3	1997.92		7.42
22			B2	1990.54	B3	1998.57		8.02
14.5	B1	1982.71	B2	1990.63	B3	1998.62	7.92	7.98
8	B1	1982.94	B2	1990.84	B3	1999.09	7.89	8.25
37			C2	1991.38	3	1998.86		7.48
22			C2	1991.38	C3	1999.02		7.64
37			D2	1992.10	D3	2000.01		7.91
22			D2	1992.09	D3	1999.84		7.76
14.5	C1+D1	1983.68	C2+D2	1991.98	C3+D3	1999.75	8.3	7.76
8	C1+D1	1983.97	C2+D2	1991.71	C3+D3	2000.03	7.74	8.32
4.8	C1+D1	1984.08	C2+D2	1992.25			8.17	

2.5.5 Summary

Using time series analysis, we have found two periods of $P_1 = 8.4 \pm 0.1$ yr and $P_2 = 4.3 \pm 0.5$ yr in the radio total flux-density light curves at five frequencies. The derived periods are 2.1 and 4.1 years in the rest frame of the source. We found that the flaring activity cycle of this source is ~ 8 years. The periods in the total flux-density light curves are in good agreement with the duration of the flaring activity cycle.

The optical monitoring of CTA 102 has shown that the 2004 optical outburst appear simultaneously with the radio outburst. It might be that we can detect similar periods in the optical light curves if we collect optical historical data. We predict the next flare of CTA 102 to appear in about 2011. The brightness of the next flare will be about 4-6 Jy and will be accompanied by an optical flare and by the ejection of a new jet component.

We found that the time period between two "core" outbursts coincides

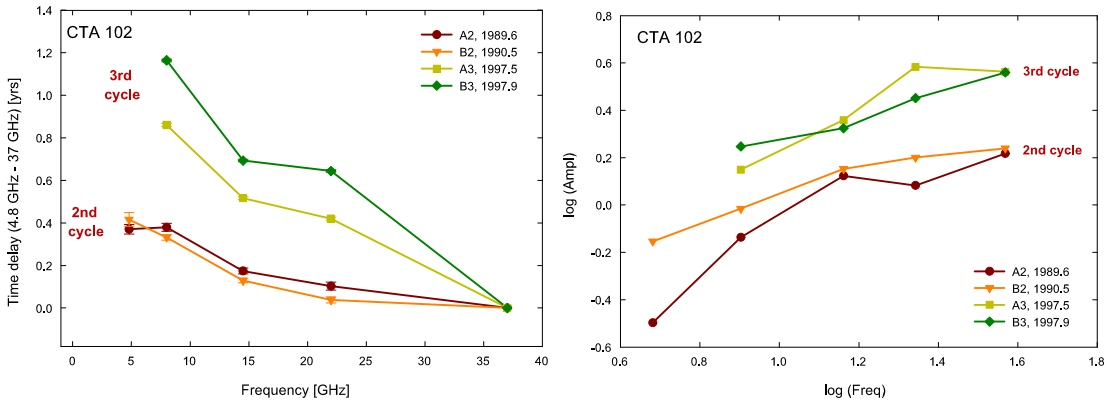

Figure 2.24: CTA 102: Time delays *(left)* and amplitudes *(bottom)* as functions of frequency for the second and third cycles.

with the timescale of the periods found with the periodicity analysis of the total flux-density variability. Therefore, similarly to 3C 454.3 we conclude that the periodical variability of this source is caused by the periodical primary perturbation in the base of the jet. However, in case of CTA 102 all the peaks have double structure, which stay at the same position relative to each other. This double structure of the peaks is similar to the double peaks in the optical light curves of OJ 287, which makes CTA 102 one of the best candidates for a binary black holes.

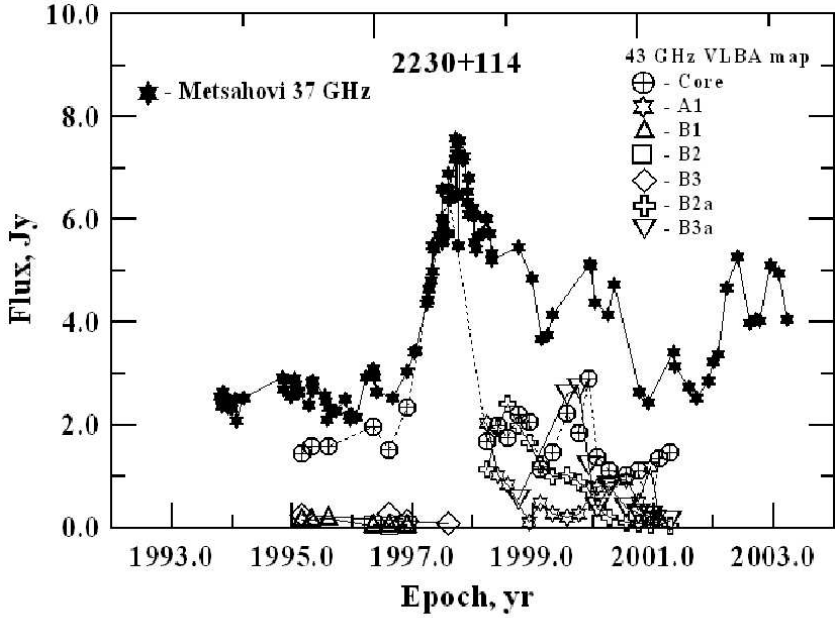

Figure 2.25: CTA 102: Evolution of the 43 GHz flux densities of the core and jet components. The VLBI data are taken from Jorstad et al. 2001, 2005.

Table 2.9: CTA 102: Parameters of outbursts

Comp.	Freq. GHz	T_{max} yr	Amplitude Jy	Θ yr	Time delay yr
A2	37	1989.57±0.01	1.649±0.050	0.74±0.03	0
	22	1989.67±0.02	1.21±0.11	0.68±0.08	0.10±0.02
	14.5	1989.74±0.01	1.328±0.026	0.70±0.03	0.17±0.01
	8	1989.95±0.02	0.730±0.024	0.80±0.04	0.38±0.02
	4.8	1989.94±0.02	0.318±0.040	0.40±0.19	0.37±0.02
A3	37	1997.48±0.01	3.656±0.058	0.57±0.08	0
	22	1997.90±0.01	3.831±0.030	0.83±0.03	0.42±0.01
	14.5	1998.00±0.01	2.284±0.024	0.90±0.02	0.52±0.01
	8	1998.34±0.01	1.411±0.023	0.67±0.05	0.86±0.01
B2	37	1990.50±0.01	1.736±0.050	0.55±0.02	0
	22	1990.54±0.01	1.59±0.10	0.62±0.05	0.04±0.01
	14.5	1990.63±0.01	1.418±0.027	0.66±0.02	0.13±0.01
	8	1990.84±0.01	0.965±0.021	0.71±0.03	0.33±0.01
	4.8	1990.92±0.03	0.702±0.014	1.34±0.08	0.42±0.03
B3	37	1997.92±0.01	3.630±0.059	0.55±0.03	0
	22	1998.57±0.01	2.83±0.11	0.48±0.06	0.64±0.01
	14.5	1998.62±0.01	2.109±0.018	0.66±0.02	0.69±0.01
	8	1999.09±0.01	1.766±0.026	0.69±0.02	1.16±0.01

2.6 Results – 0133+476

2.6.1 Introduction

The source 0133+476 (DA 55) is a quasar at a redshift of 0.859 (Lawrence et al. 1986). The source is highly variable in radio and optical wavelengths and shows high optical polarization of about 20% (Impey et al. 1991). The parsec-scale jet of 0133+476 reveals a core-jet structure (e.g. Polatidis et al. 1995). The map of 0133+476 at 15 GHz (from MOJAVE database, Lister & Homan 2005) is shown in Fig. 2.26. The radio emission is dominated by a bright compact component and a jet at PA $\sim -45^\circ$. The jet diffuses, as in many core-jet sources, into a sort of tail with several wiggles, seen at 5 GHz and 1.7 GHz north of the source (Rossetti et al. 2005). The quasar 0133+476 is an intra-day variable source, which shows rapid interstellar scintillation at 2 GHz and year-long intrinsic variations at 8 GHz (Rickett et al. 2006). The search for periodical variability, performed by Ciaramella et al. 2004 has not detected any periodicities. On the other hand, Kelly et al. 2003 studied the periodicities of the Pearson-Readhead VLBI survey sources using the Cross-Wavelet Algorithm and found a period of 566 days in the 0133+476 light curve at 4.8 GHz. A period of 811 days at 8.0 GHz and 674 days at 14.5 GHz.

2.6.2 Search for periodicity

The light curve of 0133+476 at 4.8, 8, 14.5, 22, and 37 GHz is shown in Fig. 2.27. The light curves has five prominent outbursts in 1991, 1993, 1996, 1998 and 2000, which repeat almost every 2 years. In order to check the periodicity in the light curves we used the autocorrelation and Jurkevich methods. The autocorrelation function yields a period of 2.2 ± 0.2 and the Jurkevich method gives a period of 2.1 ± 0.1. Table 2.10 gives a list of the derived periods for all five frequencies. An example of the calculated V_m^2 function for the Jurkevich method and the discrete autocorrelation function at 37 GHz and 14.5 GHz correspondingly are shown in Fig. 2.28 (Left and Right). Both methods give similar periodicities of about 2.2 years, which is actually similar to a timescale on which the main outbursts appear. Averaging the periods obtained with different methods and for different frequencies gives a period of 2.2 ± 0.3 years. This will be 1.2 years in the source rest frame. The light curve of 0133+476 spans more than 10 years and covers more than

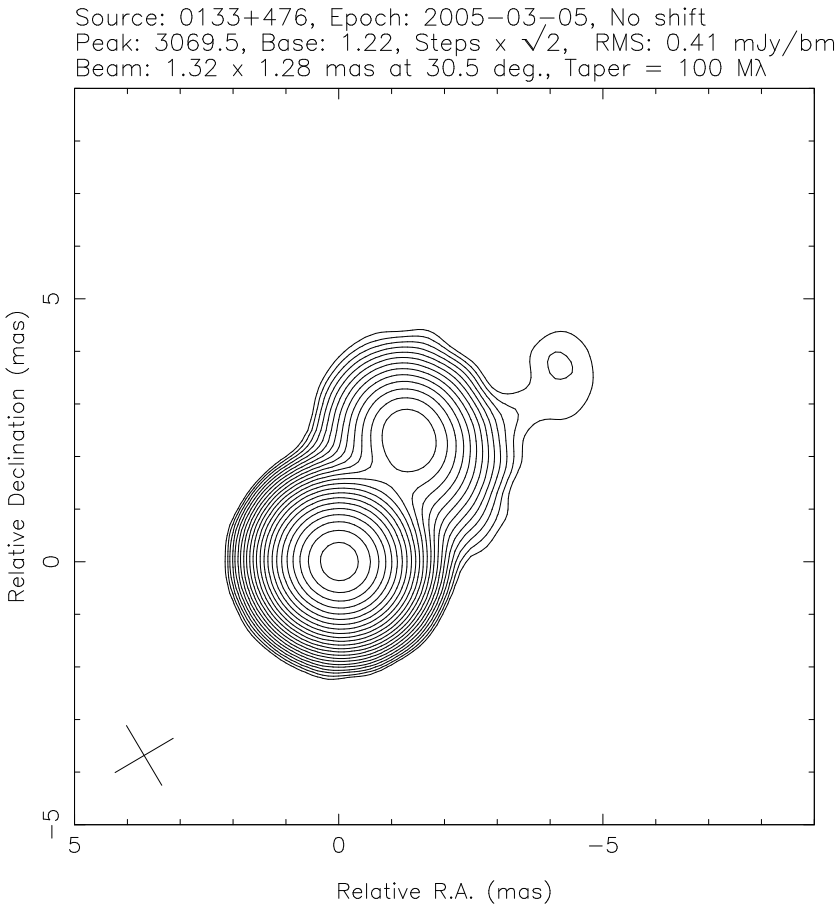

Figure 2.26: Map of 0133+476 at 15 GHz from MOJAVE database (Lister & Homan 2005).

4 cycles of a 2-year period. A visual analysis of the 0133+476 light curves at 1 and 3 mm, obtained from the Submillimeter Array (SMA) monitoring program available on the SMA website (http://sma1.sma.hawaii.edu/), suggests a new flare in 2003, which confirms a 2-year periodicity. If the 2-year period is correct and will not change, than the next predicted flare should appear in the end of 2010.

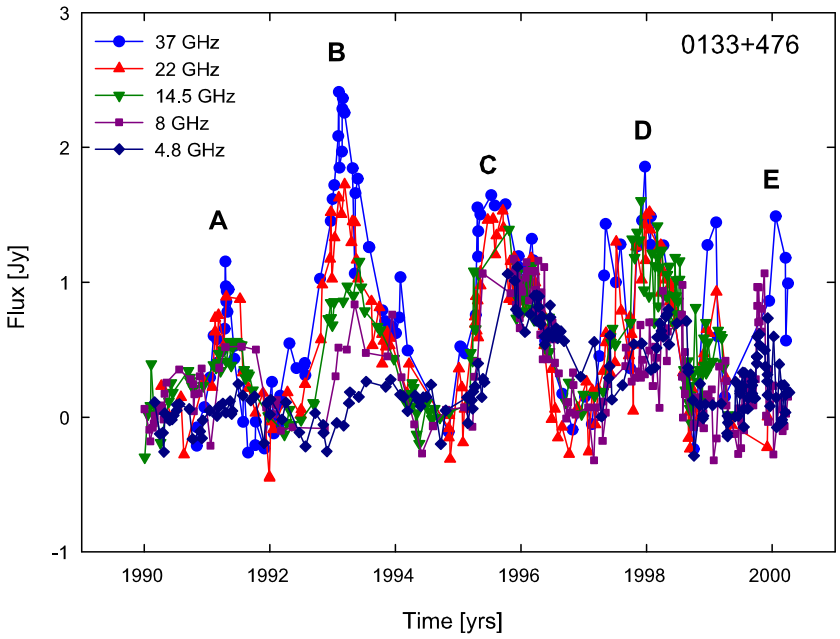

Figure 2.27: Light curve for 0133+476 at 37, 22, 14.5, 8 and 4.8 GHz. The capital letters show the names of the outbursts, decomposed by means of the Gaussian functions fitting.

2.6.3 Frequency-dependent time delays

In order to study the properties of the outbursts, we decomposed the light curves into the Gaussian components. Before the decomposition, the long-term trends were calculated via a linear interpolation across the local/global minima in 1992, 1995, 1997 and 1999. Multi-frequency light curves at frequencies from 4.8 GHz to 37 GHz are given in Fig. 2.27. The light curves cover a time interval of ∼10 yrs and show five prominent events A, B, C, D, and E with maxima in 1991, 1993, 1996, 1998 and 2000. The parameters of the Gaussian components used to decompose the outbursts are presented in Tables 2.11 and the flares shown in Fig. 2.27. The flares of 0133+476 at all frequencies appear with a strict period of 2.2 ± 0.3 years. The average time period between the flares, derived from the maxima of the fitted Gaussian functions is 2.2 ± 0.2 years (at 37 GHz). However, the amplitude of the flares is changing gradually starting from a moderate amplitude of the flare A, then reaching the maximum during the second flare B and than smoothly

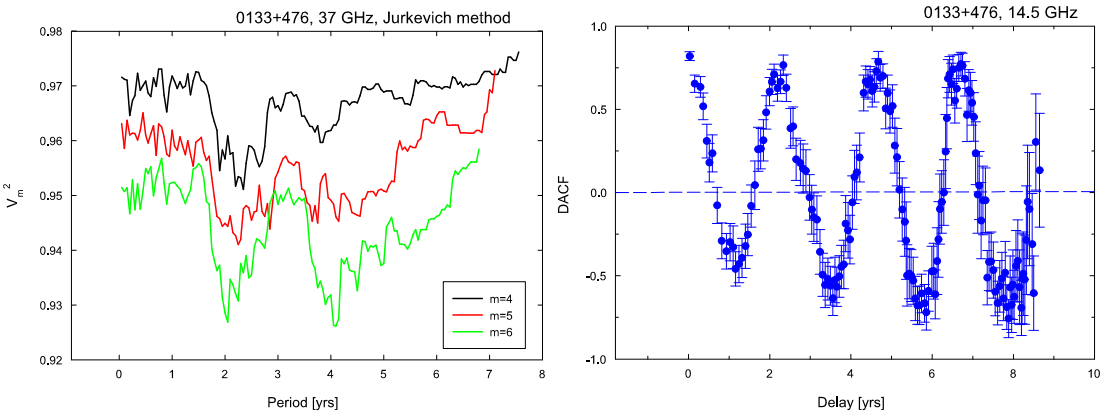

Figure 2.28: *Left:* Results of the period search for 0133+476 at 37 GHz using the method of Jurkevich. Plots for various bin numbers for the phase curve are presented.; *Right:* Discrete autocorrelation function for 0133+476 at 14.5 GHz.

Table 2.10: Detected periods for 0133+476 (DA 55)

ν (GHz)	P_{Jurk},yr	f	P_{DACF},yr	k
37 GHz	2.1 ± 0.5	0.08	2.5 ± 0.3	0.65
22 GHz	2.2 ± 0.2	0.07	2.3 ± 0.1	0.52
14.5 GHz	1.9 ± 0.1	0.08	2.2 ± 0.2	0.76
8 GHz	2.1 ± 0.1	0.06	2.2 ± 0.2	0.43
4.8 GHz	–	–	1.9 ± 0.1	0.37

decreasing during the C, D and E outbursts.

Figure 2.29 (Left) shows the time lags of all flares as functions of frequency. The low-frequency delay of the outburst A is $\sim$ 0.3 yr, the delay reaches its maximum for the outburst B and than gradually decreases during the flares C, D, and E. The maximum of the frequency-dependent time lag corresponds to the maximum of the amplitude of the flares. Figure 2.29 (Right) show the evolution of the spectra of the outbursts. The amplitude spectra of the flares A, B, D, and E are dominated by high-frequency components, whereas the spectrum of the outburst C is flat. Figure 2.30 and Fig. 2.31 show the time evolution of the flare amplitudes at 4.8 GHz, frequency-dependent time lags and flare widths for different flares. The am-

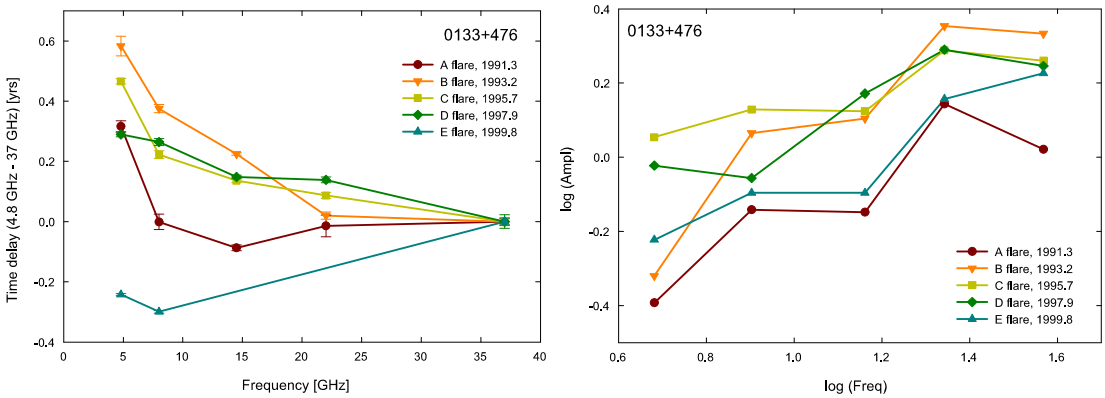

Figure 2.29: Time delays *(Left)* and amplitudes *(Right)* as functions of frequency in 0133+476.

plitude is about 0.4 - 0.5 Jy for the first two flares A and B. It reaches the maximum in about 1996 during the flare C, then gradually decreases during the flares D and E in 1998 and 2000. The flare widths show a similar evolution with time and reach the maximum simultaneously with the flare amplitudes. The frequency-dependent time lags are changing gradually from 0.3 years lag between 4.8 GHz and 37 GHz up to the maximum value in 1994 during the flare B ($\sim 0.6 yrs$). Then the delays gradually decrease during the flares C, D, and E. It is worth to notice that the amplitudes and the widths of the flares reach the maximum values simultaneously during flare B, whereas the frequency-dependent time delays reach the maximum later in 1996, during flare C, which has the flattest spectrum.

2.6.4 Jet components ejections

The jet kinematics of 0133+476 was investigated by Kellermann et al. 2004 at 15 GHz. The parsec jet of the source consists of a core and a component B, located at about 3 mas and some weaker emission in between. The jet component B is moving with an apparent speed of about 2c. Piner et al. 2007 in addition to the jet component at 3 mas found two new VLBI jet components in the 8 and 2 GHz snapshot RRFID observations, ejected in about 1996 and 1997. These two jet components are much faster than the component at 3 mas and have similar apparent speeds of about 17.2c and 18.0c. Ejections of these jet components happened during the maximum and

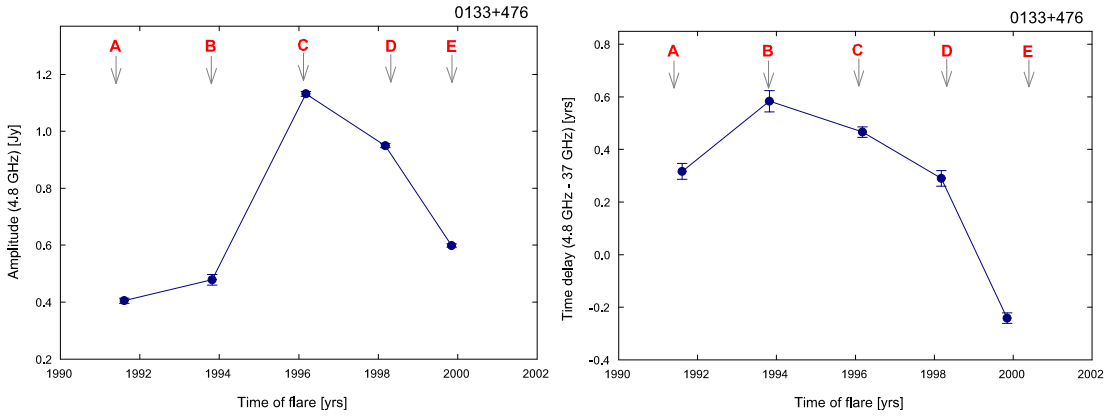

Figure 2.30: Time evolution of the amplitudes at 4.8 GHz *(Left)* and frequency-dependent time lags *(Right)* in 0133+476. It is clearly seen that the amplitudes and time lags are changing gradually with time.

decay of flare C, which has the highest amplitude. We can conclude, that the appearance of new VLBI jet components is a rare event in this source, which happens twice per ten years. Two jet components ejected in 1996 and 1997 appeared very close to each other in time and have similar apparent speeds and can therefore be caused by the same primary perturbation in the base of the jet.

2.6.5 Summary

There can be at least two different explanations for the observed gradual changes of the outbursts' spectra, opacity, amplitude and width. The long-term jet precession can explain the gradual opacity changes with time due to the changes of the amount of projected matter. In the Blandford & Königl 1979 model, the opacity of the core region depends on the angle between the jet and the line of sight and can change due to jet precession (Caproni & Abraham 2004). The change in the opacity will cause the gradual change in the frequency-dependent time lags of the flares. Our observations have shown that the gradual change in the frequency-dependent time delays has a characteristic time scale of more than 10 years, which suggests a jet precession with a period more than ten years. In this case, the 2-year period can be caused by the instabilities of the accretion disc, or possibly instabilities in the jet due to interaction of the jet material with the ambient medium.

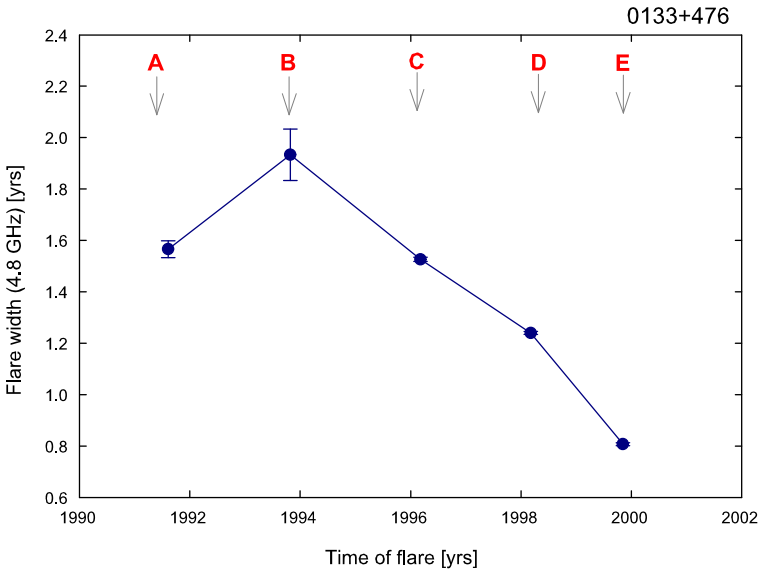

Figure 2.31: Time evolution of the width of the flares at 4.8 GHz in 0133+476. It is clearly seen that the flare widths are changing gradually with time.

However, in this case the jet precession period will be much longer than 10 years.

Another explanation is that all five flares $A--E$ are substructure of one major flare, which lasted for ten years, started in about 1990 and finished in 2000. This scenario can explain the gradual changes of the amplitude and opacity, which reveal the evolution of a primary perturbation in the jet. This will explain the VLBI jet component ejections in 1996 and 1997, which were ejected when the opacity has reached the maximum and started to become optically thinner. In this case a two-year period is a period of a substructure of the long outburst. Propagation of the primary perturbation along the jet can cause a quasi-periodic rarefaction and density increase which appears due to an unbalanced equilibrium between the jet and the ambient medium (Gomez et al. 1997). This will cause quasi-periodic flares in the light curves and can explain the observed 2-years period. If this scenario is correct, then the flaring activity cycle of the source is more than ten years.

The 2-year periodicity in the radio total flux-density light curves and gradual changes of outbursts' spectra, opacity, amplitude and width make the source 0133+476 very interesting. The long-term optical variability of 0133+476 has not been discussed in the literature and the construction and

analysis of the historical light curve in optical wavelenghts is needed in order to answer the question of the origin of 2-year periodicity in the light curves of the source. An investigation of archival long-term VLBI observations are needed in order to check which scenario is correct. The jet precession will change trajectories of the jet components and will possibly change the direction of the jet components' ejections.

Table 2.11: 0133+476: Parameters of outbursts

Comp.	Freq. GHz	T_{max} yr	Amplitude Jy	Θ yr	Time delay yr
A	37	1991.29±0.01	1.05±0.03	0.49±0.01	0.00±0.01
	22	1991.27±0.04	1.39±0.06	1.30±0.05	-0.01±0.05
	14.5	1991.20±0.01	0.71±0.01	1.87±0.02	-0.09±0.02
	8	1991.29±0.02	0.72±0.02	1.99±0.02	-0.01±0.03
	4.8	1991.60±0.02	0.40±0.01	1.56±0.03	0.32±0.03
B	37	1993.23±0.01	2.15±0.03	1.28±0.01	0.00±0.01
	22	1993.25±0.01	2.26±0.04	1.24±0.03	0.02±0.02
	14.5	1993.46±0.01	1.27±0.01	1.11±0.01	0.22±0.02
	8	1993.61±0.01	1.16± 0.06	0.98±0.02	0.37±0.02
	4.8	1993.82±0.03	0.48±0.02	1.93±0.10	0.58±0.04
C	37	1995.71±0.01	1.82±0.04	1.23±0.02	0.00±0.01
	22	1995.79±0.01	1.94±0.02	1.54±0.01	0.09±0.02
	14.5	1995.85±0.01	1.33±0.01	1.42±0.01	0.14±0.02
	8	1995.93±0.01	1.34±0.01	1.39±0.01	0.22±0.02
	4.8	1996.18±0.01	1.13±0.01	1.53±0.01	0.47±0.02
D	37	1997.88±0.02	1.76±0.05	1.10±0.02	0.00±0.02
	22	1998.02±0.01	1.95±0.02	1.36±0.01	0.14±0.03
	14.5	1998.03±0.01	1.48±0.01	1.16±0.01	0.15±0.03
	8	1998.15±0.01	0.88±0.02	1.29±0.01	0.26±0.03
	4.8	1998.17±0.01	0.95±0.01	1.24±0.01	0.29±0.03
E	37	2000.08±0.01	1.68±0.10	0.40±0.02	0.00±0.01
	22	1999.12±0.01	1.43±0.07	0.35±0.01	-0.97±0.02
	14.5	1999.12±0.01	0.80±0.02	0.36±0.01	-0.96±0.02
	8	1999.79±0.01	0.80±0.02	0.40±0.01	-0.30±0.02
	4.8	1999.84±0.01	0.60±0.01	0.81±0.01	-0.24±0.02

2.7 Shapes of the flares

Investigation of the radio total flux-density light curves of a few sources has shown, that it is possible to decompose the centimeter and millimeter radio light curves into "core" and "jet" outbursts, where the "core" flares are connected with the primary perturbation at the jet nozzle and the "jet" flares are due to the propagation of a primary perturbation along the jet. The light curves of a few sources, such as 3C 454.3, 3C 446, 3C 345, and S5 1803+784 show similar light curves and bright narrow outbursts are followed by broad fainter long-lasting flares. Figure 2.32 shows similar shapes of the light curves at 8 GHz of the sources 3C 454.3 and 3C 446. The amplitudes of the flares for the light curves of different sources are different, but the shape is the same. The light curves similarity suggests that the same physical mechanism is responsible for the light curves in different sources.

One possible explanation can be that the similar light curves show similar evolution of the flaring activity cycle, which starts as a primary perturbation in the base of the jet and then propagates along the jet. For the source 3C 454.3 the two flares in Fig. 2.32 represent one flaring activity cycle, which starts with a bright steep flare with moderate time lags. Then the spectra of the flares are flattening and the time lags become larger and at the end of a cycle, the spectra of the outbursts become steep again and the frequency-dependent time lags become smaller. For the source 3C 446, the flares show a similar evolution. The cycle starts from a steep flare with a moderate time delay, than the spectrum becomes flat in the middle of the second flare and has a large time delay and at the end of a cycle the time lags become smaller and the spectrum steeper. However, in this scenario it is difficult to explain why the primary perturbation is not evolving gradually, but rather causes a gap in the light curve.

All the sources with similar light curve shapes reveal periodical total flux-density variability. Another explanation for the similarity of the light curves can be that the main and the secondary flares are caused by a binary black hole model with two jets. In this case, one jet produces the main bump and the other jet produces the secondary bump in the light curve and in each curved jet there could be two emitting regions, one of which emits at optical and millimeter wavelengths and the other emits at centimeter. Due to orbital motion in the binary system, the two flares in the light curve appear periodically. This approach was applied to the total flux-density light curves of 3C 454.3 and the model fitted very well the observations. Figure 2.10 shows

the light curve of 3C 454.3 at 8 GHz with fitted binary black hole model. Four radio jets have been found for a few sources at kpc-scales, such as e.g. 3C 75 (Owen et al. 1985). The evidence for four jets on the parsec VLBI scales from two close black holes was also recently found for a few sources such as 0402+379 (Rodriguez et al. 2006). Multiple jets have not been observed so far in the radio maps of 3C 454.3 and 3C 446. However, if two jets are close to each other they will blend and appear as a single jet. Therefore, the four-jet model for 3C 454.3 and 3C 446 should be checked with more sensitive VLBI observations.

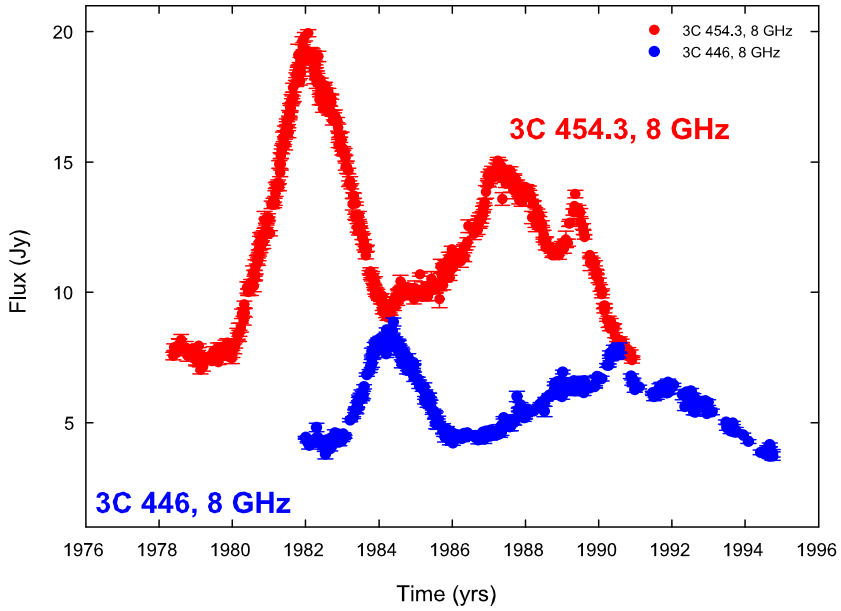

Figure 2.32: Similar shape of the light curves of 3C 454.3 and 3C 446 at 8 GHz. The light curves of both sources show a narrow bright outburst, followed by a much shallower, broader and weaker flare.

2.8 Frequency-dependent core shifts

Due to opacity variations along the jet, the absolute position of the VLBI core can be shifted. This effect is caused by synchrotron self-absorption, pressure and density gradients in the jet and free-free absorption in the ambient medium. The core shift has an immediate effect on astrometric measurements performed in radio and optical domains. In the near future, the GAIA astrometry mission and the Space Interferometry Mission will start. For both missions, a highly important problem will be matching the optical astrometric catalogues to the radio catalogues (e.g. Fey et al. 2001). The core shifts are expected to introduce offsets between optical and radio positions of the sources up to 1.5 mas (Kovalev et al. 2008), which will strongly affect the accuracy of matching of radio-optical catalogues. Core shifts are also needed for the correct reconstruction of the VLBI spectral maps.

Therefore, precise measurements of core shifts are needed. In order to obtain values of core shifts, usually phase-referencing observations are needed. They require a complicated technique and were determined only for a few sources so far. Moreover, the phase-referencing observations of the core shifts were performed only for a few sources, such as 1038+528 (Marcaide et al. 1984), 4C 39.25 (Guirado et al. 1995), 3C 395 (Lara et al. 1994), 1823+568 (Paragi et al. 2000), 3C 345 (Biretta et al. 1986), 3C 309.1 (Ros & Lobanov 2000), and 3C 66A (Sudou et al. 2002). It is worth to mention, that it is not always possible to detect core shifts, since the value of the shift depends on the activity state of the AGN.

The VLBI core is a compact detail in the VLBI map with high brightness and flat spectrum, which is part of the jet were the optical depth is $\tau = 1$. The absolute position of the core should thus depend on the frequency. According to the theoretical model of Königl 1981, a frequency-dependent core shift depends on the opacity and the frequency of the observations $r_{core} \propto (\nu_{obs})^{(-1/k_r)}$.

However, frequency-dependent time delays and frequency-dependent shifts in the VLBI core are due to the opacity of the core region, have the same origin and are caused by the same mechanisms. Since the frequency-dependent core shifts and frequency-dependent time delays are both caused by the opacity, we can assume, that the frequency-dependent core shifts can be measured as $\Delta r[mas] = \Delta t[yrs]\mu[mas/yr]$, where Δt is the frequency-dependent time delay and μ is the speed of the jet flow. We can also make a simple assumption that the speed μ equals the speed of a jet component,

ejected close to the time of the observations.

In order to check our assumption about the simple connection between frequency-dependent time delays and frequency-dependent core shifts, we calculated the time lags from the total flux-density light curves for the sources with available core shift measurements from phase-referencing observations at the same frequencies at which the light curves are available. The frequency-dependent time delays were calculated fitting the Gaussian functions into the total flux-density light curves from the University of Michigan monitoring campaign and Metsähovi Radio Observatory monitoring campaign at 4.8 GHz, 8 GHz, 14.5 GHz, 22 GHz, and 37 GHz. We used the same method of calculating frequency-dependent time delays in order to estimate the flaring activity cycles of the sources in subsection 2.2.4. In this subsection frequency-dependent time delays were also used in order to find the sources with periodicities.

Table 2.12: Comparison between frequency-dependent core shifts measured from the VLBI observations and calculated from the frequency-dependent time lags for 3C 345.

Core shift from phase-referencing observations mas	Core shift from time lags mas	Epoch yrs	Jet comp.
$\Delta r = 0.05 \pm 0.13$ (10.7 - 5 GHz)	$\Delta r = 0.06 \pm 0.02$ (4.8 - 8 GHz)	1982	C2
$\Delta r = 0.111 \pm 0.007$ (22.2 - 10.7 GHz)	$\Delta r = 0.11 \pm 0.05$ (22.2 - 8 GHz)	1983.5	C4
$\Delta r = 0.05\pm$ (5.0 - 8.4 GHz)	$\Delta r = 0.09 \pm 0.01$ (4.8 - 8 GHz)	1993.8	C7
$\Delta r = 0.21 \pm 0.06$ (8.4 - 22.2 GHz)	$\Delta r = 0.19 \pm 0.03$ (8.0 - 22.2 GHz)	1992.8	C7
$\Delta r = 0.33 \pm 0.1$ (4.8 - 22.2 GHz)	$\Delta r = 0.27 \pm 0.04$ (4.8 - 22.2 GHz)	1993.7	C7

The quasar 3C 345 (z = 0.595) is one of the best studied sources on VLBI scales. Several jet components with apparent velocities of 2 - 20c have been observed in this source, moving along strongly curved trajectories (e.g. Zensus et al. 1995, Lobanov&Zensus 1999). Klare et al. 2005 have found periodic changes in the parsec-scale jet with a 9-year period. For 3C 345 Biretta et al. 1986 measured the core shift of 0.05 ± 0.13 mas between 10.7 GHz and 5 GHz in 1982 and 0.111 ± 0.007 mas between 22.2 GHz and 10.7 GHz in 1983.5. The light curve at 4.8 GHz, 8 GHz, 14.5 GHz, 22 GHz, and 37 GHz is shown in Fig. 2.33. The phase-referencing measurements of the core shifts

by Biretta et al. 1986 were performed during the powerful flares in 1982 and 1984. During these flares two new jet components C2 and C4 were ejected. The jet component C2 has an apparent speed of 0.48 ± 0.02 mas/yr (Biretta et al. 1986). The measured time lag between 4 GHz and 8 Ghz is 0.12 ± 0.04 yrs. This corresponds to a core shift of 0.06 ± 0.02 mas. The calculated value of the core shift from the time lags 0.06 ± 0.02 mas coincides very well with a value of the core shift of 0.05 ± 0.13 measured with the phase-referencing technique. The jet component C4 has an apparent speed of 0.225 ± 0.05 mas/yr (Caproni et al. 2004a). The calculated time lag between 22 GHz and 8 GHz is 0.44 ± 0.08 yrs. This corresponds to a frequency-dependent core shift of 0.11 ± 0.05 mas/yr. This core offset calculated from the time delay also very well coincides with a core shift value 0.111 ± 0.007 measured by Biretta et al. 1986. Table 2.12 shows the measured frequency-dependent core shifts from the phase-referencing observations and calculated core shifts from the frequency-dependent. The time lags, apparent jet component speeds, time of the VLBI observations and the name of the ejected jet component are listed in the table as well.

Caproni et al. 2004 measured the core shifts of $\Delta r = 0.05 \pm 0.13$ mas (5.0 GHz-8.4 GHz), $\Delta r = 0.21 \pm 0.06$ mas (8.4 GHz-22.2 GHz), and $\Delta r = 0.33 \pm 0.1$ mas (4.8 GHz and 22.2 GHz) in $\sim$ 1993 (see Table 2.12). For calculating the core shifts we measured the time lags during the flare in 1992 (0.43 ± 0.01 yrs (4.8 GHz-8.0 GHz), 0.89 ± 0.03 yrs (8.0 GHz-22.2 GHz), and 1.32 ± 0.03 yrs (4.8 GHz-22.0 GHz)). The jet component C7 was ejected during the 1992 flare and had a speed of 0.208 ± 0.025 mas/yr (Caproni et al. 2004). Taking this speed of the newly ejected jet component C7 and using the measured time lags we can calculate the frequency-dependent core shifts. Table 2.12 shows the calculated core shifts. It is clearly seen from the table, that the measured core shifts coincide very well with the calculated core shifts.

From the Table 2.12 it is clearly seen that the core shifts measured from the phase-referencing VLBI observations and the core shifts calculated from the frequency-dependent time lags and the speeds of the jet components coincide very well. This shows that the proposed method is reliable and can be used for calculating the core shifts from the total flux-density light curves. Moreover, it indicates that the assumption that the jet component speed can be used as a jet velocity speed is correct. Since the proposed method seems to be trustworthy, we can calculate the core shifts from the time lags for other sources. An example of calculated frequency-dependent core shift from the

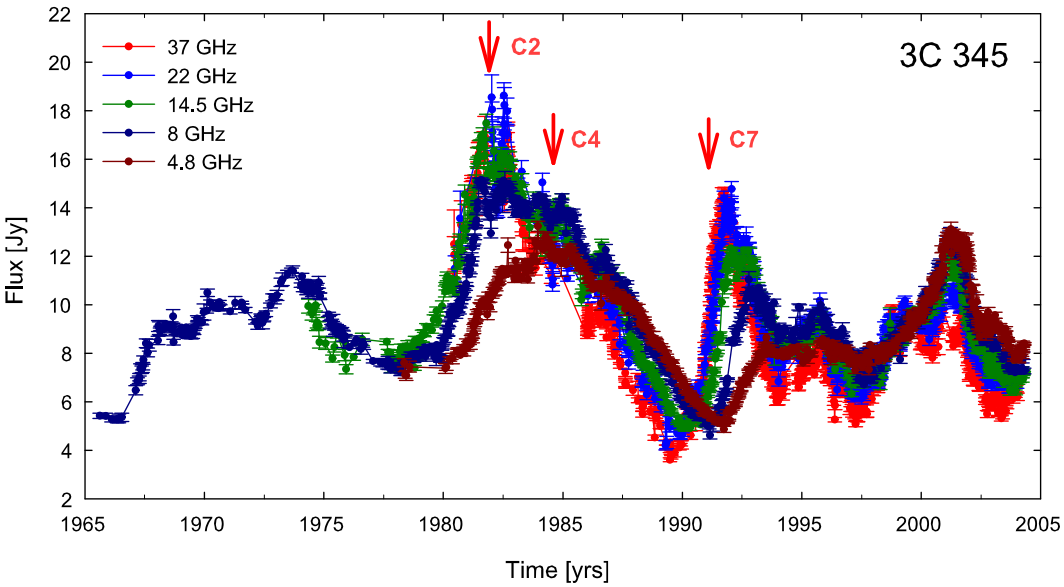

Figure 2.33: The total flux-density light curve of 3C 345 at 4.8 GHz, 8 GHz, 14.5 GHz, 22 GHz, and 37 GHz. The data are from the University of Michigan monitoring campaign and Metsähovi Radio Observatory. The arrows mark time of the ejections of new jet components C2, C4, and C7.

time lags is shown in Fig. 2.34, where the measured core shift for the sources CTA 102 and 3C 454.3 are shown as a function of frequency for the flares in 1997.5 and 1994.1 accordingly. It is clearly seen that the core shifts during the flares can reach high values, up to 0.3 mas between 5 GHz and 22 GHz.

Using the method of calculating frequency-dependent core shifts from the frequency-dependent time delays, we can study the long-term evolution of the core shifts and calculate the core shifts in any particular time where long-term radio light-curves are available. Since the total flux-density light curves are available for tenths of radio sources for more than 30 years, it makes it possible to calculate the frequency-dependent core shift evolution for more than 30 years without making complicated phase-referencing VLBI observations and constructing VLBI spectral maps. The only input that is needed from the VLBI observations is speed of the jet components.

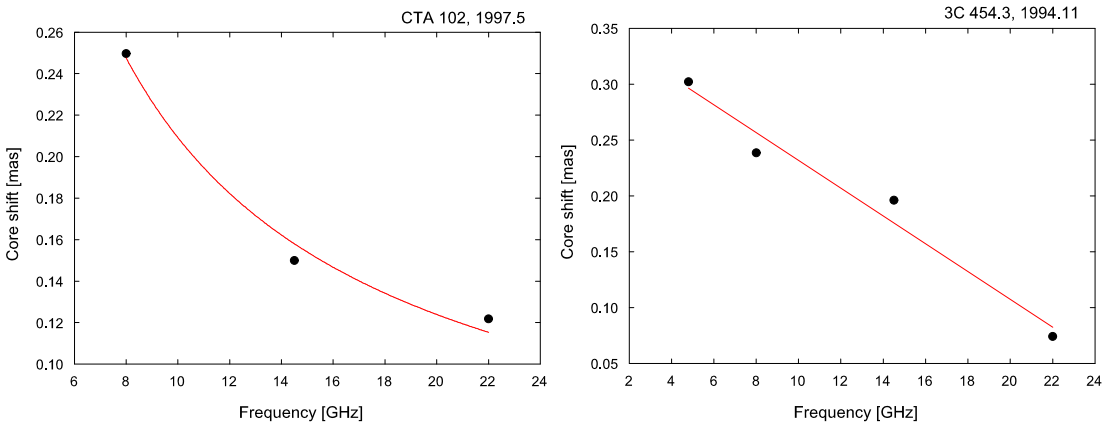

Figure 2.34: *Left:* Core shifts as function of frequency, calculated from the frequency-dependent time lags for the source CTA 102 during the 1997.5 flare. *Right:* Core shifts as function of frequency, calculated from the frequency-dependent time lags for the source 3C 454.3 during the 1994.1 flare.

Chapter 3

Kinematics of S5 1803+784

3.1 Introduction

The BL Lac object S5 1803+784 is a compact flat-spectrum radio source with a redshift of $z = 0.68$ (Stickel 1993). The dominant orientation of the inner 10 mas of the VLBI jet is nearly east-west directed (Witzel et al. 1988, Gabuzda et al. 1992). The source has been observed for more than 30 years at different frequencies and with different resolutions (e.g. Eckart 1986; Eckart 1987; Schalinski 1988; Witzel 1988; Gabuzda 1992; Kollgaard 1992; Britzen 1999). It shows a complicated geometry of the jet: the jet components of S5 1803+784 move on strongly curved trajectories (e.g., Krichbaum 1990) and accelerate and decelerate along the jet (Jorstad et al. 2005). Different authors derived different speeds of the jet components based on different time spans covered by the observations. Therefore it is of high importance to use all available VLBI observations for the apparent speed calculations. The brightest jet component at 1.4 mas has almost constant core separation and was identified as stationary (e.g. Cawthorne 1993). However, Britzen et al. (2005) showed, that this brightest jet component has "oscillatory" behavior. S5 1803+784 shows a significant misalignment between kpc- and pc-scales (Britzen 2005a) (Fig. 3.1). Further from the core, the jet begins to curve to the south (Britzen et al. 1999), towards the arcsec-scale structure (Strom & Biermann 1991; Kollgaard et al. 1992).

The goal of the present work is to combine the archival VLBI observations, to investigate the long-term evolution of the jet structure of S5 1803+784, to calculate the apparent jet component speeds, based on the longest possible

database, to explain the complex kinematics of the jet, to search for periodicities in total flux-density light curves and jet kinematics and investigate possible correlations. Part of this analysis is published in Kudryavtseva et al. 2006a, Roland et al. 2008, Britzen et al. (accepted to A&A), Kudryavsteva et al. (in prep).

3.2 Observations and data reduction

For the investigation of the long-term jet kinematics of S5 1803+784, we collected, reanalyzed, and partly analyzed 26 archival VLBI observations of S5 1803+784 at 5 frequencies ν=1.6, 2.3, 5, 15, and 43 GHz. The observations were performed between 1993.88 and 2001.87. Observations at 1.6 and 2.3 GHz have been performed by Marcaide et al. (1995, 1995a, 1997); at 5 GHz by Marcaide et al. (1995, 1995a, 1997), Guirado et al. (2001), and Gurvits et al. (priv. comm.); at 8.4 GHz by Pérez-Torres et al. (2000), Ros et al. (2000, 2001, in prep.); at 15 GHz by Pérez-Torres et al. (2000, in prep), Kellermann et al. (1998, 2004), Zensus et al. (2002). We have also used data from Britzen et al. (2005, 2005a). Figure 3.2 shows a histogram for the VLBI data used for the study of S5 1803+784 kinematics. Each circle shows how many VLBI observations of a particular frequency have been analyzed. The red font marks the frequencies for which most of the observations were obtained. The frequencies, which have the most data are 15 GHz (14 observations) and 8 GHz (61 observations). Altogether 77 archival VLBI observations were analyzed. Taking into account, that we also used in the analysis the literature data, the total number of analyzed VLBI epochs is 94. The published data had been fringe-fitted and calibrated before by the individual authors. In addition, we performed observations with the HALCA satellite at 1.6 GHz in 2001.87. These observations were scheduled for the VLBA plus HALCA. Unfortunately we did not obtain any data from ground-space baselines and use this observation as ground-station only experiment. The data have been fringe-fitted within AIPS package.

For all the data sets at all frequencies we performed model fitting of circular Gaussian components within the *difmap* package. Circular components have been chosen in order to simplify the comparison and to avoid unlikely and extremely extended elliptical components. In order to find the optimum set of components and parameters, we fitted every data set starting from a point-like model without any assumptions about the number of the jet com-

ponents. The procedure of the model-fitting was as follows: first, we fitted a point-like model, then we added another jet component to the brightest area of the jet and fitted it to the data, varying all the parameters, such as the core separation, the position angle and the flux until the chi-square value did not show significant changes; then we self-calibrated the image and added another jet component. We stopped the algorithm when the flux of the last jet component was about the noise level or when the chi-square value of the model-fit including the last component did not significantly improve. In Table 3.1, 3.2 and 3.3 we list the parameters of the best fits to the data.

The uncertainties have been derived in two ways - by comparison of different model fits (± 1 component) obtained for the same set of data. They reflect the possible parameter ranges for the individual components within model-fitting. In addition, the uncertainties have been determined by calculating the errors from approximations given by Fomalont 1999. In the latter method, the errors of the parameters of the Gaussian components are related to the signal to noise ratio of the detection of a given model fit component and can be estimated from the formulas:

$$\sigma_{peak} = \sigma_{rms}\sqrt{(1 + \frac{S_{peak}}{\sigma_{rms}})}, \tag{3.1}$$

$$\sigma_{tot} = \sigma_{peak}\sqrt{1 + \frac{S_{tot}^2}{S_{peak}^2}}, \tag{3.2}$$

$$\sigma_d = d\frac{\sigma_{peak}}{S_{peak}}, \tag{3.3}$$

$$\sigma_r = \frac{\sigma_d}{2}, \tag{3.4}$$

$$\sigma_\theta = \arctan(\frac{\sigma_r}{r}), \tag{3.5}$$

where σ_{peak}, σ_{tot}, σ_d, σ_r and σ_θ are the uncertainties of the peak flux density, total flux density, size, core separation and the position angle respectively. The σ_{rms} is the residual noise of the map after the subtraction of the model, d is the full width at half maximum (FWHM) of the component and S_{peak} is the peak flux density (Fomalont 1999). However, this formula tends to underestimate the error if the peak flux density is very high or the width of the component is small. Therefore, the final position error was calculated as the maximum value between the error bars obtained by these two

methods. Since we only used circular Gaussian components, the axial ratio is persistently 1. We also give the component identification and the reference to the original publication of the data sets.

In Fig. 3.3 we show examples of the clean maps for four frequencies 1.6 GHz (upper left), 5 GHz (upper right), 8 GHz (bottom right), and 15 GHz (bottom left). The fitted Gaussian functions are superimposed on the images.

3.2.1 Component Identification

The component identification was made on the basis of obtaining smooth changes of the position angle, the core separation and the flux for each particular component. In order to find the best solution for the component identification, we tried to connect the points in different ways and to check every time whether the position angle, the core separation and the flux are changing smoothly and do not have outliers. The best jet component identification consists of 7 components at the core separation $\sim$ 0.3 mas (jet component C0), $\sim$0.8 mas (C1), $\sim$1.4 mas (Ca), $\sim$ 2 mas (C2), 3–4 mas (C4), 6–8 mas (C8) and at 10 – 12 mas (C12). The location of the jet components is marked in Fig. 3.4. These jet components show oscillations around average core separation mentioned before and have not shown significant outward motion. At 8 GHz we have found the same jet components at similar separation. However, for the lower frequencies (5 and 1.6 GHz) it is possible to detect two more jet components at around 30 (C30) and 40 mas (C40), which are slowly moving outwards.

Core separations versus time are shown in Fig. 3.5 for 1.6 GHz, 5 GHz, 8 GHz, and 15 GHz. It is clearly seen that the jet components remain at similar core separations from 1980 until 2006 at all frequencies. On the other hand Fig. 3.6 shows that the position angles of the jet components are change with time. We find only one component, B3, moving outwards during twenty years of observations, which is shown in the upper left in Fig. 3.5. The results of the component identification for the core separation, the position angle and the flux densities are shown in Fig. 3.6 for the inner component C0 at 0.5 mas (left) and the brightest component Ca at 1.4 mas (right) at 15 GHz. It is clearly seen from the figures, that the final component identification gives smooth changes in the position angles, the core separation and the flux of the jet components.

In Table 3.4 we give the parameters of the linear regressions performed for the jet components of the core separation/time relation and calculate

the apparent speeds, calculated for 15 GHz data and average speed for all frequencies. We find no significant outward motion of the components at 15 GHz – besides **B3** – when followed over the whole observing period ($\beta_{\rm app}^{\rm all}$). The calculated ejection time of the component B3 is 1999.8 ± 1.1. However, for other frequencies the jet component are moving, but in rather oscillating way. They stay at the range of the core separations and after many years do not move outwards.

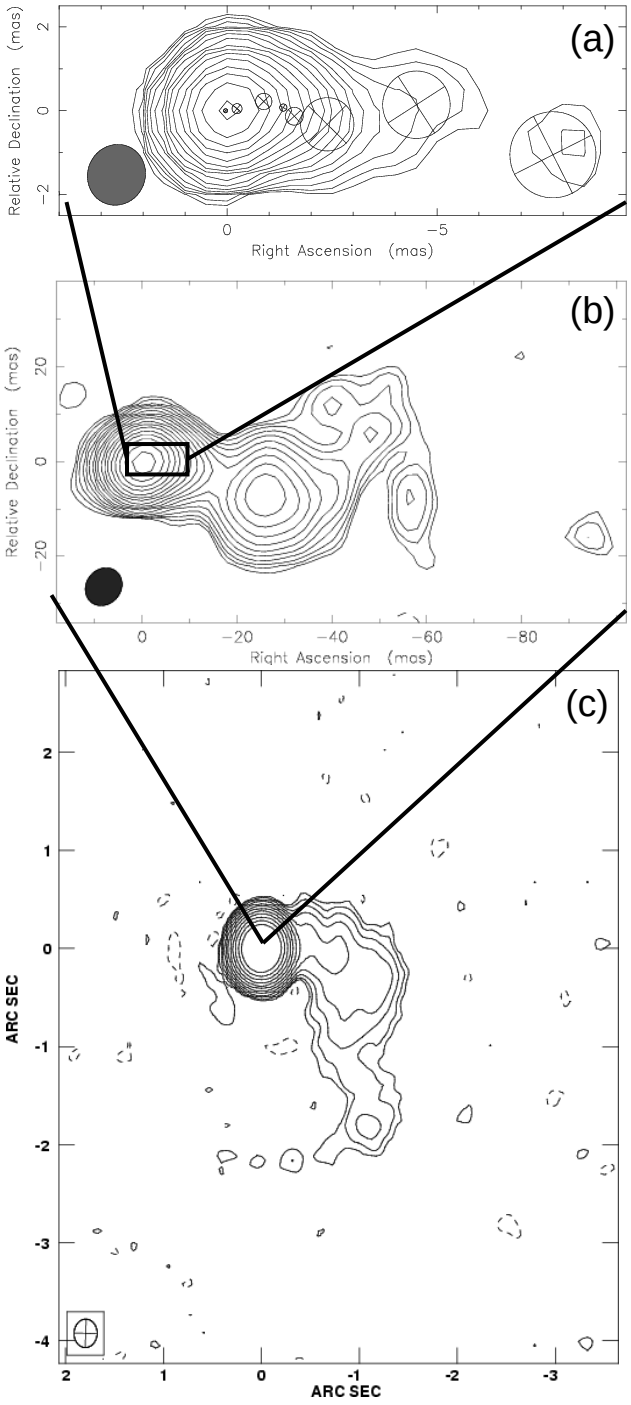

Figure 3.1: Three VLBI images of S5 1803+784 in order of decreasing angular resolution (from top to bottom, a-c), where (a) - 2cm VLBA data, (b) - Global VLBI map at 18 cm, (c) - MERLIN array map (Britzen et al. 2005a)

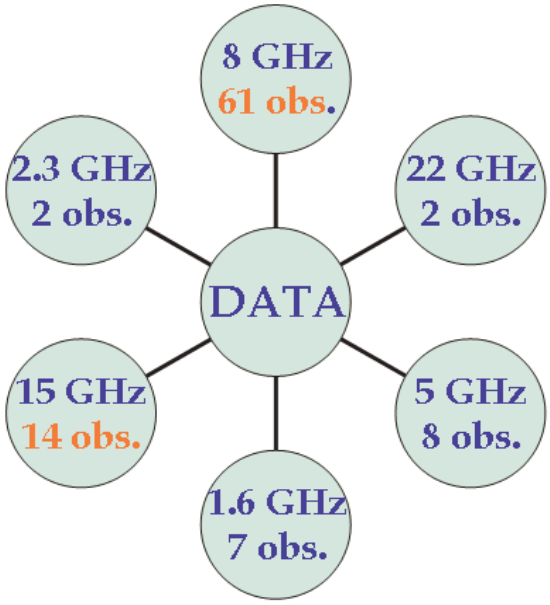

Figure 3.2: 1803+784: A histogram showing the VLBI data used for the study of kinematics of S5 1803+784. Each circle shows how many VLBI observations for a particular frequency were analyzed. The orange font marks the frequencies for which most of the observations were obtained.

Table 3.1: Model-fit results for S5 1803+784. We list the epoch of observation, the jet component identification, the flux-density, the radial distance of the component center from the center of the map, the position angle of the center of the component, and the FWHM major axis of the circular component.

Epoch	Id.	S [Jy]	r [mas]	θ [deg]	M.A. [mas]	Chi-squared
			1.6 GHz			
1998.92	**r**	0.946±0.142	0.00	0.0	0.26±0.02	38.232803
1998.92	**Ca**	0.558±0.084	1.41±0.05	262.7±0.8	0.69±0.03	
1998.92	**C4**	0.091±0.014	4.35±0.44	267.8±1.0	2.82±0.30	
1998.92	**C8**	0.059±0.009	7.99±0.80	265.4±2.0	1.30±0.35	
1998.92	**C30**	0.259±0.052	29.67±3.00	256.7±4.0	15.72±4.00	
2001.87	**r**	1.233±0.169	0.00±0.01	0.0±0.5	0.60±0.08	0.0923
2001.87	**Ca**	0.266±0.047	2.33±0.71	-94.8±1.5	1.12±0.29	
2001.87	**C8**	0.134±0.019	6.15±0.98	-96.7±1.2	3.17±0.57	
2001.87	**C12**	0.058±0.010	9.45±0.42	-97.0±0.9	3.70±0.11	
2001.87		0.010±0.001	16.85±1.10	-91.4±0.9	5.10±1.60	
2001.87	**C30**	0.241±0.034	28.94±0.49	-104.7±1.0	14.18±0.79	
2001.87		0.045±0.007	43.07±0.61	-100.0±0.8	15.98±3.20	
			2.3 GHz			
1996.42	**r**	1.642±0.246	0.00	0.0	0.00±0.01	86.988178
1996.42	**Ca**	0.481±0.072	1.43±0.07	-92.2±0.5	0.01±0.01	
1996.42	**C4**	0.041±0.006	3.91±0.39	-85.3±1.0	0.44±0.02	
1996.42	**C8**	0.124±0.025	6.71±0.80	-89.4±1.8	3.19±0.32	
1996.42	**C12**	0.028±0.010	11.92±2.38	-102.7±1.9	1.47±0.15	
1996.42	**C30**	0.204±0.069	26.67±3.00	-102.2±3.9	13.47±2.70	
			5.0 GHz			
1996.46	**r**	1.673±0.251	0.00	0.0	0.36±0.02	52.027293
1996.46	**Ca**	0.422±0.063	1.35±0.07	-96.8±1.1	0.86±0.04	
1996.46		0.090±0.014	5.58±0.60	-89.9±1.54	4.44±0.44	
1997.15	**r**	1.302±0.195	0.00	0.0	0.01±0.01	27.458208
1997.15	**C1**	0.274±0.041	0.87±0.04	-94.2±0.9	0.33±0.07	
1996.15	**Ca**	0.218±0.033	1.73±0.09	-97.3±0.7	0.53±0.08	
1997.15	**C4**	0.017±0.002	3.95±0.40	-85.0±1.4	0.47±0.10	
1997.15	**C8**	0.081±0.016	6.36±0.66	-99.7±1.9	4.42±0.44	
1997.15	**C30**	0.067±0.013	27.87±2.81	-107.6±3.9	6.48±0.84	
1999.35	**r**	1.774±0.266	0.00	0.00	0.30±0.02	15.738181
1999.35	**C1**	0.033±0.005	0.77±0.04	-69.4±0.5	0.00±	
1999.35	**Ca**	0.507±0.189	1.31±0.07	-93.0±1.5	0.81±0.12	
1999.35	**C4**	0.031±0.025	3.46±0.35	-98.1±1.1	0.81±0.41	
1999.44	**r**	1.423±0.213	0.00	0.0	0.21±0.01	
1999.44	**C1**	0.450±0.067	0.53±0.03	-75.7±1.0	0.22±0.01	
1999.44	**Ca**	0.274±0.041	1.34±0.07	-89.2±0.7	0.49±0.03	
1999.44	**C2**	0.101±0.015	1.86±0.09	-100.6±0.8	0.78±0.08	
1999.44	**C4**	0.071±0.011	4.81±0.48	-94.8±1.1	2.94±0.30	
1999.44	**C12**	0.033±0.006	10.00±1.00	-93.9±1.6	1.99±0.20	
1999.44	**C30**	0.099±0.020	28.27±2.83	-104.2±2.7	14.06±2.58	
2001.29	**r**	1.602±0.246	0.00±0.01	0.0±0.5	0.21±0.05	0.0477
2001.29	**C1**	0.511±0.071	0.85±0.08	-81.1±2.1	0.43±0.11	
2001.29	**Ca**	0.228±0.069	1.62±0.38	-91.7±3.5	0.72±0.22	
2001.29	**C4**	0.045±0.023	3.89±0.18	-84.7±4.9	1.38±0.61	
2001.29	**C8**	0.052±0.022	6.07±0.24	-98.3±0.8	2.05±0.85	
2001.29	**C12**	0.039±0.018	9.23±0.35	-95.1±1.7	3.22±0.68	
2001.29	**C30**	0.112±0.018	29.12±0.59	-103.3±1.2	11.83±0.19	
			8.4 GHz			
1993.88	**r**	1.390±0.208	0.00	0.00	0.01±	2.8677791
1993.88	**C0**	0.014±0.002	0.25±0.01	-69.3±0.7	0.00±0.01	
1993.88	**Cx**	0.262±0.039	0.33±0.02	-99.5±0.4	0.00±0.01	
1993.88	**Ca**	0.263±0.039	1.45±0.07	-91.8±0.8	0.36±0.02	
1993.88	**C4**	0.043±0.016	3.07±0.11	-87.5±1.2	1.03±0.17	
1997.90	**r**	2.467±0.370	0.00	0.00	0.45±0.02	6.8563583
1997.90	**Ca**	0.719±0.108	1.39±0.07	-97.4±1.3	0.68±0.03	
1997.90	**C4**	0.127±0.019	4.00±0.45	-89.5±1.3	1.31±0.13	
1997.93	**r**	1.353±0.203	0.00	0.00	0.12±0.01	1.7453468
1997.93	**C0**	0.270±0.041	0.28±0.01	-83.5±1.9	0.36±0.02	
1997.93	**C1**	0.176±0.026	1.01±0.05	-86.6±0.6	0.44±0.02	
1997.93	**Ca**	0.212±0.032	1.54±0.08	-98.0±0.5	0.45±0.02	
1997.93	**C2**	0.035±0.005	2.23±0.11	-97.0±1.0	0.76±0.04	
1997.93	**C4**	0.004±0.001	3.16±0.32	-109.5±1.0	0.28±0.03	
1997.93	**C4**	0.028±0.004	3.89±0.39	-89.5±1.0	1.38±0.14	
1997.93	**C8**	0.039±0.008	7.71±0.90	-96.6±3.0	3.00±0.80	

Table 3.2: Model-fit results for S5 1803+784 II

Epoch	Id.	S [Jy]	r [mas]	θ [deg]	M.A. [mas]	Chi-squared
			8.4 GHz			
1999.41	**r**	1.257±0.188	0.00	0.0	0.12±	1.5628510
1999.41	**C0**	0.496±0.074	0.33±0.02	-79.7±1.1	0.28±0.01	
1999.41	**C1**	0.171±0.026	0.92±0.05	-78.9±0.5	0.43±0.02	
1999.41	**Ca**	0.140±0.021	1.50±0.08	-92.5±0.5	0.32±0.02	
1999.41	**C2**	0.086±0.013	1.84±0.09	-96.9±0.5	0.71±0.04	
1999.41	**C4**	0.046±0.007	3.43±0.34	-93.9±1.0	1.74±0.09	
1999.41	**C8**	0.025±0.004	6.47±0.65	-95.7±0.9	2.43±0.24	
1999.41	**C12**	0.020±0.003	9.40±0.90	-95.6±1.0	2.96±0.30	
1999.41	**C30**	0.036±0.006	27.91±2.40	-103.1±3.2	7.51±0.75	
2001.09	**r**	1.317±0.146	0.00±0.01	0.0±0.5	0.13±0.09	1.1756
2001.09	**C0**	0.437±0.068	0.37±0.07	-81.0±1.1	0.30±0.03	
2001.09	**C1**	0.259±0.094	0.93±0.12	-79.4±1.7	0.42±0.19	
2001.09	**Ca**	0.179±0.032	1.47±0.04	-91.6±0.8	0.45±0.11	
2001.09	**C2**	0.059±0.008	1.95±0.04	-93.7±0.6	0.72±0.04	
2001.09	**C4**	0.055±0.010	4.11±0.33	-91.0±0.9	2.44±0.64	
2001.09	**C8**	0.027±0.003	6.12±0.15	-96.5±0.3	2.29±0.13	
2001.09	**C12**	0.024±0.008	8.95±0.73	-94.1±0.5	2.90±0.37	
2001.09	**C30**	0.018±0.003	27.61±0.12	-103.8±0.3	7.18±0.19	
			15 GHz			
1994.67	**r**	1.115±0.167	0.00	0.00	0.13±0.01	0.43219569
1994.67	**C0**	0.176±0.030	0.39±0.03	-92.8±3.9	0.40±0.05	
1994.67	**Ca**	0.097±0.015	1.46±0.04	-93.9±1.5	0.61±0.05	
1994.67	**C4**	0.030±0.010	3.43±0.10	-90.6±1.7	1.57±0.12	
1996.38	**r**	1.559±0.234	0.00	0.00	0.12±0.01	0.43219569
1996.38	**C0**	0.572±0.086	0.25±0.01	-93.7±2.1	0.23±0.01	
1996.38	**C1**	0.094±0.014	0.67±0.03	-98.0±1.1	0.35±0.02	
1996.38	**Ca**	0.191±0.029	1.44±0.07	-92.9±0.6	0.45±0.02	
1996.38	**C2**	0.124±0.019	1.74±0.09	-96.1±0.5	0.45±0.02	
1996.38	**C4**	0.022±0.003	3.38±0.34	-86.6±1.0	1.43±0.14	
1997.20	**r**	1.362±0.204	0.00	0.00	0.11±0.01	1.4601196
1997.20	**C0**	0.295±0.044	0.30±0.02	-89.0±1.6	0.31±0.02	
1997.20	**C1**	0.135±0.020	0.84±0.04	-90.3±0.9	0.55±0.03	
1997.20	**Ca**	0.111±0.017	1.47±0.07	-96.5±0.5	0.39±0.02	
1997.20	**C2**	0.101±0.015	1.78±0.09	-96.3±0.5	0.59±0.03	
1997.20	**C4**	0.030±0.005	3.13±0.31	-90.9±1.0	1.64±0.16	
1997.20	**C8**	0.034±0.005	6.81±0.68	-97.5±1.0	3.40±0.34	
1998.22	**r**	1.089±0.163	0.00	0.00	0.25±0.01	0.44147467
1998.22	**C0**	0.916±0.137	0.23±0.01	-77.2±5.3	0.30±0.02	
1998.22	**C1**	0.119±0.018	0.93±0.05	-83.7±1.2	0.47±0.02	
1998.22	**Ca**	0.247±0.037	1.49±0.07	-95.0±0.7	0.46±0.02	
1998.22	**C2**	0.049±0.007	2.04±0.20	-96.8±1.0	0.62±0.06	
1998.22	**C4**	0.038±0.008	3.40±0.34	-89.6±1.4	2.07±0.21	
1998.84	**r**	1.113±0.167	0.00	0.00	0.08±0.01	1.4787256
1998.84	**C0**	0.650±0.098	0.18±0.02	-86.2±9.4	0.35±0.02	
1998.84	**C1**	0.102±0.015	0.92±0.05	-75.6±2.8	0.60±0.03	
1998.84	**Ca**	0.141±0.021	1.42±0.07	-92.4±0.6	0.22±0.01	
1998.84	**C2**	0.147±0.022	1.67±0.08	-99.0±1.3	0.53±0.03	
1999.57	**r**	2.015±0.302	0.00	0.0	0.12±0.01	1.1925775
1999.57	**C0**	0.430±0.064	0.33±0.02	-77.0±2.1	0.26±0.01	
1999.57	**C1**	0.178±0.027	0.84±0.04	-77.1±0.9	0.31±0.02	
1999.57	**Ca**	0.048±0.007	1.32±0.07	-83.5±0.6	0.01±	
1999.57	**C2**	0.131±0.020	1.57±0.08	-92.5±0.6	0.42±0.07	
1999.57		0.040±0.006	1.98±0.10	-93.4±1.0	0.68±0.11	
1999.57	**C4**	0.032±0.005	3.28±0.33	-92.8±1.1	1.57±0.14	
1999.57		0.007±0.002	5.14±0.51	-88.7±2.0	1.01±0.18	
1999.57	**C8**	0.020±0.004	7.38±0.74	-96.2±2.0	2.47±0.34	
1999.57	**C12**	0.006±0.001	10.26±1.16	-91.7±2.0	3.04±0.71	
1999.85	**r**	1.603±0.241	0.00	0.0	0.090±0.01	1.1036355
1999.85	**C0**	0.449±0.067	0.28±0.05	-79.6±2.9	0.24±0.01	
1999.85	**C1**	0.168±0.024	0.94±0.06	-76.2±1.8	0.39±0.02	
1999.85	**Ca**	0.093±0.015	1.38±0.17	-86.8±0.6	0.17±0.01	
1999.85	**C2**	0.098±0.015	1.64±0.10	-94.5±0.5	0.42±0.02	
1999.85	**C4**	0.039±0.007	2.44±0.13	-97.5±2.8	1.27±0.13	
1999.85		0.021±0.004	4.55±0.12	-88.1±1.0	1.61±0.16	
1999.85	**C8**	0.013±0.003	7.86±0.18	-97.6±2.0	2.05±0.21	
2000.46	**r**	1.606±0.241	0.00	0.00	0.13±0.01	0.46644555
2000.46	**C0**	0.364±0.055	0.35±0.02	-79.2±1.8	0.27±0.01	
2000.46	**C1**	0.144±0.022	0.96±0.05	-79.3±0.7	0.36±0.02	
2000.46	**Ca**	0.134±0.020	1.44±0.07	-88.8±0.5	0.29±0.02	
2000.46	**C2**	0.105±0.016	1.70±0.03	-92.1±0.7	0.62±0.03	
2000.46	**C4**	0.055±0.008	3.61±0.72	-91.9±1.1	1.95±0.20	
2002.13	**r**	1.702± 0.251	0.00 ± 0.01	0.0± 0.3	0.11±0.02	1.3686
2002.13	**C0**	0.151± 0.023	0.37± 0.01	-94.6± 1.2	0.29±0.01	
2002.13	**B3**	0.008± 0.001	0.76± 0.02	-89.8± 1.2	0.14±0.03	
2002.13	**C1**	0.072± 0.012	1.02± 0.02	-75.2± 0.5	0.35±0.02	
2002.13	**Ca**	0.318± 0.043	1.43± 0.02	-88.1± 0.5	0.48±0.05	
2002.13	**C2**	0.029± 0.004	2.02± 0.02	-94.0± 0.5	0.68±0.01	
2002.13	**C4**	0.031± 0.005	3.61± 0.05	-89.0± 0.8	1.94±0.02	
2002.13	**C8**	0.044± 0.007	6.37± 0.09	-95.1± 0.8	3.40±0.02	
2002.13	**C12**	0.009± 0.001	11.36± 0.37	-94.6± 1.9	3.37±0.67	

Table 3.3: Model-fit results for S5 1803+784 III

Epoch	Id.	S [Jy]	r [mas]	θ [deg]	M.A. [mas]	Chi-squared
			15 GHz			
2003.10	**r**	1.245± 0.179	0.00± 0.02	0.0± 0.2	0.10±0.03	1.5375
2003.10	**C0**	0.310± 0.048	0.31± 0.03	-76.9± 1.7	0.27±0.01	
2003.10	**C1**	0.039± 0.008	0.66± 0.03	-84.2± 1.3	0.09±0.04	
2003.10	**Ca**	0.287± 0.058	1.42± 0.01	-88.4± 0.3	0.35±0.09	
2003.10	**C2**	0.113± 0.045	1.78± 0.24	-89.1± 0.8	1.00±0.26	
2003.10	**B3**	0.035± 0.016	2.64± 0.38	-88.9± 1.2	1.17±0.19	
2003.10	**C4**	0.039± 0.006	4.67± 0.32	-90.0± 0.8	2.01±0.35	
2003.10	**C8**	0.031± 0.004	7.44± 0.49	-97.1± 0.7	3.00±0.16	
2003.10	**C12**	0.015± 0.004	12.37± 0.78	-93.2± 0.6	4.31±0.64	
2004.27	**r**	1.264± 0.185	0.00± 0.01	0.0± 0.1	0.09±0.03	1.4844
2004.27	**C0**	0.117± 0.017	0.33± 0.01	-89.1± 1.3	0.25±0.01	
2004.27	**C1**	0.124± 0.018	1.00± 0.05	-78.0± 0.6	0.38±0.05	
2004.27	**Ca**	0.185± 0.028	1.47± 0.02	-90.6± 0.4	0.31±0.06	
2004.27	**C2**	0.046± 0.009	1.76± 0.06	-95.6± 0.5	0.49±0.04	
2004.27	**C4**	0.044± 0.007	3.64± 0.09	-86.9± 0.9	1.83±0.05	
2004.27	**C8**	0.046± 0.007	6.42± 0.24	-96.3± 0.8	2.71±0.08	
2004.27	**C12**	0.014± 0.003	9.81± 0.30	-96.3± 0.6	3.09±0.55	
2005.30	**r**	0.819± 0.119	0.00± 0.01	0.0± 0.2	0.12±0.04	0.9761
2005.30	**C0**	0.160± 0.028	0.22± 0.02	-61.6± 0.3	0.05±0.03	
2005.30	**C1**	0.091± 0.014	0.61± 0.02	-75.8± 1.3	0.35±0.02	
2005.30	**Ca**	0.297± 0.045	1.47± 0.01	-87.4± 0.6	0.42±0.03	
2005.30	**C2**	0.040± 0.011	1.98± 0.06	-84.1± 0.5	0.51±0.07	
2005.30	**C4**	0.018± 0.005	3.98± 0.09	-84.9± 0.8	1.12±0.34	
2005.30	**C8**	0.064± 0.009	6.08± 0.30	-94.7± 1.0	3.04±0.23	
2005.30	**C12**	0.010± 0.005	9.80± 0.97	-91.9± 2.5	2.90±0.70	
2005.68	**r**	1.381± 0.203	0.00± 0.01	0.0± 0.3	0.09±0.02	0.8685
2005.68	**C0**	0.146± 0.022	0.25± 0.03	-74.2± 1.5	0.21±0.02	
2005.68	**C1**	0.048± 0.008	0.75± 0.02	-78.0± 0.8	0.32±0.03	
2005.68	**Ca**	0.244± 0.064	1.44± 0.02	-89.0± 0.3	0.31±0.09	
2005.68	**C2**	0.120± 0.019	1.71± 0.04	-88.8± 0.5	0.55±0.02	
2005.68	**C4**	0.021± 0.007	3.44± 0.29	-87.0± 1.3	1.50±0.20	
2005.68	**B3**	0.013± 0.001	4.72± 0.06	-83.7± 0.4	1.16±0.03	
2005.68	**C8**	0.058± 0.006	6.37± 0.11	-97.4± 0.6	2.49±0.18	
2005.68	**C12**	0.022± 0.001	8.98± 0.20	-93.7± 0.7	3.68±0.22	

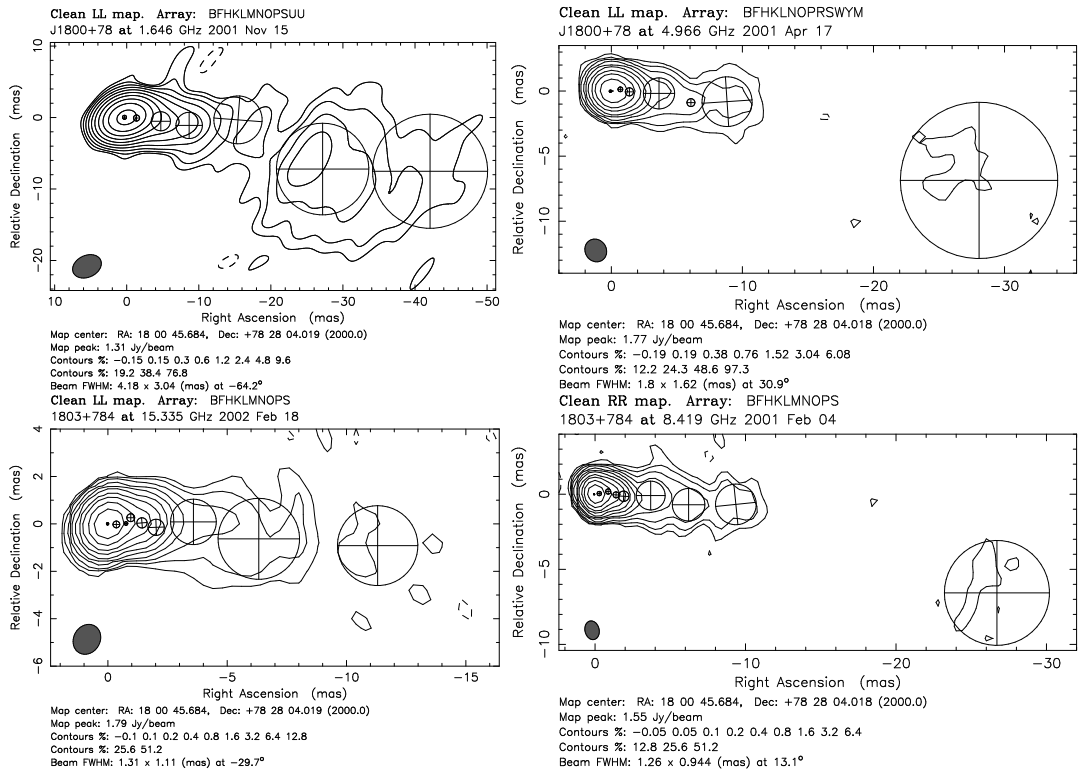

Figure 3.3: 1803+784: Clean maps with superimposed modelfit Gaussian jet components at 1.6 GHz (*Upper left*), 5 GHz (*Upper right*), 15 GHz (*Bottom left*), and 8 GHz (*Bottom right*).

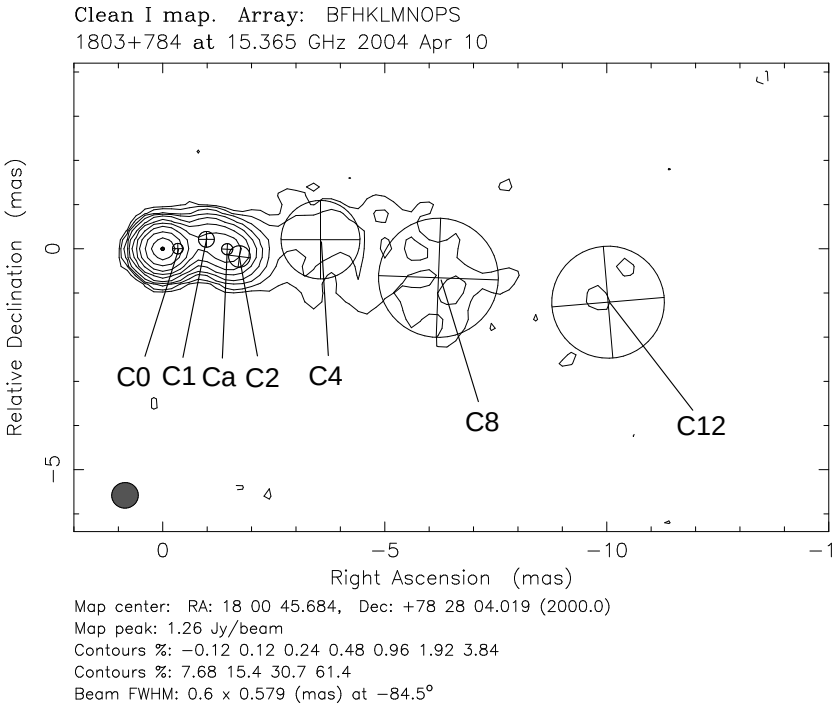

Figure 3.4: 1803+784: Map at 15 GHz with position of the jet components C0, C1, Ca, C2, C4, and C8 marked.

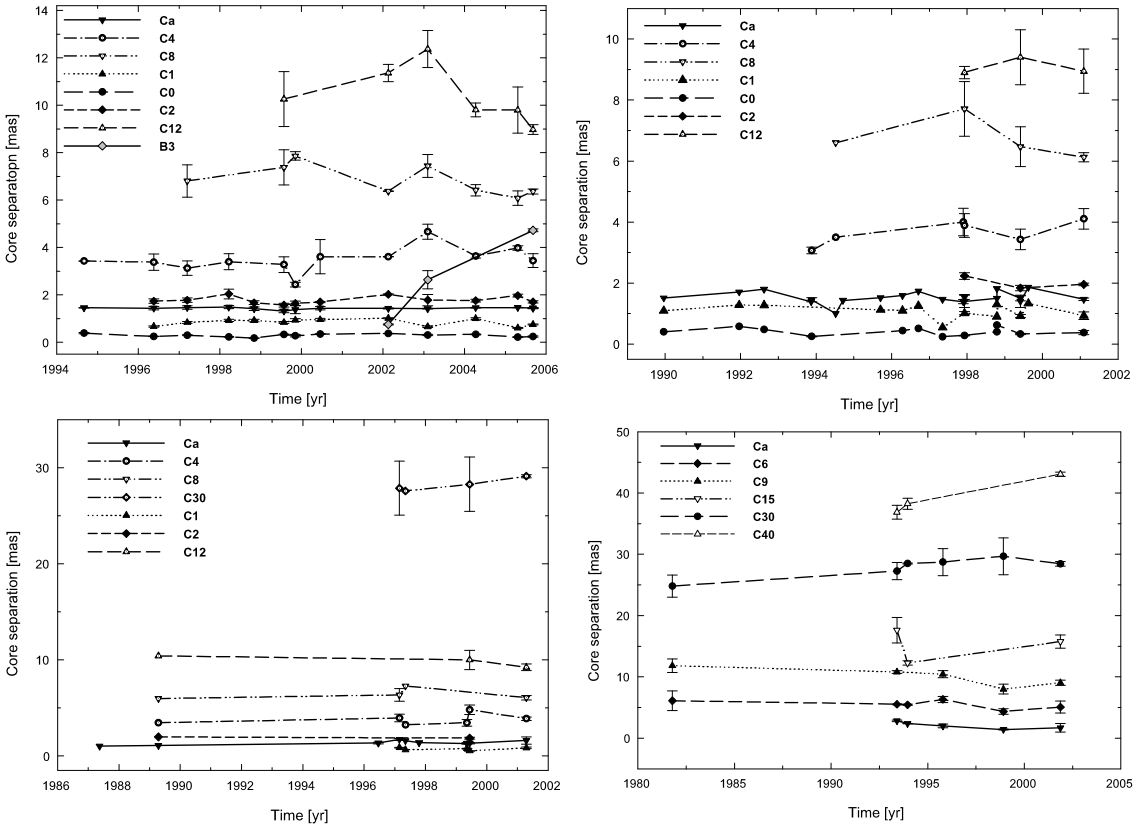

Figure 3.5: We show in (*Upper left*) the core separation as function of time for those jet components detected at 15 GHz. Individual components are denoted by different symbols and different lines (same symbols and lines for all images). Please note the straight line for **Ca** and the fast moving component **B3**. In (*Upper right*) and (*Bottom left*) we show the same relation as in (*Upper left*) based on data collected from the literature (at 8 GHz in (*Upper right*) and at 5 GHz in (*Bottom left*)). The literature data in (*Upper right*) and (*Bottom left*) have been re-identified with the new scenario we propose in this paper. Obviously the published data are compatible with this new identification. In (*Bottom right*) the same relation for components further out along the jet based on 1.6 GHz data is displayed.

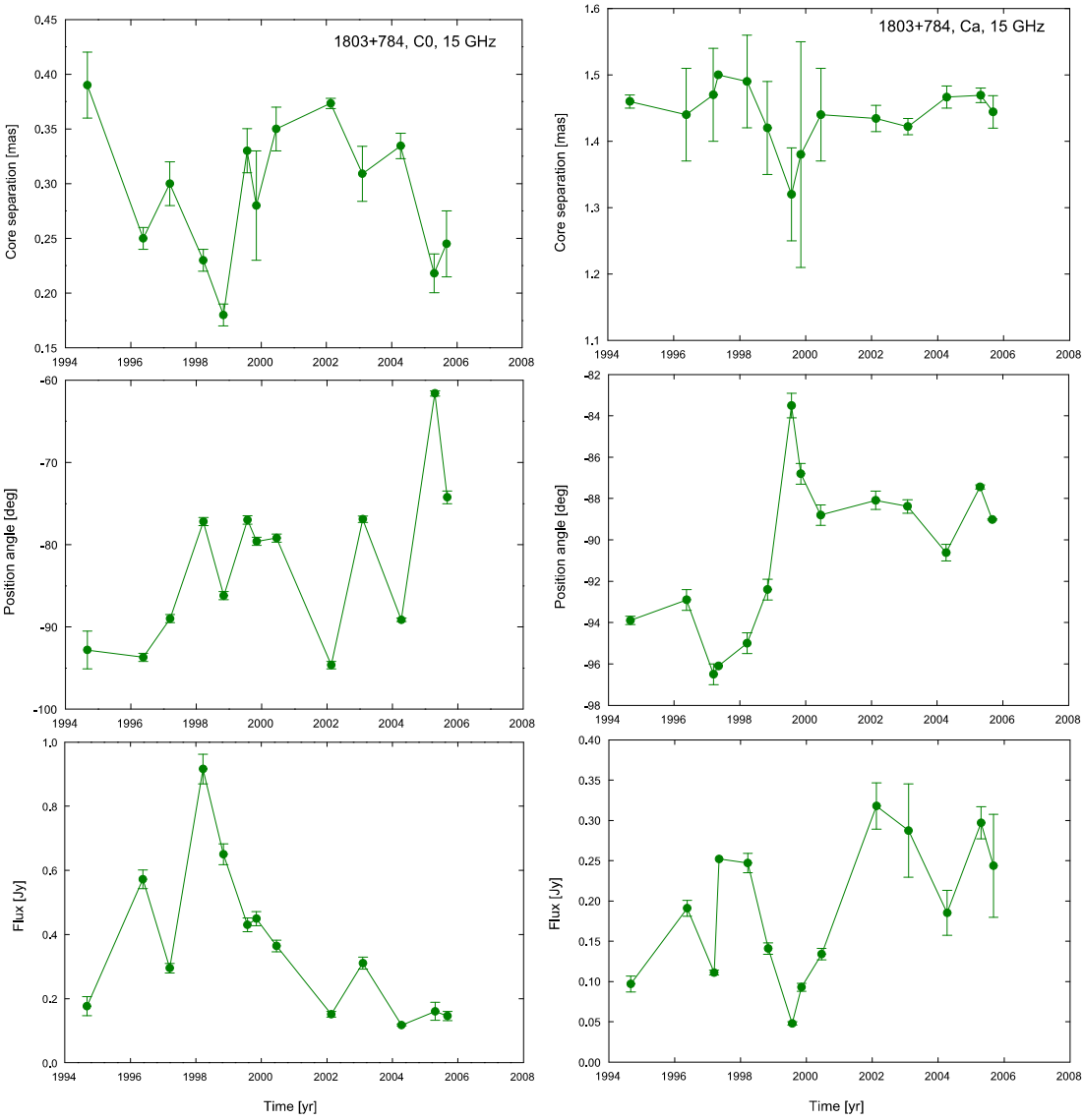

Figure 3.6: *Left:* Core separation, position angle and flux versus time for the jet component C0. *Right:* Core separation, position angle and flux versus time for the jet component Ca.

3.3 Oscillating jet components

In addition to the formerly so-called *stationary* component (**Ca**) at $\sim$ 1.4 mas we found six jet components, none of which shows – based on the new data presented here – significant evidence for a long-term outward motion. Besides **C12**, they remain at similar core separations between 1993.88 and 2005.68. Since the identification of **C12** suffers from a reduced number of data points, we do not take this component in our further analysis into account. In Fig. 3.5 we present an overview over the core separation/time relation found for all model jet components in the jet of S5 1803+784 at all frequencies (up to a core separation of $\sim$40 mas). In Fig. 3.5 (Upper left) we show the relation at 15 GHz, in (Upper right) at 8 GHz, in (Bottom left) at 5 GHz, and in (Bottom right) at 1.6 GHz. (b) and (c) show data collected from the literature but re-identified with the scenario we present in this paper. It is easy to see that all the stationary components we found are seen at all four frequencies. Our new motion scenario is supported by the literature data. Altogether we present data over a time span of twenty years in Fig. 3.5.

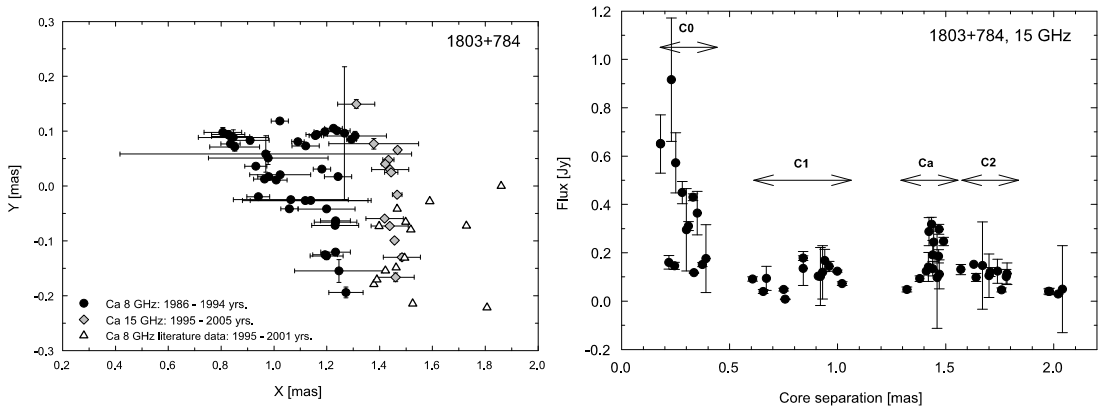

Figure 3.7: In (*Left*) we show the evolution of **Ca** in rectangular coordinates. We find a displacement between the earlier (1986-1994) and newer (1995-2001) 8 GHz data towards larger x-values. The 15 GHz data for **Ca** are found at an average position of the 8 GHz data for the same component. In (*Right*) the flux-density evolution along the jet based on the 15 GHz data is presented.

3.3.1 Comparison with literature data

In order to check whether the components we find showed a similar or different kinematic behavior in earlier times, we collected all available VLBI information for S5 1803+784 from the literature. We list the model-fit parameters derived for the total intensity VLBI observations in Table 3.5 and 3.6. We re-identified all the literature-components in a similar way, trying to find the component identification which will lead to the smoothest changes of the core separation, the position angle, and the flux density of the components. We found jet components at the same core separations showing similar stationary behavior as we found for 15 GHz. We plot the results in Fig. 3.5 (Upper right) and (Bottom left). At both frequencies (5& 8.4 GHz), the components have remained at similar core separations for almost 20 years. No long-term outward motion is found based on the collected data. Although different kinematic scenarios have been proposed by different authors, the data are fully consistent with a scenario where all components remain at similar core separations.

In Fig. 3.5 (Bottom right) we show the same relation again for the 1.6 GHz data. For the inner components (up to 12 mas) we again find stationarity while the outer components (**C30** and **C40**) show some evidence for outward motion.

Table 3.4: Summary for modelled components in S5 1803+784: component identification, mean core separation, proper motion of the component (calculated for 15 GHz only, based on a linear regression fitted to the core separation/time relation), and apparent speeds of the components (calculated for the whole dataset for all frequencies) are listed.

Comp.	$r_{\rm mean}$ [mas]	$\mu_{\rm r}^{15}$ [mas yr^{-1}]	$\beta_{\rm app}^{15}$ [c]	$\mu_{\rm r}^{\rm all}$ [mas yr^{-1}]	$\beta_{\rm app}^{\rm all}$ [c]
C0	0.30 ± 0.02	0.017 ± 0.001	0.39 ± 0.02	0.006 ± 0.001	0.14 ± 0.02
C1	0.79 ± 0.03	-0.037 ± 0.003	-0.86 ± 0.07	0.001 ± 0.001	0.02 ± 0.02
Ca	1.27 ± 0.03	0.007 ± 0.004	0.16 ± 0.09	0.022 ± 0.001	0.51 ± 0.02
C2	1.93 ± 0.03	0.017 ± 0.007	0.39 ± 0.16	-0.002 ± 0.001	-0.05 ± 0.02
C4	3.70 ± 0.08	0.145 ± 0.017	3.37 ± 0.39	0.001 ± 0.001	0.02 ± 0.02
C8	6.78 ± 0.18	-0.182 ± 0.005	-4.23 ± 0.12	-0.182 ± 0.005	-4.23 ± 0.12
C12	10.02 ± 0.38	-0.715 ± 0.113	-16.62 ± 2.63	-0.197 ± 0.069	-4.58 ± 1.60
B3	/	0.807 ± 0.151	18.76 ± 3.51	/	/

Table 3.5: Model-fit results for S5 1803+784 obtained from the literature. We list the epoch of observation, the jet component identification, the flux-density, the radial distance of the component center from the center of the map, the position angle of the center of the component, the FWHM major axis of the circular component, the position angle of the major axis of the component and we give a reference to the publication.

Epoch	Id.	S [Jy]	r [mas]	θ [deg]	Ma.A. [mas]	Reference
				2.32 GHz		
1994.52	**1**	1.63	0.00	0.00	1.37	Fey et al. 1996
1994.52	**2**	0.34	4.0	-94	7.24	
1994.52	**3**	0.28	27.6	-105	12.11	
				5 GHz		
1997.79	**C1**	0.413	1.38	-98	0.65	Lister et al. 2001
				8 GHz		
1998.79	**Core**	2.45	0.00	0.0	0.1	Tateyama et al. 2002
1998.79	**C1**	0.23	1.50	-95	0.1	
1998.79	**C2**	0.21	0.90	-95	0.1	
1989.96	**Core**	2.77	0.00	0.0	0.1	Tateyama et al. 2002
1989.96	**C1**	0.22	1.51	-94	0.1	
1989.96	**C2**	0.20	1.09	-90	0.3	
1989.96	**E**	0.65	0.40	-81	0.2	
1991.96	**Core**	1.38	0.00	0.0	0.1	Tateyama et al. 2002
1991.96	**C1**	0.14	1.71	-90.9	0.1	
1991.96	**C2**	0.27	1.28	-87.4	0.1	
1991.96	**E**	0.06	0.58	-85.1	0.1	
1992.62	**Core**	1.68	0.00	0.0	0.2	Tateyama et al. 2002
1992.62	**C1**	0.11	1.80	-90	0.1	
1992.62	**C2**	0.40	1.27	-95	0.1	
1992.62	**E**	0.32	0.48	-93	0.01	
1993.87	**Core**	1.25	0.00	0.0	0.2	Tateyama et al. 2002
1993.87	**C2**	0.33	1.39	-97.2	0.1	
1994.71	**Core**	1.49	0.00	0.0	0.2	Tateyama et al. 2002
1994.71	**C2**	0.17	1.43	-96.2	0.1	
1995.71	**Core**	2.10	0.00	0.0	0.25	Tateyama et al. 2002
1995.71	**C2**	0.28	1.52	-93.0	0.1	
1995.71	**C3**	0.18	1.12	-93.1	0.1	
1996.29	**Core**	1.57	0.00	0.0	0.2	Tateyama et al. 2002
1996.29	**C2**	0.10	1.59	-91	0.1	
1996.29	**C3**	0.04	1.10	-97	0.1	
1996.29	**E**	0.18	0.44	-101	0.1	
1996.71	**Core**	1.56	0.00	0.0	0.2	Tateyama et al. 2002
1996.71	**C2**	0.15	1.73	-92.4	0.1	
1996.71	**C3**	0.10	1.25	-96.1	0.1	
1996.71	**E**	0.17	0.51	-89.2	0.1	
1998.79	**Core**	1.60	0.00	0.0	0.2	Tateyama et al. 2002
1998.79	**C2**	0.13	1.82	-97.0	0.1	
1998.79	**C3**	0.26	1.30	-93.7	0.1	
1998.79	**E**	0.41	0.40	-93.3	0.1	

Table 3.6: Model-fit results for S5 1803+784 obtained from the literature II.

Epoch	Id.	S [Jy]	r [mas]	θ [deg]	Ma.A. [mas]	Reference
				8 GHz		
1999.62	**Core**	1.89	0.00	0.0	0.2	Tateyama et al. 2002
1999.62	**C2**	0.09	1.86	-90.0	0.1	
1998.79	**C3**	0.19	1.33	-88.1	0.1	
1998.79	**E**	0.28	0.62	-77.8	0.1	
				8.4 GHz		
1997.93	**XA**	1.493±0.001	0.00		0.2±0.1	Ros et al. 2001
1997.93	**XB**	0.231±0.001	0.6±0.2	-86±19	0.7±0.1	
1997.93	**XC**	0.274±0.001	1.4±0.2	-97±8	0.6±0.1	
1997.93	**XD**	0.036±0.001	2.0±0.2	-98±5	0.5±0.1	
1997.93	**XE**	0.024±0.001	2.7±0.2	-97±4	1.4±0.1	
1997.93	**XF**	0.018±0.001	3.9±0.2	-89±3	1.1±0.1	
1997.93	**XG**	0.019±0.001	6.3±0.2	-96±3	2.8±0.2	
1997.93	**XH**	0.025±0.001	8.9±0.2	-95±1	4.1±0.2	
1999.41	**XA**	1.517±0.001	0.00		0.2±0.1	Ros et al. 2001
1999.41	**XB**	0.374±0.001	0.5±0.2	-81±21	0.5±0.1	
1999.41	**XC**	0.192±0.001	1.4±0.2	-93±8	0.5±0.1	
1999.41	**XD**	0.058±0.001	1.9±0.2	-94±6	0.6±0.1	
1999.41	**XE**	0.030±0.001	2.7±0.2	-93±4	1.9±0.1	
1999.41	**XF**	0.030±0.001	4.0±0.2	-97±3	2.4±0.1	
1999.41	**XG**	0.020±0.001	7.0±0.2	-97±2	2.9±0.2	
1999.41	**XH**	0.017±0.001	9.4±0.2	-97±1	3.6±0.3	
				8.55 GHz		
1994.52	**1**	1.91	0.00		0.19	Fey et al. 1996
1994.52	**2**	0.38	1.0	-92	1.53	
1994.52	**3**	0.05	3.5	-86	1.26	
1994.52	**4**	0.05	6.6	-95	2.57	
				86 GHz		
1993.29	**C**	0.448±0.063	0.00		0.08±0.03	Lobanov et al. 2000
1993.29	**J1**	0.376±0.056	0.27±0.06	-0.9±8.0	0.08±0.03	

3.3.2 Comparison with geodetic VLBI data

Britzen et al. (2005a) presented an analysis of the kinematics in the pc-scale jet of S5 1803+784 based on geodetic VLBI data. These observations are performed in general more frequently than astronomical observations and usually are obtained every few months (please find details in Britzen et al. 2005). In order to have comparable numbers of observations per time from astronomical and geodetic observations, we smoothed the geodetic modelfit results at 8 GHz in the period 1986.21 – 1993.95 with the following sliding mean algorithm. The new data points were produced, replacing the original data m_i for each time t_i with the weighted mean:

$$m_i' = -2.5 \log \left(\frac{1}{\sum p_j} \sum_{j=1}^{k} p_j \cdot 10^{-0.4 m_j} \right), \tag{3.6}$$

where k is the number of data points within interval $[t_i - \Delta, t_i + \Delta]$, and the weight of jth point is determined as

$$p_j = \exp\left[-(\delta t_j / \Delta)^2 \right], \tag{3.7}$$

where δt_j is the time span from the jth point to the center of the window. For our analysis we selected a window value of $\Delta = 0.3$ years, which is consistent with the temporal resolution of data points obtained at other frequencies.

In order to check whether the components we find at 15 GHz and 1.6 GHz and also in the literature data at 8 GHz and 5 GHz showed a similar or different kinematic behavior in earlier times, we re-identified the components in the geodetic 8 GHz data in a similar way to our component identification at other frequencies. We tried to find the component identification which will lead to the smoothest changes of the core separation, the position angle and the flux density of the components. This way of finding a correct identification of the jet components should provide the best solution. We found jet components C0, C1, C2, and C4 at the same core separations and showing similar stationary behavior as we found for other frequencies. However, in this case the component C2 consists of two components $C2_1$ and $C2_2$. The total flux of these two components is comparable with the flux of C2 component at 8 GHz, which we found from the literature data. We plot the results of the component identification in Fig. 3.8. It is clearly seen, that the components have remained at similar core separations for almost 10 years and no long-term outward motion is found based on the collected data.

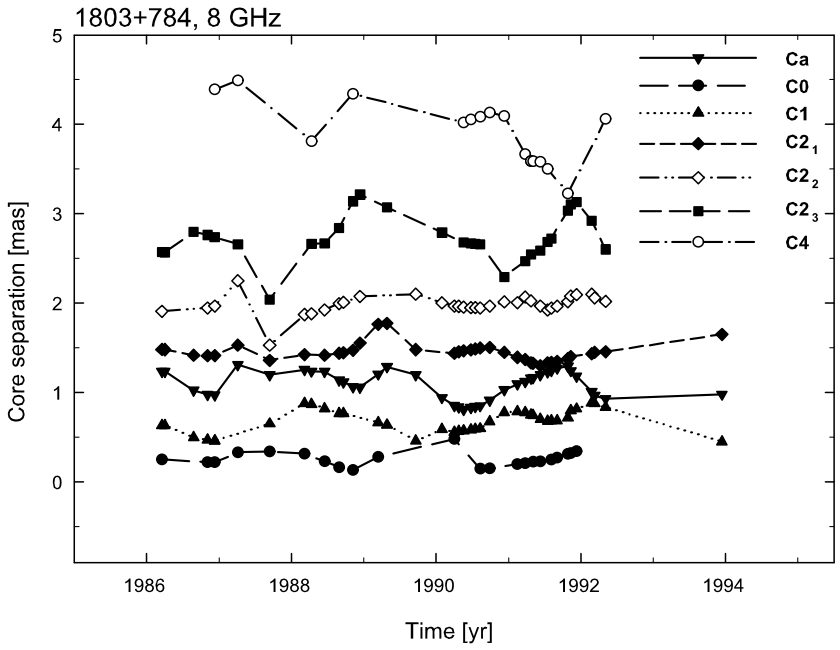

Figure 3.8: We show the core separation as function of time for those jet components detected at 8 GHz in the smoothed geodetic data. Individual components are denoted by different symbols and different lines.

3.3.3 Flux-density evolution along the jet

In Fig. 3.7(right) we show the evolution of the flux-density (15 GHz) as function of the length of the jet (up to a jet length of 2 mas). We find maxima in the observed distribution at ∼0.9 mas and 1.4 mas, which correspond to the position of the jet components C1 and Ca at about 1 and 1.4 mas. For the component at 1.4 mas we find an evolution towards a sharp peak in flux-density. The flux density evolution along the jet is independent of component identification. However, it shows the prominent peaks at the positions, which correspond to the positions of the component C1 and Ca which might suggest that there is a bend of the jet or some increase in the flux in this particular position and can be an additional evidence for our component identification.

3.3.4 Displacement of Ca

In Fig. 3.7 (Left) the rectangular coordinates of the component **Ca** in different symbols indicate a possible average positional shift by ~ 0.3 mas during ten years. We show 8 GHz data obtained between 1986 and 1994, 15 GHz data obtained between 1995 and 2005, and literature data at 8 GHz between 1995 and 2001. The average position of the 8 GHz data in right ascension seems to be shifted in the newer data with characteristic changes of 0.03 mas/yr. However, we need to take into account that we compare here the geodetic data with astronomical data. In the case of the geodetic data, taken from Britzen et al. (2005a), we assumed, the brightest component is identical with component **Ca**. The displacement of the stationary jet component **Ca** reveals, that although the jet components of S5 1803+784 are stationary and not moving outwards fast, they still have very slow motion of about 0.03 mas/yr. This motion can be explained in a few different ways. The stationary jet components can be either due to a bend of the jet or due to recollimation shock in the jet. It is possible, that due to interaction with the ambient medium, the position of the recollimation shocks is changing with time. On the other hand, if the jet is precessing and changing the position with time, than we will also see the slow movement of the jet components. Another explanation can be that the jet components, which we see now as stationary were ejected long time ago and are moving slowly outwards with a speed of 0.03 mas/yr. These different explanations will be discussed in sections 3.12 and 3.13.

3.4 The "fast" component B3

In addition to the *stationary* components, one fast moving component has been observed in the time between 2002.1 and 2005.7 (**B3**). As shown in Fig. 3.5 (Upper left) and Fig. 3.9, this component does show outward motion with an apparent velocity of $\sim 19 \pm 4c$. **B3** shows a kinematical behavior which differs significantly from the apparent stationarity of the other components. The calculated ejection time of this component is 1999.8 ± 1.1. The flux density of this component is quite low and varies between 0.01 and 0.04 Jy. Unfortunately, the calculated time of the ejection is in the middle of the two-year gap in the observations after the ejection. However, the VLBI monthly monitoring at 43 GHz performed by Jorstad et al. (2005) showed

a fast jet component ejection in 1998.6 with apparent speed of $\sim 16c$ (B2). The average position angle of our component **B3** is $-87.5^\circ \pm 0.5^\circ$ which is comparable with the position angle of $-62.2^\circ \pm 20.8^\circ$ of B2 by Jorstad et al. (2005). The comparable values of the component ejection, apparent speed, and position angle provide some evidence that our fast **B3** component and B2 from Jorstad et al. (2005) are the same.

3.5 Significant position angle changes

As shown before, most of the components remain at similar core separations for the time covered by the observations. In this section we show, that the *stationary* components show significant position angle changes. In Fig. 3.10 – 3.11 we show the evolution of the position angle for four jet components at different frequencies. The position angles vary between 35° in the case of **C0** (3.10 Left) and 15° in the case of **C2** (3.11 Right). We find very similar relations at 5 and 8 GHz for **C0**, at 5, 8, and 15 GHz for **C1**, at 8 and 15 GHz for **C2**, and at 5, 8, and 15 GHz for **Ca**. One outlier for **C0** in Fig. 3.10 (Left) in 1994 can probably be explained by a blending effect with the core or a new component due to the closeness of the core. In the case of the core separation for **C0** and **C2**, the evolution is similar at the two frequencies. For **C2** we find some indication, that the lower frequency-data can be found at larger core separations.

3.6 Evolution of the mean jet ridge line

In Fig. 3.13 we show the jet ridge line for all epochs obtained at 15 GHz in Cartesian coordinates. The jet ridge line is defined by a line connecting all component positions at a given epoch. We find that the jet ridge line changes its shape between epochs in a periodic way. Fig. 3.13(a) shows the temporal evolution of jet component positions at 15 GHz for the time period 1994 – 2005. Each dot represents the position of one jet component in rectangular coordinates X and Y. The lines connect all the components for one particular epoch of observation. Figs. 3.13(b) and (c) show this evolution with time in more detail. From an almost straight line in 1994.67, the shape of the jet evolves into a sinusoidal contour with the northernmost value at a right ascension of $\sim$ 1 mas and the southernmost value at a right ascension of $\sim$

2 mas. The amplitude of the sinusoid reaches its maximal values at epoch 1998.84 and decreases again, forming an almost straight line in 2003.10. One period is completed after $\sim$ 8.5 years and the jet shape starts to evolve into a sinusoid again. However, the position of the straight lines in 1994.67 and 2003.10 are different and the difference in the declination is 0.1 mas. We thus see an evolution of the jet ridge line with time and can follow the individual components position within this overall evolution of the jet which have never been seen before. It is worth to notice that this result does not depend on the jet component identification and is an independent evidence for characteristic timescale of $\sim$ 8.5 years. Usually in blazars and quasars jet components are moving outwards along fixed path. However, in S5 1803+784 we see that a set of oscillating jet components are not moving outwards, but rather show changes in the jet ridge line with a timescale of $\sim$8.5 years.

3.7 Evolution of the jet width

In this section we investigate the width of the jet as defined by the position angle distribution that the jets components span. In Fig. 3.14 we show the position angle as function of time for all jet components seen at all observed frequencies. This plot shows that the jet changes its width with time: around 1995 the jet width appears to be quite small ($\sim$5°), around 1999.5 the jet width appears to be much broader ($\sim$ 40°) and is narrower again in 2004. To investigate the longterm evolution of this effect, we include data taken from the literature in Fig. 3.14 (b) and find a similar effect of broadening as before. The complete dataset (our data + literature data) seems to cover two cycles of jet-width broadening with a mean duration of 8–9 years. To investigate whether this broadening is mainly a frequency dependent effect, we show the distribution at 15 GHz in (c) and at 8 GHz in (d). In both figures we confirm the trend of changing jet width. To exclude that less-well defined model components at large core separations with large position angles produce this effect, we checked whether the shape of the plot changes when we take jet components within a maximum core separation. We checked the data for the jet components within the inner 1 mas, 2 mas and increased the core separation by one milliarcsecond up to 7 mas. However, the shape of the position angle distribution is stable and does not change when we take the data within a certain core separation. We show the distribution for the inner 5 mas based on well defined model fit parameters in (c) and (d).

In order to exclude that the more frequent observations can produce more outliers in position angles and affect the position angle distribution, we selected the data within 5 mas, then binned the data in 0.3 year bins and calculated the standard deviation in position angle within particular bin, both for 5 GHz and 8 GHz. The evolution of standard deviations for each bin with time is plotted in Fig. 3.12 (The outliers were removed from the plot). Time was calculated as a central position of a time bin. The position angle spread with time shows a smooth increase in position angles, which starts in 1985 and reaches its maximum in 1988–1992, then decreases again and has the second maximum in about 1998. It is clearly seen that the spread of the position angle evolution has two cycles with a characteristic timescale of about 8–9 years. The autocorrelation function gives the value of the timescale: 9.9 ± 0.2 with a correlation coefficient of 0.79, which is similar to a period of the jet ridge line evolution. Binning the data a different bin length, such as 0.5 or 1.0 years gives the same results. In order to check whether the different number of jet components for different epochs of observations can affect this results, we selected only data points within 0.5 mas core separation, took into account only first three jet components for each particular epoch and binned the position angles into 0.3 year bins. However, the evolution of the standard deviations of position angles looked completely similar, so we conclude, that the shape of the plot and characteristic time scale of the position angle changes does not depend on the number of the jet components for particular epochs of observations.

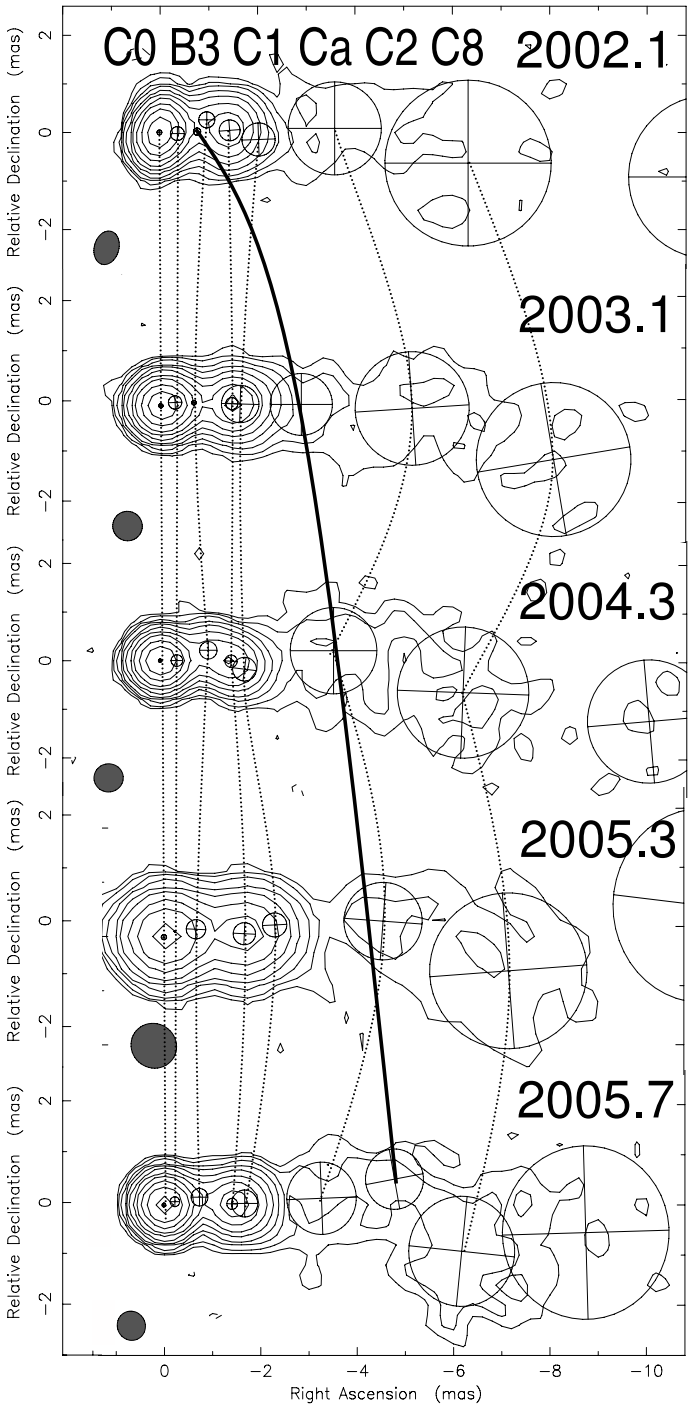

Figure 3.9: Model fits superimposed on the hybrid maps (obtained from the Clean and self-calibration) are shown for the most recently observed five epochs. The component positions are connected by dotted lines. The positions of the fast component **B3** are marked by a solid line. Please note that the elapsed time between adjacent epochs differs.

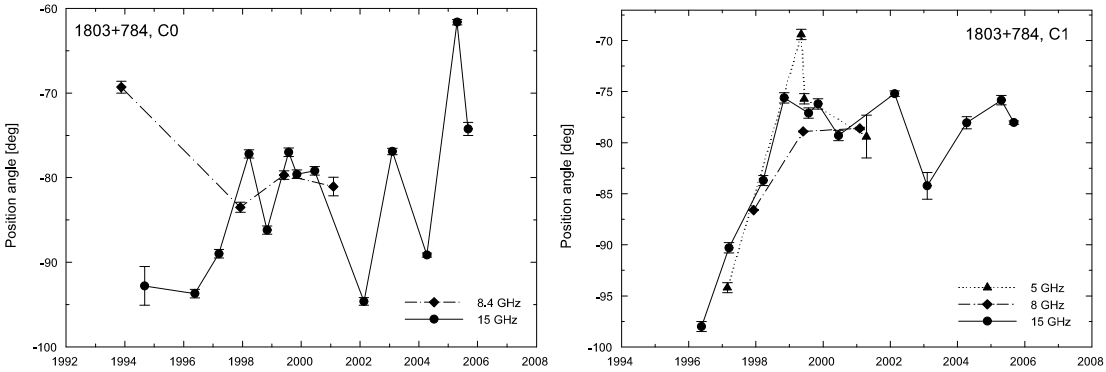

Figure 3.10: Position angle as function of time at different frequencies for the components C0 and C1.

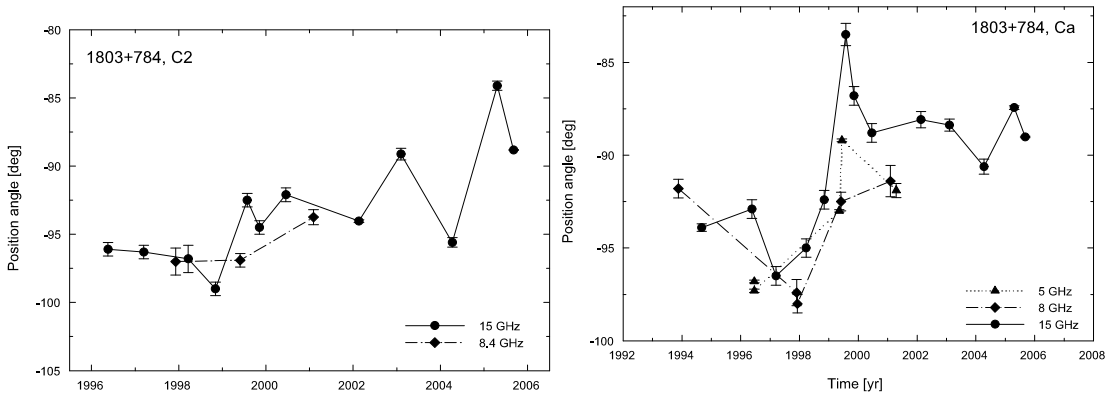

Figure 3.11: Position angle as function of time at different frequencies for the components Ca and C2.

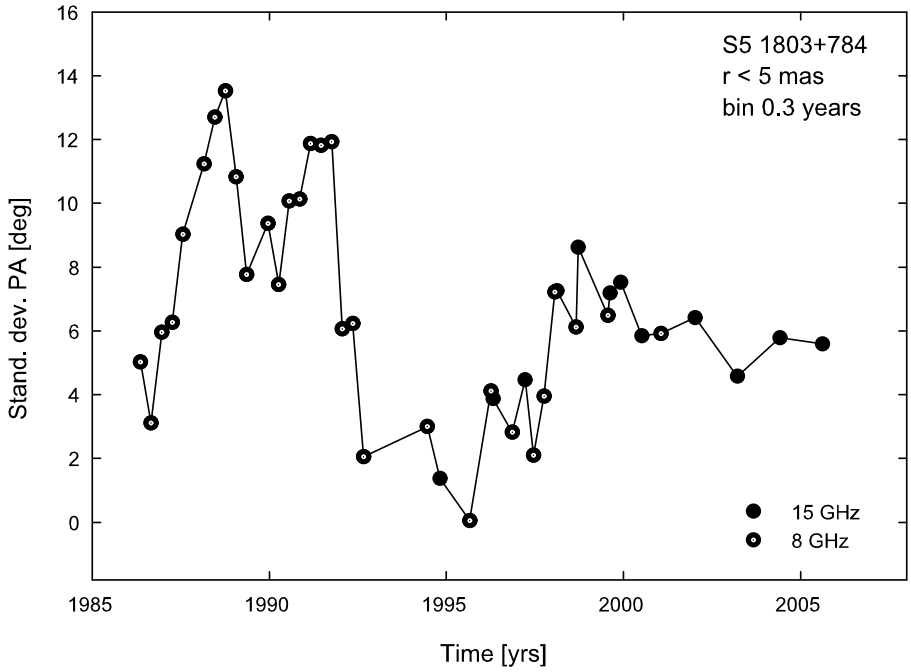

Figure 3.12: Time evolution of the standard deviation of position angles, calculated for 0.3 year bins. Dotted circles show 8 GHz data, whereas circles represent 15 GHz data.

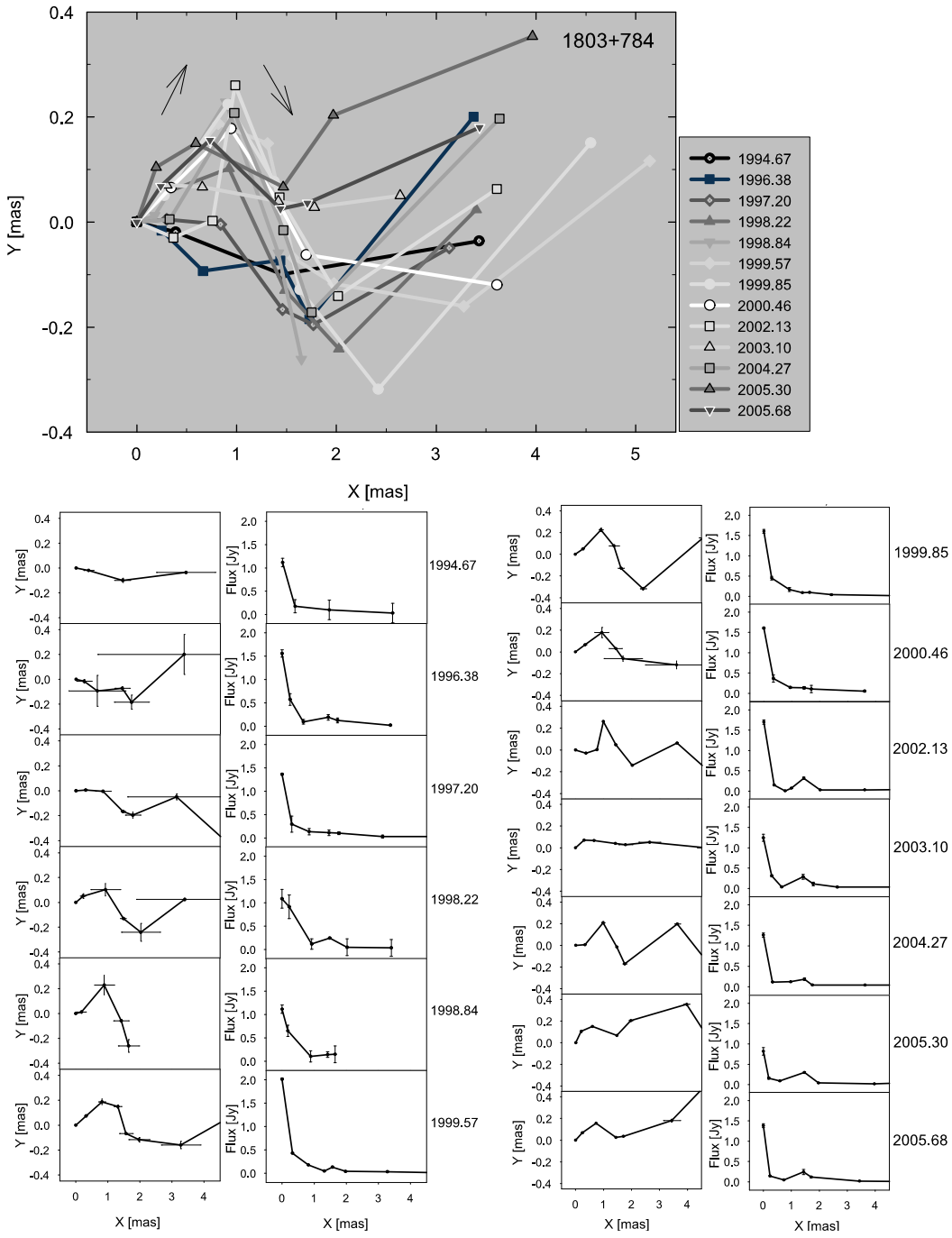

Figure 3.13: The jet ridge line (see text for details) is shown for all components detected from 15 GHz observations within 6 mas of core separation in (a). The shape of the ridge line changes from epoch to epoch. This is shown in detail in (b) and (c). The left hand side panels show the evolution in x- and y-coordinates. The right hand panels show the flux density along the jet.

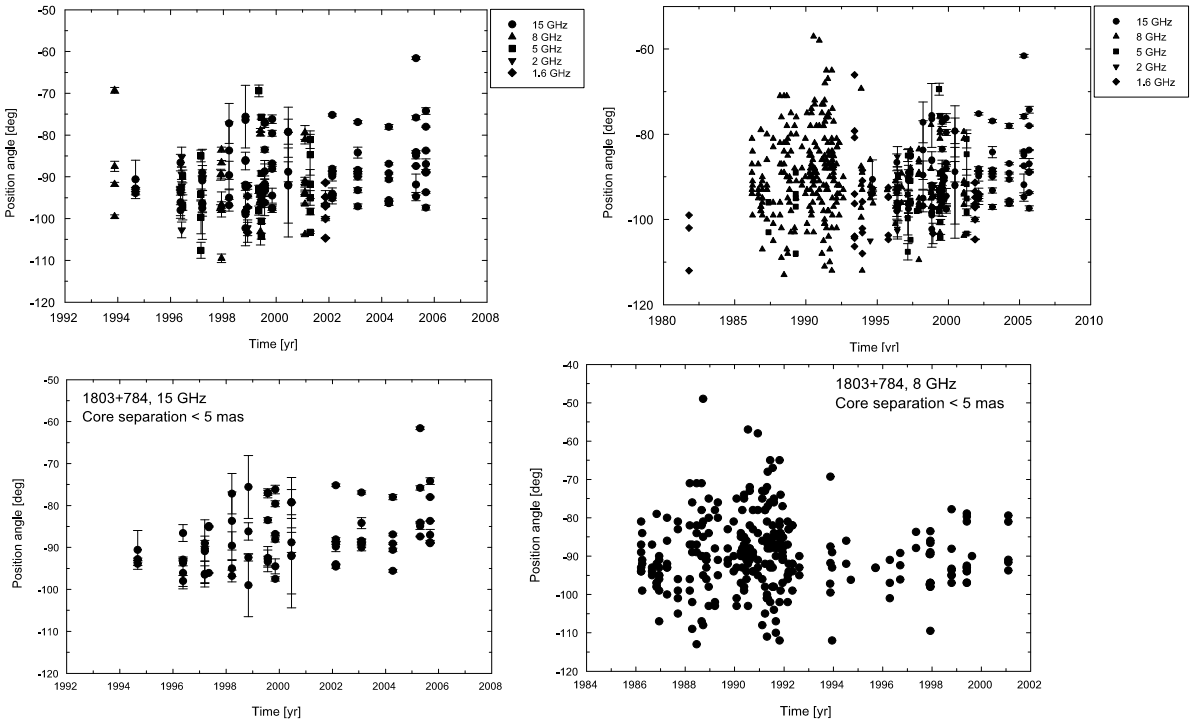

Figure 3.14: Position angle distribution along the jet of the individual epochs as function of frequency: (a) shows the data of this paper. (b) shows all data. Components within a core separation of 5 mas only at 15 GHz and 8 GHz are shown in panels (c) and (d), respectively.

3.8 Summary: kinematic results

Before we describe the periodicities and correlations found in S5 1803+784, we give a brief summary of the results of the kinematic analysis. In Britzen et al. (2005a) we presented an identification scenario for pc-scale jet component motion in S5 1803+784 based on the assumption that the most prominent jet component is the brightest component seen in every observing epoch. The most plausible identification scenario resulting from this assumption was the one presented in the paper: the coexistence of several superluminally moving and one *oscillating* component.

The data presented in this paper cover a broader range in frequency and time. Thus, a more detailed investigation of the jet component motion is possible. In addition, we collected kinematic information from the literature and tested our hypothesis against these data. In total, 94 data sets have been investigated.

- Based on a kinematic analysis of altogether 94 VLBI observations performed at frequencies between 15 and 1.6 GHz we find evidence for a rather constant core separation with time for all jet components – besides one – in the pc-scale jet of S5 1803+784 (see Fig. 3.5).
- Whereas the core separations of the individual jet components remain more or less the same, the position angles change significantly (see Fig. 3.11).
- One component (**B3**) is observed to move with apparent superluminal speed of $\sim 19 \pm 4c$ (see Figs. 3.5 (a) and 3.9).
- A significant evolution of the mean jet ridge line with time with a likely period of ∼8.5 years is observed (see Fig. 3.13). This finding is independent of any component identification.
- The width of the jet changes periodically with a period of ∼8–9 years (see Fig. 3.14).
- The timescale of the maximum changes in the position angle correlate well with maxima in the total flux -density observed within the Michigan monitoring programme (see Figs. 3.21 and 3.22).
- We find convincing correlations between parameters such as the flux-density, core separation, position angle, and describe them below.

3.9 Opacity of 1803+784

In order to check our model of S5 1803+784 jet, where during more than 20 years of observations only one fast jet component B3 was observed, we investigated in details the opacity and spectra evolution of the total flux density light curves. Emergence of a new jet component, according to the shock-in-jet model (e.g. Marscher 1996; Gomez et al. 1997) is caused by a shock induced by a primary excitation at the base of the jet, which is manifest in radio light curves as an outburst that is delayed at lower frequencies due to the combined effects of the frequency stratification of the emitting electrons, non-zero opacity and light-travel delays. Such time-delayed outbursts are associated observationally on milliarcsecond scales with brightening of the VLBI core and accompanied by the ejection of a new optically thin jet component.

In order to investigate the individual outbursts of the source as well as to calculate the frequency-dependent time delays we decomposed the total flux density light curves at 4.8 GHz, 8 GHz and 14.5 GHz from UMRAO monitoring campaign (Aller et al. 1999, 2003) of S5 1803+784 into Gaussian components, as was described in Pyatunina et al. 2006, 2007. Figure 3.15 shows the light curve of S5 1803+784 at 14.5 GHz and the Gaussian decomposition of it. There are three prominent outbursts in 1985 (A) and 1988 (B), after which a very prolong outburst starts in about 1992 and ends in 2005 with a peak in 1997 (C). The Gaussian parameters, fitted into the light curve are shown in Table 3.7. We calculated frequency-dependent time delays for each flare as the time difference between the Gaussian peaks at each frequency with respect to the position of the peak at 14.5 GHz. Time delays for different outbursts as functions of frequency are shown in Fig. 3.16. Flares A and B show moderate time delays of 0.3 years, whereas the prolonged flare C shows an enormous time delay of 3.2 years between 4.8 GHz and 14.5 GHz, which is an indication of a high opacity in the source during outburst C. We calculated quasi-simultaneous spectra, using the measurements at all three frequencies with a time separation less than two weeks and fitted a power law in each spectra. Figure 3.17 shows the spectral evolution. The behavior changes significantly after $\sim$1996, when the spectra are flat and then gradually become steeper. The beginning of a bright, prolong flare C is accompanied by the significant spectral changes which can be caused by evolution of outburst C. High frequency-dependent time delays of the C flare indicate a high opacity of the source. The flat spectrum which becomes gradually steep can be explained with the jet component ejection, which we

actually see in VLBI observations of S5 1803+784 (B3). Moreover, small frequency-dependent time delays and steep spectra of other observed flares of the source suggest that there probably were no jet component's ejections before 1995 which is in good agreement with our model of S5 1803+784 jet.

Outburst C shows a very broad profile at all frequencies ($\Theta \sim 8$ yr). Similar broad outbursts were observed for the source 1308+326 in Pyatunina et al. 2007. The authors mentioned that such a broad outburst can be associated with the development of a dense region, some kind of "cocoon" that confines the innermost part of the jet that is excited by the primary perturbation.

Table 3.7: S5 1803+784: Parameters of outbursts

Comp.	Freq. GHz	Amplitude Jy	T_{max} yr	Θ yr	Time delay yr
A	8.0	1.94 ± 0.02	1985.19 ± 0.02	1.41 ± 0.02	0.00 ± 0.02
A	4.8	0.77 ± 0.04	1985.39 ± 0.04	1.41 ± 0.04	0.20 ± 0.06
B	14.5	2.01 ± 0.01	1988.93 ± 0.01	2.63 ± 0.01	0.00 ± 0.01
B	8.0	2.15 ± 0.02	1988.86 ± 0.01	4.07 ± 0.02	-0.07 ± 0.02
B	4.8	1.25 ± 0.01	1989.19 ± 0.01	2.54 ± 0.01	0.26 ± 0.02
C	14.5	1.46 ± 0.01	1996.94 ± 0.02	9.83 ± 0.03	0.00 ± 0.02
C	8.0	1.57 ± 0.02	1998.34 ± 0.04	7.89 ± 0.04	1.40 ± 0.06
C	4.8	0.93 ± 0.01	2000.13 ± 0.04	6.28 ± 0.05	3.20 ± 0.06

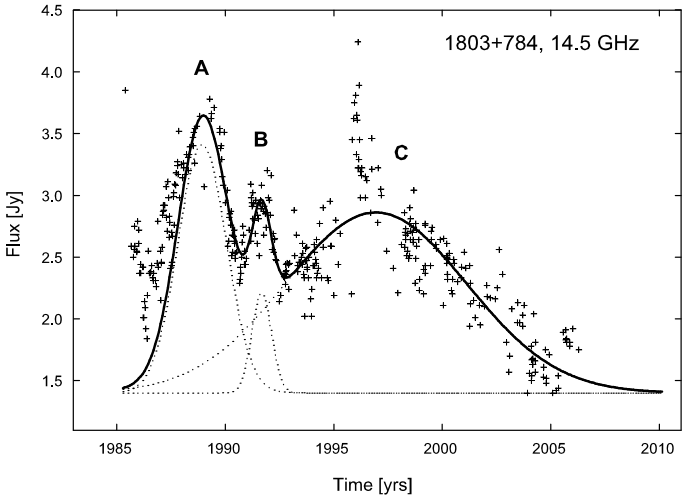

Figure 3.15: S5 1803+784: Gaussian decomposition of the light curve at 14.5 GHz. Solid line shows the sum of the Gaussian functions and dotted lines show individual Gaussian functions. Letters indicate the names of the flares.

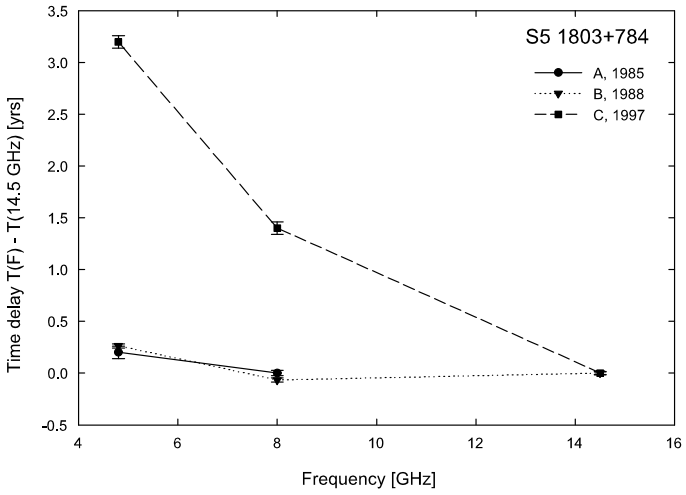

Figure 3.16: S5 1803+784: Time lags of individual outbursts as functions of frequency.

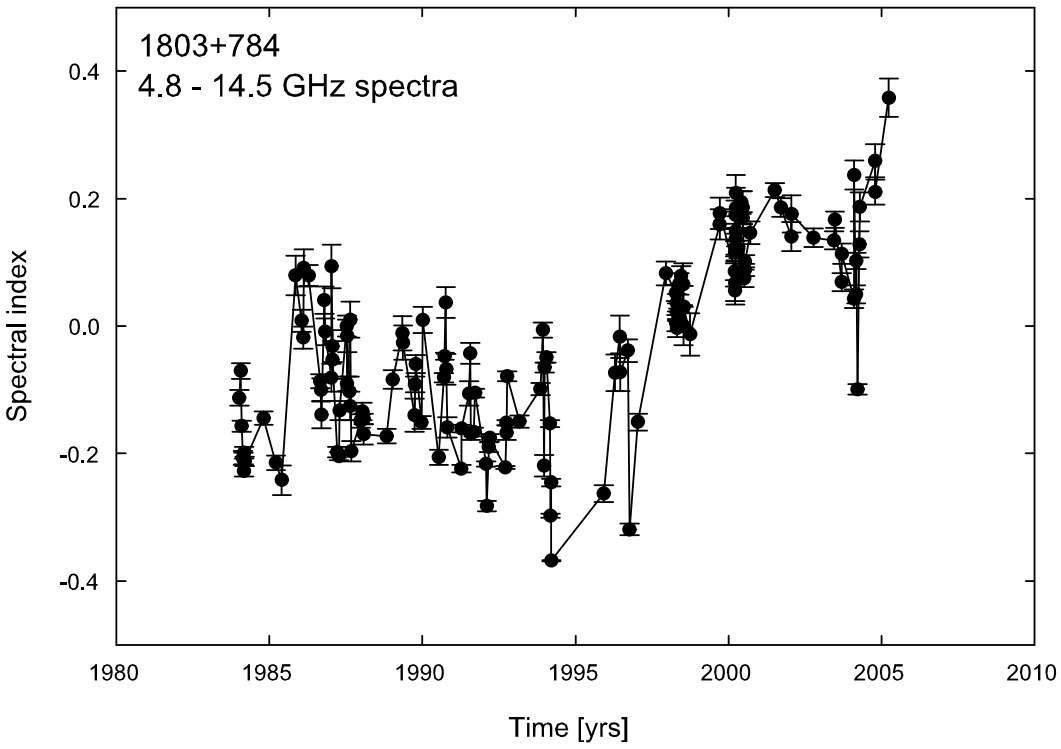

Figure 3.17: [S5 1803+784: spectral evolution]S5 1803+784: Time evolution of the quasi-simultaneous spectra indices, calculated for the 4.8 GHz, 8 GHz, and 14.5 GHz frequencies.

3.10 Correlations & Anti correlations

As shown in previous sections, the jet width changes with time and the mean jet ridge line of S5 1803+784 reveals an evolution with a characteristic time scale of $\sim$ 8.5 yrs. Both facts could result from a geometric origin, such as jet precession. This would also produce a correlation between the core separation, the position angle, and the flux-density changes for each jet component. In addition, the motion and the flux-density evolution of different components would be correlated. If the trajectories of the jet components are caused by the jet precession, we can also expect that the motion of the stationary jet components will be correlated with the total flux-density variability, since the total flux-density variability in this case will be caused mostly by the changes of the Doppler factor.

To investigate this, we performed a visual analysis of the changes of the position angle and the maxima and minima in the variations of the core separation, the position angle, and the flux of each component at 8 and 15 GHz. Maxima and minima at 8 GHz are listed in Table 3.8. Major changes in the variations of the jet parameters at 8 GHz occurred in 1987, 1988.5, 1990 and 1991 for **C0**, **C1**, **Ca** and the core. The core-flux reached a maximum in 1987, accompanied by minima in flux, position angle, and core separation of **C1**, maxima of the core separation of **C0** and maxima for flux and position angle of **Ca**. In 1988.5, the values that were maximal became minimal and vice versa and switched again in 1990 and 1991. This indicates that changes in flux, position angle and core separation of the components and the core-flux are correlated and change with characteristic time scales of a few years. The same behavior was found as well at 15 GHz (Table 3.9). The 15 GHz data were obtained at another time. The major changes in core separation, position angle, and flux variations of the inner components occurred in 1998 and 2000.

To investigate this more carefully, we calculated the discrete cross-correlation functions (Edelson & Krolik 1988) as well as the z-transformed correlation functions (Alexander 1997) for the pairs of parameters (such as core separation, flux density, position angle) for each of the components (**C0**, **C1**, **Ca**, **C2**, **C4**) at 8 GHz. Component **C2** at 15 GHz is possibly comprised of 3 components at 8 GHz. We call these three **C2** components at 8 GHz $\mathbf{C2}_1$, $\mathbf{C2}_2$, and $\mathbf{C2}_3$. We find the following results:

Table 3.8: Correlation between flux density, position angle and core separation during the epochs 1987, 1988.5, 1990, and 1991 at 8 GHz. Results of the visual inspection.

Time	**1987**			**1988.5**			**1990**			**1991**		
Comp. ID	Flux	P.A.	Core sep.	Flux	P.A.	Core sep.	Flux	P.A.	Core sep.	Flux	P.A.	Core sep.
Core	max			min			max			min		
C0			max			min			max	min		min
C1	min	min	min	max	max	max	min	min	min	max	max	max
Ca	max	max	min	min	min	max	max	max	min			

Table 3.9: Correlation between the flux density, the position angle and the core separation during the epochs 1998 and 2000 at 15 GHz. Results of the visual inspection.

Time	**1998**			**2000**		
Comp. ID	Flux	P.A.	Core sep.	Flux	P.A.	Core sep.
Core	min			max		
C0	max	max	min			
C1				max	max	max
Ca	max	min	max	min	max	min

3.10.1 Correlation between core separation, position angle and the flux for each particular jet component:

For the brightest jet components **Ca** and **C1** all the parameters, such as the core separation, the flux density and the position angle are correlated at 8 GHz. As an example, we show in Fig. 3.23 the variation of the core separation, the position angle, and the flux density of the component **C1** in the time between 1984 and 1996. Fig. 3.18 (Left) shows an example of the calculated correlated function for the jet component **C1** position angle and core separation. Correlation between position angle and core separation of the jet component **C1** is the most convincing case. It is clearly seen from the figure, that the position angle and the core separation of this jet component are well correlated with a correlation coefficient reaching the value of 0.5. Table 3.10 (second section) shows the results of the cross-correlation analysis

at 8 GHz. The table lists the frequency of the observations, the jet component, first and second parameters for which the cross-correlation function was calculated (such as position angle, core separation and the flux), correlation coefficient and the time lag. The last two columns show Pearson's correlation coefficient, and the probability of getting such a Pearson's correlation by chance. Table 3.10 shows only the results for the cross-correlation analysis if the correlation coefficient was more than 0.4, which reveals positive correlation. From the table it is clearly seen that changes of the core separation, the position angle and the flux of **C1** are correlated with the correlation coefficients from 0.4 to 0.6. The core separation and the position angle and the core separation and the flux of **Ca** are anti-correlated, whereas the flux and position angle are correlated with high correlation coefficients (from 0.4 to 0.7).

In the case of the 15 GHz data, the VLBI data at this frequency are too sparse to calculate the discrete correlation function. Therefore, we performed a similar analysis using the Pearson's correlation coefficients. Table 3.10 (Third section) shows the results of the Pearson's correlation analysis for the jet component for which we found a correlation coefficient more than 0.4. Similarly to 8 GHz, the core separation and the position angle and the core separation and the flux of the jet component **C1** are correlated with the Pearson's correlation coefficient of 0.4 – 0.5. For the jet component **Ca**, the core separation and the position angle are anti-correlated similarly to 8 GHz. The core separation, the position angle and the flux of the jet components **C0**, **C2**, and **C4** are showing high Pearson's correlation coefficients. However, it is worth to notice, that the Pearson's correlation coefficients are less reliable than the discrete correlation function.

3.10.2 Correlations between the core flux and the core separation, position angle and the flux for each particular jet component:

If the jet is precessing, we expect that the core flux will change due to a change of the Doppler factor when the viewing angle changes between the jet and the line of sight. The flux of the jet component will also change due to similar reasons in this case and we can expect that the core flux and the brightness of the jet component will be correlated. As we mentioned before, we found that flux of the inner jet components are correlated with their core

separation and position angle. Because of that we can expect that the core flux might be correlated not only with the fluxes of the jet components, but also with their core separation and position angle. Therefore, we performed a cross-correlation analysis for the core flux variability and flux, core separation and position angle changes.

The analysis has shown that the core flux is correlated with the core separation and the position angle changes of all inner jet components **C0**, **C1**, **Ca**, $\mathbf{C2}_1$, $\mathbf{C2}_2$ and $\mathbf{C2}_3$ at 8 GHz with the correlation coefficients from 0.5 to 0.9. The core flux is correlated with the flux of only one jet component **Ca**, which is the brightest component in the S5 1803+784 jet. Table 3.11 (Second section) lists the frequency of the VLBI observations, the first (in this case it is the core) and the second jet components which were used for cross-correlation analysis, correlated variability those parameters that were checked (such as core separation, position angle of flux), correlation coefficient of the discrete correlation function and time lag. The last two columns show the Pearson's correlation coefficient and the probability of getting such a Pearson's correlation by chance. It is clearly seen from the table that the core flux is correlated with the core separation and the position angle changes of the jet components **C0**, **C1**, **Ca**, $\mathbf{C2}_1$, $\mathbf{C2}_2$ and $\mathbf{C2}_3$. Figure 3.18 (Right) shows as an example the discrete autocorrelation function, calculated for the core flux and the flux-density changes of the jet component **Ca**, where it is clearly seen that they are correlated with a correlation coefficient of 0.59 ± 0.06.

We have also checked for correlations between the core flux and the parameters of the jet components (such as core separation, position angle and flux) at 15 GHz using the Pearson's correlation coefficients. Table 3.11 (Third section) shows the result of this analysis. We found that the core flux and the core separation of the jet components **C0**, **Ca**, and **C2** are correlated, as well as the core flux and the position angles of the components **Ca** and **C4**, which is similar to the results at 8 GHz. Figure 3.20 shows as an example the core separation versus the position angle of the brightest jet component **Ca**. It is clearly seen from the figure that these two parameters of **Ca** are correlated.

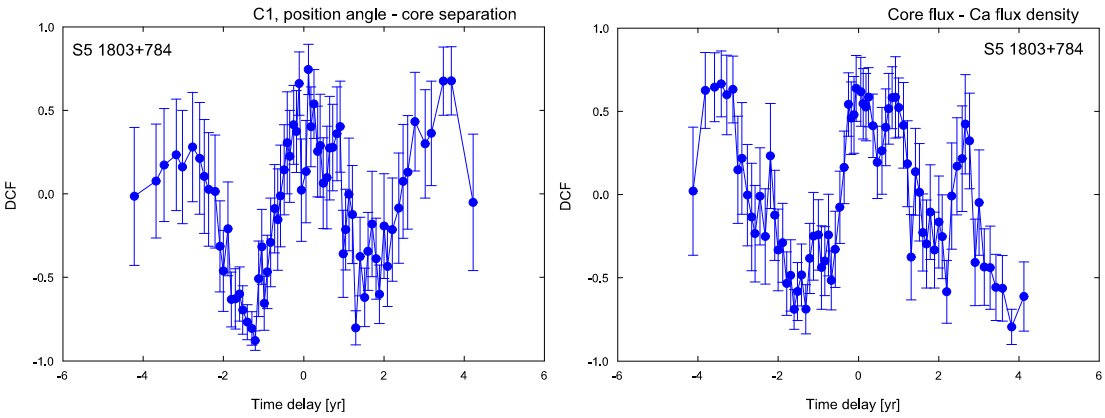

Figure 3.18: S5 1803+784: (*Left*) Discrete autocorrelation function, calculated for the position angle and the core separation changes of the jet component C1. (*Right*) Discrete autocorrelation function, calculated for the core flux and the flux-density changes of the jet component Ca.

3.10.3 Correlation between the core separation, position angle and the flux for different jet components:

We found that the jet of S5 1803+784 consists of several oscillating jet components. On the other hand, the evolution of the jet ridge line and the position angle spread suggests that the jet might be precessing. In case of the jet precession, the stationary VLBI components in the jet should follow similar trajectories, which can be delayed to each other since the stationary jet components are located at different positions in the jet and we can expect correlated motion of different jet components. Therefore we searched for correlated changes of the core separation, the position angle and the fluxes of different jet components. We cross-correlated the core separation of each VLBI component with the core separation of other jet components, as well as the position angles and the fluxes.

We find evidence for correlated motion of different jet components at 8 GHz. Table 3.11 (First section) shows the results of the discrete correlation function calculation. The core separation of the inner jet components are correlated. The core separation of the jet component **Ca** is correlated with the core separation of the components **C0**, **C1**, $C2_1$, and $C2_3$. The core separation of **C1** is correlated with the core separation of **Ca**, $C2_1$, $C2_2$, and

Table 3.10: Cross-correlation function results and results of the Pearson's correlation coefficient calculation, calculated for various jet parameters and the total flux-density variability. ν is the frequency of the analyzed data set, Comp. ID identifies the individual components, Par. 1 and Par. 2 give the parameters used for the correlation and cross-correlation, DCF peak is the peak of the discrete correlation function, τ is a time-lag in years, Corr. coeff. is the value of the Pearson's correlation coefficient, and p - the probability of getting such a correlation by chance.

ν [GHz]	Comp. ID	Par. 1	Par. 2	DCF peak	τ	Corr. coeff.	p
8	Ca	core sep.	total flux 8 GHz	-0.68 ± 0.06	-1.12 ± 0.05		
		p.a.	total flux 8 GHz	-0.77 ± 0.04	0.72 ± 0.06		
	$C2_1$	core sep.	total flux 8 GHz	0.56 ± 0.06	-0.07 ± 0.08		
	$C2_3$	p.a.	total flux 8 GHz	0.60 ± 0.07	-0.15 ± 0.08		
	C1	core sep.	total flux 14.5 GHz	0.41 ± 0.07	-0.07 ± 0.04		
		p.a.	total flux 14.5 GHz	0.61 ± 0.05	0.06 ± 0.06		
8	C1	p.a.	core sep.	0.54 ± 0.09	0.20 ± 0.05		
		p.a.	flux	0.53 ± 0.08	-0.08 ± 0.04		
		core sep.	flux	0.41 ± 0.06	-0.58 ± 0.06		
	Ca	p.a.	core sep.	-0.59 ± 0.06	-0.59 ± 0.05		
		p.a.	flux	0.42 ± 0.06	-0.56 ± 0.06		
		core sep.	flux	-0.64 ± 0.06	-0.03 ± 0.04		
	$C2_1$	p.a.	core sep.	-0.53 ± 0.09	0.31 ± 0.08		
	$C2_2$	p.a.	core sep.	-0.61 ± 0.08	-0.42 ± 0.04		
	C4	p.a.	core sep.	0.97 ± 0.10	0.09 ± 0.03		
15	C0	p.a.	core sep.			-0.44 ± 0.09	0.131
		core sep.	flux			-0.52 ± 0.08	0.067
	C1	p.a.	core sep.			0.40 ± 0.10	0.198
		core sep.	flux			0.46 ± 0.09	0.164
	Ca	p.a.	core sep.			-0.73 ± 0.05	0.008
		core sep.	flux			0.57 ± 0.07	0.054
	C2	core sep.	flux			-0.83 ± 0.03	0.002
	C4	p.a.	core sep.			0.58 ± 0.07	0.064
		p.a.	flux			-0.51 ± 0.08	0.107

$C2_3$. The position angles are less correlated, for example the position angles of the jet component **C1** are correlated with the position angles of the jet components **Ca**, $C2_1$, $C2_2$, and $C2_3$ with the correlation coefficients of 0.5 - 0.96.

When cross-correlating core separation changes of **Ca** and core separations of other components in the case of a significant correlation (e.g., **C0**, **C1**, $\mathbf{C2}_1$ and $\mathbf{C2}_3$), the time lags, where the peaks of the discrete correlation function appear, are changing gradually with distance from the core of these components. Fig. 3.19 shows the changes of time lags with core separation fitted with a linear regression. The core separation was calculated as the mean distance from the core of **C0**, **C1**, $\mathbf{C2}_1$ and $\mathbf{C2}_3$. The time lags increase linearly with core separation.

The same effect is found for the cross-correlation between the core sepa-

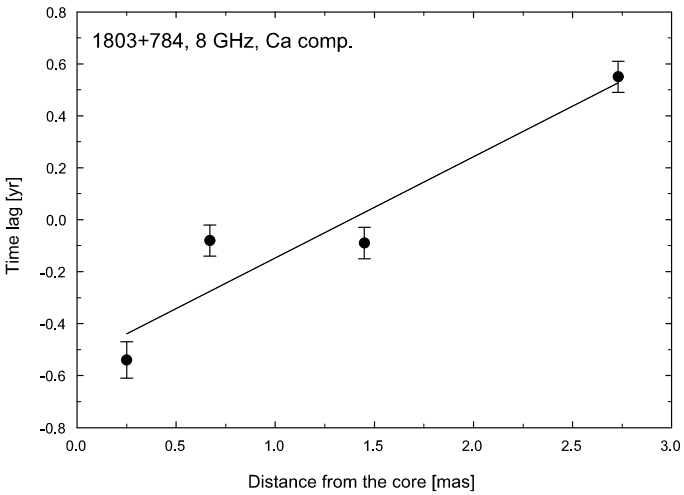

Figure 3.19: Time lag of the cross-correlation function as a function of distance from the core. The time lag of the cross-correlation function was calculated for the core separation of the component **Ca** and the core separations of the components **C0**, **C1**, $\mathbf{C2}_1$ and $\mathbf{C2}_3$. The distance from the core was obtained as a mean value of the positions of the components **C0**, **C1**, $\mathbf{C2}_1$ and $\mathbf{C2}_3$. The line shows the linear regression, fitted to the data points. The time lag increases with the distance from the core.

ration changes of **C1** and **Ca**, $\mathbf{C2}_1$, $\mathbf{C2}_2$, and $\mathbf{C2}_3$. This can be explained if we assume that the motion of the components is mostly due to a geometrical origin. The components are following almost the same trajectories, but with a certain time delay. The components are connected with each other and the information is spreading with a proper motion of about 2.3 mas/yr if the reference point is the component **Ca** and 0.79 mas/yr if the reference point is the **C1** component. This corresponds to extremely fast speeds of $53c$ and $18.2c$ correspondingly.

It is worth to notice, that since the Gaussian modelfitting method connects the positions of all jet components with the core position and the core is assumed to be stationary, such correlated behavior of the jet component motions can be due to core motion. However, the amplitude of the core separation changes and the position angle changes are different for different components and the correlation can not only be explained by the core motion.

We also checked for correlations between the core separations, the po-

sition angles and the fluxes of different jet components at 15 GHz using Pearson's correlation analysis. Table 3.11 (Fourth section) shows the results of the study. We found that the position angles and the fluxes of the pair of jet components **Ca**–**C2** and **Ca**–**C1** are correlated with the correlation coefficients from 0.5 to 0.9. The core separations of **Ca** and **C2** and the position angles of **C2** and **C0** are also correlated. Figure 3.20 (Right) shows as an example the flux-density of **C1** versus the flux-density of **Ca**. It is clearly seen from the figure that the fluxes of these jet components are clearly correlated.

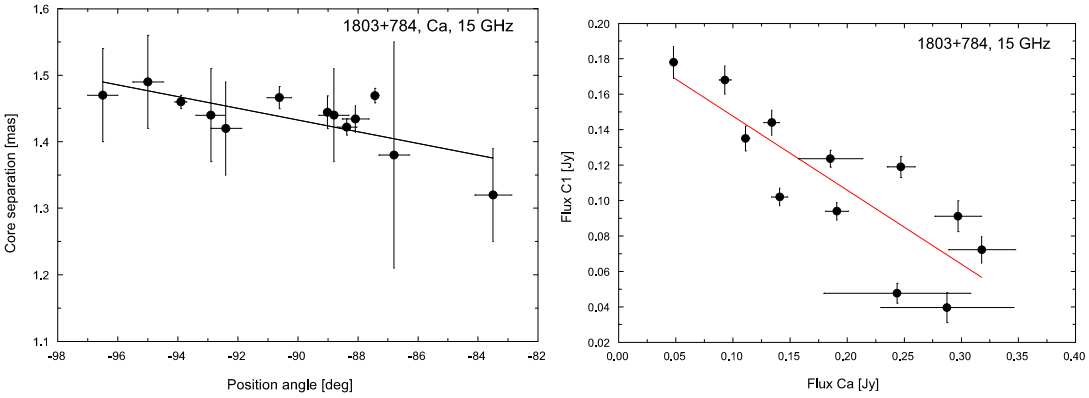

Figure 3.20: (a) Core separation of the brightest component **Ca** at 15 GHz as function of the position angle. (b) Flux of components **C1** against flux of **Ca** for the different epochs.

3.10.4 Correlation between the core separation, position angle and the total flux-density variability:

If the jet of S5 1803+784 is precessing, than we can expect that due to changes of the Doppler factor, the total flux-density variability will change and might be correlated with the core separation, the position angle and the fluxes of the VLBI components of S5 1803+784. We investigated possible correlations between the jet component parameters and the total flux-density variability. For this purpose we used the data of the AGN monitoring of the University of Michigan Radio Observatory (UMRAO data, Aller et al. 1999, 2003), spanning almost 30 years for S5 1803+784 (see Fig. 3.22). We selected

the same data range (1986 – 1994) as the VLBI data are covering and the same frequency of 8 GHz. Table 3.10 (First section) shows the results of the correlation analysis at 8 GHz.

We find:

- the core separation changes of **Ca** and $\mathbf{C2}_1$ are correlated with the total flux-density variability (see Table 3.10 for the details) with correlation coefficients from 0.6 to 0.7.
- position angle changes of **Ca** and $\mathbf{C2}_3$ are correlated with the total flux-density changes with correlation coefficients of about 0.6.
- the core separation and the position angle changes of **C1** are correlated with the total flux density at 14.5 GHz (see Fig. 3.23), but do not show any correlation at 8 GHz.

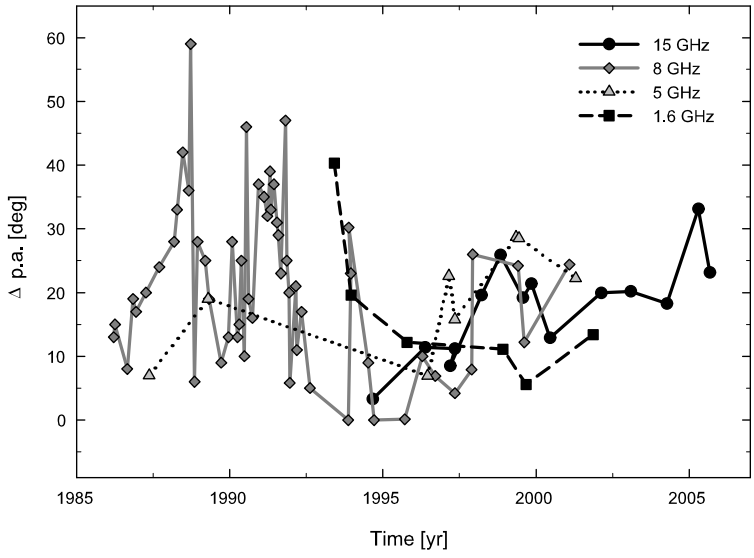

Figure 3.21: The spread in the position angle (see text for a more detailed description) with time is shown for four different frequencies based on all the data (this paper + literature). We clearly find several maxima that are correlated with the maxima found in the total flux-density data.

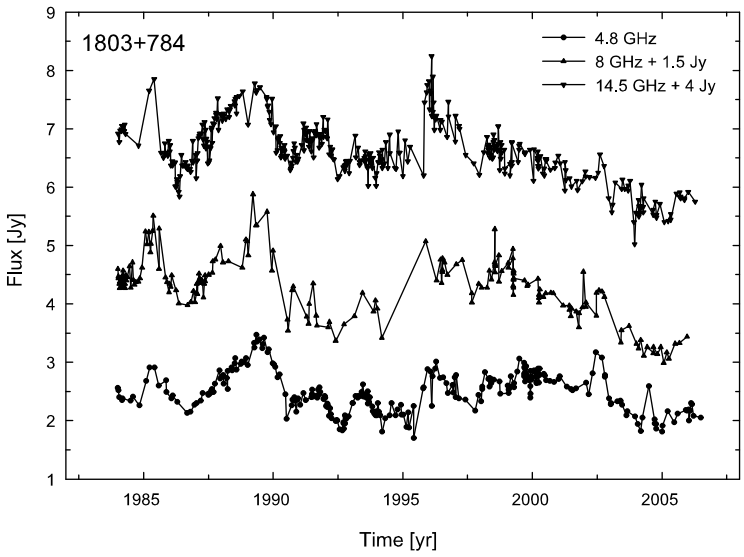

Figure 3.22: Total single-dish flux-density light-curve for S5 1803+784 at 4.8, 8 and 14.5 GHz. The 8 and 14.5 GHz light curves are shifted by 1.5 and 4 Jy accordingly in order to see the details better. All the data are from the UMRAO monitoring campaign.

Table 3.11: Cross-correlation function results, calculated for various jet parameters of the inner jet components at 8 GHz and results of the Pearson's correlation coefficient calculation. ν is the frequency of the analyzed data set, Comp. ID 1 & 2 identify the individual components, Par. is the parameter used for calculating the correlation function, DCF peak is the peak of the discrete correlation function, τ is a time-lag in years, Corr. coeff. is the value of the Pearson's correlation coefficient, and p - the probability of getting such a correlation by chance.

ν [GHz]	Comp. ID 1	Comp. ID 2	Par.	DCF peak	τ	Corr. coeff.	p
8	C0	Ca	core sep.	-0.48 ± 0.12	0.54 ± 0.07		
	C0	$C2_1$	p.a.	-0.49 ± 0.14	-0.32 ± 0.06		
	C0	$C2_3$	p.a.	0.69 ± 0.18	0.14 ± 0.08		
	C1	Ca	core sep.	0.47 ± 0.06	0.08 ± 0.06		
			p.a.	-0.48 ± 0.07	0.48 ± 0.07		
	C1	$C2_1$	core sep.	-0.59 ± 0.09	-0.80 ± 0.09		
			p.a.	-0.45 ± 0.09	-0.29 ± 0.09		
	C1	$C2_2$	core sep.	0.53 ± 0.14	-0.02 ± 0.06		
			p.a.	0.96 ± 0.03	-0.02 ± 0.02		
	C1	$C2_3$	core sep.	0.83 ± 0.06	0.81 ± 0.02		
			p.a.	0.72 ± 0.09	-0.06 ± 0.06		
	Ca	$C2_1$	core sep.	-0.48 ± 0.09	-0.09 ± 0.06		
	Ca	$C2_3$	core sep.	0.62 ± 0.09	0.55 ± 0.06		
			p.a.	-0.61 ± 0.07	0.49 ± 0.08		
	$C2_1$	$C2_2$	p.a.	-0.53 ± 0.08	0.42 ± 0.05		
	$C2_1$	$C2_3$	core sep.	0.62 ± 0.09	-0.42 ± 0.06		
			p.a.	-0.78 ± 0.09	0.17 ± 0.02		
	$C2_2$	$C2_3$	p.a.	0.79 ± 0.05	-0.21 ± 0.05		
8	Core	C0	core sep.	0.62 ± 0.09	-0.23 ± 0.07		
			p.a.	0.77 ± 0.10	-0.09 ± 0.05		
	Core	C1	core sep.	-0.47 ± 0.07	0.35 ± 0.08		
			p.a.	-0.45 ± 0.07	-0.31 ± 0.04		
	Core	Ca	flux	0.59 ± 0.06	0.49 ± 0.10		
			core sep.	-0.91 ± 0.04	0.23 ± 0.03		
			p.a.	-0.83 ± 0.04	-0.92 ± 0.04		
	Core	$C2_1$	core sep.	0.64 ± 0.07	0.02 ± 0.05		
	Core	$C2_2$	p.a.	-0.47 ± 0.08	-0.29 ± 0.05		
	Core	$C2_3$	core sep.	0.77 ± 0.05	-0.36 ± 0.04		
			p.a.	0.54 ± 0.08	0.37 ± 0.10		
15	Core	C0	core sep.			0.65 ± 0.05	0.021
	Core	Ca	core sep.			-0.72 ± 0.05	0.008
			p.a.			0.49 ± 0.09	0.146
	Core	C2	core sep.			-0.49 ± 0.08	0.124
	Core	C4	p.a.			-0.56 ± 0.08	0.074
15	C0	C2	p.a.			0.77 ± 0.04	0.006
	C1	Ca	flux			-0.84 ± 0.03	0.001
			p.a.			-0.67 ± 0.06	0.025
	Ca	C2	flux			-0.60 ± 0.07	0.051
			core sep.			0.69 ± 0.06	0.019
			p.a.			0.54 ± 0.08	0.084

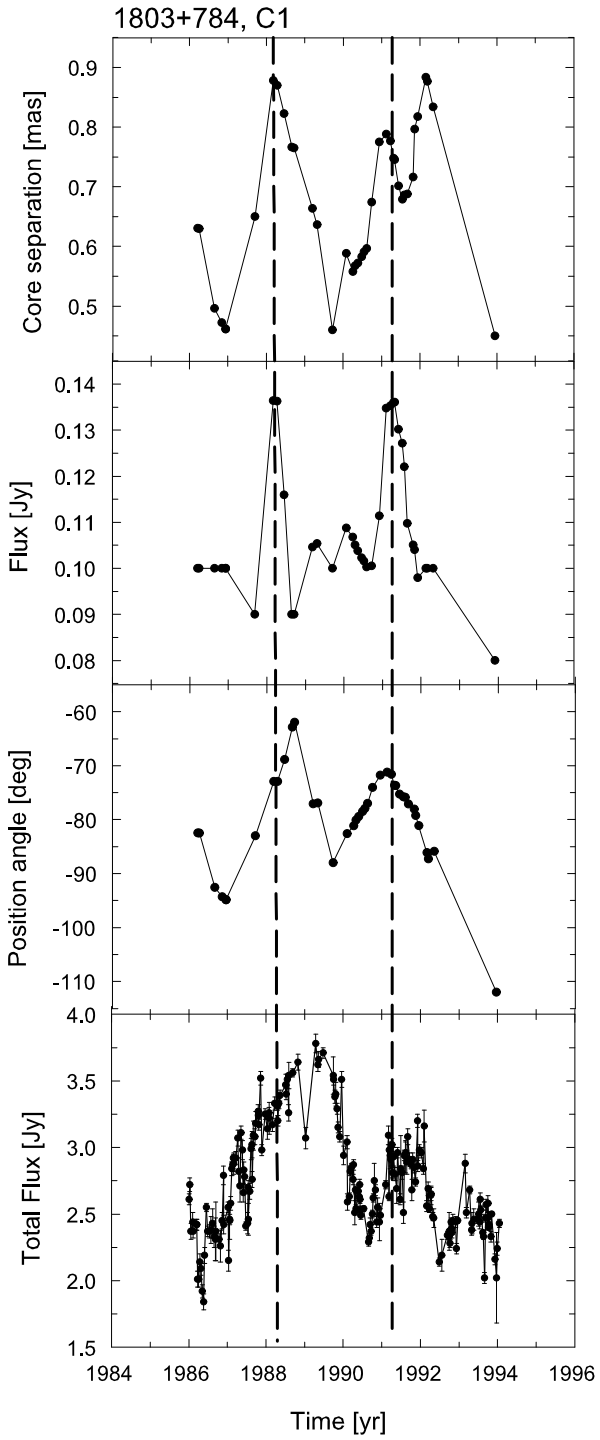

Figure 3.23: Core separation, flux density, position angle of component **C1**, and total flux-density light curve at 8 GHz in the period 1984–1996. The two dashed lines indicate the nearly simultaneous peaks in all four plots.

3.11 Periodicity analysis

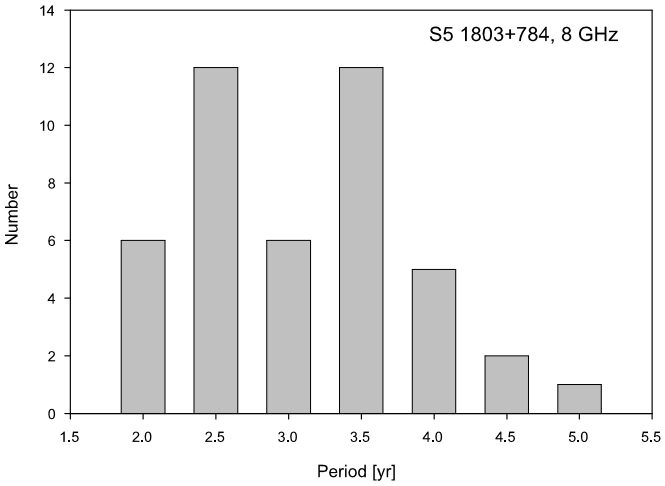

Figure 3.24: Results of the periodicity analysis: histogram, showing the number of periods found for the core separation, the position angle and the flux of all inner jet components in different ranges of periods. It is clearly seen that most of the periods are in the ranges from 2 to 2.5 years and from 3 to 3.5 years.

If the jet of S5 1803+784 is precessing, we can expect to see the periodical changes of the core separation, the position angles of the stationary jet components with a period, which will be equal to the jet precession period. We can also expect periodical changes of the fluxes of these components due to changes of the Doppler factor. We can detect this periodical changes if the jet precession period is shorter than the time duration of observations. Since, the historical VLBI observations span more than 20 years, we can use standard methods of the time series analysis for the VLBI data.

For the time series analysis of the changes of the core separation, the position angle, and the flux-density of the jet components we used three different methods, the date-compensated discrete fourier transform, the discrete autocorrelation function, and the Jurkevich method. The Date-Compensated Discrete Fourier Transform (DCDFT) method (Ferraz-Mello 1981) was created in order to avoid the problem of finitness of the Fourier transform and allows to calculate the periods of unevenly sampled data with better precision. The method is based on the estimation of the power spectrum by means of

least-square fitting of a sinusoid with different frequencies to the data set. In the case of a periodic process, formed by several waves, the DCDFT method allows to filter the time series with a known frequency and to find additional harmonics. The Discrete auto-correlation method and Jurkevich method are explained in chapter 2.2.2.

The results of the periodicity analysis at 8 GHz for different methods are shown in Table 3.12. In this table we list the results, obtained with three different time series methods. The first two columns show the name of the jet component for which we calculated the periodograms and auto-correlation functions and for which parameter, such as the core separation, the position angle or the flux density. The third and the fourth columns show the value and amplitude of the period found with the date-compensated fourier transform method. The fifth and sixth columns show the period and the correlation coefficients found with the DACF method, whereas the seventh and the eighth column show the Jurkevich periods with the f function values. The last column shows the mean period, calculated as a mean value for all three time series methods.

For three inner jet components **C0**, **C1**, and $C2_1$ all three methods have shown similar results. The last column in Table 3.12 shows the average periods, calculated as an average value for all three methods. These average values for the last column were calculated only if the same period was detected by all three methods. For the core separation of **C0** all three methods give a value of 2.1 ± 0.3 years with the amplitude of 0.1 mas and high probability. Figure 3.25 shows the calculated periodogram (b), correlation function (c) and the Jurkevich periodogram (d) with a clear peak at 2.1 years. It is clearly seen from a Fig. 3.25 (a) that a sinusoid with a period of 2.1 ± 0.3 years and amplitude of 0.1 mas fit very well the core separation changes of the jet component **C0**.

For the core separation of the jet component **C1** all three methods give a period of 3.4 ± 0.5 years, which is different from a period found for the jet component **C0**. Fig. 3.26 shows the calculated periodograms with all three methods and it is clearly seen, that the found periodicity of 3.4 years fit very well the observed variability of the core separation of this jet component. Figures 3.29 and 3.27 show as an example the time series results for the core separation and the position angle of jet components **Ca** and **C1**.

The average periods for all jet parameters as the core separation, the position angle and the flux are 1.9 ± 0.4 and 3.5 ± 0.5 yrs (calculated for the periods found with all three methods). If we plot the number of periods in a

particular range (Fig. 3.24) we can also see that there are two maxima for the number of periods, located in the ranges of periods from 2 to 2.5 years and from 3 to 3.5 years. The most significant periods are 1.9 ± 0.4 and 3.5 ± 0.5 yrs.

The interesting fact is that the same periods of 2 and 3.4 years were found by Kelly et al. in the total flux density light curves of S5 1803+784 using wavelet transform analysis. As it was shown in the previous section, the core separation, the position angle and the flux of the jet components of S5 1803+784 are correlated with the total flux density variability. The coincidence of the periods found in the total flux-density and the changes of the core separation, the position angle and the flux of the inner jet components of S5 1803+784 can be the consequence of the correlated behavior of the total flux-density variability and structure changes and can be explained if we assume that the same mechanism is producing the characteristic time scale of the flux-density variability and jet structure evolution. The total flux-density light curves and the jet structural changes show similar periodicities. This can be explained within the jet precession scenario. In this case, the structural changes are cause by changes of the jet orientation, which actually cause Doppler factor and produce periodical modulations of the total flux-density light curves.

Table 3.12: The periodicities found with the data-compensated discrete Fourier transform in the different parameters of the jet components at 8 GHz. The component identification name, the period found in the position angle changes, the periods found in core separation changes and the period found in flux density changes are listed.

Comp. ID	Par	DCDFT P [yr]	DCDFT Ampl	DACF P [yr]	DACF peak	Jurk P [yr]	f	Mean P [yr]
core	flux							
C0	r	2.25	0.09	2.14 ± 0.11	0.43	2.00 ± 0.15	2.88	2.1 ± 0.3 (3)
C0	p.a.	–	–	–	–	2.05 ± 0.12	1.87	
c0	flux	–	–	–	–	2.15 ± 0.10	1.64	
						3.42 ± 0.15	1.81	
C1	r	3.46	0.15	3.43 ± 0.22	0.78	3.4 ± 0.3	1.56	3.4 ± 0.5 (3)
		2.26	0.06			2.7 ± 0.3	1.06	
C1	p.a.	3.05	7.72	–	–	3.55 ± 0.2	1.38	
C1	flux	3.39	0.01	–	–	3.67 ± 0.15	0.82	
		1.61	0.01					
Ca	r	2.92	0.14	3.48 ± 0.03	0.56	2.8 ± 0.3	1.35	
Ca	p.a.	1.69	1.48			2.2 ± 0.15	0.64	
		5.41	4.34	3.91 ± 0.09	0.59			
Ca	flux	4.26	0.11	–	–	2.75 ± 0.22	1.45	
$C2_1$	r	4.07	0.11	3.54 ± 0.14	0.36	3.40 ± 0.18	1.45	3.7 ± 0.3 (3)
$C2_1$		1.6	0.05	1.55 ± 0.04	0.34	1.70 ± 0.10	1.61	1.6 ± 0.1 (3)
$C2_1$	p.a.	2.01	3.95	1.73 ± 0.34	0.54	–	–	
$C2_1$	flux	–	–	–	–	2.64 ± 0.09	5.18	
						3.98 ± 0.17	2.90	
$C2_2$	r	–	–	2.32 ± 0.13	0.47	3.07 ± 0.18	4.22	
$C2_2$	p.a.	2.66	6.41	2.32 ± 0.13	0.56	3.47 ± 0.25	2.56	
$C2_2$	flux	2.04	0.01	–	–	–	–	
$C2_3$	r	3.22	0.23	3.48 ± 0.62	0.38	2.07 ± 0.12	1.07	
		1.59	0.21					
$C2_3$	p.a.	–	–	–	–	–	–	
$C2_3$	flux	–	–	–	–	–	–	
C4	r							
C4	p.a.							
C4	flux							

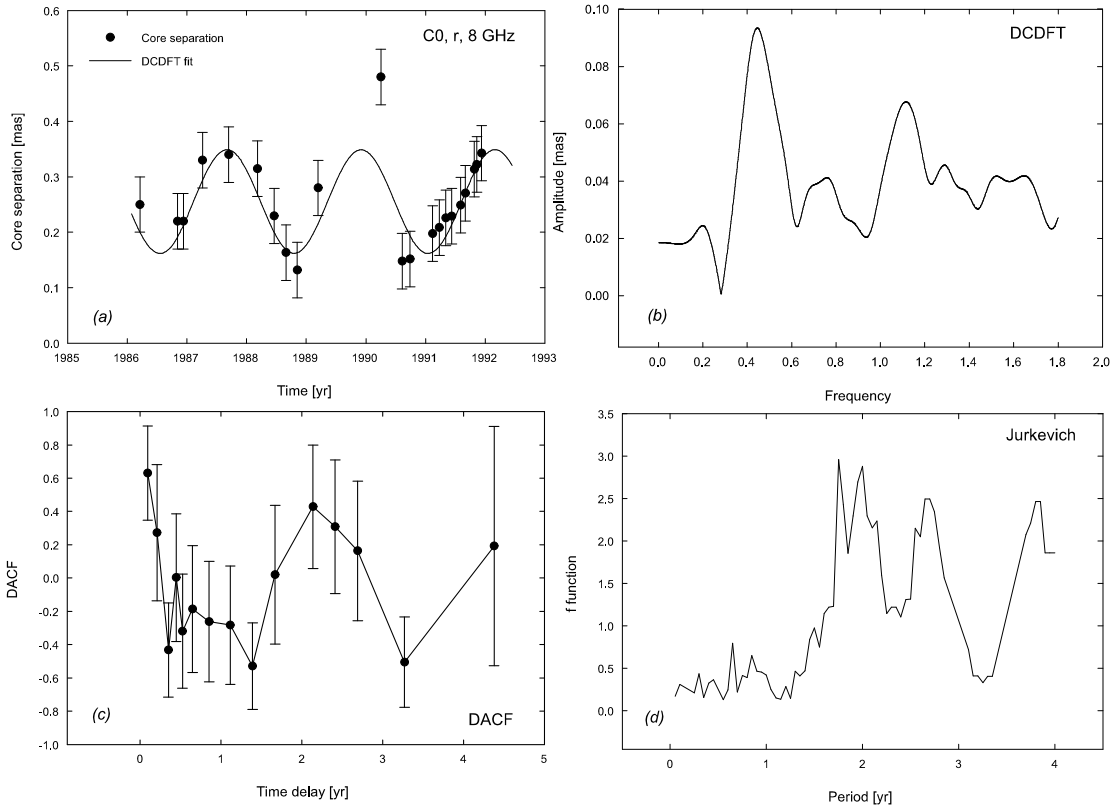

Figure 3.25: Results of the periodicity analysis for the core separation of the jet component C0 at 8 GHz. (a) shows the core separation vs. time for the jet component C0 at 8 GHz. The solid line shows the sinusoid, calculated with the DCDFT method, corresponding to a period of 2.25 years; (b) Periodogram, calculated with the DCDFT method; (c) Correlation function, obtained with the DACF method; (d) Results of the Jurkevich method, applied to the core separation of the component C0.

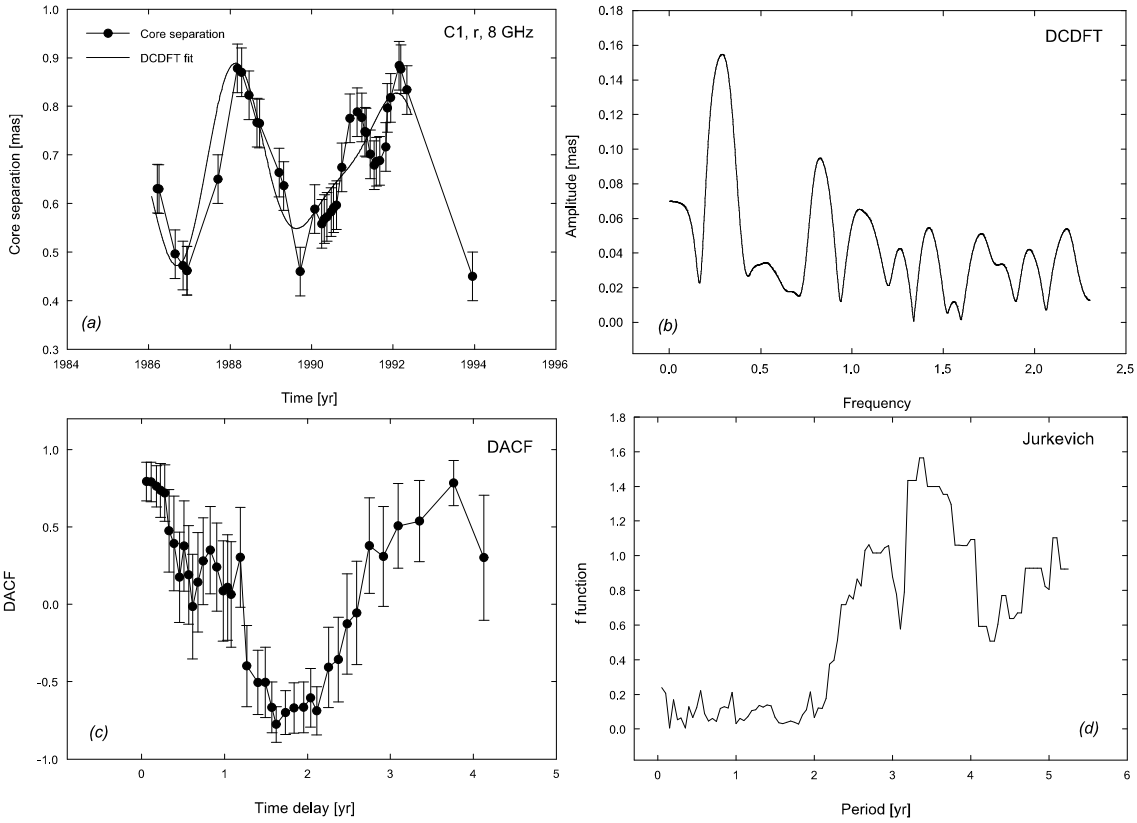

Figure 3.26: Results of the periodicity analysis for the core separation of the jet component C1 at 8 GHz. (a) shows the core separation vs. time for the jet component C1 at 8 GHz. The solid line shows the sinusoid, calculated with the DCDFT method, corresponding to two periods of 3.46 and 2.26 years; (b) Periodogram, calculated with the DCDFT method; (c) Correlation function, obtained with the DACF method; (d) Results of the Jurkevich method, applied to the core separation of C1.

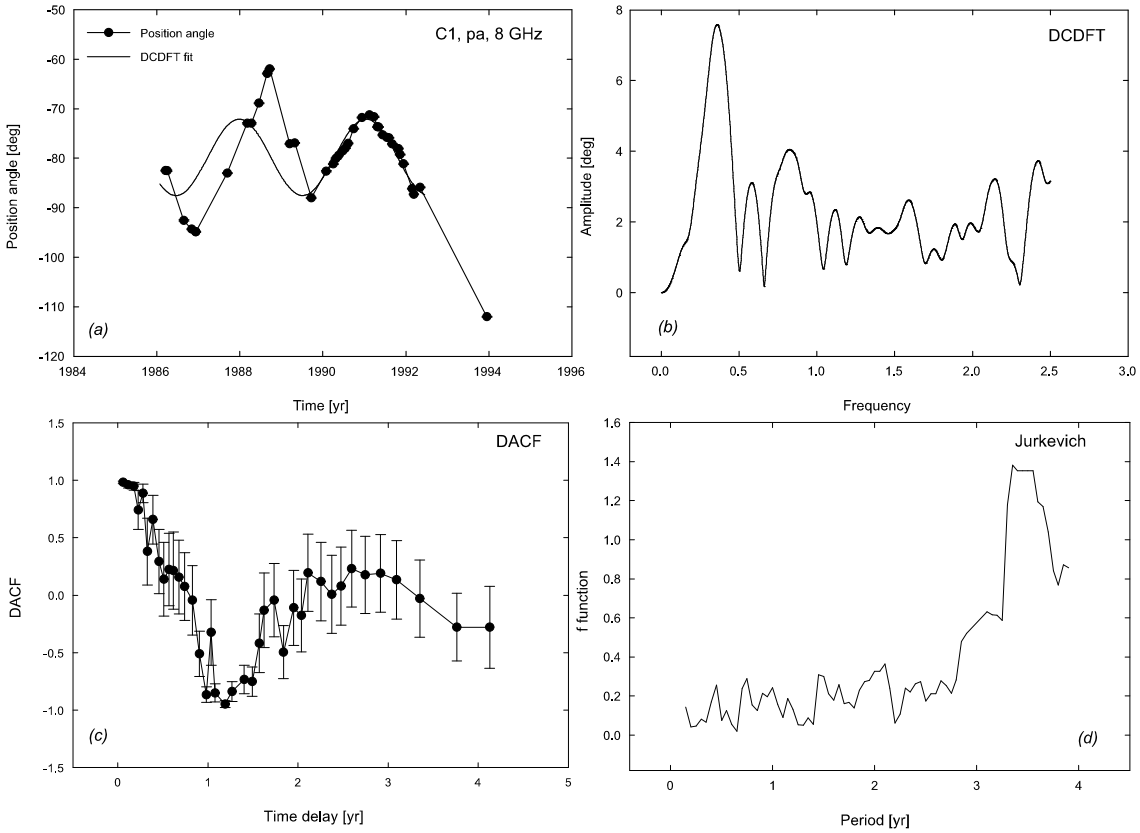

Figure 3.27: Results of the periodicity analysis for the position angle of the C1 at 8 GHz. (a) shows the position angle vs. time for C1 at 8 GHz. The solid line shows the sinusoid, calculated with the DCDFT method, corresponding to a period of 3.05 years; (b) Periodogram, calculated with the DCDFT method; (c) Correlation function, obtained with the DACF method; (d) Results of the Jurkevich method, applied to the position angle of C1.

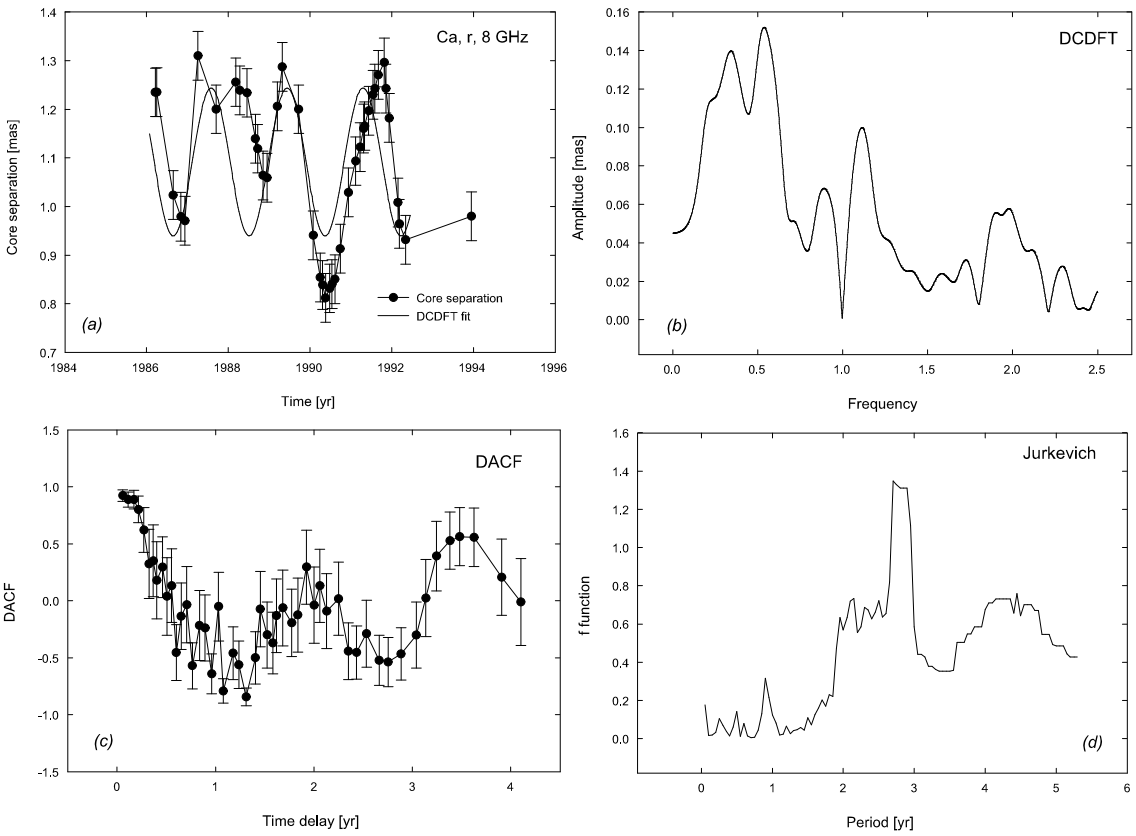

Figure 3.28: Results of the periodicity analysis for the core separation of Ca at 8 GHz. (a) shows the core separation vs. time for Ca at 8 GHz. The solid line shows the sinusoid, calculated with the DCDFT method, corresponding to a period of 2.92 years; (b) Periodogram, calculated with the DCDFT method; (c) Correlation function, obtained with the DACF method; (d) Results of the Jurkevich method, applied to the core separation of Ca.

3.12 Binary black holes

In order to check which can cause the jet precession, we applied together with Dr. J. Roland a binary black hole model to the VLBI data of S5 1803+784. We assumed that the presence of a BBH system produces 2 perturbations of the VLBI ejection, which are due to the precession of the accretion disk and the motion of the black holes around the gravity center of the BBH system. We build a geometrical model of the ejection and as we use only the VLBI coordinates, the problem we have to solve reduces to an astrometrical problem. The knowledge of the variations of the VLBI coordinates as a function of time contains the kinematical information, so we are able to deduce the inclination angle of the source and the bulk Lorentz factor of the ejected component. However, we could not find a unique mass for the BBH system. Using the fact that the jet component Ca slowly changes its position we assumed that possibly it can be explained with the slow motion of a jet perturbation. Therefore, for the binary black hole model fit we used trajectories of both jet components C0 and C1, assuming that after 10 years jet perturbation which correspond to C0 will move to the position of C1.

Figure shows result of a binary black hole model fit to the data. It is seen from the figure that the model describe the data very well. The inclination of the source is $i_o \approx 5.8^o\ ^{+1.7}_{-1.8}$ and the VLBI component is ejected with a bulk Lorentz factor $\gamma \approx 3.7\ ^{+0.3}_{-0.2}$. We determined the family of the BBH system which provides the best fit, assuming in a first step that the masses of the 2 black holes are equal and in a second step that the masses are different. The families found are characterized by $T_p/T_b \approx 2.0$, i.e. the precession period of the accretion disk of the black hole ejecting the VLBI component is in resonance with the orbiting period of the BBH system.

3.13 Discussion

The analysis of 94 VLBI epoch of observations at five frequencies has shown that the jet consists of seven "oscillating" jet components, which are stationary with regard to the core separation and stay near an average value of the core separation, but which move with regard to position angle. For the first time we found "stationary" jet components stay at the same positions for more than 20 years. Moreover, only one jet component ejection was detected during these 20 years. The jet component appeared during the bright opti-

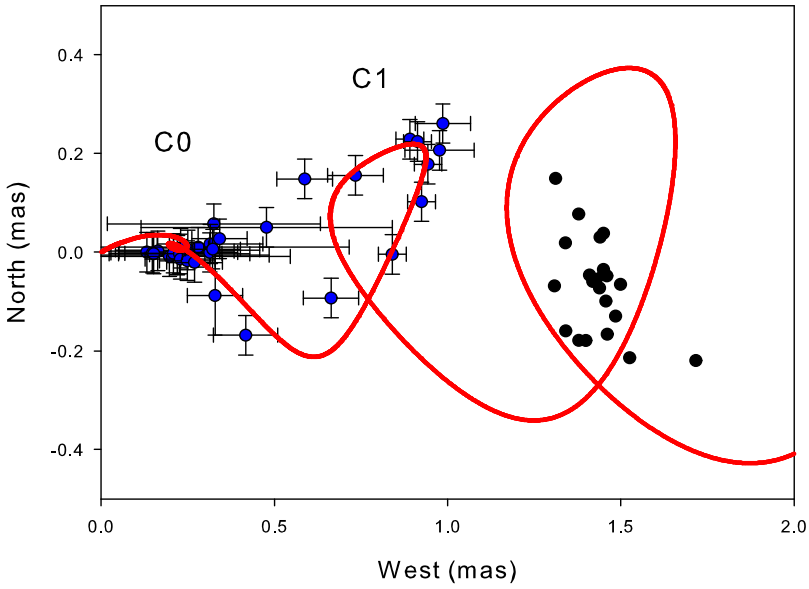

Figure 3.29: Fitted trajectories of the jet components C0 and C1 with a binary black hole model. We also plotted the trajectory of Ca for comparison.

cally thick flare. The separation of the total flux-density flares has shown that during 20 years of observations only one "core" outburst was observed and therefore the flaring activity cycle of S5 1803+784 is more than 20 years. This result is consistent with the fact, that the jet consists of several stationary jet components. The oscillating jet components of S5 1803+784 are located at regular core separations from each other and show brightness decrease along the jet. Therefore, we conclude that the presence of the oscillating jet components over more than 20 years can be explained with an unperturbed jet, where the stationary jet components are standing shocks, which appear due to interaction of the jet material with the ambient medium (Gomez et al. 1997).

Based on our investigation we propose a new definition of stationary jet components. They are jet features in a jet, which are staying at particular range of distances from the VLBI core ($r \pm 0.5$ mas) over long period of time,

but can move perpendicular to the jet ridge line. In over words, the core separation of a stationary jet component stays within the range of the core separations $r \in [r - \Delta r, r + \Delta r]$ and can have all possible position angles.

We found that the jet components appear stationary, but there is an evidence that the jet component **Ca** is moving very slowly with a speed of 0.03 mas/yr. This motion can be explained by different reasons. If the stationary jet components are caused by the standing shocks in the jet, than due to interaction with the ambient medium the position of the shocks can change with time and we can see a slow movement. On the other hand, if the jet is precessing, than the position of the stationary jet component will change.

We found that the jet component parameters, such as core separation, position angle and flux density change in a periodic way with a period of $\sim$2 and $\sim$4 years for the inner jet components at 8 GHz. A similar 2 and 3.9-year period is found in the total flux density light curves by Kelly et al. (2003). Moreover, changes of the core separation, position angle and flux are correlated with the total flux density variability. We also found that the core separation, the position angles and the fluxes of the jet components are correlated for different jet components and correlated with the core flux. That means, that the jet components show correlated movements, which have similar pattern as the core flux. Moreover, the time lags between the core separation and the position angle changes for two different jet components are changing gradually along the jet, which is an evidence that all the jet components are connected and that the movement is repeated with a delay which depends on the position along the jet. We also found jet ridge line changes on a timescale of about 8 years, which is twice as much as the periodicities in the motion of the jet components. The overall jet width is changing with time with a time scale of about 9 years which is similar to the jet ridge line changes.

Based on the results presented here, we conclude that a scenario incorporating a periodic form of motion (e.g. rotation, precession), with a non-negligible geometrical contribution, can possibly describe the behaviour of the jet components, such as jet ridge line and jet width changes, periodical motion of the jet components, correlated motion and fluxes of the jet components with the total flux-density, the core flux and between each other.

Chapter 4

Kinematics of 0605-085

4.1 Introduction

The quasar 0605-085 has a redshift of 0.872 (Stickel et al. 1993a). The jet kinematics of 0605-085 was studied by Kellermann et al. (2004) as part of the kinematic investigations of the 2-cm survey sources. Two components were found at 1.6 and 3.8 mas at three epochs in 1996, 1999 and 2001, with apparent speeds of 0.10±0.21c and 0.18±0.02c accordingly. The time of the ejection of the component at 3.8 mas was calculated to be 1977.9±2.0. It is worth to notice that the component at 1.6 mas was not classified as a well-defined feature in the jet.

High-resolution VSOP observations with the orbiting 8-m radio telescope HALCA show that the jet propagates in the south-east direction and at ∼0.2 mas turns to the north-east (Scott et al. 2004). At centimeter wavelengths the jet continues to extend in the south-east direction with multiple turns. The quasar 0605-085 was studied with CHANDRA and HST telescopes by Sambruna et al. (2004) which lead to an X-ray jet detection of two X-ray knots and no optical counterparts in the HST image. Moreover, the X-ray emission peaks at 4".0, before the radio knot, which peaks at 4".5 arcseconds. At kpc-scales it goes eastwards with a south-east bend at ∼3 arcsesonds (Cooper et al. 2007). The quasar 0605-085 has sinusoidal shape of the total flux-density light curves. One of the main goal of this chapter is to analyze total flux-density light curves together with the jet kinematics in order to find the origin of such strict period and sinusoidal shape of the light curves. Part of this analysis is published in Kudryavtseva et al. (close to submission).

4.2 Total flux-density light curves

In order to investigate the long-term radio variability of the source we combined data at ten frequencies 408 MHz, 4.8 GHz, 6.7 GHz, 8 GHz, 10.7 GHz, 14.5 GHz, 22 GHz, 37 GHz, 90 GHz, and 230 GHz from the monitoring campaigns of the University of Michigan Radio Astronomical Observatory (Aller et al. 1985), Metsähovi Radio Astronomical Observatory (Teräsranta et al. 1998), Haystack observatory (Dent et al. 1974, 1976), Bologna interferometer (Bondi et al. 1996), Algonquin Radio Observatory (Medd et al. 1972), and the SEST telescope (Steppe et al. 1988, 1992, Reuter et al. 1997, Tornikoski et al. 1996).

The historical light curves are shown in Fig. 4.1 and span almost 40 years of observations. The longest light curves at individual frequencies span more than 30 years at 8 GHz, more than 25 years at 4.8 GHz and 14.5 GHz and $\sim$ 10 years at 22 GHz and 37 GHz and are shown in Fig. 4.2. The total-flux density variability of 0605-085 shows clearly a sinusoidal pattern with four maxima at epochs 1972.5, 1981.5, 1988.3, and 1995.8. The last three peaks have similar brightness at centimeter wavelengths, whereas the first one is 1 Jy brighter. Moreover, at higher frequencies, one can see that the main peak reveals a substructure and shows a double-peak structure. The data at 22 GHz and 37 GHz are less frequent and cover less time of observations, but it is still possible to see that the last peak in 1995.8 is of similar shape and reaches the maximum at the same time as the lower frequencies.

The three main peaks in the total flux-density light curve clearly show a periodical behavior of about 8 years and if the period preserves over time, we expected the next powerful outburst to happen in $\sim$ 2003. However, after year 2000, the flux-density of 0605-085 did not reveal any peaks and stayed at the same level of about 1.7 Jy at all five frequencies. The absence of the peak in 2003 can be due to several reasons. First, it is possible that some mechanism causes the increase of the length of the quiescent state during the minima. For example, the 1985th minimum was really sharp and did not last for long time. The minimum in 1991 lasted for three years, whereas the last minima lasted for more than seven years. If the minima length increase also during the next outburst we can expect that the next powerful flare will be delays and can appear in 2008-2009. Another explanation is that the physical mechanism causing the quasi-periodical variability of the total flux-density light curves has stopped for some reason in about year 2000.

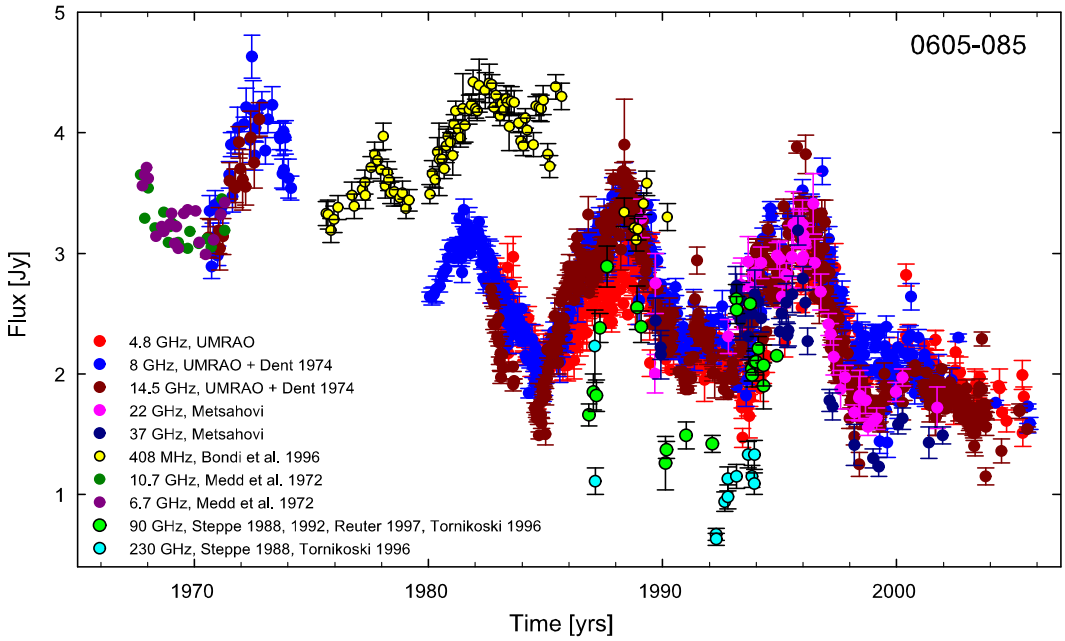

Figure 4.1: 0605-085: Historical radio light curves of 0605-085 at 0.4 GHz, 4.8 GHz, 6.7 GHz, 8 GHz, 10.7 GHz, 14.5 GHz, 22 GHz, 37 GHz, 90 GHz, and 230 GHz (see references in the text).

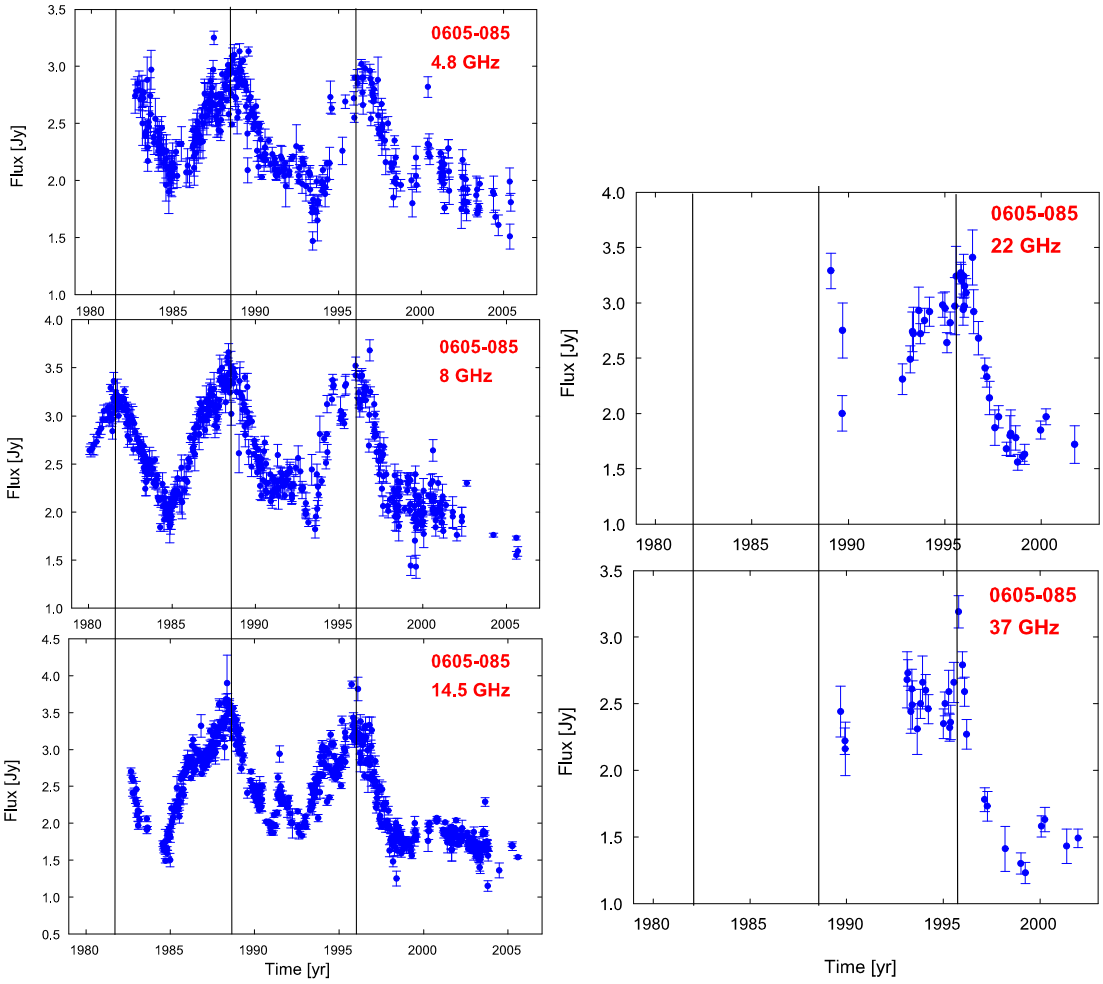

Figure 4.2: 0605-085: The total flux density light curve at 4.8 GHz, 8 GHz, 14.5 GHz (*Left*) and 22 GHz, 37 GHz (*Right*). The solid lines mark the position of the brightest flares maxima.

4.3 Periodicity analysis

In order to find the period in the total flux-density radio light curves, we applied the discrete autocorrelation function method (Edelson & Krolik 1988) and the date-compensated discrete Fourier transform method (Ferraz-Mello 1981). The Discrete Auto-Correlation Function (DACF) method allows us to study the level of auto-correlation in unevenly sampled data sets without any interpolation or addition of artificial data points. The values of the data sets are combined in pairs (a_i, b_j), for each $0 \leq i, j \leq N$, where N is the number of data points. First, the unbinned discrete correlation function is calculated for each pair

$$UDCF_{ij} = \frac{(a_i - \bar{a})(b_j - \bar{b})}{\sqrt{\sigma_a^2 \sigma_b^2}}, \tag{4.1}$$

where $\bar{a}$, $\bar{b}$ are the mean values of the data series and σ_a, σ_b are the corresponding standard deviations. The discrete correlation function for each time interval $\Delta t_{ij} = t_j - t_i$ is calculated as an average of all UDCF values, whose time intervals fall into the range $\tau - \Delta\tau/2 \leq \Delta t_{ij} \leq \tau + \Delta\tau/2$. The higher is the value of $\Delta\tau$ the better is the accuracy and the worse is the time resolution of the correlation curve. The error of the DACF is calculated as a standard deviation of the DCF value from the group of unbinned UDCF values

$$\sigma(\tau) = \frac{1}{M-1}\{\sum[UDCF_{ij} - DCF(\tau)]^2\}^{1/2}. \tag{4.2}$$

The DACF method yields different number of UDCF per bin, which can affect the final correlation curve. In order to check the results from the DACF we also applied the Fisher z-transformed DACF method, which allows to create the data bins with equal number of pairs (Alexander 1997).

The Date-Compensated Discrete Fourier Transform (DCDFT) method was created in order to avoid the problem of finitness of the Fourier transform and allows to calculate periods of unevenly sampled data with better precision. The method is based on the estimation of the power spectrum by means of least-square fitting of a sinusoid with different frequencies to the data set. In the case of a periodic process formed by several waves, the DCDFT method allows to filter the time series with a known frequency and find additional harmonics. We searched for the periods in the light curves at 4.8, 8, and 14.5 GHz only, which span more than 30 years since the data at

other frequencies are too sparse and cover only less than 10 years of observations.

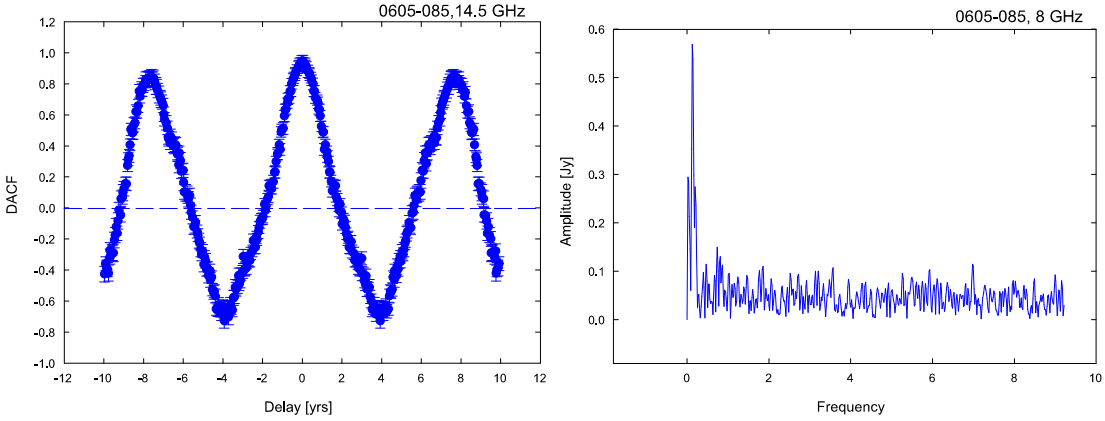

Figure 4.3: *Left:* The discrete autocorrelation function for 0605-085 at 14.5 GHz; *Right:* Results of the date-compensated discrete Fourier transform for 0605-085 at 8 GHz.

The auto-correlation method gives us periods of 7.7±0.2 years at 14.5 GHz, 7.2±0.1 at 8 GHz, and 8.0±0.2 at 4.8 GHz with high correlation coefficients of 0.84 (14.5 GHz), 0.77 (8 GHz), and 0.83 (4.8 GHz). An example of the calculated discrete auto-correlation function at 14.5 GHz is shown in Fig. 4.3 (left). The date-compensated Fourier transform method also shows the presence of a strong periodicity of about 8 years. This method indicates a period of 8.4 years with an amplitude of 0.6 Jy for 14.5 GHz, 7.9 years with amplitudes of 0.6 Jy at 8 GHz (Fig. 4.3, right), and 8.5 years with an amplitude of 0.3 Jy at 4.8 GHz. How good these periods represent the data is shown in Figs. 4.4 and 4.5, where the sinusoids with the calculated periods are overplotted on the light curves. It is clearly seen that the derived periods represent well the total flux-density variability of 0605-085. Both methods give consistent results and one can calculate an average period for all three frequencies and for the two methods, which is about 7.9 ± 0.5 years.

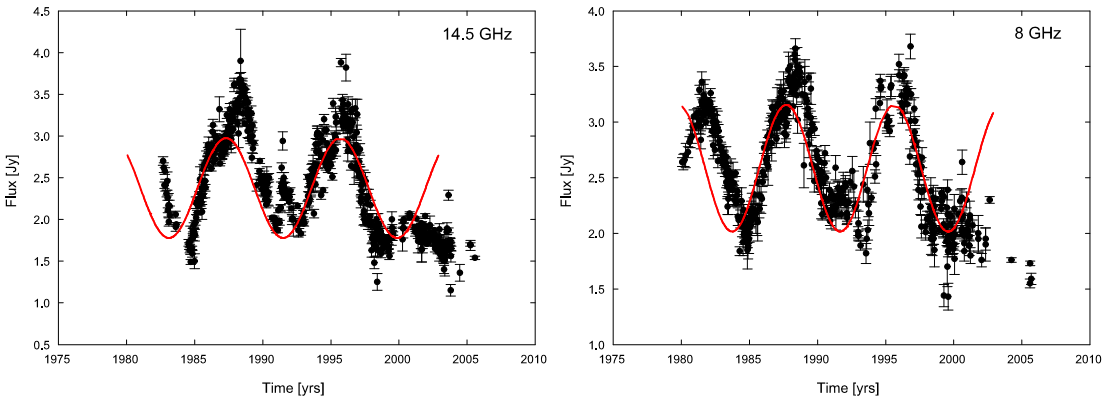

Figure 4.4: 0605-085: The total flux-density light-curves at 14.5 GHz and 8 GHz. The red line shows the sinusoids with the periods of 8.4 and 7.9 years accordingly, which were found with the date-compensated Fourier transform method

4.4 Frequency-dependent time delays

In case of variability caused solely by jet precession we can expect that the flares will appear simultaneously at all frequencies. In order to check whether the peaks at different frequencies reach the maximum at the same time, we calculated the frequency-dependent time delays. The Gaussian functions were fitted to the light curves at 4.8 GHz, 8 GHz, 14.5 GHz, 22 GHz, 37 GHz, and 90 GHz as it was described in Pyatunina et al. 2006, 2007. The frequency-dependent time delays were estimated as the time difference between the Gaussian peaks at different frequencies. Due to insufficient data, it was possible to calculate frequency-dependent time delays only for the outbursts in 1988 and 1996. However, from Fig. 4.1 it is seen that the 1973 flare happened almost simultaneously at 8 GHz and 14.5 GHz.

The Gaussian parameters, fitted into the light curves, are shown in Table 4.1. We calculated frequency-dependent time delays as the time difference between the Gaussian peaks at each frequency with respect to the position of the peak at 22 GHz for the 1996 flare and at 90 GHz for the 1988 flare. It is clearly seen that the C outburst in 1988 appeared almost simultaneously at all four frequencies with the negligible difference in time between individual frequencies of about 0.08 years. The 1995 flare D shows similar properties, the light curves at all frequencies have reached the maxima almost simulta-

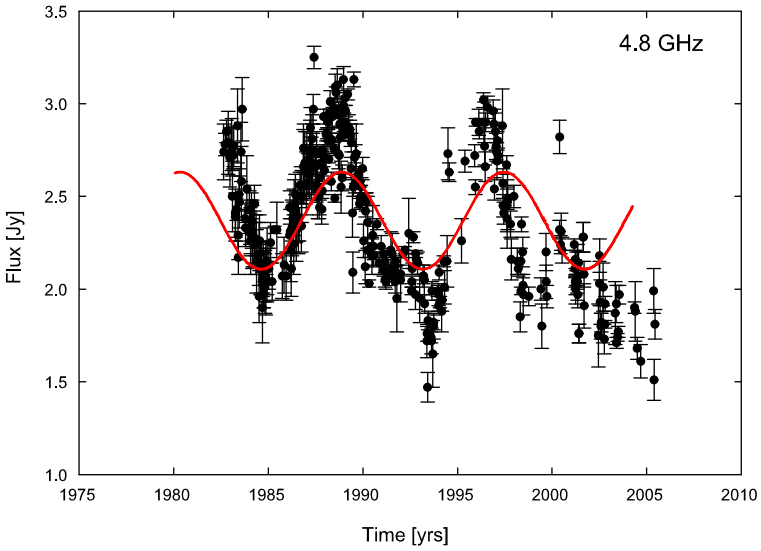

Figure 4.5: 0605-085: The total flux density light-curves at 4.8 GHz. The red line shows a sinusoid with a period of 8.5 years, which was found with the date-compensated Fourier transform method

neously in about 1995.9, except the 4.8 GHz, for which a delay of 0.4 years was calculated. On the other hand, the data at 4.8 GHz are poorly sampled in the rise of the flare, which could shift the Gaussian peak by this amount. Therefore, we can conclude from the Gaussian fitting and from the visual analysis of the flares, that the 1973, 1988, and 1996 outbursts appeared almost simultaneously at different frequencies. This can be an evidence for the periodic total flux-density variability caused by jet precession.

4.5 Spectral evolution

In order to check whether all outbursts in the total flux-density light curves have similar spectral properties, we constructed the quasi-simultaneous spectra from all available frequencies (see Fig. 4.1). We selected and plotted the spectra for different states of 0605-085. Fig. 4.6 shows the spectral evolution for the 1988 (left) and 1996 (right) flares. The 1988 flare starts from a steep spectrum in 1983 and 1984, which then shows a change of the turnover frequency in 1986. During the maximum of the 1988 flare, the spectrum becomes flat and then steepens again during the minimum state after the flare.

Table 4.1: 0605-085: Parameters of outbursts

Freq. *[GHz]*	Amplitude *[Jy]*	T_{max} *[yr]*	Θ *[yr]*	Time delay *[yr]*
C flare				
4.8	1.36 ± 0.01	1988.22 ± 0.02	5.61 ± 0.02	-0.02 ± 0.06
8.0	1.66 ± 0.01	1988.29 ± 0.01	3.94 ± 0.01	0.06 ± 0.05
14.5	1.93 ± 0.01	1988.30 ± 0.01	3.32 ± 0.02	0.08 ± 0.05
90.0	2.21 ± 0.25	1988.22 ± 0.04	1.71 ± 0.05	0.00 ± 0.04
D flare				
4.8	1.30 ± 0.01	1996.24 ± 0.02	4.51 ± 0.02	0.43 ± 0.07
8.0	1.71 ± 0.02	1995.84 ± 0.01	3.33 ± 0.02	0.03 ± 0.07
14.5	1.67 ± 0.01	1995.91 ± 0.01	3.16 ± 0.01	0.09 ± 0.07
22.0	1.56 ± 0.04	1995.81 ± 0.05	2.71 ± 0.05	0.00 ± 0.05

The 1996 flare shows a similar spectral evolution, with a steep spectrum in the beginning and at the end of the flare and a flat spectral shape during the maximum (Fig. 4.6).

The light curve of 0605-085 consists of four periodical flares in 1973, 1981, 1988, and 1996. The last two flares have similar spectral evolution and similar brightness. The observations during the 1973 flare are much sparser, but it is seen from the historical radio light curve that the fluxes at 8 GHz and 14.5 GHz are similar, which can be an evidence for a flat spectrum. However, it is worth to notice that the second 1981 flare shows a completely different spectral behavior. It is clearly seen from the historical light curve (see Fig. 4.1) that the spectrum of this flare is steep, since the brightness at 408 MHz significantly exceeds the brightness at centimeter wavelengths. Therefore, we can conclude that although the periodical flares look similarly, they have surprisingly different spectral properties.

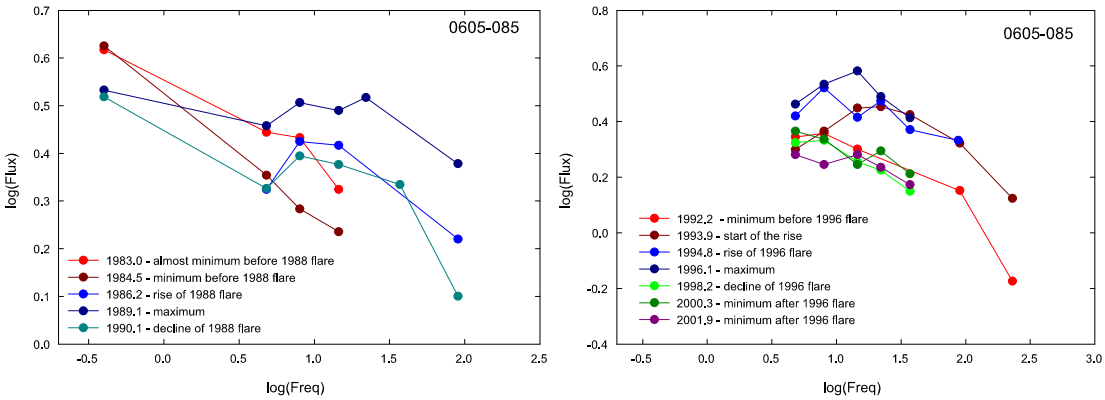

Figure 4.6: 0605-085: Spectral evolution of 0605-085 during the 1988 flare (*Left*) and 1996 (*Right*). It is clearly seen how the spectral shape changes from steep in the beginning and at the end of the flares to flat during the maxima.

4.6 Kinematics of 0605-085

For an investigation of the kinematics of 0605-085 we analyzed 9 epochs of VLBA observations at 15 GHz from the MOJAVE 2cm survey (http://www.physics.purdue.edu/astro/MOJAVE/). The observations were performed between 1995.6 and 2005.7 and span almost 10 years. The data were fringe-fitted and calibrated before by the MOJAVE group (Lister & Homan 2005, Kellermann et al. 2004). For all epochs we performed the clean maps and model fitting of circular Gaussian components using the *Difmap* package (Shepherd 1997). Circular components were chosen in order to avoid extremely elongated components and to simplify the comparison of the components. In order to find the optimum set of components and parameters, we fitted every data set starting from a point-like model. The position errors for the core separation and the position angle are given by the formulas $\Delta r = (d\sigma_{rms}\sqrt{1 + S_{peak}/\sigma_{rms}})/2S_{peak}$ and $\Delta\theta = \arctan(\Delta r/r)$, where σ_{rms} is the residual noise of the map after the subtraction of the model, d is the full width at half maximum (FWHM) of the component and S_{peak} is the peak flux density (Fomalont 1999). However, this formula tends to underestimate the error if the peak flux density is very high or the width of the component is small. Therefore, we also calculated uncertainties by comparison of different model fits (± 1 component) obtained for the same set of data. They reflect the possible parameter ranges for the individual components within model-fitting. The final position error was calculated as the maximum value between the error bars obtained by these two methods.

The final maps with fitted Gaussian components are shown in Fig. 4.7. We list all the parameters of the fitted Gaussian components, such as the core separation, the position angle, the flux-density, the size, and identification for all the epochs in Table 4.3.

The component identification was made in such a way, that the core separation, the position angle and the flux of the components change smoothly between adjacent epochs. In order to obtain the best component identification, the jet components were connected in different ways and the identification which gave the smoothest changes was chosen as final. The core separation and the fluxes of each individual jet component are shown in Fig. 4.8, left and right correspondingly. We found one stationary jet feature $C1$ at an average core separation of 3.7 mas with a flux density of about 0.1 Jy. This stationary feature is well-detected at the first four epochs, but after 2002 is blended with the moving outwards jet component $d2$, which was ejected in

about 1998. Therefore we observe a co-existence of a stationary component and jet features moving outwards. Four of these components, namely da, $d0$, $d1$, $d2$ and $d3$, were ejected during the period of the observations, whereas the components $d6$ and $d7$ are located at core separations of about 6 and 8 mas. The further investigation of older archival VLBI observations is required in order to determine when these jet components were ejected.

4.6.1 Component ejections

We found seven jet components moving outwards with apparent speeds from 0.12 ± 0.03 to 0.66 ± 0.01 mas/yr, which correspond to the speeds from 5.6 ± 1.4 c to 31.1 ± 0.5 c. Component $d3$ was ejected in 1996.9 during a maximum of the 1996 outburst. All other components ejected after $d3$, like $d1$, $d0$, and da show speeds which decrease for each following component. The jet component $d3$ shows a speed of 0.66 ± 0.01 mas/yr, the next ejected component has speed of 0.57 ± 0.01 mas/yr, $d1$ and $d0$ – about 0.45 ± 0.01 mas/yr and the last component da – 0.12 ± 0.03 mas/yr. A few faint Gaussian components could not be identified with any other jet component (marked by black dots in Fig. 4.8). These components reveal flux-densities of the order of 0.05 Jy, and can either be blobs which were ejected before 1995 and can not be traced because of a lack of data are possibly trailing components. The Doppler factor of the jet depends on the Lorentz factor γ, angle between the jet flow direction and the line of sight ϕ and the speed of the component in the source frame β:

$$\delta = \frac{1}{\gamma(1 - \beta \cos \phi}. \tag{4.3}$$

Taking the jet component with the maximum speed we can calculate the maximal viewing angle $\sin \phi_{max} = 2\beta_{app}/(1 + \beta^2_{app})$ and the lower limit for the Lorentz factor $\gamma_{min} = \sqrt{1 + \beta^2_{app}}$. The fastest jet component of 0605-085 is $d3$, which has a speed of 31.1 ± 0.5c. The corresponding Lorentz factor is $\gamma_{min} = 31$ and the upper limit for the viewing angle is $\phi_{max} = 3.7°$, which gives us an estimation for the Doppler factor $\delta_{min} = 12.4$. For smaller viewing angles ($\phi \to 0$) the Doppler factors approach a value of 62, which yields the range of the Doppler factors $\delta = 12.4$ to 62 at the viewing angles between 3.7° and 0° for the component $d3$.

We calculated the instant speeds of the jet components as the core separation between two subsequent position of a jet component divided by the time

Table 4.2: Summary of modelled component parameters in 0605-085: component identification, mean core separation, proper motion of the component, apparent speed of the component, time of the back-extrapolated component ejection and the maximum viewing angle are listed.

Comp. ID	$r_{\rm mean}$ [mas]	$\mu_{\rm r}$ [mas/yr]	$\beta_{\rm app}$ [c]	t_0 [yr]	ϕ_{max} [deg]
d7	9.26 ± 0.44	0.20 ± 0.10	9.4 ± 4.7		12.1
d6	7.35 ± 0.32	0.26 ± 0.06	12.2 ± 2.8		9.4
d3	4.31 ± 0.67	0.66 ± 0.01	31.1 ± 0.5	1996.9 ± 0.3	3.7
C1	3.71 ± 0.17	0.09 ± 0.01	4.2 ± 0.5		26.8
d2	3.11 ± 0.56	0.57 ± 0.01	26.8 ± 0.5	1997.9 ± 0.3	4.3
d1	1.78 ± 0.34	0.44 ± 0.01	20.7 ± 0.5	2000.2 ± 0.3	5.5
d0	1.33 ± 0.22	0.46 ± 0.02	21.7 ± 0.9	2001.8 ± 0.2	5.3
da	0.39 ± 0.03	0.12 ± 0.03	5.6 ± 1.4	2001.9 ± 0.3	20.2

passed between two observations. The change of the instant speeds indicates that the jet components $d1$, $d3$, and $C1$ experience acceleration and deceleration along the jet. Averaging the instant speeds of all the jet components in 1-mas core separation bins shows that all jet components accelerate at about 2 mas, 5 mas, and 7 mas and decelerate at 3 mas, 6 mas, and 9 mas (see Fig. 4.9). It is clearly seen that the jet is helical with a characteristic scale of 3 mas. It is worth to notice, that the characteristic spatial scale of 3 mas corresponds to the timescale of about 7.7 years (using the average speed of the jet components 0.39 mas/yr), which is similar to the period in the total flux-density light curves.

4.6.2 Stationary component $C1$

The stationary feature $C1$ is well-detected at the first four epochs from 1995 to 2001 (see Fig. 4.8). However, after 2002 it is most probably blended with the moving jet component $d2$. It is worth to notice that before 2002, when the stationary component is well-observed, there were no moving jet components. However, as the newly ejected jet features approach the position of component $C1$, it becomes difficult to distinguish between them and it is more likely that we see two components blended. Blending and dragging of the stationary jet components by the moving components was predicted

from the magneto-hydrodynamical simulations by Gomez et al. (1997) and Aloy et al. (2003) and was observed in a large number of sources (e.g. 3C 279 Wehrle et al. 2001, S5 1803+784 Britzen et al. 2005, 0735+178 Gabuzda et al. 1994).

Presence of a stationary jet component $C1$ can have different physical reasons. It can be produced by jet bending or by stationary conical shock waves due to an interaction with the ambient medium (e.g. Alberdi 2000, Gomez et al. 1997). However, when we plot the flux-density versus the core separation of all the detected Gaussian components (independent of the component identification) at Fig. 4.10 we see, that at a range of the core separations between 2.5 and 5.5 mas, there is a significant increase in the flux-density values. This increase in the flux-densities of all Gaussian components can be due to a bend in the jet close to 4 mas. Moreover, this jet bending can explain the existence of the stationary jet feature $C1$, which is at the same core separation of about 3.7 mas.

The high-resolution VLBI maps of the quasar 0605-085 were discussed in several papers (e.g. Padrielli et al. 1986, 1991, Bondi et al. 1996). A stationary jet component at the core separation similar to $C1$ was detected before by Fey&Charlot 2000. They found jet components at the core separation of 3.0 mas and $PA = 100°$, which is similar to the position of the $C1$ component. The existence of a bright jet component at a similar core separation for more than 15 years can be an additional evidence for jet bending at about 4 mas.

The stationary jet component $C1$ is located at an average core separation of 3.7 mas. However, the position of this component changes with time from 2.95 to 4.32 mas. The position angle and the flux-density of $C1$ are also variable. Fig. 4.11 shows the variability of the core separation, the position angle and the flux-density of this stationary component. There is a possible connection between the position angle and the flux-density of the component. The first part of the plots show tentative anti-correlation. The position angle reaches its maximum value of 125 degrees in 2001, when the flux has its minimum of 0.013 ± 0.002 Jy. There is also a possible correlation between the core separation and the flux-density of $C1$ – both of them have minima in about 2001–2003 and then experience a rise with a maximum in 2005. In rectangular coordinates, the trajectory of the stationary jet component $C1$ follows a helical path. Fig. 4.12 (Left and Right) shows the trajectory of $C1$ in rectangular coordinates in three-dimensional and two-dimensional plots. It is seen from the plot that the stationary component follows a spiral trajectory. Moreover, the characteristic time scale of a helix turn is about 8 years. This

time scale is very similar to the period of the total flux-density light curves.

4.6.3 Comparison of the trajectories

In order to get an overview of the position angle evolution along the jet and the shape of the trajectories of the individual jet components, we plotted the position angles of all features *da*–*d*7, including the stationary component C1 versus the core separation in Fig. 4.13. The paths of the components *d*1, *d*2, *d*6, *d*7, and *C*1 follow significantly curved trajectories, whereas the trajectories of *d*0 and *d*3 follow a smoothed path. This can be seen as some evidence for a possible co-existence of two types of jet component trajectories, similar to the source 3C 345 (Klare et al. 2005, Zensus et al. 1995).

The spread of the position angles of all components is changing with core separation. In the inner part of the jet, within the first mas, the position angles are in the range of 123–150 degrees, in the middle part of the jet between 1 – 5 mas, the position angles are $110° \leq PA \leq 125°$, whereas in the outer part of the jet from 5 mas to 10 mas, $95° \leq PA \leq 115°$.

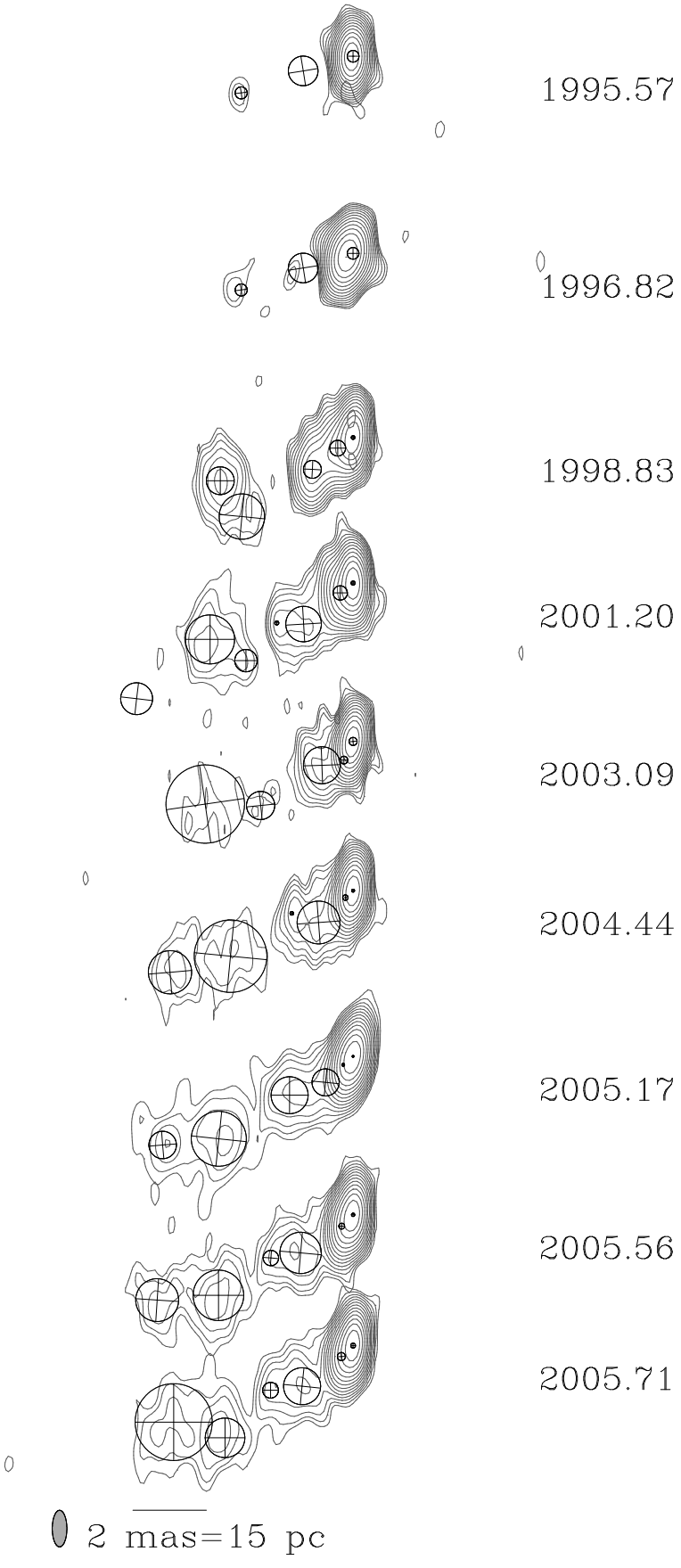

Figure 4.7: 0605-085: Model-fit results at 15 GHz.

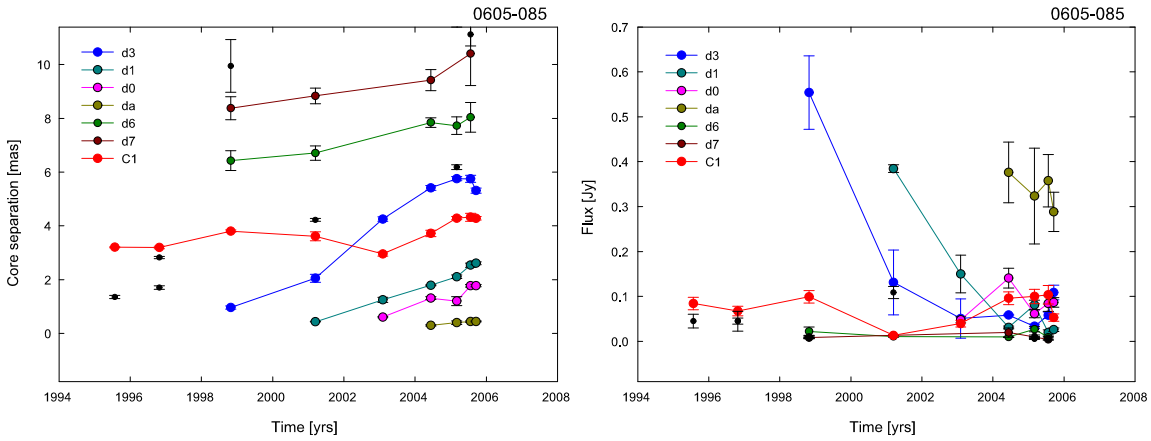

Figure 4.8: 0605-085: We show in the left panel the core separation as function of time at 15 GHz. Individual jet components are marked by different colors. In the right panel we show the flux density evolution of individual jet components with time.

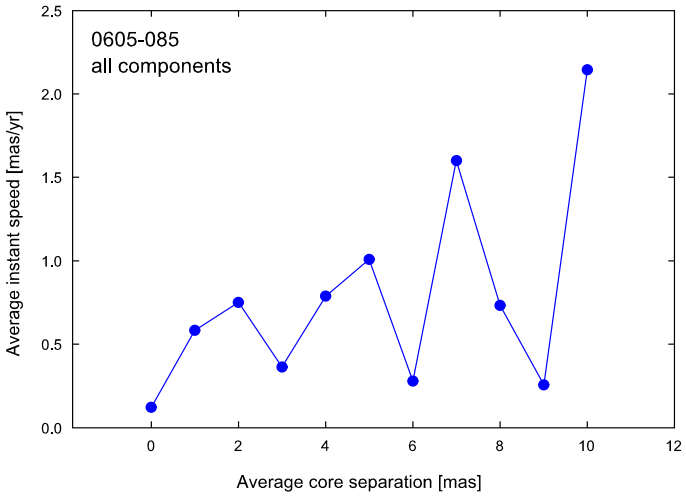

Figure 4.9: 0605-085: The instant speeds of all jet components averaged in each 1 mas bin of the core separation. The plot shows that the jet is helical with a characteristic scale of 3 mas.

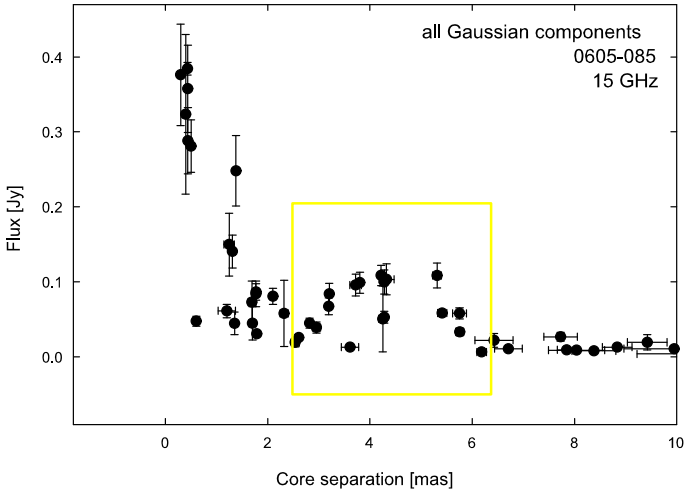

Figure 4.10: 0605-085: Flux-density of all Gaussian components found in the jet of 0605-085 at 15 GHz. It is clearly seen that all components become significantly brighter when they are in the range of the core separations from 2.5 to 5.5 mas, which can be explained by the jet bending.

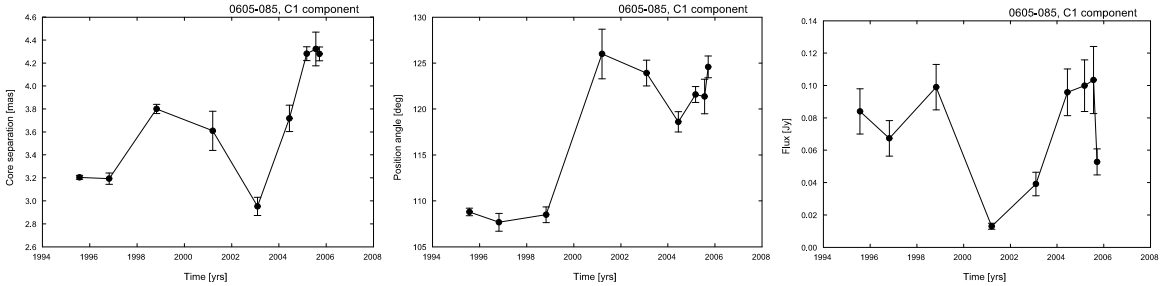

Figure 4.11: 0605-085: The time evolution of the core separation (*Left*), the position angle (*Middle*) and the flux-density (*Right*) of the "stationary" component $C1$.

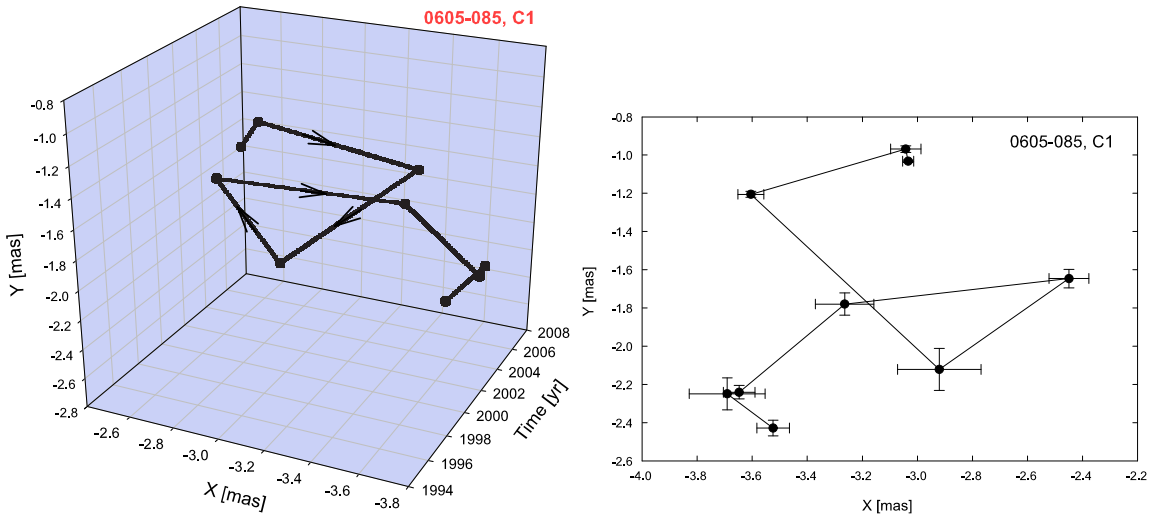

Figure 4.12: 0605-085: Trajectory of the stationary component $C1$ in rectangular coordinates in three-dimensional space with the third axis showing the time (*Left*) and in two dimensions (*Right*). The trajectory of the component follows the helical path.

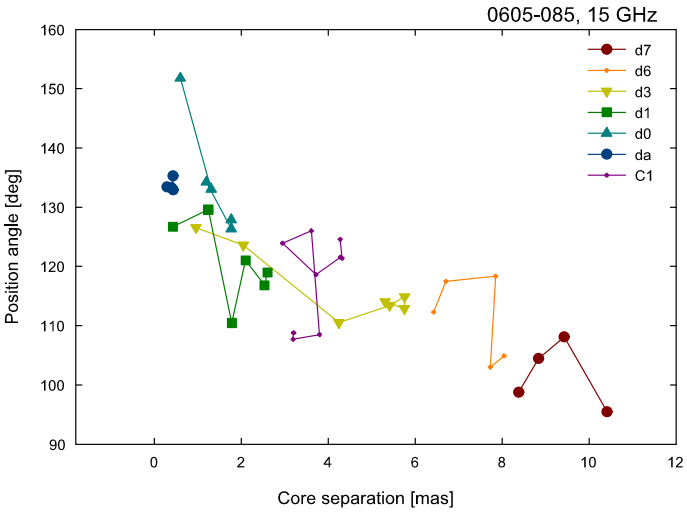

Figure 4.13: 0605-085: Change of the position angle of the jet components da-d7, including a stationary component C1 at 15 GHz.

Table 4.3: Model-fit results for 0605-085 at 15 GHz. We list the epoch of observation, the jet component identification, the flux-density, the radial distance of the component center from the center of the map, the position angle of the center of the component, the FWHM major axis of the circular component, the position angle of the major axis of the component.

Epoch	Id.	S [Jy]	r [mas]	θ [deg]	Ma.A. [mas]	Axial ratio	Φ [deg]
1995.57	**D**	2.533±0.382	0.0±0.04	0.0±1.0	0.32	1.00	0.0
1995.57		0.045±0.015	1.35±0.06	103.59±4.51	0.81	1.00	9.1
1995.57	**C1**	0.084±0.014	3.20±0.02	108.79±0.41	0.33	1.00	7.6
1996.82	**D**	2.001±0.319	0.0±0.16	0.0±0.6	0.55	1.00	2.6
1996.82		0.045±0.022	1.70±0.07	110.22±2.05	0.20	1.00	0.0
1996.82		0.045±0.007	2.82±0.04	125.70±0.90	0.30	1.00	3.6
1996.82	**C1**	0.067±0.011	3.19±0.05	107.67±0.97	0.53	1.00	2.1
1998.83	**D**	0.770±0.107	0.0±0.03	0.0±1.2	0.10	1.00	-2.7
1998.83	**d3**	0.554±0.082	0.96±0.06	126.55±2.78	0.92	1.00	-2.7
1998.83	**C1**	0.099±0.014	3.80±0.04	108.49±0.86	0.76	1.00	90.0
1998.83	**d6**	0.022±0.009	6.43±0.37	112.29±3.20	2.59	1.00	85.9
1998.83	**d7**	0.008±0.001	8.38±0.43	98.75±3.01	0.84	1.00	85.6
1998.83		0.011±0.002	9.95±0.98	108.37±5.50	1.66	1.00	0.0
2001.20	**D**	0.978±0.144	0.0±0.02	0.0±1.1	0.11	1.00	90.0
2001.20	**d1**	0.384±0.008	0.43±0.01	126.68±1.09	0.39	1.00	0.0
2001.20	**d3**	0.131±0.072	2.05±0.15	123.60±2.19	1.08	1.00	90.0
2001.20	**C1**	0.013±0.002	3.61±0.17	126.00±2.70	0.61	1.00	0.0
2001.20		0.109±0.013	4.22±0.05	112.50±0.76	1.34	1.00	0.0
2001.20	**d6**	0.011±0.002	6.71±0.27	117.50±2.30	0.87	1.00	83.2
2001.20	**d7**	0.013±0.002	8.83±0.29	104.45±1.90	1.21	1.00	2.6
2003.09	**D**	1.145±0.167	0.0±0.02	0.0±1.6	0.22	1.00	4.0
2003.09	**d0**	0.048±0.007	0.60±0.02	151.77±1.70	0.21	1.00	0.0
2003.09	**d1**	0.150±0.042	1.24±0.10	129.60±1.99	1.01	1.00	2.1
2003.09	**C1**	0.039±0.007	2.95±0.08	123.91±1.40	0.77	1.00	5.9
2003.09	**d3**	0.051±0.044	4.25±0.08	110.50±2.68	2.14	1.00	8.2
2004.44	**D**	0.843±0.119	0.0±0.07	0.0±0.2	0.08	1.00	0.0
2004.44	**da**	0.376±0.067	0.30±0.03	133.42±3.42	0.15	1.00	6.1
2004.44	**d0**	0.141±0.022	1.31±0.06	133.02±2.01	1.17	1.00	94.0
2004.44	**d1**	0.031±0.003	1.79±0.02	110.46±0.63	0.10	1.00	4.0
2004.44	**C1**	0.096±0.014	3.72±0.12	118.60±1.11	1.98	1.00	84.4
2004.44	**d3**	0.058±0.002	5.41±0.09	113.42±0.73	1.18	1.00	94.7
2004.44	**d6**	0.009±0.001	7.85±0.18	118.32±1.30	0.56	1.00	90.0
2004.44	**d7**	0.019±0.010	9.42±0.39	108.10±6.79	3.76	1.00	3.4
2005.17	**D**	0.835±0.119	0.0±0.06	0.0±1.5	0.05	1.00	0.0
2005.17	**da**	0.323±0.106	0.40±0.06	133.26±5.41	0.08	1.00	0.0
2005.17	**d0**	0.061±0.009	1.20±0.17	134.21±2.60	0.74	1.00	-5.5
2005.17	**d1**	0.081±0.011	2.10±0.07	121.01±1.27	1.01	1.00	0.0
2005.17	**C1**	0.100±0.016	4.28±0.06	121.57±0.87	1.50	1.00	83.8
2005.17	**d3**	0.033±0.005	5.75±0.08	114.90±0.80	0.75	1.00	94.7
2005.17		0.007±0.002	6.18±0.09	106.30±0.90	0.13	1.00	0.0
2005.17	**d6**	0.027±0.006	7.73±0.33	103.00±2.50	2.94	1.00	-5.5
2005.17		0.005±0.001	11.73±0.34	103.70±1.70	0.48	1.00	0.0
2005.17		0.007±0.001	13.26±0.31	101.00±1.40	0.49	1.00	0.0
2005.17		0.012±0.002	19.83±1.24	111.90±3.60	3.99	1.00	90.0
2005.56	**D**	0.907±0.132	0.0±0.03	0.0±0.6	0.09	1.00	0.0
2005.56	**da**	0.358±0.058	0.44±0.02	135.27±1.18	0.16	1.00	90.0
2005.56	**d0**	0.084±0.017	1.77±0.05	126.35±1.53	1.13	1.00	84.9
2005.56	**d1**	0.019±0.006	2.54±0.08	116.81±1.83	0.42	1.00	-4.3
2005.56	**C1**	0.103±0.021	4.32±0.15	121.36±1.88	1.38	1.00	0.0
2005.56	**d3**	0.058±0.007	5.75±0.13	112.87±0.77	1.17	1.00	86.1
2005.56	**d6**	0.009±0.001	8.04±0.55	104.90±4.00	1.68	1.00	90.0
2005.56	**d7**	0.004±0.001	10.41±1.19	95.45±6.50	1.46	1.00	0.0
2005.56		0.008±0.001	11.12±0.43	110.02±2.20	1.05	1.00	90.0
2005.56		0.003±0.001	21.24±3.66	113.30±9.80	3.38	1.00	90.0
2005.71	**D**	0.822±0.123	0.0±0.04	0.0±0.7	0.13	1.00	0.0
2005.71	**da**	0.288±0.044	0.44±0.02	132.92±1.41	0.22	1.00	2.7
2005.71	**d0**	0.086±0.011	1.77±0.04	127.87±1.42	1.01	1.00	-5.8
2005.71	**d1**	0.026±0.004	2.61±0.05	118.97±1.20	0.43	1.00	0.0
2005.71	**C1**	0.053±0.008	4.28±0.06	124.57±1.18	1.08	1.00	0.0
2005.71	**d3**	0.108±0.016	5.31±0.09	114.02±0.98	2.10	1.00	0.0

4.7 Precession model

The strong periodical variability of the radio total flux-density light curves of 0605-085 and the helical motion of a stationary jet component $C1$ can be explained by jet precession. We used a precession model, described in Abraham & Carrara (1998) and Caproni et al. (2004) for fitting the helical movement of $C1$. In this model, due to jet precession the rectangular coordinates of a precessing jet cone in the source frame are changing with time t':

$$X(t') = [\cos\Omega \sin\phi_0 + \sin\Omega \cos\phi_0 \sin\omega t'] \cos\eta_0 - \sin\Omega \cos\omega t' \sin\eta_0 \quad (4.4)$$

$$Y(t') = [\cos\Omega \sin\phi_0 + \sin\Omega \cos\phi_0 \sin\omega t'] \sin\eta_0 - \sin\Omega \cos\omega t' \cos\eta_0, \quad (4.5)$$

where Ω is the semi-aperture angle of the precession cone, ϕ_0 is the angle between the precession cone axis and the line of sight and is average viewing angle of the source, and η_0 is the projected angle of the cone axis on the plane of the sky. The angular velocity of the precession $\omega = 1/P$, where P is a precession period. We took a precession period equal to the 8-year period of the total flux-density radio light curves and the time scale of a helical movement of $C1$. The time in the source frame (t') and the frame of the observer (t) are related by the Doppler factor δ as

$$\Delta t' = \frac{\delta(\phi, \gamma)}{1+z} \Delta t. \quad (4.6)$$

However, the only time-dependent term in the equations 4.4 and 4.5 is ωt, which does not depend on this time corrections since $\omega \sim 1/t$. Therefore, we can fit the trajectory in rectangular coordinate $X(t)$ of a stationary jet component $C1$, using the formula 4.4. We assumed that the motion of $C1$ indicates the movement of the jet. The non-linear least squares method was used for fitting the precession model. The angular velocity of the precession ω, the redshift of the source z are known, whereas the aperture angle of a precessing cone Ω, ϕ_0, and η_0 are free parameters. The results of the fit are shown in Fig. 4.14 (left) and the parameters of the precession model for the parsec jet of 0605-085 are listed in Table 4.4. It can be seen from the

figure, that the precession model can explain the trajectory of a stationary jet component $C1$. The same parameters were used to describe the motion of $C1$ in the Y coordinate. The model for the Y coordinate is shown in Fig. 4.14 (right). We found another set of parameters $\Omega = 92.2°$, $\phi_0 = 69.8°$, $\eta_0 = 12.9°$, but the viewing angle is too large for the quasar 0605-085 and therefore this solution is false.

Table 4.4: Parameters of the precession model for the parsec jet of 0605-085.

Parameter description	Parameter	Value
Precession period	P	8 yr
Aperture angle	Ω	$23.9° \pm 1.9$
Viewing angle	ϕ_0	$2.6° \pm 2.2$
Projection angle	η_0	$33.6° \pm 6.5$

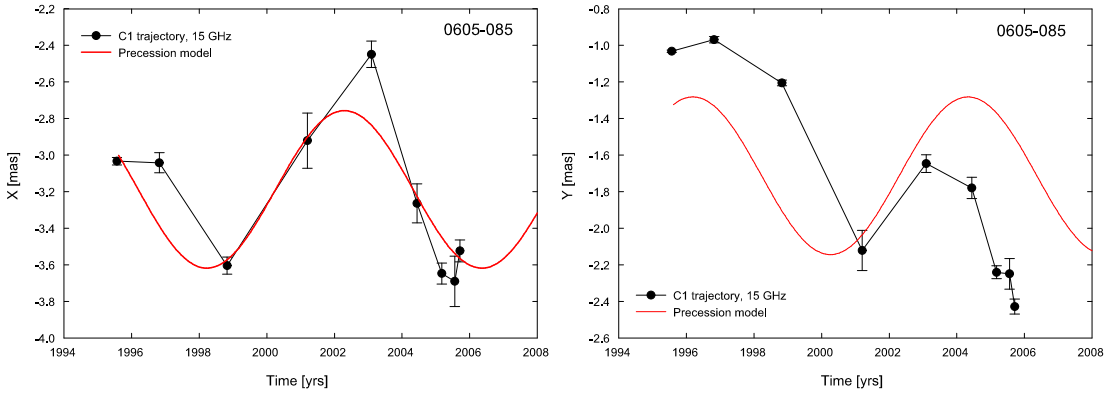

Figure 4.14: 0605-085: Trajectory of the stationary component $C1$ in rectangular coordinates X (*Left*) and Y(*right*). The solid line shows the fit of the precession model. The precession model can explain the trajectory of a stationary jet component $C1$

4.8 Summary of the results

Before we describe the possible physical reasons for the total flux-density variability and jet kinematics of 0605-085, we give a brief summary of the results of the analysis.

- We found a strict period of 7.9 ± 0.5 years in the total flux-density light curves at 4.8 GHz, 8 GHz and 14.5 GHz, which was observed for four cycles.

- The measurement of the frequency-dependent time delays for the 1973, 1988, and 1996 outbursts has shown that these flares appeared almost simultaneously at different frequencies.

- Analysis of the spectral properties of the flares has shown, that the main flares in 1973, 1988, 1996 have flat spectra, whereas the flare in 1981 has a steep spectrum. This suggests that the four cycles of the 8-year period have different spectral properties.

- The average instant speeds of the jet component $C1$ show clear helical pattern along the core separation with a characteristic scale of 3 mas. This scale corresponds to the time scale of about 7.7 years.

- The stationary jet component $C1$ follows the prominent helical path on a timescale of 8 years. This time scale is similar to the 8-year period found in the total flux-density light curves.

- The jet components of 0605-085 follow two different types of trajectories. Some components move along straight lines, whereas other component reveal significantly curved paths.

- The fit of the precession model to the trajectory of the stationary jet component $C1$ has shown that it can be explained by a precession model with a precession period (in the observers frame) of $P = 8$ yrs. The aperture angle of a precessing cone is $\Omega = 23.9^\circ \pm 1.9^\circ$, the viewing angle $\phi_0 = 2.6^\circ \pm 2.2^\circ$ and the projection angle is $\eta_0 = 33.6^\circ \pm 6.5^\circ$.

4.9 Discussion

Assuming that the helical motion of a stationary jet component $C1$ is caused solely by jet precession with a period of 8 years, we were able to determine the geometrical parameters of the jet, such as the aperture angle of a precessing cone, the viewing angle and the projection angle. The fitted viewing angle $\phi_0 = 2.6^\circ \pm 2.2^\circ$ agrees well with the upper limit for the viewing angle which we calculated from the apparent speeds of the jet components to be $\phi_{max} = 3.7^\circ$. Jet precession will also cause the periodical variability of the radio total flux-density light curves with the same period of 8 years due to periodical changes of the Doppler factor. The flux density S_j is changing with the Doppler factor due to jet precession $S_j = S'_j \delta(\phi, \gamma)^{p+\alpha}$, where α is the spectral index (Lind & Blandford 1985). From this equation we can expect that the flares due to jet precession will appear simultaneously at different frequencies, which is actually observed for the major outbursts in 1973, 1988, and 1996. Therefore, the main conclusion is that the jet precession causes the total flux-density variability and the helical motion of the stationary jet component $C1$. However, it is still unclear why the four major outbursts in the total flux-density light curve repeat periodically with an 8-year period have different spectral properties.

Another possible explanation of the $C1$ helical motion is that the jet itself is not precessing, but rather the jet component $C1$ is moving along a helical trajectory. Due to the bend in the jet we see this component moving towards us as stationary.

The strict periodicity of 0605-085 makes this source a good binary black hole candidate. The flares appear periodically, the jet of 0605-085 is precessing with the same period and the flares have double structure, which was observed in optical wavelengths for OJ 287 and was explained by a secondary black hole which is diving into the accretion disc of a primary black hole (e.g. Pursimo et al. 2000).

The next total flux-density flare of the source can be either in 2008 or in 2012. If the 8 year period in the light curve preserves over time, we would expect the next powerful outburst to happen in $\sim$ 2008. However, since the spectral properties of the flares is different, it might be that the period of the source is different. The time duration between the outbursts with the flat amplitudes reveals a timescale of about 12 years, which is less stable than the 8-years period. In this case the next outburst will happen in about 2012. Observations of 0605-085 in optical and radio total flux, including VLBI

observations will answer the question about the stability of an 8 year period of 0605-085.

Chapter 5

Summary

In this thesis we presented and analyzed multi-frequency very long baseline interferometry observations together with multi-frequency total flux-density variability data of compact relativistic jets in active galactic nuclei in order to investigate

- physics of the jets
- periodical processes in the radio total flux-density light curves and jet structural changes
- flaring activity cycles
- jet precession.

Periodicities in the radio light curves

We searched for periodicities in the radio total flux-density light curves and found five sources with clear periods at all analyzed frequencies (3C 454.3, 3C 446, CTA 102, 0133+476 and 0605-085). A new method was proposed for searching the periods in appearance of optically thick "core" outbursts, which have large frequency-dependent time delays, show a specific spectral evolution and are accompanied by a rise in the VLBI core flux. The "core" outbursts are probably connected with the closest vicinity of a supermassive black hole in the center of a galaxy and are possibly caused by the appearance of a primary perturbation in the base of the jet. Thus, periodicities in the "core" outbursts can be regarded as periodical processes in the closest vicinity of a supermassive black hole.

In order to investigate which possible physical mechanisms cause periodical variability, we analyzed the spectral variability, time lags, width and opacity of the radio total flux-density flares. We found for the first time that opacity, spectra and widths show periodical modulations which coincide with periodicities in the light curve for three sources (3C 454.3, 3C 446, and CTA 102). Moreover, for two sources (3C 454.3, 3C 446) we predicted the outbursts and they were observed at the predicted time. Only for one source OJ 287 the predicted flare has been observed before (e.g. Pursimo et al. 2000 and references therein), which makes 3C 454.3 and 3C 446, similar to OJ 287 another good sources for studying total flux-density periodicities. This makes the new proposed method of searching for periodicities not only in the fluxes but also in other physical parameters of the flares, such as opacity, a very good tool for searching periodicities in blazars and quasars. The comparison of the periods in the radio light curves with the characteristic timescales of parsec-scale jet variability has shown a possible coincidence between periods in the light curves, spectral and opacity changes with the characteristic timescale of ejections.

We can explain periodicities in the analyzed sources with different physical mechanisms. For three sources for which we found periods in "core" outbursts, the period is most likely connected with a periodical process near the base of the jet and we can already exclude a few reasons for periodicity, such as shock propagation along the jet (Gomez et al. 1997), jet recollimation or helical trajectories of the jet components (Camenzind & Krockenberger 1992). Instabilities in the accretion disc or presence of supermassive binary black hole can be the reason for observed periodicities. However, for the sources 0133+476 and 0605-085 we found that the most likely reason for their periodicty can be jet precession, based on the VLBI observations for 0605-085 and based on the opacity changes for 0133+476.

Comparison with optical light curves have revealed that for a few sources (3C 454.3, 3C 446) periodicity in the radio variability coincides with the period in the optical light curve. Such coincidences of optical and radio variability was observed before only in seven sources. According to Rieger 2005 such coincidences can be most likely caused by presence of a binary black hole in the middle of a galaxy. Taking into account that for this sources we have also detected periodicity in the "core" flares, opacity and spectra, 3C 454.3 and 3C 446 become the best known candidates into supermassive binary black holes together with OJ 287.

Core shifts

We have applied a new method for frequency-dependent VLBI core shift estimation from the total flux-density light curves. Frequency-dependent core shifts are necessary for astrometrical measurements and for astrometrical catalogues comparisons (e.g. Kovalev et al. 2008). The frequency-dependent time delays between the outbursts are caused by opacity as the frequency-dependent core shifts. We used an assumption that time delays and core shifts are linearly connected with a coefficient which equals to the apparent speed of the jet component. For the first time we have shown that this method and this assumption is working well for the source 3C 345. Using this method we have also derived the frequency-dependent VLBI core shift evolution for several other sources. These sources have calculated core shifts of values up to $\sim$0.5 mas between 22 GHz and 8 GHz, which are actually changing with time. We conclude, that the proposed new method is a good alternative to the core shift measurement based on the VLBI spectral maps and requires much less VLBI observations. Moreover, with this method it is possible to investigate the time evolution of the frequency-dependent core shifts.

Stationary jet components

We found that stationary jet components can show oscillations around a certain core separation and position angles. For a few sources (S5 1803+784, 0605-085) we found oscillating components in the jet. These components are staying at an average core separation and show changes in the position angle. However, for S5 1803+784 we found for the first time that the jet consists almost only of oscillating component, whereas in the case of 0605-085 an oscillating jet component co-exist with moving superluminal jet features as in case of e.g. 4C 39.25 (Alberdi 2000). A detailed study of the jet kinematics reveals a new picture for jet component motion in the blazar S5 1803+784. For the first time, in contrast to previous scenarios, we found that the jet consists mainly of a set of "oscillating" jet components within the inner 12 mas which stay at particular range of distances from the core and show significant changes of the position angles. Only one weak jet component during 20 years of observations reveals superluminal motion with an apparent speed of $\sim$19c. (for details see Britzen et al. 2008).

Stationary jet components can appear due to bends in the jet (e.g. Alberdi et al. 2000), jet recollimation shocks or sudden variations in the external pres-

sure that result in strong, isolated recollimation shocks (Gomez et al. 1997). The bends of the jet can be located at any position in the jet and should show much brighter flux due to Doppler beaming as well as isolated recollimation shocks. On the other hand, unperturbed recollimation shocks should show a regular pattern and a regular brightness decrease along the jet (Gomez et al. 1997). The oscillating jet components of S5 1803+784 are located at regular core separations from each other and show a brightness decrease along the jet. Different models can explain observed properties of S5 1803+784, such as recollimation shock waves, bends in the jet or jet precession. However, none of these models can explain all observed phenomena in S5 1803+784 and a new model explaining all the properties is needed.

Since these oscillating jet components have limited range of core separations, but can show different position angles within a certain range, if we observe them during the short period of observations we will see them as moving (either outwards or backwards) and will not be able to detect these oscillating jet components. We could detect these oscillating jet components only analyzing long-term VLBI observations which are long enough (spanning more than 20 years). Recent analysis of long-term observations of 0716+714 showed similar results (Meyer et al. 2007, Meyer 2007a, Britzen et al. 2006). Therefore, we can expect that the long-term analysis of VLBI observations of other blazars and quasars can also show that the jet consists mainly of non-moving outwards oscillating jet components if we consider long periods of observations.

Jet precession

For a few sources (S5 1803+784 and 0605-085) the analysis of multi-frequency VLBI observations has shown evidence for the jet precession. However, relativistic jets of these two sources has shown different properties and different physical mechanisms should be responsible for jet precession in S5 1803+784 and 0605-085. The comparison with the radio total flux-density variability has shown for both sources that position angles are correlated with the total flux-density variability. Moreover, position angles of the oscillating jet components show periodical changes. For both sources the movement of oscillating jet components in these sources also shows similar timescales to the period in the radio total flux-density light curves. This behavior can most likely be explained by a geometric motion of the jet, such as jet precession. The jet is changing its orientation and thus the viewing angle of the jet is changing

and the position angle of the oscillating jet components are changing as well. This causes the periodical modulations of the Doppler factor and the flares in the total flux-density light curves. The application of the jet precession model to the trajectory of the jet component of 0605-085, gave a good fit to the data. Therefore, we can explain periodicities in the total flux-density light curves of these sources with jet precession.

A few physical mechanisms can explain jet precession, including jet instabilities such as Kelvin-Helmholtz instability (e.g. Camenzind & Krockenberger 1992, Hardee & Norman 1988), a secondary black hole (e.g. Lobanov & Roland 2005), and accretion disc instabilities. The application of a binary black hole model to the data of S5 1803+784 has shown that trajectories of oscillating jet components can be described with the model where the jet is precessing due to accretion disc precession and orbital motion in the binary system.

Flaring activity cycles

We have applied a new method for calculating the flaring activity cycles, where flaring activity cycle is defined as characteristic time scale between "core" outbursts. "Core" outbursts are optically thick flares with large frequency-dependent time delays, special spectral evolution and are connected with the appearance of a primary perturbation in the jet. For the first time we successfully found "core" and "jet" outbursts, based on the shock-in-jet theory predictions (Gomez et al. 1997) and calculated flaring activity cycles for several sources (e.g. 3C 454.3, 3C 446, CTA 102, S5 1803+784, 0133+476). We found that the method of separation between "core" and "jet" outbursts is well suited for searching the connection between jet component ejections in the VLBI maps and total flux-density outbursts with a probable connection between jet components ejections and "core" outbursts. For a few sources (e.g. 3C 454.3) we found that during the flaring activity cycle (which based on our analysis can last up to tenths of years) frequency-dependent time delays, the opacity and the spectral evolution is changing gradually with time (in accordance with the shock-in-jet model). Thus, we actually observe substructure of the powerful outbursts rather than single outbursts.

Based on the analysis of the long-term multi-frequency light curves and VLBI observations, we conclude that flaring activity cycles in these sources last from 8 years (CTA 102) up to > 25 years (S5 1803+784), which means

that the appearance of a primary perturbation in the base of the jet, which causes the brightening of the VLBI core, powerful total flux-density outbursts and the appearance of new jet component(s), is a rare event. However, a detailed analysis of a complete sample of active galactic nuclei is necessary in order to check whether the primary perturbation in the base of the jet is a rare event for all the sources or only for a particular subclass and whether the duration of the flaring activity cycle is correlated with the luminosity of the sources.

Chapter 6

Abbreviations

Table 6.1 shows a list of often used abbreviations.

Table 6.1: List of abbreviations.

Abb.	Meaning
AGN	Active Galactic Nuclei
DACF	Discrete Auto-Correlation Function
DCDFT	Date-Compensated Discrete Fourier Transform
FWHM	Full Width Half Maximum
RRFID	Radio Reference Frame Interferometric Database
SED	Spectral Energy Distribution
SMA	SubMillimeter Array
UMRAO	University of Michigan Radio Astronomical Observatory
VLBI	Very Long Baseline Interferometry

List of Figures

1.1 Cartoon of an active galactic nucleus 12
1.2 M 87 jet at different resolutions 13
1.3 Cartoon visualizing jet precession 16
1.4 Cartoon of the physical structure of AGN 18

2.1 Shape of a centimeter outburst. Gaussian decomposition . . . 30
2.2 Map of 3C 454.3 32
2.3 Radio light curve for 3C 454.3 33
2.4 Results of the period search for 3C 454.3 34
2.5 Light curve for 3C 454.3 - II 36
2.6 Amplitudes and time delays of 3C 454.3 38
2.7 Time variability of time lags and amplitudes in 3C 454.3 . . . 39
2.8 Width evolution in 3C 454.3 40
2.9 3C 454.3: flux densities of VLBI components 41
2.10 Binary black hole fit in 3C 454.3 42
2.11 Map of 3C 446 48
2.12 Radio light curve of 3C 446 49
2.13 Results of the period search for 3C 446 51
2.14 100 GHz map of 3C 446 52
2.15 Radio light curve of 3C 446 - predicted flare 53
2.16 Amplitudes and time lags in 3C 446 54
2.17 Time evolution of 3C 446 widths 55
2.18 Map of CTA 102 60
2.19 Radio light curve of CTA 102 61
2.20 Optical light curve of CTA 102 62
2.21 Results of the period search for CTA 102 64
2.22 Radio light curve of CTA 102 - II 65
2.23 CTA 102: Quasi-periodicity of outbursts 66

2.24 Time lags and amplitudes of CTA 102 68
2.25 Flux-densities of VLBI components of CTA 102 69
2.26 Map of 0133+476 72
2.27 Light curve for 0133+476 73
2.28 Results of the period search for 0133+476 74
2.29 Time delays and amplitudes of 0133+476 75
2.30 Time evolution of amplitudes and time lags of 0133+476 . . . 76
2.31 Time evolution of 0133+476 widths 77
2.32 Similar shapes of the flares in different sources 81
2.33 The total flux-density light curve of 3C 345 85
2.34 Frequency-dependent core shifts 86

3.1 Maps of S5 1803+784 92
3.2 S5 1803+784: VLBI data 93
3.3 Clean maps of S5 1803+784 97
3.4 15 GHz map of S5 1803+784 98
3.5 S5 1803+784: Core separations versus time 99
3.6 S5 1803+784: trajectories of C0 and Ca 100
3.7 S5 1803+784: trajectory of Ca in rectangular coordinates . . . 101
3.8 S5 1803+784: core separation versus time for geodetic data . . 106
3.9 S5 1803+784: Gaussian model fits 111
3.10 S5 1803+784: C0 and C1 time evolution of position angles . . 112
3.11 S5 1803+784: Ca and C2 time evolution of position angles . . 112
3.12 S5 1803+784: position angles 113
3.13 S5 1803+784: jet ridge line 114
3.14 S5 1803+784: position angles as function of frequency 115
3.15 S5 1803+784: Gaussian decomposition of the light curve . . . 119
3.16 S5 1803+784: Time lags of individual outbursts as functions of frequency. 119
3.17 [S5 1803+784: spectral evolution]S5 1803+784: Time evolution of the quasi-simultaneous spectra indices, calculated for the 4.8 GHz, 8 GHz, and 14.5 GHz frequencies. 120
3.18 S5 1803+784: periodicity analysis of core separation of C1 . . 125
3.19 S5 1803+784: time lags 127
3.20 S5 1803+784: Ca correlations 128
3.21 S5 1803+784: spread in the position angle 129
3.22 S5 1803+784: radio light curve 130
3.23 S5 1803+784: correlations in C1 132

3.24 S5 1803+784: periodicity analysis 133
3.25 S5 1803+784: periodicity analysis of core separation of C0 . . 137
3.26 S5 1803+784: periodicity analysis of core separation of C1 . . 138
3.27 S5 1803+784: periodicity analysis of position angle of C1 . . . 139
3.28 S5 1803+784: periodicity analysis of core separation of Ca . . 140
3.29 S5 1803+784: binary black hole model 142

4.1 Radio light curve of 0605-085 147
4.2 Radio light curve of 0605-085 - II 148
4.3 Search for periods in 0605-085 150
4.4 Amplitudes of the periods in 0605-085 - I 151
4.5 Amplitudes of the periods in 0605-085 - II 152
4.6 0605-085 spectral evolution 154
4.7 0605-085: Model-fit results at 15 GHz. 160
4.8 Core separation vs. time for 0606-085 161
4.9 0605-085: instant speeds 161
4.10 Flux-density of jet components for 0605-085 162
4.11 Trajectory of a stationary jet component of 0605-085 162
4.12 Trajectory of a stationary jet component of 0605-085 - II . . . 163
4.13 0605-085: changes of the position angles 163
4.14 0605-085: rectangular coordinates of C1 166

List of Tables

2.1 Detected periods for 3C 454.3 35
2.2 3C 454.3: Parameters of outbursts I - Cycle 2 44
2.3 3C 454.3: Parameters of outbursts II - Cycle 3 45
2.4 Component ejections in the jet of 3C 454.3 46
2.5 Detected periods for 3C 446 (2223-052) 50
2.6 3C 446: Parameters of outbursts 58
2.7 Detected periods for CTA 102 (2230+114) 63
2.8 CTA 102: Quasi-period in activity 67
2.9 CTA 102: Parameters of outbursts 70
2.10 Detected periods for 0133+476 (DA 55) 74
2.11 0133+476: Parameters of outbursts 79
2.12 Frequency-dependent core shifts 83

3.1 Model-fit results for S5 1803+784 94
3.2 Model-fit results for S5 1803+784 II 95
3.3 Model-fit results for S5 1803+784 III 96
3.4 Speeds of S5 1803+784 jet components 102
3.5 Model-fit results for S5 1803+784 obtained from the literature 103
3.6 Model-fit results for S5 1803+784 obtained from the literature II. 104
3.7 S5 1803+784: Parameters of outbursts 118
3.8 S5 1803+784: correlations 122
3.9 S5 1803+784: correlations II 122
3.10 S5 1803+784: correlations III 126
3.11 S5 1803+784: correlations IV 131
3.12 S5 1803+784: periodicities 136

4.1 0605-085: Parameters of outbursts 153

4.2 Speeds of 0605-085 jet components 157
4.3 Gaussian modelfits of 0605-085 164
4.4 0605-085:precession model 166

6.1 List of abbreviations 177

Bibliography

[1] Abraham, Z., & Carrara, E.A. 1998, ApJ, 496, 172

[2] Abraham, Z. 2000, A&A, 355, 915

[3] Agudo, I., Gómez, J. L., Martí, J. M. et al. 2001, ApJ, 549, 183

[4] Agudo, I., Bach, U., Krichbaum, T. P. et al. 2007, A&A, 476, 17

[5] Alberdi, A., Gómez, J. L., Marcaide, J. M., Marscher, A. P., Pérez-Torres, M. A. 2000, A&A, 361, 529

[6] Alexander, T. 1997, in Astronomical Time Series, ed. D. Maoz, A. Sternberg, and E.M. Leibowitz, (Dordrecht:Kluwer) 163

[7] Aller, H. D., Aller, M. F., Latimer, G. E., Hodge, P. E. 1985, ApJS, 59, 513

[8] Aller, M. F., Aller, H. D., Hughes, P. A., Latimer, G. E. 1999, ApJ, 512, 601

[9] Aller, M. F., Aller, H. D., Hughes, P. A. 2003, ApJ, 586, 33

[10] Aloy, M.Á., Martí, J.-M., Gómez, J.-L. et al. 2003, ApJ, 585, 109

[11] Antonucci, Robert 1993, ARA&A, 31, 473

[12] Barbieri, C., Omizzolo, S., Romano, G., Cristiani, S. 1985, A&A, 142, 316

[13] Barbieri, C., Vio, R., Cappellaro, E., Turatto, M. 1990, ApJ, 359, 63

[14] Belov, V. N., Hagen-Thorn, V. A., & Marchenko, S. G., Astrophysics, 30, 7, 1989

[15] Biretta, J. A., Moore, R. L., Cohen, M. H. 1986, ApJ, 308, 93

[16] Blandford, R. D. & Königl, A. 1979, ApJ, 232, 34

[17] Blom, J.J., Bloemen, H., Bennett, K. et al., 1995, A&A, 295, 330

[18] Bondi, M., Padrielli, L., Fanti, R. et al. 1996, A&AS, 120, 89

[19] Bondi, M., Padrielli, L., Fanti, R. et al. 1996a, A&A, 308, 415

[20] Bregman, J. N., Glassgold, A. E., Huggins, P. J. et al. 1986, ApJ, 301, 708

[21] Britzen, S., Witzel, A., Krichbaum, T. P., Muxlow, T. W. B. 1999, NewAR, 43, 751

[22] Britzen, S., Witzel, A., Krichbaum, T. P. et al. 2005, MNRAS, 362, 966

[23] Britzen, S., Krichbaum, T. P., Strom, R. G. et al. 2005, A&A, 444, 443

[24] Britzen, S., Meyer, V., Witzel, A. et al. 2006, the 8th European VLBI Network Symposium. September 26-29, 2006,Torun, Poland, 6

[25] Britzen, S., Vermeulen, R. C., Campbell, R. M. et al. 2008, A&A, 484, 119

[26] Britzen, S., Kudryavtseva, N.A., Beckert, T. et al. accepted for publication to Astronomy and Astrophysics journal

[27] Camenzind, M. & Krockenberger, M. 1992, A&A, 255, 59

[28] Caproni, A. & Abraham, Z. 2004, MNRAS, 349, 1218

[29] Caproni, A. & Abraham, Z. 2004a, ApJ, 602, 625

[30] Cawthorne, T.V., Wardle, J.F.C., Roberts, D.H., Gabuzda, D. C., Brown, L. F. 1993, ApJ, 416, 496

[31] Cawthorne, T.V. & Gabuzda, D.C. 1996, MNRAS, 278, 861

[32] Ciaramella, A., Bongardo, C., Aller, H.D., et al. 2004, A&A, 419, 485

[33] Cooper, N. J., Lister, M. L., Kochanczyk, M. D. 2007, ApJS, 171, 376

[34] Dent, W. A., Kapitzky, J. E., & Kojoian, G. 1974, AJ, 79, 1232

[35] Dent, W.A. & Kapitzky, J.E. 1976, AJ, 81, 1053

[36] Dhawan, V., Kellerman, K. I., Romney, J. D. 1998, ApJ, 498, 111

[37] Eckart, A., Witzel, A., Biermann, P. et al. 1986, A&A, 168, 17

[38] Eckart, A., Witzel, A., Biermann, P. et al. 1987, A&AS, 67, 121

[39] Edelson, R. A. & Krolik, J. H. 1988, ApJ, 333, 646

[40] Fan, J.H., Lin, R.G., Xie, G.Z. et al. 2002, A&A, 381, 1

[1981] Ferraz-Mello, S. 1981, AJ, 86, 619

[41] Fey, A. L. & Charlot, P. 2000, ApJS, 128, 17

[42] Fey, A. L., Boboltz, D. A., Gaume, R. A., Eubanks, T. M., Johnston, K. J. 2001, AJ, 121, 1741

[43] Flett, A.M. & Henderson, C. 1981, MNRAS, 194, 961

[44] Flett, A.M. & Henderson, C. 1983, MNRAS, 204, 1285

[45] Fomalont, E.B. 1999, in ASP Conf. Ser. 180: Synthesis Imaging in Radio Astronomy II, ed. G.B. Taylor, C.L. Carilli, & R.A. Perley, 301

[46] Gabuzda, D. C., Cawthorne, T. V., Roberts, D. H., Wardle, J. F. C., 1992, ApJ, 388, 40

[47] Gabuzda, D. C., Wardle, J. F. C., Roberts, D. H., Aller, M. F., Aller, H. D. 1994, ApJ, 435, 128

[48] Gómez, J. L., Alberdi, A., Marcaide, J. M. 1994, A&A, 284, 51

[49] Gómez, J.L., Martí, J.M.A., Marscher, A.P., Ibáñez, J.M.A. & Alberdi, A. 1997, ApJ, 482, 33

[50] Gómez, J.L., Marscher, A.P., Alberdi, A. 1999, ApJ, 522, 74

[51] Gómez, J.L. 2005, Future Directions in High Resolution Astronomy: The 10th Anniversary of the VLBA, ASP Conference Proceedings, 340, 13

[52] Gubbay, J., Legg, A.J., Robertson, D.S. et al. 1977, ApJ, 215, 20

[53] Guirado, J. C., Marcaide, J. M., Alberdi, A. et al. 1995, AJ, 110, 2586

[54] Guirado, J.C., Ros, E., Jones, D.L., et al. 2001, A&A, 371, 766

[55] Hagen-Thorn, V. A., Larionov, V. M., Jorstad, S. G., Larionova, E. G. 2002, AJ, 124, 3031

[56] Hardee, P. E. & Norman, M. L. 1988, ApJ, 334, 70

[57] Hewitt, A. & Burbidge, G. 1980, ApJS, 43, 57

[58] Hughes, P.A., Aller, H.D., Aller, M.F. 1985, ApJ, 298, 301

[59] Hughes, P. A., Aller, H. D., Aller, M. F. 1992, ApJ, 396, 469

[60] Hutchings, J. B., Morris, S. C., Gower, Ann C., Lister, M. L. 1994, PASP, 106, 642

[61] Impey, C. D., Lawrence, C. R., Tapia, S. 1991, ApJ, 375, 46

[62] Jorstad, S.G., Marscher, A.P., Mattox, J.R. et al. 2001, ApJS, 134, 181

[63] Jorstad, S. G., Marscher, A. P., Lister, M. L. et al. 2005, AJ, 130, 1418

[64] Jurkevich, I. 1971 AP&SS, 13, 154

[65] Kellermann, K.I., Vermeulen, R.C., Zensus, J.A., Cohen, M. H. 1998, AJ, 115, 1295

[66] Kellermann, K.I., Lister, M.L., Homan, D.C. et al. 2004, ApJ, 609, 539

[67] Kelly, B. C., Hughes, P. A., Aller, H. D., Aller, M. F. 2003, ApJ, 591, 695

[68] Kidger, M. R., Takalo, L., Sillanpää, A. 1992, A&A, 264, 32

[69] Kidger, M. R. 2000, AJ, 119, 2053

[70] Klare, J., Zensus, J. A., Lobanov, A. P. et al. 2005, Future Directions in High Resolution Astronomy: The 10th Anniversary of the VLBA, ASP Conference Proceedings, 340, 40

[71] Kollgaard, R. I., Wardle, J. F. C., Roberts, D. H., Gabuzda, D. C. 1992, AJ, 104, 1687

[72] Königl, A. 1981, ApJ, 243, 700

[73] Kovalev, Y. Y., Lobanov, A. P., Pushkarev, A. B., Zensus, J. A. 2008, A&A, 483, 759

[74] Krichbaum, T. P. 1990, Parsec-scale radio jets, Proceedings of a workshop, held at NRAO, Socorro, New Mexico, October 17-18, 1989, 83

[75] Kudryavtseva, N. A. & Pyatunina, T. B. 2006, ARep, 50, 1

[76] Kudryavtseva, Nadezhda, Britzen, S., Witzel, A. et al. 2006a, the 8th European VLBI Network Symposium. September 26-29, 2006,Torun, Poland, 7

[77] Kudryavtseva, N.A., Britzen, S., Witzel, A. et al. close to submission to Astronomy and Astrophysics journal

[78] Lainela, M. & Valtaoja, E. 1993, ApJ, 416, 485

[79] Lainela, M., Takalo, L. O., Sillanpää, A. et al. 1999, ApJ, 521, 561

[80] Lara, L., Alberdi, A., Marcaide, J. M., Muxlow, T. W. B. 1994, A&A, 285, 393

[81] Lawrence, C. R., Pearson, T. J., Readhead, A. C. S., Unwin, S. C. 1986, AJ, 91, 494

[82] Lerner, M. S., Baath, L. B., Inoue, M. et al. 1993, A&A, 280, 117

[83] Lind K. R. & Blandford R. D. 1985, ApJ, 295, 358

[84] Lister, M. L. 2001, ApJ, 561, 676

[85] Lister, M. L. 2005, Future Directions in High Resolution Astronomy: The 10th Anniversary of the VLBA, ASP Conference Proceedings, 340, 20

[86] Lister, M. L. & Homan, D. C. 2005, AJ, 130, 1389

[87] Lobanov, A.P. 1998, A&A, 330, 79

[88] Lobanov, A. P. & Zensus, J. A. 1999, ApJ, 521, 509

[89] Lobanov, A. P. & Roland, J. 2002, 6th European VLBI Network Symposium on New Developments in VLBI Science and Technology, held in Bonn, June 25th-28th 2002, 121

[90] Lobanov, A. P. & Roland, J. 2005, A&A, 431, 831

[91] Marcaide, J. M. & Shapiro, I. I. 1984, ApJ, 276, 56

[92] Marcaide, J.M., Alberdi, A., Ros, E. et al. 1995, Nature, 373, 44

[93] Marcaide, J. M., Alberdi, A., Ros, E. et al. 1995a, Science, 270, 1475

[94] Marcaide, J. M.; Alberdi, A.; Ros, E. et al. 1997, ApJ, 486, 31

[95] Marscher, A.P. & Gear, W.K. 1985, ApJ, 298, 114

[96] Marscher, A.P. 1996, Blazar continuum variability Astronomical Society of the Pacific Conference Series 110, Proceedings of an international workshop held at Florida International University, Miami, Florida, USA, 4-7 February 1996, 248

[97] Marscher, A. P., Travis, J. P., Gear, W. K., 1992, in Valtaoja E., Valtonen M., eds, Variability of Blazars. Cambridge Univ. Press, Cambridge , 85

[98] Marscher, A. P. 2005, Memorie della Societa Astronomica Italiana, 76, 13

[99] Medd, W. J., Andrew, B. H., Harvey, G. A., Locke, J. L. 1972, MmRAS, 77, 109

[100] Mead, A.R.G., Ballard, K.R., Brand, P.W.J.L. et al. 1990, A&AS, 83, 183

[101] Meyer, V., Britzen, S., Witzel, A. et al. 2007, Astronomische Nachrichten, 328, 672

[102] Meyer, V., Diplomarbeit 2007a, University of Cologne

[103] Nesci, R., Massaro, E., Rossi, C. et al. 2005, AJ, 130, 1466

[104] Nolan, P. L., Bertsch, D. L., Fichtel, C. E. et al. 1993, ApJ, 414, 82

[105] Owen, F. N., Odea, C. P., Inoue, M., Eilek, J. A. 1985, ApJ, 294, 85O

[106] Padrielli, L., Romney, J. D., Bartel, N. et al. 1986, A&A, 165, 53

[107] Padrielli, L., Eastman, W., Gregorini, L., Mantovani, F., Spangler, S. 1991 A&A, 249, 351

[108] Paragi, Z., Fejes, I., Frey, S. 2000, International VLBI Service for Geodesy and Astrometry: 2000 General Meeting Proceedings, 342

[109] Pauliny-Toth, I. I. K., Porcas, R. W., Zensus, J. A., Kellermann, K. I. 1984, IAUS, 110, 149

[110] Pauliny-Toth, I.I.K., Porcas, R.W., Zensus, J.A. et al. 1987, Nature, 328, 778

[111] Pérez-Torres, M.A., Marcaide, J.M., Guirado, J.C. et al. 2000, A&A, 360, 161

[112] Pian, E., Foschini, L., Beckmann, V. et al. 2006, A&A, 449, 21

[113] Piner, B. G., Mahmud, M., Fey, A. L., Gospodinova, K. 2007, AJ, 133, 2357

[114] Polatidis, A. G., Wilkinson, P. N., Xu, W. et al. 1995, ApJS, 98, 1

[115] Pyatunina, T.B., Marchenko, S.G., Marscher, A.P. et al. 2000, A&A, 358, 451

[116] Pyatunina, T.B., Rachimov, I.A., Zborovskii, A.A. et al. 2003, High Energy Blazar Astronomy, ASP Conference Proceedings, 299, 89

[117] Pyatunina, T.B., Kudryavtseva, N.A., Gabuzda, D.C. et al. 2006, MNRAS, 373, 1470

[118] Pyatunina, T.B., Kudryavtseva, N.A., Gabuzda, D.C. et al. 2007, MNRAS, 381, 797

[119] Pursimo, T., Takalo, L. O., Sillanpää, A. et al. 2000, A&AS, 146, 141

[120] Qian, Shan-Jie, Kudryavtseva, N. A., Britzen, S. et al. 2007, ChJAA, 7, 364

[121] Raiteri, C. M., Villata, M., Aller, H. D. et. al. 2001, A&A, 377, 396

[122] Rantakyrö, F. T., Bååth, L. B., Backer, D. C. et al. 1998, A&AS, 131, 451

[123] Rantakyrö, F.T., Wiik, K., Tornikoski, M., Valtaoja, E., Bååth, L. B. 2003, A&A, 405, 473

[124] Reuter, H.-P., Kramer, C., Sievers, A. et al. 1997, A&AS, 122, 271

[125] Rickett, B. J., Lazio, T. J. W., Ghigo, F. D. 2006, ApJS, 165, 439

[126] Rieger, F. M. 2005, ChJAS, 5, 305

[127] Rieger, F. M. 2007, Ap&SS, 309, 271

[128] Rodriguez, C., Taylor, G. B., Zavala, R. T. et al. 2006, ApJ, 646, 49

[129] Roland, J., Britzen, S., Kudryavtseva, N. A., Witzel, A., Karouzos, M. 2008, A&A, 483, 125

[130] Ros, E., Marcaide, J.M., Guirado, J.C., Sardón, E., Shapiro, I. I. 2000, A&A, 356, 357

[131] Ros, E., Marcaide, J.M., Guirado, J.C., Pérez-Torres, M. A. 2001, A&A, 376, 1090

[132] Ros, E. & Lobanov, A. P. Proceedings of the 15th Workshop Meeting on European VLBI for Geodesy and Astrometry, 208

[133] Rossetti, A., Mantovani, F., Dallacasa, D., Fanti, C., Fanti, R. 2005, A&A, 434, 449

[134] Rusk, R. 1990, Royal Astronomical Society of Canada Journal, 84, 199

[135] Salonen, E., Lehto, H., Urpo, S. et al. 1983, A&AS, 51, 47

[136] Salonen, E., Terasranta, H., Urpo, S. et al. 1987, A&AS, 70, 409

[137] Sambruna, R.M. 1997, ApJ, 487, 536

[138] Sambruna, R. M., Gambill, J. K., Maraschi, L. et al. 2004, ApJ, 608, 698

[139] Savolainen, T., Wiik, K., Valtaoja, E., Jorstad, S. G., Marscher, A. P. 2002, A&A, 394, 851

[140] Savolainen, T., Wiik, K., Valtaoja, E., Tornikoski, M. 2006, A&A, 446, 71

[141] Schalinski, C. J., Alef, W., Witzel, A., Campbell, J., Schuh, H. 1988. The Impact of VLBI on Astrophysics and Geophysics; Proceedings of the 129th IAU Symposium, Cambridge, MA, May 10-15, 1987, 359

[142] Scott, W. K., Fomalont, E. B., Horiuchi, S. et al. 2004, ApJS, 155, 33

[143] Shepherd, M.C., 1997, Astronomical Data Analysis Software and Systems VI, A.S.P. Conference Series, Vol. 125, Gareth Hunt and H. E. Payne, eds., 77

[144] Sholomitsky, G.B. 1965, IBVS, 83, 1

[145] Sillanpää, A., Haarala, S., Valtonen, M. J., Sundelius, B., Byrd, G. G. 1988, ApJ, 325, 628

[146] Spencer, R. E., McDowell, J. C., Charlesworth, M. et al. 1989, MNRAS, 240, 657

[147] Steppe H., Salter C.J., Chini R. et al. 1988, A&AS, 75, 317

[148] Steppe H., Liechti S., Mauersberger R. et al. 1992, A&AS, 96, 441

[149] Steppe, H., Paubert, G., Sievers, A. et al. 1993, A&AS, 102, 611

[150] Stickel, M., Fried, J. W., Kühr, H. 1993, A&AS, 98, 393

[151] Stickel, M., Kühr, H., Fried, J. W. 1993a, A&AS, 97, 483

[152] Stirling, A. M., Cawthorne, T. V., Stevens, J. A. et al. 2003, MNRAS, 341, 405

[153] Strom, R. G. & Biermann, P. L. 1991, A&A, 242, 313

[154] Su, C.Y. 2001, ChA&A, 25, 153

[155] Sudou, H., Iguchi, S., Murata, Y., Taniguchi, Y. 2002, The Proceedings of the IAU 8th Asian-Pacific Regional Meeting, Volume II, 403

[156] Sundelius, B., Wahde, M., Lehto, H. J., Valtonen, M. J. 1997, ApJ, 484, 180

[157] Teräsranta, H., Tornikoski, M., Mujunen, A. et al., 1998, A&AS, 132, 305

[158] Terzian, Y. 1966, AJ, 71, 1030

[159] Tornikoski, M., Valtaoja, E., Teräsranta, H. et al. 1994, A&A, 289, 673

[160] Tornikoski, M., Valtaoja, E., Teräsranta, H. et al. 1996, A&AS, 116, 157

[161] Urry, C. M. & Padovani, P. 1995, PASP, 107, 803

[162] Urry, C. 2004, AGN Physics with the Sloan Digital Sky Survey, Proceedings of a conference held in Princeton, NJ, USA, 27-31 July 2003, ASP Conference Series, 311, 49

[163] Valtaoja, E., Lähteenmäki, A., Teräsranta, H. & Lainela, M. 1999, ApJS, 120, 95

[164] Villata, M., Raiteri, C.M., Balonek, T.J. et al. 2006, A&A 453, 817

[165] Villata, M., Raiteri, C. M., Aller, M. F. et al. 2007, A&A, 464, 5

[166] Wagner, Stefan J. 1999, BL Lac Phenomenon, a conference held 22-26 June, 1998 in Turku, Finland, 279.

[167] Wehrle, A. E. & Cohen, M. H. 1989, ApJ, 346, 69

[168] Wehrle, A. E., Piner, B. G., Unwin, S. C. et al. 2001, ApJS, 133, 297

[169] Witzel, A., Schalinski, C. J., Johnston, K. J. et al. 1988, A&A, 206, 245

[170] Webb, J.R., Smith, A.G., Leacock, R.J. et al. 1988, AJ, 95, 374

[171] Wright, A. E., Ables, J. G., Allen, D. A. 1983, MNRAS, 205, 793

[172] Wu, Sheng-Yin 1988, ChA&A, 12, 283

[173] Zensus, J. A., Cohen, M. H., Unwin, S. C. 1995, ApJ, 443, 35

[174] Zensus, J. A. 1997, ARA&A, 35, 607

[175] Zensus, J. A., Ros, E., Kellermann, K. I.et al. 2002, AJ, 124, 662

[176] Zhou, J.F., Hong, X.Y., Jiang, D.R. & Venturi, T. 2000, ApJ, 541, 13

Chapter 7

Acknowledgements

I would like to express my gratitude and to thank all the people who supported and inspired me during my thesis work and without whom this thesis would not be possible.

First of all I would like to thank my supervisor Priv. Doz. Dr. Silke Britzen and my advisor Dr. Arno Witzel, who guided me and support during the last few years. I thank you for so enjoyable and inspiring scientific discussions that we had during my thesis work.

I would like to express my gratitude to Prof. Dr. Anton Zensus and Prof. Dr. Andreas Eckart for being the members of examination board. I would like to thank Prof. Dr. Anton Zensus for so many valuable advices and providing me opportunity to prepare this work in the VLBI group. I would like to thank Prof. Dr. Andreas Eckart for such great hospitality in Köln University and such interesting discussions about active galactic nuclei, Sgr A* and science in general.

I am specially grateful to the directors of the Max-Planck-Institut für Radioastronomie who supported me by the International Max Planck Research School (IMPRS) for Astronomy and Astrophysics.

I would like to thank entire VLBI group of Max-Planck-Institut für Radioastronomie. First of all I would like to thank Dr. Thomas Krichbaum, who guided me and support during the last few years. Special thanks to Dr. Eduardo Ros for support, giving me so many important advices, teaching me how to organize scientific work, and unforgettable discussions about everything, starting from active galactic nuclei and science to philosophical problems of life in general. I am grateful to Dr. Richard Porcas and Dr. John McKean for such great help with conference talk preparations. Especially I

thank Dr. Richard Porcas for advices how to make a good research and to be critical of yourself. I thank Dr. Alan Roy for being a member of my thesis committee and for his support. I would like to express my gratitude to Dr. Thomas Beckert, Simone Bernhart, Violette Impelizzeri, Nicola Marchili, Dr. Manolis Angelakis, Veronika Meyer, Marios Karouzos for so wonderful scientific discussions about active galactic nuclei, as well as science in general. I thank Christian Fromm for making the pictures and for amazing questions which sometimes is really difficult to answer. Special thanks to Simone Bernhart for help with the German language. I indebted to Dr. Alex Kraus and Dr. Manolis Angelakis for great help with the Effelsberg observations. Special thanks to Gabi Breuer who helped me so much with every question.

Many thanks to my Bonn-time friends Kora, Chin-Shin, Simone, Violette, John, Marios, Oxana, Hyunjoo, Nicola, Kazi, and Manolis. I would also like to thank my friends Andrei A. Bliok, Konstantin Molodykh, Sagar Godambe, Sanhita Aditi Joshi, Adam Deller, Dr. Willem A. Baan, and Marcel Hoek whom I was really happy to meet during the last years and meeting whom changed me and my world view.

Finally, I wish to thank my parents and grandparents, Inara Kudrjavceva, Prof. Aleksandrs Ogurcovs and Valentina Aksjonova for their endless love and support.

Chapter 8

Erklärung

Ich versichere, daß ich die von mir vorgelegte Dissertation selbständig angefertigt, die benutzen Quellen und Hilfsmittel vollständig angegeben und die Stellen der Arbeit – einschließlich Tabellen, Karten und Abbildungen–, die anderen Werken im Wortlaut oder dem Sinn nach entnommen sind, in jedem Einzelfall als Entlehnung kenntlich gemacht habe; daß diese Dissertation noch keiner anderen Fakultät oder Universität zur Prüfung vorgelegen hat; daß sie – abgesehen von unten angegebenen Teilpublikationen – noch nicht veröffentlicht worden ist sowie, daß ich eine solche Veröffentlichung vor Abschluß des Promotionsverfahrens nicht vornehmen werde. Die Bestimmungen dieser Promotionsverfahrens sind mir bekannt. Die von mir vorgelegte Dissertation ist von Prof. Dr. Andreas Eckart betreut worden.

Köln, 14.08.2008

Teilpublikationen

1. *N.A. Kudryavtseva*, S. Britzen, A. Witzel, E. Ros, M. Karouzos, M.F. Aller, H.D. Aller, H. Teräsranta, A. Eckart, J.A. Zensus, "A possible helical trajectory in a strongly periodic quasar 0605-085", close to submission to Astronomy and Astrophysics journal.

2. S. Britzen, *N.A. Kudryavtseva*, T. Beckert, A. Witzel, R.M. Campbell, E. Ros, M. Karouzos, A. Mehta, M. Aller, H. Aller, J.A. Zensus, "Stationary components in S5 1803+784. A twisted jet model applied to S5 1803+784", accepted for publication to Astronomy and Astrophysics journal.

3. J. Roland, S. Britzen, *N.A. Kudryavtseva*, J. Laskar, A. Witzel, "Modelling nuclei of radio galaxies from VLBI radio observations. Applications to the BL Lac object 1803+784", Astronomy and Astrophysics, v. 483, pp. 125-135, 2008

4. T.B. Pyatunina, *N.A. Kudryavtseva*, D.C. Gabuzda, S.G. Jorstad, M.F. Aller, H.D. Aller, H. Terasranta, "Frequency-dependent time delays for strong outbursts in selected blazars from the Metsahovi and UMRAO monitoring data bases - II", MNRAS, v. 381, 2, pp. 797-808, 2007

5. S.J. Qian, *N.A. Kudryavtseva*, S. Britzen, T.P. Krichbaum, L. Gao, A. Witzel, J.A. Zensus, M.F. Aller, H.D. Aller, X.Z. Zhang, "A possible periodicity in the Radio Light Curves of 3C 454.3", Chinese Journal of Astronomy and Astrophysics, v.7, 3, pp. 364-374, 2007

6. *N.A. Kudryavtseva*, S. Britzen, A. Witzel, E. Ros, M.F. Aller, H.D. Aller, R.M. Campbell, J.A. Zensus, A. Eckart, J. Roland, A. Mehta, "The kinematics of S5 1803+784", proceedings of the 8th European VLBI Network Symposium held in Torun, Poland, September 2006a, p. 7

7. T.B. Pyatunina, *N.A. Kudryavtseva*, D.C. Gabuzda, S.G. Jorstad, M.F. Aller, H.D. Aller, H. Terasranta, "Frequency-dependent time-delays for strong outbursts in selected blazars from the Metsahovi and the University of Michigan Radio Astronomy Observatory monitoring databases - I", MNRAS, v.373, 4, pp. 1470-1482, 2006

8. *N.A. Kudryavtseva*, T.B. Pyatunina, "A search for periodicity in the light curves of selected blazars", Astronomy Reports, v.50, 1, p. 1-11, 2006.

8.1 Curriculum Vitae

Persönliche Daten

Name: Nadezhda Alekseevna Kudryavtseva
Geburtstdatum: 01.12.1980
Geburtsort: Riga, Lettland
Staatsangehörigkeit: russisch

Anschrift:

Nadia Kudryavtseva
Max-Planck-Institut für Radioastronomie
Auf dem Hügel 69
53121 Bonn Germany
(+49)-228525281
nadia@mpifr-bonn.mpg.de

Schulische und universitäre Ausbildung:

June 1997: Abschluss am Physikalischen und Mathematischen Lyceum Nr. 239, St. Petersbug, Russland

September 1997 – June 2002: Studium der Astronomie an der Fakultät für Mathematik und Mechanik an der Staatlichen Universität von St. Petersburg, Russland; Abschluss: Master

seit September 2002: Wissenschafltiche Mitarbeiterin am Astronomischen Institut der Staatlichen Universität von St. Petersburg, Russland

September/Oktober 2003: Studienaufenthalt am University College Cork, Irland auf Einladung von Dr. Denise Gabuzda, Projekt "Helical magnetic fields in active galactic nuclei" (Helikale Magnetfelder in Aktiven Galaxienkernen)

seit September 2005: Doktorandin in der VLBI-Gruppe des Max-Planck-Instituts für Radioastronomie in Bonn unter Betreuung von Priv. Doz. Dr. Silke Britzen, Prof. Dr. J.A. Zensus und Prof. Dr. Andreas Eckhart; Arbeitsgebiet: Untersuchung der zentralen Regionen von Aktiven Galaxienkernen; Mitglied der International Max Planck Research School